JOURNAL OF THE

Electrochemical Society

ol. 115, No. 4 April 1968

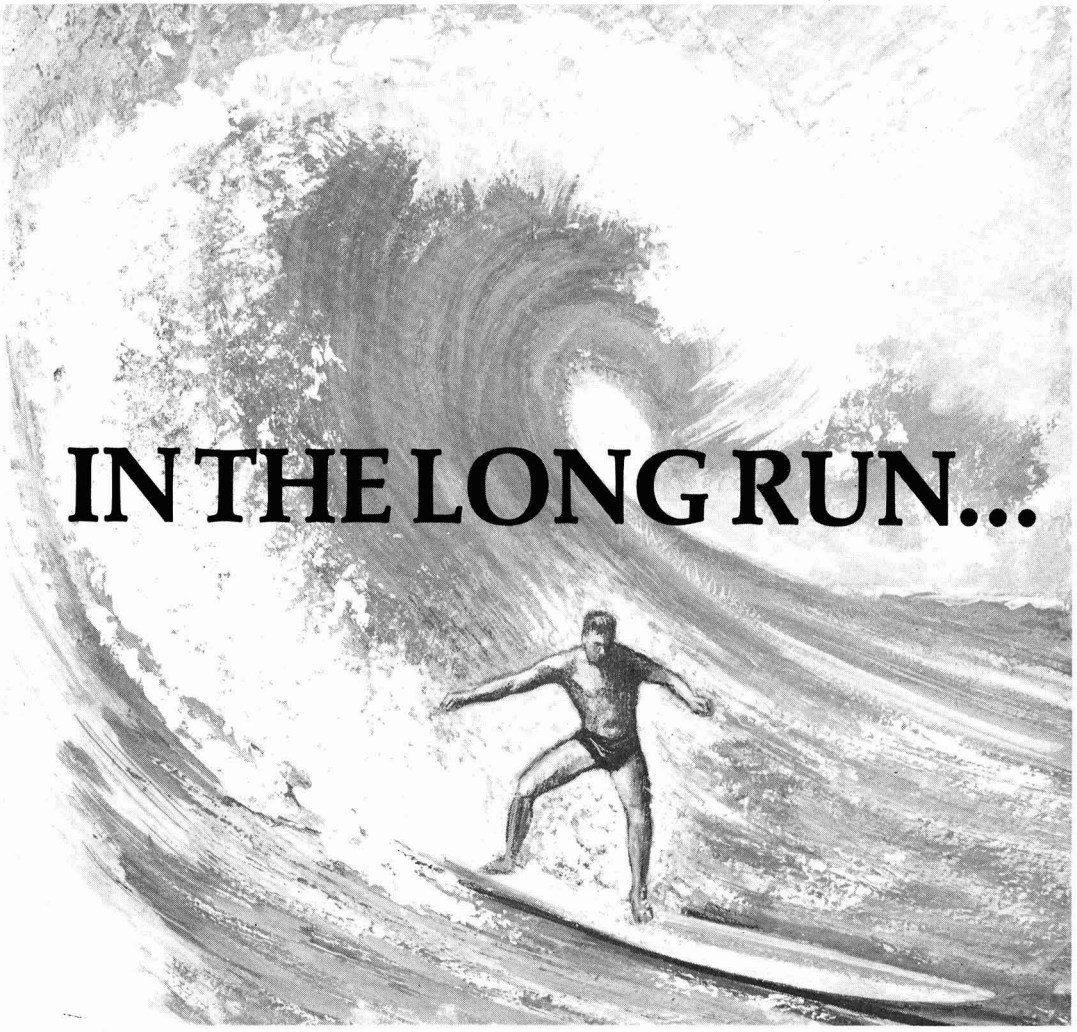

You'll be ahead with GLC Anodes for chlor-alkali production.

PRODUCTS YOU CAN TRUST ® GLC

GRAPHITE PRODUCTS DIVISION
GREAT LAKES CARBON CORPORATION
299 Park Avenue • New York, N.Y. 10017
OFFICES AND AGENTS FROM COAST-TO-COAST AND AROUND THE WORLD

Great Lakes Carbon Corporation is one of the world's largest manufacturers of graphite for electrochemical and electrothermic processes—and for aerospace, nuclear, metallurgical and other industrial uses.

You can improve the battery performance of everything from radios to rockets when you use Webril* nonwoven fabrics for separators and absorbers

If primary and secondary battery systems are to perform much more reliably, they must inhibit dendrite growth and passage. Be permitted free ionic passage. Remain unaffected by acid or alkali. Loss of active plate material must be minimized. And electrolyte contact with plates must be assured. Webril non-woven fabrics can do all this.

They have been performance-tested for over millions of hours in mercury, silver-zinc, silver-cadmium, lead-acid, cuprous-chloride, and nickel-cadmium systems.

The unusually broad line of fine Webril products gives you greater design flexibility . . . even in fuel cells. You can choose from polypropylene, Dynel**, nylon, highly purified cotton, modified cellulose, and other fibers.

Find out more today. Write to Electrical Specialities Department.

KENDALL

The Kendall Company
Fiber Products Division
Walpole, Mass. 02081

*Registered Trademark of The Kendall Company
**Union Carbide Corp. trademark for its modacrylic fiber

JOURNAL OF THE

C. L. Faust, Chairman, Publication Committee

Charles B. Moore, Director of Publications

EDITORIAL STAFF

Cecil V. King, Editor

Norman Hackerman, Technical Editor

Ruth G. Sterns, Managing Editor

Julius Kleror, Book Review Editor

Daniel J. Immediato, Assistant Editor

ADVERTISING OFFICE

Daniel J. Immediato, Assistant Editor

APRIL 1968

ELECTROCHEMICAL SCIENCE

TECHNICAL PAPERS

TECHNICAL NOTES

SOLID STATE SCIENCE

TECHNICAL PAPERS

ELECTROCHEMICAL SOCIETY

Vol. 115 • No. 4

Manuscripts submitted to the Journal should be sent, in triplicate, to the Editorial Office at 30 East 42 St., New York, N. Y., 10017. They should conform to the revised Instructions to Authors available from Society Headquarters. Manuscripts so submitted, as well as papers presented before a National technical meeting, become the property of the Society and may not be published elsewhere in whole or in part without written permission of the Society. Address such requests to the Society Director of Publications.

The Electrochemical Society does not maintain a supply of reprints of papers appearing in its Journal. A photoprint copy of any particular paper, however, may be obtained by corresponding direct with the Engineering Societies Library, 345 E. 47 St., New York, N. Y., 10017.

Inquiries re positive microfilm copies of volumes should be addressed to University Microfilms, Inc., 300 N. Zeeb St., Ann Arbor, Mich.

Walter J. Johnson, Inc., 111 Fifth Ave., New York, N. Y., 10003, have reprint rights to out-of-print volumes of the Journal, and also have available for sale back volumes and single issues, with the exception of the current calendar year. Anyone interested in securing back copies should correspond direct with them.

Published monthly by The Electrochemical Society, Inc., at 215 Canal St., Manchester, N. H.; Executive Offices, Editorial Office and Circulation Dept., and Advertising Office at 30 East 42 St., New York, N. Y., 10017, combining the JOURNAL and TRANSACTIONS OF THE ELECTROCHEMICAL SOCIETY. Statements and opinions given in articles and papers in the JOURNAL OF THE ELECTROCHEMICAL SOCIETY are those of the contributors, and The Electrochemical Society assumes no responsibility for them.

Claims for missing numbers will not be allowed if received more than 60 days from date of mailing plus time normally required for postal delivery of JOURNAL and claim. No claims allowed because of failure to notify the Circulation Dept., The Electrochemical Society, 30 East 42 St., New York, N. Y., 10017, of a change of address, or because copy is "missing from files." Subscription to members as part of membership service; subscription to nonmembers $24.00 plus $1.50 for postage outside U.S and Canada Single copies $1 70 to members, $2.25 to nonmembers.

Entered as second-class matter at the Post Office at Manchester N. H., under the act of August 24, 1912. Postage paid at Manchester, N. H.

Report from

BELL LABORATORIES

The Anatomy of Vibrating Crystals

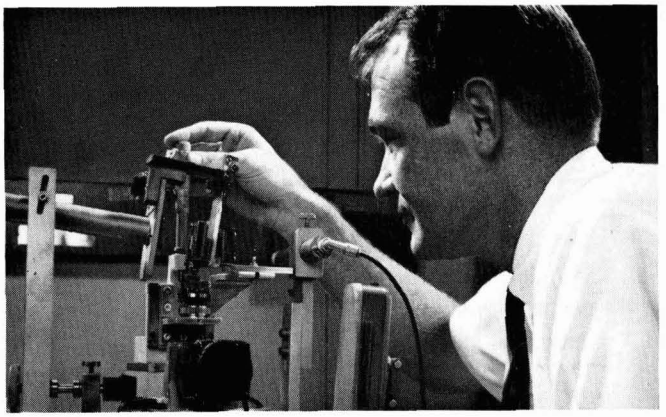

William J. Spencer with equipment for detecting vibrational modes. Through sloped tube, left, X-rays strike crystal (in frame at center of apparatus). A portion of beam is diffracted by the crystal (drawing, right) and passes through the slit. The main X-ray beam is stopped at the edge of the slit. During exposure, crystal and film are driven from left to right so that entire crystal area is photographed. The X-ray beam is set at a particular angle to the crystal (the Bragg angle), which for good crystals produces a diffracted intensity greater than at other orientations. Vibrating the crystal reduces destructive interference and increases diffracted-beam intensity.

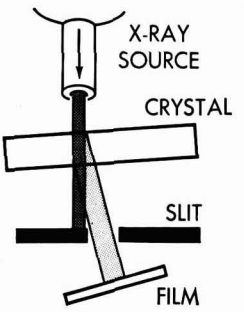

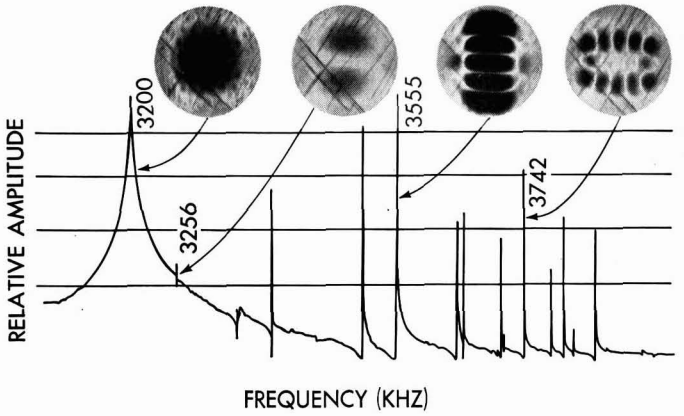

X-ray photographs of a crystal showing four modes of vibration selected from the many modes indicated by the resonance peaks on the curve. Dark areas are due to displacement antinodes in the vibrating quartz disk. Diagonal lines are intrinsic crystal-lattice defects.

In modern amplifiers, filters, and oscillators, piezoelectric crystals are widely used to select signals at certain frequencies. Such crystals —of quartz, for example—provide electronic selectivity because of their ability to convert electric waves into mechanical waves, and mechanical waves back into electric waves, at certain resonant frequencies. For any particular application, the principal resonant frequency is determined by the size and geometry of the crystal, but in addition to this principal vibrational mode, the crystal will vibrate in a number of other modes.

To suppress these unwanted resonances, they must first be identified. And until recently we did this by observing patterns created when a crystal, coated with a fine powder, is vibrated at high intensity. Since the powder collects where the crystal surface is stationary, a vibrational pattern or mode is revealed. But the pattern at such high signal levels may not correspond to the modes produced at the lower signal levels of actual operation.

Recently, however, W.J. Spencer, at the Bell Telephone Laboratories location in Allentown, Pa., has used X-ray diffraction as an accurate and flexible method of observing vibrational amplitude under realistic conditions. The new method depends on the fact that the intensity of diffracted X-rays is extremely sensitive to distortion of the crystal lattice. The transmission of the rays is greater through vibrating regions of a crystal, and this darkens such areas on the X-ray film. Stationary regions are light.

Vibration amplitudes of less than a millionth of an inch are easily observed. Thus, we obtain a quick, sensitive photographic record of displacement associated with any crystal resonance under conditions simulating actual use. This technique helps us design better filters for the Bell System.

Bell Telephone Laboratories
Research and Development Unit of the Bell System

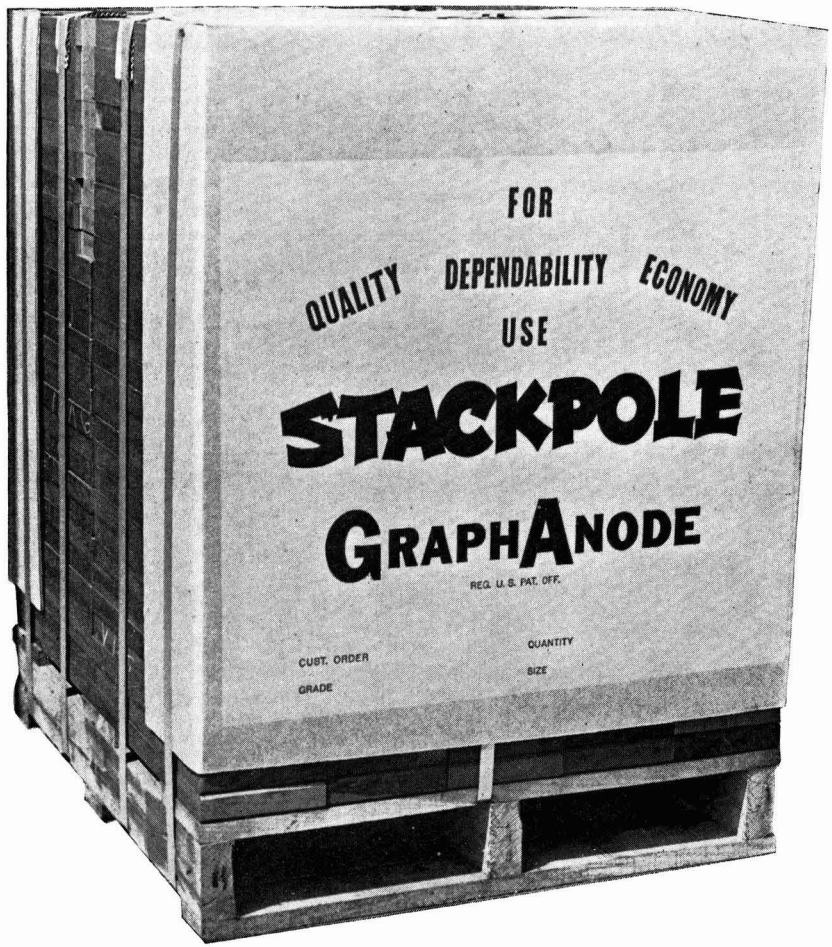

GET A LOAD OF THIS

If you're looking for improved performance, greater productivity, and reduced operating costs, investigate the savings of Stackpole GraphAnodes®. Rigid manufacturing controls assure material uniformity and permit proper cell alignment that makes for even wear and longer life. Whatever your anode needs, Stackpole GraphAnodes® can help you cut costs. Try a load. Write or call: Stackpole Carbon Company, Carbon Division, St. Marys, Pennsylvania 15857. Phone: 814-781-8463. TWX: 510-693-4511.

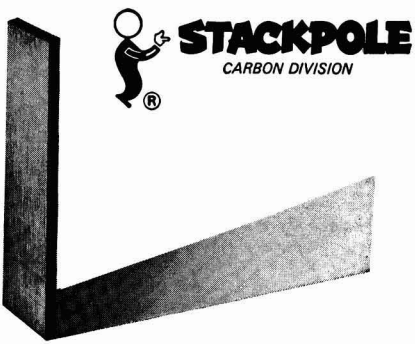

NATIONAL

electrolytic anodes have a new name...

UCAR

...the new name for 70 years of graphite/anode know-how

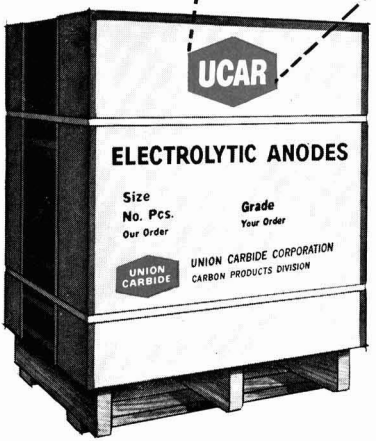

Today's field reports indicate that NATIONAL—pardon us, UCAR—electrolytic anodes are doing an outstanding job of meeting the increasingly critical needs of cell operators.

UCAR anode quality reaches back to the pioneering of manufactured graphite in 1897. This unique experience is a distinctive reason why—over the years—cell operators have received maximum value per dollar from anodes produced by Union Carbide.

The change is in name only—people, product, service, and everything else remain the same. Through research and development, and production control, we will continue working to improve UCAR anodes.

UNION CARBIDE

"Ucar" and "National" are registered trademarks of
UNION CARBIDE CORPORATION
CARBON PRODUCTS DIVISION
270 Park Avenue • New York 10017
Export: International Department, New York
In Canada: Union Carbide Canada Ltd., Toronto

JOURNAL OF THE ELECTROCHEMICAL SOCIETY

ELECTROCHEMICAL SCIENCE

APRIL 1968

Journal of The Electrochemical Society is the fundamental research journal serving the interdisciplinary interests of chemistry, physics, electronics, biology, medicine, and engineering as they pertain to electrochemistry and to electrochemical phenomena. Written for the research scientist in industry, government, the independent laboratory and the university, it publishes contributed Technical Papers, Technical Notes and Brief Communications describing current basic research of original character, and is edited in two sections: 1) ***Electrochemical Science*** including such areas as batteries, fuel cells, corrosion and corrosion mechanisms, electrothermics and metallurgy, electrodeposition, electroorganic reactions and phenomena, and allied work of theoretical electrochemical nature. 2) ***Solid State Science*** including such areas as dielectrics and insulation, electrothermics and metallurgy, semiconductors, luminescence and related solid state Investigations.

Measurement of Electrolyte Gradient in an Operating Fuel Cell

M. L. Miller and H. J. Fornasar

Central Research Division, American Cyanamid Company, Stamford, Connecticut

ABSTRACT

Reference mercury, mercuric oxide electrodes have been developed for monitoring the concentration of potassium hydroxide in hydrogen-oxygen fuel cells operating at 27° and 70°C.

The distribution of electrolyte in the matrix of an operating fuel cell can be measured by imbedding appropriate reference electrodes in various parts of the fuel cell matrix. Knowledge of the concentration distribution in a fuel cell is important for understanding the operation of a cell and for designing fuel cells. Mercury, mercuric oxide electrodes have been shown to be reversible to hydroxyl ions (1, 2) at concentrations less than 0.85*M*. These electrodes will be useful for measuring the distribution of potassium hydroxide in fuel cells provided the electrodes can be shown to respond to hydroxyl ions at the higher concentrations encountered in an operating fuel cell.

Experimental

Fuel cells.—Two types of hydrogen-oxygen fuel cells were used in the development of reference electrodes. One was a small poly(methylmethacrylate) cell similar to the cell described by Bone (3). A circular area of matrix 2.5 cm in diameter was exposed to gases. This cell was run at room temperature without temperature control, and at 70°C in an air bath. A second cell, which is described in ref. (4), was made from stainless steel plates separated by polytetrafluoroethylene gaskets. The surface of the matrix exposed to gases in this cell was 5.0 x 5.0 cm. The larger cell was heated externally by two electric heaters, and its temperature was regulated by a temperature-control unit connected to a thermocouple within the cell. The pattern of gas flow in each cell was determined by the position of the ports through which gases entered and left the cell. These positions are shown in Fig. 1. The catalytic electrodes were Cyanamid AB1 electrodes (5). The gel membrane was made from crosslinked poly(vinyl alcohol) and contained filler (6). The matrix asbestos was Fuel Cell Asbestos supplied by Johns-Manville.

Calibration electrodes.—The ability of mercury, mercuric oxide electrodes to respond to changes in hydroxyl ion concentration at high concentrations of potassium hydroxide was determined in a series of experiments which made use of relatively large electrodes, referred to as "calibration electrodes." The calibration electrodes were made from 2.4 mm diameter glass tubes, one end of which was covered with a poly(vinyl alcohol) membrane (unfilled) which allowed transport of water and ions, but retained solid materials within the tube. A slurry of mercury and mercuric oxide (prepared by triturating with a solution of potassium hydroxide having the concentration of the standard solution in which the electrode was to be used) was placed in the electrode tube together with a platinum wire that had been gold plated and then amalgamated.

Electrodes were made with potasisum hydroxide solutions containing 3.25, 4.67, 6.00, 6.56, 7.40, 8.85, and 10.58 moles of potassium hydroxide per kg of water. These electrodes were compared in the cell

$$\text{Hg, HgO KOH}(C_1)::\text{KOH}(C_2)\text{HgO, Hg} \qquad [1]$$

at 27° or 70°C. The potential of cell 1 was measured with a Minneapolis Honeywell Potentiometer—Model 2700. The concentration of the reference solution, C_1, was arbitrarily chosen as 6.56*M* (6*N* at 27°). The concentration C_2 ranged from 3.25 to 10.58*M*. The potentials (in millivolts) of cell 1 at 27° and at 70°C are plotted against C_2 (in molality) in Fig. 2.

Microelectrodes and matrix assembly.—The electrodes used to determine the relationship between potential and concentration were not suited for use in an operating fuel cell. Electrodes had to be small enough to insert into a cell without disrupting the gas-tight seal of the gaskets. Gold-plated platinum wires (0.075 mm diameter), amalgamated with mercury to hold the mercury immobile during operation, were used to make these small electrodes. The tip of each amalgamated platinum wire was painted with a slurry of mercuric oxide in a potassium hydroxide solution having the concentration of the solution to be used in the fuel cell (~8*M*). Laminated matrices (maximum thickness one millimeter) incorporating microelectrodes and gel membranes were assembled as shown in the inserts in Fig. 3. A new set of microelectrodes was used whenever a cell was reassembled. When cells were run at room temperature, polytetrafluoroethylene-coated glass filter sheets (Bel-Art Company, Pequannock, New Jersey) separated the outer reference elecrodes from the catalytic electrodes. When cells were run at 70°C with gel membranes, the filter sheets (which decomposed in alkali at high temperatures) were replaced by thin gel membranes. When cells were run at 70°C with Fuel Cell Asbestos the outer reference electrodes were placed in a pocket in the outer layer of asbestos. During assembly, a wick of etched polytetrafluoroethylene felt was inserted in the matrix laminate to serve as a salt bridge. The polytetrafluoroethylene felt (American Felt Company) was etched by treatment with a 10% solution of potassium in liquid ammonia at −50°C. Between measurements the wick was kept dry and covered to prevent carbonate formation. Prior to making a potential

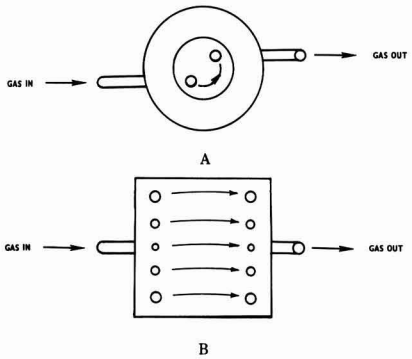

Fig. 1. Location of gas ports in (A) 2.5 cm diameter cell and (B) 5 x 5 cm cell.

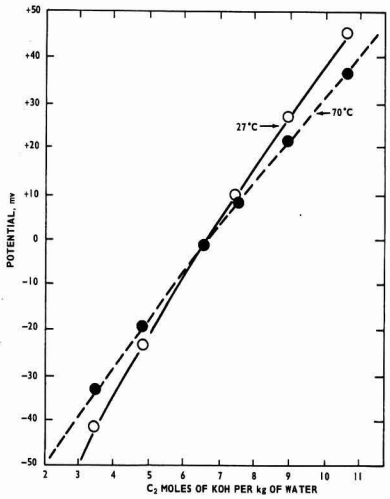

Fig. 2. Relationship between the potential of cell 1 and C_2 when C_1 is 6.56*M*.

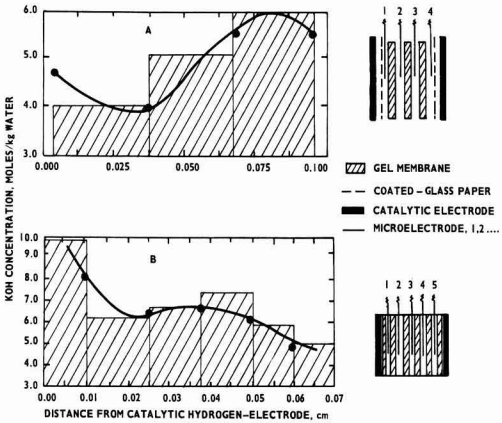

Fig. 3. Electrolyte profiles in cells with gel-type matrices. Cross-hatched areas obtained by titration, —●— by reference electrode. (A) 2.5 cm cell 27°C, 65 ma/cm², 0.623v. Gas flows: O_2—21.5 ml/min, H_2—41.0 ml/min. (B) 5 x 5 cm, 70°C, 100 ma/cm², 0.816v. Gas flows: O_2—350 ml/min, H_2—350 ml/min.

measurement the wick was wetted thoroughly with 6.56*M* potassium hydroxide solution.

The arrangement of a fuel cell containing reference electrodes is shown in Fig. 4. Cells at room temperature, approximately 27°C, were run without temperature control. At 70°C the external reference electrode was held at 27°C and the cell temperature was thermostatically controlled at 70°C. The fuel-cell current was interrupted for approximately 30 sec when the potential was measured. After each potential reading the fuel-cell current was restored and the fuel cell was allowed to re-equilibrate (2-3 min) before proceeding with the next reading. Electrolyte concentrations in the matrix were estimated from measured potentials by the plots in Fig. 2.

Reliability of the microelectrodes.—Comparison with calibrating electrodes.—Microelectrodes were placed between asbestos sheets soaked in various concentrations of potassium hydroxide. These sheets were placed in a fuel cell in which no gas was flowing and the potential difference between the microelectrodes in the cell and the large calibrating electrodes outside of the cell was measured. The potential differences

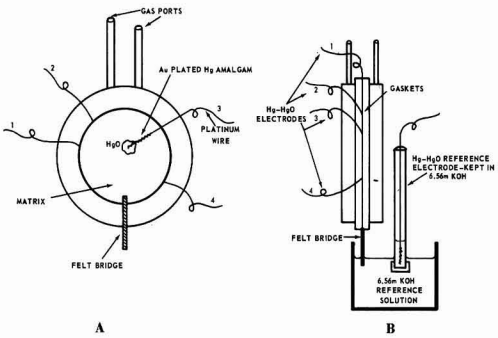

Fig. 4. Assembly for observing potassium hydroxide concentrations in an operating fuel-cell matrix. (A) Section of matrix laminate containing microelectrodes; (B) fuel cell and reference electrodes.

observed in this test at 26° and at 70°C were identical with the potential difference between the large calibration electrodes shown in Fig. 2.

Reliability of microelectrodes in an operating fuel cell.—To determine the reliability of the microelectrodes in an operating fuel cell, it was necessary to find a technique for determining the concentration of potassium hydroxide in the individual layers of the matrix by another method. One method for doing this was to freeze the fuel cell rapidly while running and to separate and titrate individual layers of the frozen matrix. Fuel Cell Asbestos could not be used for this test because the asbestos lacks wet strength. Gel membranes are, however, much stronger than asbestos when saturated with potassium hydroxide solution. Laminates consisting of gel membranes can be frozen, separated and titrated without tearing. In previous work at 27° and 70°C we operated fuel cells containing gel membranes, and fuel cells containing Fuel Cell Asbestos, continuously under constant loads of 55 to 150 ma/cm² for periods of 150-200 hr. In these tests the cells containing gel membranes performed exactly the same as the cells containing Fuel Cell Asbestos.

A fuel cell was assembled using a gel matrix which consisted of three layers of gel membrane each approximately 0.4 mm thick. A microelectrode was placed at each interface. The cell was run at constant current for 24 to 48 hr after the microelectrodes indicated that a stable distribution of electrolyte had been established in the cell. Then the cell (while running) was placed in a polyethylene bag and quickly frozen in a dry ice-alcohol mixture. The rapid freezing slowed diffusion of hydroxyl ions and enabled the cell to be disassembled without changing the electrolyte distribution. The laminated gel matrix was separated into layers, the thickness of each layer was measured and the hydroxyl content of each layer was determined by titration. The concentration of potassium hydroxide in each layer was computed by assuming that a section of gel membrane, 5 x 5 x 0.025 cm, after compression and use in a fuel cell, contained 0.03 ml of electrolyte solution. This figure was obtained by titrating a membrane (saturated with 6.56*M* potassium hydroxide solution) that had been compressed in a fuel cell. Since cells used at 70°C were assembled at room temperature the same figure was used for calculating the volume of electrolyte in membranes used at 70°C. The concentration of electrolyte in the fluid contained in the catalytic electrodes in contact with the membranes was not measured. Figure 3A is a plot of the concentration gradient that was observed after 48 hr in a 2.5 cm diameter cell operated at ambient temperature (~27°C). Figure 3B is a similar plot of the concentration gradient in a 5 x 5 cm cell operated at 70°C. Filled circles represent concentrations mea-

sured with microelectrodes, and crosshatched areas represent concentrations measured by titration. The good agreement between the two types of data attests to the reliability of the microelectrodes at both temperatures.

Effect of continuous operation in a fuel cell on microelectrodes.—Two other questions remain to be answered before we can use microelectrodes with confidence to monitor fuel-cell concentrations. These questions are: Does the presence of microelectrodes effect the operation of a fuel cell, and can the microelectrodes withstand continuous exposure to a fuel cell environment? In order to answer these questions a fuel cell containing microelectrodes was run at ambient temperature for 215 hr. During this time the output averaged 0.537v at 100 ma/cm^2. This is the same performance that we observed with similar fuel cells operating under the same conditions but without microelectrodes. At the end of this test neither the fuel cell nor the microelectrodes showed visible deterioration. Microelectrodes removed from a fuel cell after 200 hr of continuous operation gave correct readings in standard potassium hydroxide solutions.

Results

Effect of gas-flow ratios.—The foregoing experiments establish the reliability of microelectrodes in an operating fuel cell. These electrodes can now be used to measure the effect of operational variables on electrolyte distribution. In the work reported in this paper the electrodes were placed in the center of the matrix. Thus the profile of electrolyte concentrations which we observed is the electrolyte profile in the center of the cell between the catalytic hydrogen and the catalytic oxygen electrodes. The fraction of water removed by the hydrogen (or oxygen) gas streams in an operating fuel cell can be varied by varying the ratio of hydrogen to oxygen in the total gas flow. The data in Fig. 5 show that in a 2.5 cm cell operating at 0.70v with gel matrix, the fraction of water removed by the hydrogen (or oxygen) gas stream is proportional to the percentage of hydrogen (or oxygen) in the total gas flow. The data in Fig. 5 were obtained by passing the emergent gas streams through gas-absorption bottles filled with anhydrous calcium sulfate and weighing the bottles. Before the cell was used for this test it was allowed to operate at a steady rate of 0.70v and 70 ma/cm^2 for 24 hr at a 1:1 (v:v) gas-flow ratio. Then the water collection was started and the gas-flow ratio varied from 3:1 to 1:1 to 1:3 keeping the total gas flow (hydrogen plus oxygen) constant at 74-83 ml/min. In all these tests the amount of water recovered was within 5% of the total water formed.

Figure 6 shows the electrolyte profiles observed under similar conditions in a 2.5 cm diameter cell using Fuel Cell Asbestos at room temperature. Notice that the general character of the profile is the same at the various gas ratios indicating that the transfer of water through the matrix is rapid compared to the changes in other variables that influence the shape of the electrolyte profile.

Effect of current density.—The effect of current density on electrolyte was observed in a 5 x 5 cm cell (asbestos matrix) that was run continuously for 348 hr at 70°C. During this time the cell was operated

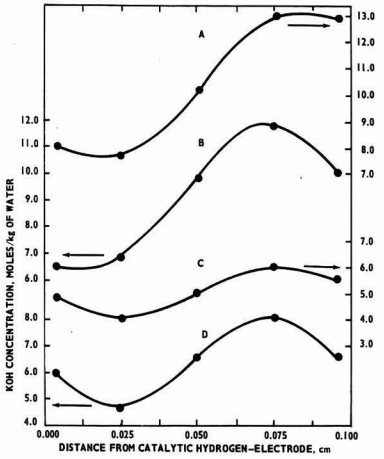

Fig. 6. Electrolyte profiles in a 2.5 cm cell, with Fuel Cell Asbestos matrix at 27°C. (A) Gas flows: O_2—10.5 ml/min, H_2—73.5 ml/min, 55 ma/cm^2, 0.550v; (B) gas flows: O_2—22.5 ml/min, H_2—67.5 ml/min, 57 ma/cm^2, 0.568v; (C) gas flows: O_2—43 ml/min, H_2—43 ml/min, 64 ma/cm^2, 0.641v; (D) gas flows: O_2—60 ml/min, H_2—30 ml/min, 60 ma/cm^2, 0.594v. Arrows indicate scale to be used in reading a particular plot.

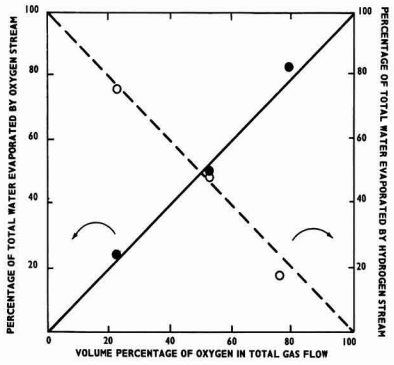

Fig. 5. Percentage of water evaporated by oxygen and hydrogen gas-streams for a 2.5 cm diameter cell at 27°C. Total gas flow 74-83 ml/min, current 70 ma/cm^2, 0.70v, gel matrix. Arrows indicate scale to be used in reading a particular plot.

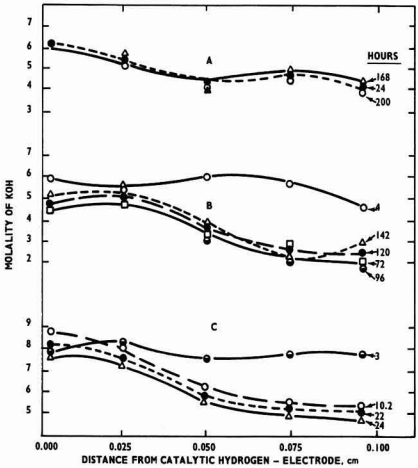

Fig. 7. Electrolyte profiles in 5 x 5 cm cell after various times of operation at a steady performance. (A) ~27°C, 100 ma/cm^2, 0.710v; (B) 70°C, 100 ma/cm^2, 0.810v; (C) 70°C, 100 ma/cm^2, 0.831v.

for periods of 3 to 4 days at loads ranging from 50 to 150 ma (±1 ma) per cm^2. These tests showed that current densities between 50 and 150 ma/cm^2 have little effect on the shape of the electrolyte profile in the center of this cell.

Time required to establish a steady-state electrolyte distribution.—Experiments showed that although a stable operation with respect to current and voltage was established in minutes after start-up of operation, the attainment of a steady state in the electrolyte distribution required between 3 and 6 hr in the 2.5 cm diameter cell at room temperature and approximately the same length of time in the 5 x 5 cm cell at 70°C. However, some other cells which had less uniform gas flow-patterns required as long as 48 hr to reach a steady electrolyte distribution. The time required to attain a steady electrolyte profile and the constancy of the shape of this profile, once attained, is shown by the curves in Fig. 7.

It is evident that the general shape of the concentration profiles in Fig. 3A and 3B is characteristic of the particular cell used and is not radically altered by changes in temperature (Fig. 7), flow rate (Fig. 6), or current density (Fig. 7). The difference in shape of the profiles in Fig. 3A and 3B appears to be related to the difference in gas-flow patterns in the two types of cells. Apparently it will be necessary to measure concentration profiles over the whole face of the exposed matrix, not just through the center, in order to understand the operation of the cell.

Acknowledgment

The authors wish to thank Dr. R. G. Haldeman and Professor B. E. Conway for advice and encouragement during the course of this work, Mr. J. Skogman for carrying out the water-balance experiments, Dr. K. E. Olsen, Mr. D. Gershberg, and Mrs. D. Bernstein for valuable suggestions in connection with the preparation of the manuscript. They are also indebted to Professor Conway for suggesting the mercury, mercuric oxide electrodes to them.

Manuscript received Sept. 19, 1967; revised manuscript received Nov. 3, 1967.

Any discussion of this paper will appear in a Discussion Section to be published in the December 1968 JOURNAL.

REFERENCES

1. Ming Chow, *J. Am. Chem. Soc.*, **42**, 488 (1920).
2. G. J. Samuelson and D. J. Brown, *ibid.*, **57**, 2711 (1935).
3. J. S. Bone, *Proc. Ann. Power Sources Conf.*, **14**, 62 (1960).
4. R. G. Haldeman, W. A. Barber, W. P. Coleman, J. DiPalma, D. Gershberg, and J. P. Ward, NASA Report #CR 54436.
5. R. G. Haldeman, W. P. Colman, S. H. Langer, and W. A. Barber, Advan. Chem. Ser. No. 49, Am. Chem. Soc., Washington, D. C. (1965).
6. M. L. Miller, J. Skogman, and J. E. Sutherland, U.S. Pat. 3,265,536 (1966).

The Alkaline Manganese Dioxide Electrode

II. The Charge Process

David Boden,* C. J. Venuto,* D. Wisler, and R. B. Wylie

ESB Incorporated, Research Center, Yardley, Pennsylvania

ABSTRACT

The reactions occurring during the discharge and charge of manganese dioxide electrodes in 7M KOH are studied by x-ray diffraction and charge and discharge curves. The discharge at first results in the formation of an amorphous oxide by incorporation of protons and electrons into the MnO_2 lattice. Then the amorphous compound is electroreduced to give Mn_3O_4 and finally $Mn(OH)_2$ depending on the electrode potential. When electrodes are recharged, the amorphous phase is converted to MnO_2 whereas the Mn_3O_4 remains unchanged in the electrode. It is proposed that on recharge $Mn(OH)_2$ is oxidized to Mn_3O_4. The cause of failure of electrodes during cycling seems to be the formation of a film of Mn_3O_4 around the electrical contact wire.

The reactions occurring during the discharge of a manganese dioxide electrode in alkaline electrolyte have been investigated by several workers (1-7). However, the charge process, after the electrodes have been discharged, appears not to have been studied. This is of practical importance in understanding the reactions which limit the performance of the rechargeable alkaline manganese dioxide battery.

It is observed in these cells, that if the discharge is limited to a relatively small fraction of the total manganese dioxide capacity, a considerable number of discharge/charge cycles can be obtained, whereas if the cells are deeply discharged, very few cycles are obtainable. At the present time, the source of this restriction is unknown. It was thought desirable, therefore, to investigate the reactions occurring at the manganese dioxide electrode when it is charged after varying degrees of partial discharge.

This paper presents the results of a study whereby x-ray crystallography, chemical analysis, and the analysis of potential-time transients are used to characterize the reactions.

* Electrochemical Society Active Member.

Experimental

The method of preparation, the size and weight of the electrodes, and the electrolytic cell were identical to those described previously (7). Available oxygen analyses conducted by the arsenious acid method (8) showed the sample of MnO_2 had an empirical formula of $MnO_{1.92}$, giving the electrodes a calculated capacity of 0.45 amp-hr based on the following reaction

$$MnO_{1.92} + 1.92\,H_2O + 1.84e = Mn(OH)_2 + 1.84\,OH^-$$

All the discharge and charge operations were carried out at 25°C in 7M KOH solution and the electrode potentials were recorded against a Hg/HgO reference electrode in the same electrolyte using a Texas Instruments Servoriter in conjunction with a Hewlett Packard vacuum tube voltmeter Model 412A.

X-ray Crystallographic Analyses

Groups of electrodes were discharged at 5 ma · cm^{-2} (12.5 ma total) in 7M KOH at 25°C in 0.1C increments of the theoretical capacity (0.1C, 0.2C, 0.3C, *etc.*). Representative samples were removed from the

Table I. *d* Values of MnO_2 electrodes during discharge and charge

Dis. to	Chg. to																			
1.00 C				3.35	3.11											2.40				
														2						
0.90 C				3.35	3.11									2.43		2.40				
	1.00 C			3.35	3.11							2.44				2.40				
0.80 C				3.35	3.11						2.47					2.40		2.19		
	0.90 C			3.34	3.11							2.44				2.40				
	1.00 C			3.34	3.11										2.41					
0.70 C				3.34					2.51							2.40		2.19		
	0.80 C			3.34	3.11					2.49		2.44								2.18
	0.90 C			3.34	3.11							2.44								
	1.00 C			3.34	3.11										2.41					
0.60 C				3.35				2.53								2.40				
	0.70 C			3.34					2.51							2.40		2.20		
	0.80 C			3.34		2.98					2.48					2.40				2.18
	0.90 C			3.34	3.11		2.75							2.43						
	1.00 C			3.34	3.11										2.42					
0.50 C				3.35			2.75				2.48					2.41				
	0.60 C	4.92		3.34	3.07	2.87	2.75				2.48							2.19		
	0.70 C	4.90		3.34	3.07	2.87	2.74				2.48									
	0.80 C			3.34	3.07		2.74				2.48									
	0.90 C			3.34	3.07		2.74				2.48				2.42					
	1.00 C			3.35	3.07		2.74				2.48				2.42					
0.40 C		4.90	4.71	3.35	3.07	2.87	2.76				2.48					2.41		2.36		
	0.50 C	4.90	4.70	3.35	3.07	2.87	2.76				2.48					2.41		2.35		
	0.70 C	4.90		3.35	3.08	2.87	2.75				2.48	2.45						2.35		
	0.80 C	4.90		3.35	3.08	2.88	2.75				2.48	2.46						2.36		
	1.00 C	4.90		3.35	3.08	2.88	2.75				2.48							2.36		
0.30 C		4.90	4.71	3.35	3.07	2.87	2.76				2.48					2.41		2.36		
	0.40 C	4.90	4.72	3.35	3.08	2.88	2.76				2.48	2.45						2.36		
	0.60 C	4.90		3.35	3.08	2.88	2.75				2.48	2.45						2.36		
	0.80 C	4.90		3.35	3.08	2.88	2.75				2.48							2.35		
	1.00 C	4.89		3.35	3.08	2.88	2.75				2.48					2.41		2.35		
0.20 C		4.92	4.71	3.35	3.08	2.87	2.76				2.48	2.45						2.36		
	0.40 C	4.90	4.73	3.35	3.08	2.88	2.76				2.48	2.46						2.36		
	0.60 C	4.90		3.35	3.08	2.89	2.76				2.48	2.45				2.41		2.35		
	0.80 C	4.90		3.35	3.08	2.87	2.76				2.48	2.45						2.35		
	1.00 C	4.90		3.35	3.08	2.88	2.76				2.48	2.45						2.35		
Dis. to	Chg. to																			
0.1 C		4.90	4.71	3.35	3.08	2.87	2.76				2.48	2.45						2.36		
	0.20 C	4.90	4.71	3.35	3.08	2.87	2.76				2.48	2.45						2.36		
	0.40 C	4.90	4.72	3.34	3.08	2.88	2.76				2.48	2.45						2.36		
	0.60 C	4.90		3.35	3.08	2.88	2.76				2.48	2.45						2.36		
	0.80 C	4.90		3.35	3.08	2.88	2.75				2.48							2.35		
	1.00 C	4.90		3.34	3.07	2.87	2.75				2.48	2.45						2.35		
0.0 C		4.90	4.71	3.34	3.08	2.86	2.76				2.47	2.45						2.36		
	0.20 C	4.90	4.71	3.35	3.08	2.87	2.76				2.48	2.45						2.36		
	0.40 C	4.90		3.34	3.07	2.87	2.76				2.48	2.45						2.35		
	0.60 C	4.90		3.35	3.08	2.88	2.75				2.48							2.36		
	0.90 C	4.90		3.35	3.08	2.87	2.76				2.48	2.45						2.35		
	1.00 C	4.89		3.35	3.08	2.88	2.75				2.48							2.35		

cells at each 0.1C increment, crushed, and analyzed with a G. E. XRD-5 x-ray diffractometer using vanadium filtered Cr $K\alpha$ radiation. Groups of electrodes which had been partially discharged were then charged at 2.5 ma · cm^{-2} and samples were analyzed as before at 0.1C charge intervals. For example, a group of electrodes would be discharged to 0.5C with samples being analyzed at 0.9, 0.8, 0.7, 0.6, and 0.5C. The remaining electrodes would then be charged with samples being withdrawn for x-ray analysis at 0.6, 0.7, 0.8, 0.9C, and C. No washing or drying procedures were carried out and all the samples were immediately x-rayed after being covered with a thin film prepared from Duco cement and acetone to prevent possible atmospheric oxidation during the analysis. The *d*-values calculated from the x-ray patterns are shown in Table I. For comparison, the ASTM values for the *d* values and the relative intensities of the peaks for various manganese oxides are shown in Table II.

The starting material is essentially γMnO_2 but there appears to be a small amount of βMnO_2 present as indicated by the line at $d = 3.11$Å. As discharge proceeds the lattice expansion noted previously (7) is again observed and is most clearly seen in the peaks at 2.43 and 2.14Å in the electrode discharged to 0.90 of its calculated capacity ($MnO_{1.82}$). The peak originally appearing at 2.43Å shifts through 2.47, 2.51, and 2.53Å before any new phase is observed, while the peak originally appearing at 2.11Å shifts through 2.14, 2.17, and 2.19Å in the same discharge period. No new compounds are identified in the x-ray pattern until the electrodes have been discharged to 0.5C ($MnO_{1.46}$) at which point Mn_3O_4 is produced. By referring to the x-ray diffraction patterns of Fig. 1, it can be seen that as the discharge proceeds, the x-ray peaks become increasingly less well defined which is characteristic of the take up of protons by the lattice to form an amorphous, strained phase according to

$$MnO_2 + nH^+ + ne \rightarrow MnO_{2-n}(OH)_n \quad [1]$$

or

$$MnO_2 + nH_2O + ne \rightarrow MnO_{2-n}(OH)_n + nOH^- \quad [2]$$

At a discharge depth equivalent to 0.50C peaks characteristic of Mn_3O_4 can be seen.

If electrodes which have been reduced in the range of 1.0 to 0.60C are recharged, the original γMnO_2 structure is regained although there is still evidence of some residual lattice expansion. This is evident from examination of Table I and also from Fig. 2 which shows the x-ray diffraction patterns of an electrode being charged after an initial discharge to 0.6C. Since chemical analyses were not performed on the charged electrodes, the data are given in terms of the fraction

Table II. *d* Values and relative intensities of manganese oxides

γMnO_2 ASTM 14-644		γMn_2O_3 ASTM 6-0540		Mn_3O_4 ASTM 1-1127		$Mn(OH)_2$ ASTM 12-696	
d (Å)	I/I_1	*d* (Å)	I/I_1	*d* (Å)	I/I_1	*d* (Å)	I/I_1
3.96	100	4.93	40	4.92	20	4.726	100
2.60	60	3.08	60	3.08	31	2.870	18
				2.87	8		
2.42	100	2.74	70	2.75	63	2.453	40
2.32	80	2.48	100	2.48	100	2.361	6
				2.36	13		
				2.03	15		
2.12	80	2.39	40	1.79	18	1.825	25
				1.70	5		
				1.64	5		
2.05	40	2.03	20	1.57	50	1.658	6
						1.567	4
1.637	80	1.83	30	1.54	50	1.381	8
				1.47	3	1.346	4
1.605	60	1.79	20	1.44	18	1.180	4
1.486	10			1.38	4		
				1.34	8		
				1.30	3		
1.422	60	1.59	30	1.28	13		
1.362	40	1.55	60	1.24	4B		
1.306	10						
1.250	10			1.19	5B		
1.211	Tr			1.12	4		
1.169	Tr						
1.104	Tr						
1.066	40						

				2.11											1.63								
	2.14																						
	2.14									1.68		1.66											
			2.12							1.68					1.63								
2.17		2.13								1.68						1.62							
	2.15										1.67	1.66											
			2.12							1.68					1.63								
									1.685	1.68													
									1.685	1.68		1.66											
	2.15										1.67	1.66											
		2.13								1.68				1.64									
								1.69		1.68										1.54	1.53		1.43
								1.69		1.68													
										1.68													
		2.13									1.67		1.65										
			2.12							1.68				1.64									
								1.69		1.68													
					2.03	1.796				1.68								1.575					
2.17					2.03					1.68										1.54			
					2.03					1.68										1.54			
		2.13			2.03					1.68													
		2.13			2.03					1.68													
					2.03	1.825	1.794																
					2.03		1.79	1.70						1.64				1.573	1.56	1.54			
					2.03		1.79	1.70		1.68				1.64				1.573		1.54		1.44	
					2.03	1.82	1.79	1.70		1.68				1.64				1.574		1.54			
					2.03	1.83	1.79	1.70		1.68	1							1.57		1.54		1.44	
					2.03	1.83	1.79																
					2.04	1.82	1.79	1.70			1.67			1.64			1.58			1.54		1.44	
					2.04	1.82	1.79				1.67			1.64				1.57		1.54		1.44	
					2.03	1.82	1.79	1.70			1.67			1.64				1.57		1.54		1.44	
					2.03		1.79	1.70			1.67			1.64				1.57		1.54		1.44	
					2.03	1.82	1.79	1.70		1.68				1.64				1.574	1.56				
					2.04	1.82	1.79	1.70			1.67			1.64				1.57		1.54		1.44	
					2.03	1.82	1.79	1.70			1.67			1.64				1.57		1.54			
					2.03	1.83	1.79	1.70			1.67			1.64				1.57		1.54		1.44	
					2.03	1.83	1.79	1.70			1.67			1.64				1.57		1.54			
					2.03	1.825	1.79	1.70			1.615	1.657		1.64				1.57	1.56				
					2.03	1.82	1.79																
					2.04	1.82	1.79	1.70			1.67	1		1.64			1.58			1.54		1.44	
					2.03	1.82	1.79	1.70			1.67			1.64				1.57		1.54			
					2.03	1.82	1.79	1.70			1.68			1.64			1.58			1.54		1.44	
					2.03	1.82	1.79	1.70			1.68			1.64				1.57		1.54			
					2.03	1.825	1.796	1.698			1.67	1.657		1.64				1.57	1.56				
					2.03	1.82	1.79	1.70			1.68	1.66		1.64				1.57		1.54			
					2.03		1.79	1.70			1.67			1.64				1.57		1.54			
					2.03	1.82	1.79	1.70			1.67			1.64				1.57		1.54		1.44	
					2.03	1.82	1.79	1.70			1.67			1.64				1.57		1.54			
					2.03		1.79	1.70						1.64				1.57		1.54		1.44	

of the theoretical capacity based on the number of coulombs passed. The diffraction peaks characteristic of γMnO_2 reappear in the fully charged electrode but are considerably less well defined than in the original starting material.

When electrodes are discharged to 0.50 of their initial capacity ($MnO_{1.46}$) diffraction peaks characteristic of Mn_3O_4 are found. The reasons for assigning these peaks to Mn_3O_4 and not to γMn_2O_3 were discussed in a previous paper (7). Mn_3O_4 is probably formed by electroreduction of the amorphous phase according to

$$3MnO_{2-n}(OH)_n + (4-3n)H^+ + (4-3n)e = Mn_3O_4 + 2H_2O \quad [3]$$

When electrodes containing Mn_3O_4 are recharged, it is seen that the Mn_3O_4 remains unchanged in the final product (see Table I). Figure 3 shows the x-ray diffraction patterns of an electrode which had been discharged to 0.0C ($MnO_{1.16}$) and then recharged. It is clear that the x-ray diffraction peaks corresponding to Mn_3O_4 are unaffected thus indicating that no oxidation of the Mn_3O_4 has been accomplished, whereas the peaks characteristic of $Mn(OH)_2$ have disappeared. To further substantiate the stability of Mn_3O_4 in this electrolyte, two electrodes, each prepared from a mix of 0.7g of spectrographically pure (99.99%) Mn_3O_4 and 0.1g of graphite were charged for 12 hr. Available oxygen analysis on the charged electrodes yielded 99.7 and 99.6% Mn_3O_4 remaining.

As the discharge proceeds to 0.4C ($MnO_{1.34}$), $Mn(OH)_2$ is observed to form and this continues until the electrode is fully discharged. X-ray patterns of an electrode undergoing full discharge are shown in Fig. 4. The question arises as to whether $Mn(OH)_2$ is formed by reduction of Mn_3O_4 or from the amorphous phase previously discussed. Earlier work (7) has shown that Mn_3O_4 cannot be discharged under the conditions of this experiment and thus it is concluded that $Mn(OH)_2$ forms as a result of reduction of the amorphous phase according to

$$MnO_{2-n}(OH)_n + (2-n)H^+ + (2-n)e = Mn(OH)_2 \quad [4]$$

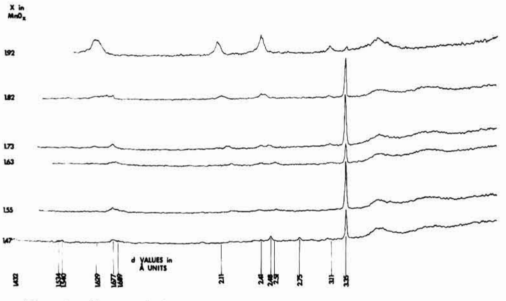

Fig. 1. X-ray diffraction patterns of γMnO_2 electrodes discharged in increments to $MnO_{1.47}$.

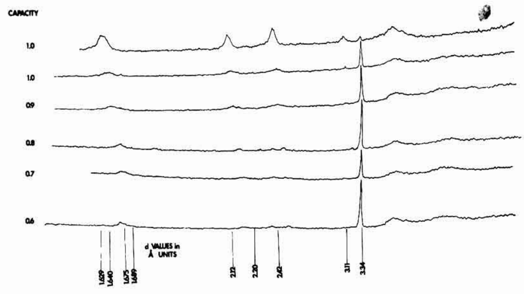

Fig. 2. X-ray diffraction patterns of γMnO_2 electrodes charging in 0.1C increments after discharge to 0.6C. Top curve shows original starting material for reference.

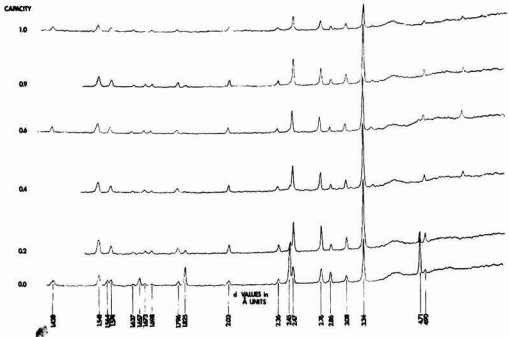

Fig. 3. X-ray diffraction patterns of γMnO_2 electrodes charging in increments after discharge to 0.0C.

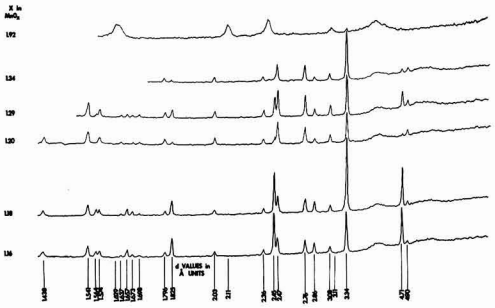

Fig. 4. X-ray diffraction patterns of γMnO_2 electrodes discharged in increments to $MnO_{1.16}$.

When the fully discharged electrode is charged the $Mn(OH)_2$ peaks disappear as shown in Fig. 3 and no new peaks are observed in the x-ray patterns. This indicates that $Mn(OH)_2$ is oxidized to either Mn_3O_4 or to the amorphous phase noted previously. We think it unlikely that $Mn(OH)_2$ can be oxidized to the amorphous phase directly without passing through the lower oxide Mn_3O_4. It is thus probable that $Mn(OH)_2$ is oxidized to Mn_3O_4 which then remains unchanged. The reaction can probably be written as

$$3Mn(OH)_2 + 2(OH)^- \rightarrow Mn_3O_4 + 4H_2O + 2e \quad [5]$$

Discharge and Charge Curves

Four groups of electrodes were discharged and charged as follows: the first group was discharged at 5 ma · cm^{-2} to 0.9C ($MnO_{1.82}$) and then recharged to 1.0C ($MnO_{1.92}$) at 2.5 ma · cm^{-2}, the second was discharged to 0.6C ($MnO_{1.55}$) and recharged, the third to 0.3C ($MnO_{1.29}$) and recharged, and the fourth to 0.0C ($MnO_{1.16}$) and recharged. The empirical formulas in parentheses are the experimentally determined values obtained by chemical analysis of the discharged electrodes. The lack of agreement between the calculated and experimental values is due to the low current efficiency towards the end of discharge because of concurrent hydrogen evolution.

These electrodes thus encompassed a range of composition where in the first series only the amorphous phase was present, in the second, amorphous phase plus Mn_3O_4, in the third, amorphous phase plus Mn_3O_4 and $Mn(OH)_2$, and in the fourth, Mn_3O_4 and $Mn(OH)_2$.

The discharge/charge curves obtained from group one are shown in Fig. 5. The discharge curve proceeds smoothly and the charge curve shows two fairly well defined steps. The first step is attributed to the oxidation of the amorphous compound to MnO_2, the quantity of electricity consumed in this reaction almost being equal to that withdrawn during the discharge. The oxidation of the amorphous phase probably occurs according to the reverse of Eq. [1]. After completion of the first oxidation step, the potential increases rapidly to a well defined plateau at 1.45v. This is probably a mixed potential due to the evolution of oxygen and the oxidation of MnO_2 to K_2MnO_4. This is supported by the appearance in the electrolyte of a green color due presumably to $MnO_4^=$ ions. The charging curves of electrodes in groups 2, 3, and 4 are shown in Fig. 6. The curve of the electrodes discharged to 0.6C again shows two steps and as before, the quantity of electricity consumed in the first step is almost equal to that withdrawn on discharge indicating that, at this point, the electrodes are still chemically reversible. In the electrodes discharged to 0.3C, the existence of highly irreversible Mn_3O_4 is evidenced by the rapid increase in polarization at the start of charge. A plateau occurs at 0.65v which most probably corresponds to the oxidation of $Mn(OH)_2$ to Mn_3O_4. An inflection is observed after about 8 hr which corresponds to the passage of 0.050 amp · hr. If the reaction is assumed to be identical to Eq. [5], this amount of electricity corresponds to 0.248g of $Mn(OH)_2$ or approximately 25% of the electrode weight. A fairly rapid rise in potential then occurs followed by a poorly defined plateau which probably corresponds to the oxidation of the residual amorphous compound to MnO_2.

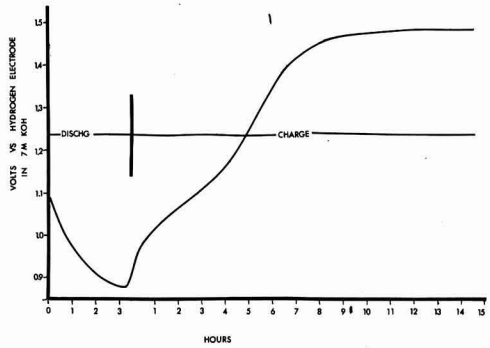

Fig. 5. Alkaline MnO_2 electrode discharge-charge potentials at 0.9C.

The electrodes of the fourth group contain the same discharge products as those of group three except that

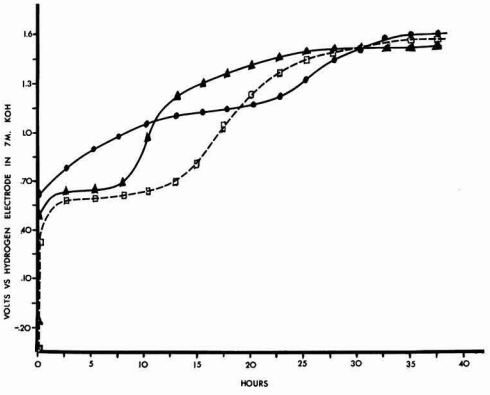

Fig. 6. MnO_2 potentials during charge

	Discharge to	Charge to
Group 2 ●——●	0.6C	1.0C
Group 3 ▲——▲	0.3C	1.0C
Group 4 □- - -□	0.0	1.0C

Charge current density 2.5 ma/cm^2.

the amount of $Mn(OH)_2$ is now larger and little or no MnO_2 or amorphous phase exists in the electrode. Thus the plateau at 0.65v due to oxidation of $Mn(OH)_2$ is longer and is followed again by an increase in the potential to the final plateau.

Cycling Experiments

A group of electrodes was cycled by discharging at 5 ma · cm^{-2} for 8 hr and charging at 2.5 ma · cm^{-2} for 16 hr. This was equivalent to a cycling between a depth of 1.0C and 0.89C. The potential/time curves of Fig. 7 show that up to 45 cycles, the electrodes cycle with only slight loss in performance. At cycle 63, a large polarization was observed after which the potential was erratic. This was also observed on the charge curve.

The behavior of the electrode suggested that a rapid increase in resistance had occurred at this point. This was thought to be perhaps due to the formation of a film of Mn_3O_4 around the electrical contact wire or the electrode/electrolyte interface. To investigate this, electrodes were prepared containing two electrical contacts; one embedded in the center of the mix and the other tightly wound around the outside. It was thought that if failure was caused by the formation of a layer of Mn_3O_4 around the contact wire, then switching from one contact to the other after failure should restore the performance. These electrodes were cycled between 1.0 and 0.75C using the same conditions as before. The IR drop was determined by use of an interruptor technique employing a Tektronix oscilloscope Model No. 535. The potential time curves are shown in Fig. 8 and the IR measurements in Fig. 9. The electrodes were seen to fail at cycle 9 at which point a high polarization was observed together with an increase in the IR drop. At this point, the current was switched to pass through the other contact. Immediately, the high polarization disappeared and the IR drop fell to that of a fresh electrode. Several additional cycles were obtained before the electrodes failed again.

It is clearly seen that the source of electrode failure is at the MnO_2/contact wire interface. From the potential of the electrodes, when they fail, it can be concluded that this film is Mn_3O_4. The magnitude of the IR drop at failure was insufficient to account for the high total polarization observed at this point. Since previous experiments (7) have shown the extremely high irreversibility of Mn_3O_4, it is not surprising that its precipitation is accompanied by a very large increase in polarization.

A second experiment was conducted using an electrode which, after failure, had a thin concentric layer cut away from the electrode/electrolyte interface and

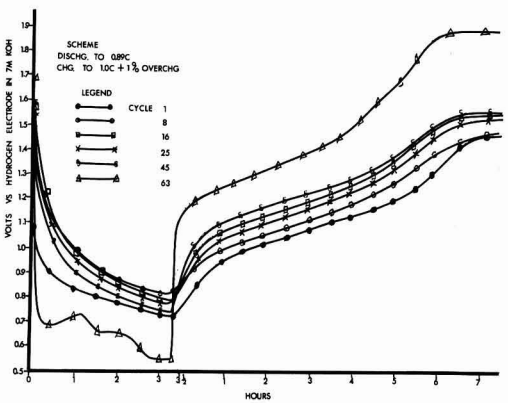

Fig. 7. Alkaline MnO_2 electrode cycle test. Discharge to 0.89C, C.D. 5 ma·cm^{-2}; charge to 1.0C + 1% overchg., C.D. 2.5 ma·cm^{-2}.

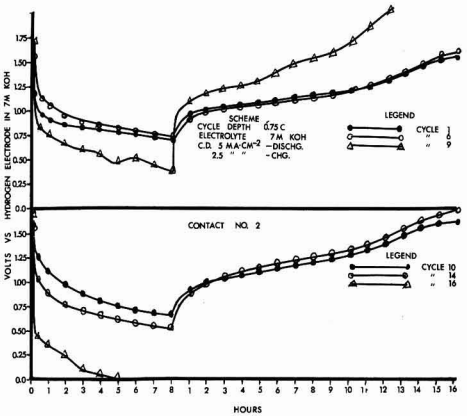

Fig. 8. Double contact alkaline MnO_2 electrode potential *vs.* time. Discharge to 0.75C, C.D. 5 ma·cm^{-2}; charge to 1.0C, C.D. 2.5 ma·cm^{-2}.

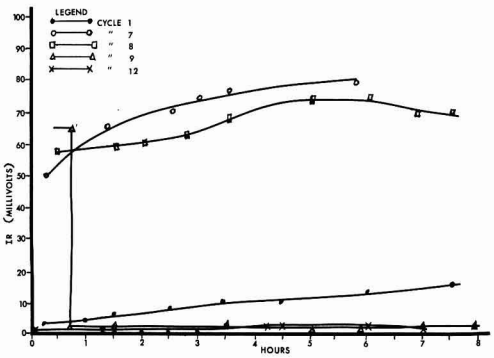

Fig. 9. Alkaline MnO_2 electrode IR measurements of a double contact electrode, cycling at 0.76C.

then was recycled. This treatment did not reduce the polarization thus indicating once again that the film is formed at the contact/MnO_2 interface.

Discussion

The x-ray diffraction data show, as observed before, that in the initial stages of discharge, a lattice expansion occurs with the formation of an amorphous product which cannot be ascribed to any of the well known manganese oxides. This is in agreement with results obtained by Brenet (9) and co-workers in LeClanche cells and appears to be general feature of the discharge of MnO_2 electrodes. No evidence of MnO(OH) was obtained in contradiction to the results of some other investigations. In the early stages of the discharge, the electrodes are rechargeable as evidenced by the x-ray data and the discharge and charge curves. The charge/discharge reaction can be written as Eq. [2]. At greater depth of discharge, the amorphous phase is reduced to Mn_3O_4 which is evidently not rechargeable and thereafter remains unchanged in the electrode. As the electrode approaches full discharge, $Mn(OH)_2$ is formed and this is the final product. On recharge, $Mn(OH)_2$ is observed to disappear from the electrodes as indicated by the disappearance of the $Mn(OH)_2$ peaks in the x-ray diffraction patterns and the plateau in the charge curves at 0.6v. It is proposed that on recharge, $Mn(OH)_2$ is oxidized to Mn_3O_4 according to Eq. [5].

On the basis of the x-ray and discharge/charge curve data, one would expect a manganese dioxide electrode in 7M KOH to be rechargeable provided that

the depth of discharge is restricted so that Mn_3O_4 is not formed. This is in fact so, as shown by the data in Fig. 7. However, a gradual deterioration in the performance occurs which allows the electrode potential to fall to the level at which Mn_3O_4 is produced. The IR curves and the data from electrodes containing two contacts show that failure is caused by the precipitation of a film of Mn_3O_4 around the current collector wire.

Manuscript received Aug. 28, 1967; revised manuscript received Nov. 25, 1967.

Any discussion of this paper will appear in a Discussion Section to be published in the December 1968 JOURNAL.

REFERENCES

1. W. S. Herbert, *This Journal*, **99**, 190C (1952).
2. N. C. Cahoon and M. P. Korver, *ibid.*, **106**, 745 (1959).
3. G. S. Bell and R. Huber, *Electrochim. Acta.*, **10**, 509 (1965).
4. G. S. Bell and R. Huber, *This Journal*, **111**, 1 (1964).
5. A. Kozawa and J. F. Yeager, *ibid.*, **112**, 959 (1965).
6. A. Kozawa and R. A. Powers, *ibid.*, **113**, 870 (1966).
7. D. P. Boden, C. J. Venuto, D. Wisler, and R. B. Wylie, *ibid.*, **114**, 415 (1967).
8. I. M. Kolthoff and E. B. Sandell, "Textbook of Quantitative Inorganic Analysis," Macmillan Co., New York (1946).
9. J. P. Brenet and S. Ghosh, *Electrochim. Acta.*, **7**, 449 (1962).

The Diffusional Properties of Oxygen in Niobium Pentoxide Crystals and Scales Formed on Niobium

J. S. Sheasby[1] and W. W. Smeltzer*

Department of Metallurgy and Materials Science, McMaster University, Hamilton, Ontario, Canada

and A. E. Jenkins

School of Metallurgy, University of New South Wales, Kensington, N.S.W., Australia

ABSTRACT

Single crystals of α-Nb_2O_5 were grown by the Verneuil technique and machined into cylinders. Measurements of electrical conductivity of these specimens as a function of temperature and oxygen pressure were made and compared with similar work by previous investigators. By following the resistance change as a function of time on changing the environmental pressure, determinations of the diffusion coefficient of oxygen were made at varying degrees of nonstoichiometry. Oxygen diffusion coefficients were several hundredfold lower in oxide of large nonstoichiometry. Similar work was performed on γ-Nb_2O_5 scales stripped from niobium specimens after oxidation. Although absolute measurements could not be undertaken on these extensively cracked specimens, γ-Nb_2O_5 showed similar properties to α-Nb_2O_5. The relationship is considered of these conclusions to be oxidation behavior of niobium.

In an analysis of the effect of oxygen pressure on the parabolic oxidation rate constants of niobium, Sheasby *et al.* (1) suggested that oxygen diffusion was most rapid in near stoichiometric γ-Nb_2O_5. Other investigators (2-4) have reported in their studies on both α- and γ-Nb_2O_5 that equilibrium was attained far more rapidly in nearly stoichiometric oxide than at larger departures from stoichiometry. As such behavior is not predicted by proposed models of the defect structure of these oxides, the purpose of this investigation was to determine oxygen diffusion constants in α- and γ-Nb_2O_5 at various oxide compositions.

Terao (5) has suggested that the structures of α- and γ-Nb_2O_5 are closely related. The structure of α-Nb_2O_5, particularly when nonstoichiometric, is not known with certainty (6) but can be indexed by a monoclinic cell (5). Brauer (7) reports a composition range for this phase expressed as NbO_x where $2.4 < x < 2.5$, but Norin and Magneli (8) have identified two compounds $NbO_{2.46}$ and $NbO_{2.48}$ in this region. Isopiestic experiments of Blumenthal *et al.* (2) did not indicate the presence of these phases; a value of —164 kcal/mole was determined for the relative partial molar enthalpy of oxygen for the pentoxide phase, its lower stoichiometric limits being $x = 2.42$ and 2.44 at 1090° and 889°C, respectively.

Although the defect structure of γ-Nb_2O_5 has not been extensively studied (3), the defect equilibria describing oxygen deficiency in α-Nb_2O_5 has been studied by several investigators using electrical conductivity and gravimetric techniques (4, 9-14). The majority of investigators agree that in the temperature range 600°-1400°C and pressure range $1\text{-}10^{-6}$ atm the isothermal conductivity is proportional to $P_{O_2}{}^{-1/4}$, and that the conductivity exhibits an exponential temperature dependence with an activation energy of 1.4-1.7 ev (electron volt). These results are interpreted by a defect model involving oxygen vacancies with one trapped electron. At larger departures from stoichiometry at lower oxygen pressures, the picture is less clear. The work of Blumenthal *et al.* (2) suggests no change in defect type, whereas Kofstad and Anderson (14) find that both the isothermal weight change and conductivity of α-Nb_2O_5 are proportional to $P_{O_2}{}^{-1/6}$. These results are interpreted in terms of oxygen ion vacancies without trapped electrons due to a decrease in the ionization energy of electrons from these defects as their concentration increased, in agreement with the work of Jannick and Whitmore (12).

Experimental

Two sources of reagent grade α-Nb_2O_5 powder and high purity niobium sheet, both 99.5 w/o (weight per cent) pure, were utilized as materials.

Coarse-grained boules of α-Nb_2O_5 were grown by the Verneuil technique using a hydrogen-oxygen flame. The boules were split into individual crystals and these were machined, using an air-abrasive unit, into cylinders approximately 1 mm diameter and 6

[1] Present address: Faculty of Engineering Science, University of Western Ontario, London, Ontario, Canada.
* Electrochemical Society Active Member.

mm long, Fig. 1. The [010] monoclinic direction was approximately parallel to the cylinder axis. Polycrystalline plates of γ-Nb_2O_5 approximately 1 cm^2 and 190 or 270μ thick, Fig. 2, were obtained by anodically dissolving the metal from specimens oxidized at 770°C. The oxide was composed of columnar crystals oriented with the [100] tetragonal axis perpendicular to the plane. The oxide plates were extensively cracked and could not be heated above 750°C without transforming to the alpha modification.

Resistances were measured by two and four point probe direct current techniques. Platinum current and potential leads were wrapped directly on the specimen and contact improved with platinum paint. Four point probe measurements were initially taken; however, the contact resistances were found to be negligible, so many of the experiments were performed using two point contacts. A Keithley 610A electrometer was used as a source of constant current and the potential drop across a specimen was measured either with this instrument, or a Leeds and Northrup Type K3 potentiometer or a Honeywell recorder. Resistances measured in the forward and reverse directions were ohmic within experimental errors of ± 1%.

The diffusion assembly was of a conventional glass design for attaining vacuo of 10^{-4} Torr. Medical grade oxygen, high purity argon, carbon dioxide of 99.95 v/o (volume per cent) purity, and carbon monoxide of 96.6 v/o purity were dried by passage through columns containing phosphorous pentoxide. A specimen was suspended by the electrical leads into the hot zone of a vertically mounted mullite tube heated by an electrical resistance tubular furnace. The temperature was measured with a Pt-Pt 10% Rh thermocouple sited adjacent to the specimen. Pressures in the range 10^{-3}-1 atm were effected statically. To achieve environmental purity in the range 10^{-3}-10^{-5} atm, oxygen was continually admitted through a needle valve, the pressure being automatically controlled by magnetic valves in the vacuum line. At oxygen pressures below 10^{-5} atm, flowing atmospheres of either CO/CO_2 or Ar/O_2 were passed through the reaction tube. The oxygen potentials of these latter atmospheres were measured with a stabilized zirconia galvanic cell placed adjacent to the specimen and controlled by manipulation of needle valves in the gas lines.

To measure the oxygen diffusion constant for α-Nb_2O_5, the specimens were held at a fixed temperature and pressure until the resistance was constant. The pressure was then changed and the variation in the resistance was recorded with time. Specimens were considered as infinite cylinders of radius r and analyzed using the diffusion equation (15)

$$\frac{C_t - C_f}{C_i - C_f} = \sum_1^\infty \frac{4}{\xi_v^2} \exp\left[-\frac{\xi_v^2 Dt}{r^2}\right] \qquad [1]$$

ξ_v are the roots of the equation $J(x) = 0$ where $J(x)$ is the Bessel function of zero order, C_i, C_f, and C_t are the initial, final, and value at time t of the oxide oxygen concentration. These concentrations, in turn, are directly related to the corresponding electrical conductivities. Consequently, this equation was solved for Dt/r^2 for each experimental point on a computer and these values plotted *vs.* time to obtain the best value of D/r^2. The oxygen diffusion constant for γ-Nb_2O_5 was determined under the same experimental conditions and the results analyzed by the diffusion equation for a plate (16).

X-ray diffractometer patterns of powdered oxide were obtained using copper radiation with a nickel filter.

Results

Alpha-niobium pentoxide.—Values of the resistivity at various temperatures of specimens equilibrated with oxygen over the range 10^{-5}-1 atm are shown in Fig. 3. The resistance was proportional to the ¼ power of the pressure. Specimens were also equilibrated with atmospheres of much lower oxygen potentials to 10^{-16} atm. Because of the excessively long equilibration periods of several days, the resistance measurements were not as precise as those at higher pressures. However, the oxygen pressure dependence of the resistance remained within experimental error to the ¼ power, Fig. 4. This relationship was valid for crystals prepared from both stocks of α-Nb_2O_5.

The specific resistances of several specimens prepared from the oxide materials obtained from two sources agreed well and gave a good fit to an Arrhenius plot, Fig. 5. The activation energy was 1.61 ev

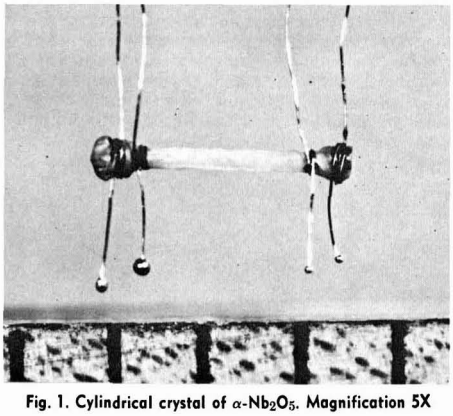

Fig. 1. Cylindrical crystal of α-Nb_2O_5. Magnification 5X

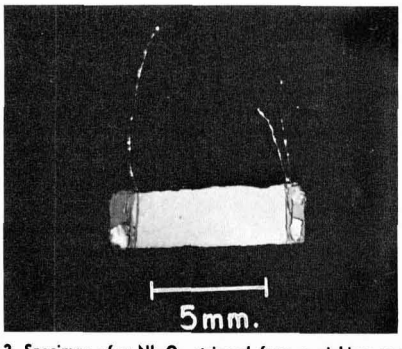

Fig. 2. Specimen of γ-Nb_2O_5 stripped from a niobium specimen oxidized at 760° in 1 atm oxygen for 120 min.

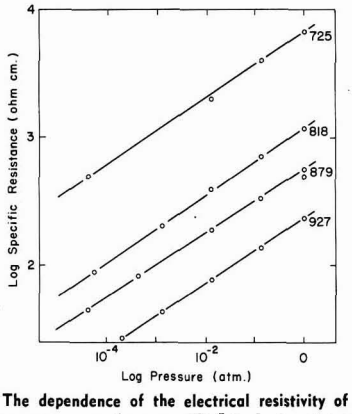

Fig. 3. The dependence of the electrical resistivity of α-Nb_2O_5 on oxygen pressure over the range 10^{-5} to 1 atm at temperatures of 927°, 879°, 818°, and 725°C.

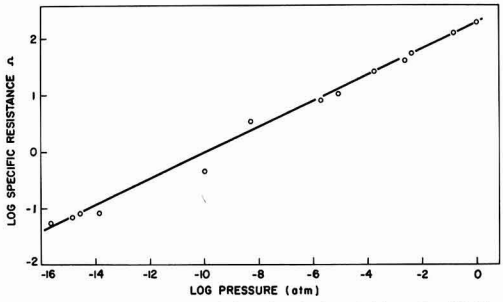

Fig. 4. The dependence of the electrical resistivity of α-Nb_2O_5 on oxygen pressure over the range 10^{-16} to 1 atm at 909°C.

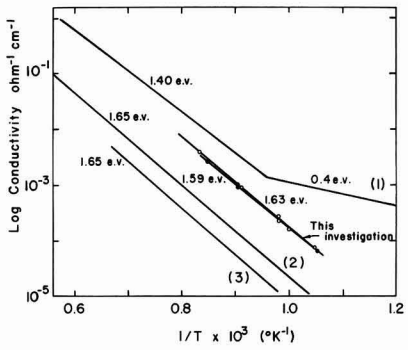

Fig. 5. Arrhenius plots with determinations for the activation energy for the electrical conductivity of α-Nb_2O_5 at 1 atm. The plots 1, 2, and 3 are from references (4), (10), and (3), respectively.

which is to be compared to the value of 1.4-1.65 ev from previous investigators (3,4,10).

The diffusion constant was evaluated from data obtained by changing the pressure over a narrow range and recording the resistance change with time. On plotting Dt/r^2 *vs.* time as described in the last section to obtain the best value of D/r^2 the linear plots intersected the co-ordinates close to the origin, Fig. 6. However the values of D/r^2 obtained from different determinations under the same experimental conditions varied by as much as a factor of 3. Further difficulty was encountered on raising the pressure to close to atmospheric, *e.g.*, 100-760 Torr, at low temperatures,

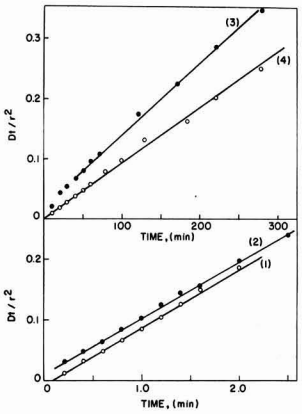

Fig. 6. Plots of Dt/r^2 *vs.* time at 909°C for α-Nb_2O_5 for oxygen pressure changes of 104 to 7.38 Torr, curve 1; 6.28 to 127 Torr, curve 2; 5.0×10^{-9} atm to 2.5×10^{-15} atm, curve 3; and 2.3×10^{-16} to 1.2×10^{-14} atm, curve 4.

when the equilibrium specimen resistance was attained in an unexpectedly short time.

Values for the oxygen diffusion constant at various pressures and temperatures are recorded in Table I. An Arrhenius plot is shown in Fig. 7 of diffusion constant determinations from four specimens. The data points form two bands with the determinations relating to pressure changes in the range 10^{-5}-1 atm being approximately 300 times larger than those made at pressures lower than 10^{-13} atm. The activation energies of 2.2 and 2.3 ev demonstrate that the temperature dependence for diffusion did not change significantly over the investigated pressure range.

A comparison of the powder x-ray diffraction patterns of black nonstoichiometric with white stoichiometric oxide gave an extra line corresponding to d = 3.85Å and 1.693Å while the lines at d = 2.684Å and 1.219Å were absent, and the line at d = 2.070Å was greatly reduced in intensity.

Gamma-niobium pentoxide.—The instability of this oxide imposed restrictions on the system that could be studied. Since the specimens were cracked, no attempt was made to obtain specific resistances. As illustrated in Fig. 8, the resistances of the specimens studied were proportional to the 0.25 ± 0.04 power of the oxygen pressure.

Oxygen diffusion in the oxide as a function of oxygen pressure was determined in the range 10^{-6}-1 atm

Table I. Oxygen diffusion constants in α-Nb_2O_5

Temperature, °C	Initial pressure, atm	Final pressure, atm	D, cm²/sec	Temperature, °C	Initial pressure, atm	Final pressure, atm	D, cm²/sec
			Specimen 435μ diameter				
965	8.5×10^{-5}	6.8×10^{-9}	1.47×10^{-8}	965	1.52×10^{-6}	3.6×10^{-11}	3.16×10^{-8}
965	2.0×10^{-13}	2.1×10^{-11}	5.5×10^{-8}	965	9.8×10^{-14}	2.2×10^{-12}	6.75×10^{-8}
909	1.0	1.32×10^{-1}	1.10×10^{-6}	909	1.32×10^{-1}	7.15×10^{-3}	1.22×10^{-6}
909	7.15×10^{-3}	6.05×10^{-4}	2.53×10^{-6}	909	2.08×10^{-4}	6.45×10^{-5}	1.51×10^{-6}
909	9.01×10^{-6}	8.16×10^{-5}	1.17×10^{-6}	909	8.25×10^{-5}	1.07×10^{-5}	8.64×10^{-7}
909	1.04×10^{-4}	1.16×10^{-5}	1.00×10^{-6}	909	1.16×10^{-5}	1.84×10^{-4}	1.80×10^{-6}
909	1.37×10^{-4}	1.15×10^{-5}	8.79×10^{-7}	909	1.15×10^{-5}	1.84×10^{-4}	1.44×10^{-6}
909	1.37×10^{-4}	9.72×10^{-6}	7.55×10^{-7}	909	8.27×10^{-6}	1.67×10^{-4}	7.03×10^{-7}
909	3.95×10^{-3}	1.32×10^{-1}	1.41×10^{-6}	909	1.32×10^{-1}	1.0	1.82×10^{-6}
909	1.26×10^{-15}	2.09×10^{-10}	7.45×10^{-9}	909	2.3×10^{-10}	1.18×10^{-14}	7.48×10^{-9}
909	5.02×10^{-9}	2.52×10^{-15}	8.93×10^{-9}	909	7.1×10^{-5}	5.1×10^{-14}	8.24×10^{-9}
819	1.0	1.30×10^{-1}	9.49×10^{-7}	819	1.0	8.10×10^{-1}	7.00×10^{-7}
819	1.34×10^{-1}	1.0	2.04×10^{-6}	819	8.10×10^{-1}	1.0	1.34×10^{-6}
819	1.0	1.32×10^{-1}	2.51×10^{-6}	737	1.0	1.32×10^{-1}	1.15×10^{-7}
737	1.04×10^{-2}	1.32×10^{-1}	3.96×10^{-7}	737	1.32×10^{-1}	1.04×10^{-2}	1.52×10^{-7}
737	8.62×10^{-3}	1.32×10^{-1}	4.60×10^{-7}	737	1.32×10^{-1}	8.62×10^{-3}	1.71×10^{-7}
680	2.03×10^{-4}	4.14×10^{-5}	2.04×10^{-8}	680	4.14×10^{-5}	1.85×10^{-4}	2.51×10^{-8}
680	1.03×10^{-5}	3.86×10^{-5}	2.36×10^{-8}	680	3.86×10^{-5}	1.57×10^{-4}	1.62×10^{-8}
680	1.40×10^{-4}	3.83×10^{-5}	1.25×10^{-8}	680	3.83×10^{-5}	1.76×10^{-4}	2.28×10^{-8}
680	1.71×10^{-4}	3.68×10^{-5}	8.25×10^{-9}	661	1.01	1.45×10^{-1}	8.48×10^{-9}
			Specimen 330μ diameter				
809	1.47	8.48	1.23×10^{-6}	809	8.48	1.32	2.82×10^{-6}
809	6.31×10^{-15}	1.26×10^{-10}	2.18×10^{-9}	809	1.59×10^{-18}	5.1×10^{-20}	1.08×10^{-9}
809	5.1×10^{-20}	5.1×10^{-17}	2.32×10^{-9}	809	5.1×10^{-17}	1.0×10^{-14}	2.98×10^{-9}

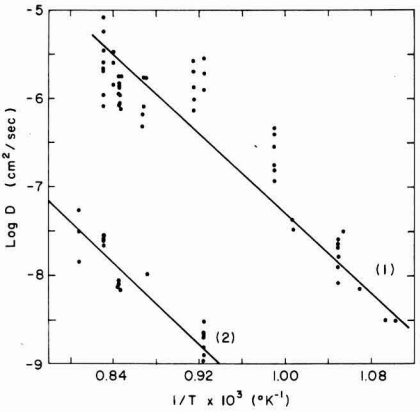

Fig. 7. Oxygen diffusion constants from four α-Nb_2O_5 specimens as a function of temperature at different pressures. Values in pressure range 10^{-5}-1 atm, curve 1; values in pressure range 10^{-13}-10^{-16} atm, curve 2.

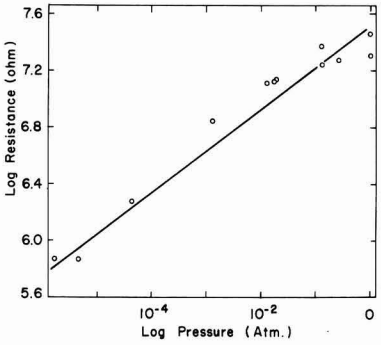

Fig. 8. The dependence of the electrical resistance of a γ-Nb_2O_5 specimen on oxygen pressure over the range 10^{-6} to 1 atm at 658°C.

and typical data for plates of thickness, a, are shown in Fig. 9. Although absolute values of diffusion constants for the cracked specimens could not be obtained, the relative values at different pressures are recorded in Table II. It can be seen that the oxygen diffusivity was insensitive to pressure from 0.5-10^{-4} atm, but decreased rapidly at pressures below this value.

White stoichiometric oxide transformed readily to black nonstoichiometric oxide in an oxygen atmosphere of 10^{-5} atm pressure at 750°C. The powder x-ray diffraction pattern of the black compared with the white oxide gave extra lines corresponding to d = 3.643Å, 3.311Å, and 2.971Å and the lines at d = 5.18Å and 1.54Å were absent.

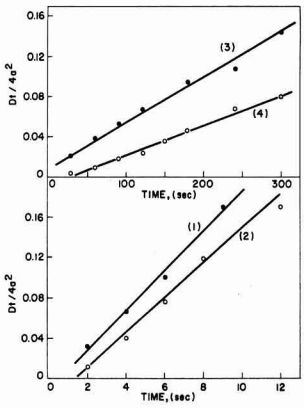

Fig. 9. Plots of $Dt/4a^2$ vs. time at 628°C for γ-Nb_2O_5 for oxygen pressure changes of 43 to 96 Torr, curve 1; 160 to 73, curve 2; 1.4 to 2.0, curve 3; and 2.5 to 0.14 Torr, curve 4.

Discussion

The conductivity of α-Nb_2O_5 at pressures in the range 10^{-5}-1 atm was proportional to $P_{O_2}^{-1/4}$ in agreement with previous results on polycrystalline specimens (14) but only in partial agreement with those for single crystals. The decreased pressure dependence below 800°C reported by Chen and Swalin (4) was not observed. Moreover, the conductivity at 907°C obeyed this pressure relation to 10^{-16} atm whereas a $P_{O_2}^{-1/6}$ relation was found for polycrystalline specimens in the pressure range 10^{-13}-10^{-18} atm by Kofstad and Anderson (14).

Arrhenius plots of the specific conductivities from four investigations were illustrated in Fig. 5. The conductivities of polycrystalline material were smaller by an order of magnitude than those for single crystals but the activation energies, irrespective of the type of material, were of the same magnitude 1.4-1.65 ev. Although Chen and Swalin (4) accounted for the high conductivity of their single crystal specimens at temperatures below 800°C by ionization of impurities, the present results demonstrate that the conductivity is determined entirely by oxide stoichiometry at pressures close to atmospheric over the temperature range 600°-1400°C. Also, the conductivity experiments demonstrated that the rapidity with which a specimen changed its conductivity was itself a function of the conductivity (stoichiometry). In relating these relaxation periods to the oxygen diffusion constant it was assumed that in the pressure increment under analysis the electron concentration was directly proportional to the oxygen concentration. As it has been shown that the conductivity of Nb_2O_5 is proportional to log (P_{O_2}) in this study, and that the weight loss of Nb_2O_5 is a

Table II. Relative oxygen diffusivities in γ-Nb_2O_5 at 628°C

Initial pressure, atm	Final pressure, atm	D	Initial pressure, atm	Final pressure, atm	D
		Oxide nominally 190μ thick			
5.26×10^{-1}	2.58×10^{-1}	7.65×10^{-5}	9.08×10^{-5}	2.90×10^{-5}	3.83×10^{-6}
2.38×10^{-1}	5.26×10^{-1}	1.07×10^{-4}	6.58×10^{-5}	3.42×10^{-5}	3.02×10^{-6}
2.58×10^{-1}	1.16×10^{-1}	6.13×10^{-5}	3.01×10^{-5}	2.38×10^{-5}	1.09×10^{-5}
1.26×10^{-1}	2.38×10^{-1}	3.95×10^{-5}	2.50×10^{-6}	1.80×10^{-6}	1.26×10^{-6}
5.66×10^{-2}	1.26×10^{-1}	7.20×10^{-5}	1.80×10^{-6}	2.63×10^{-6}	1.59×10^{-6}
5.92×10^{-4}	2.24×10^{-4}	4.17×10^{-5}	1.97×10^{-6}	3.29×10^{-6}	2.45×10^{-6}
4.87×10^{-4}	2.10×10^{-4}	7.25×10^{-5}	3.29×10^{-6}	1.84×10^{-7}	1.12×10^{-6}
2.10×10^{-4}	9.60×10^{-5}	5.75×10^{-5}			
		Oxide nominally 270μ thick			
1.63×10^{-1}	5.92×10^{-2}	3.50×10^{-4}	5.92×10^{-2}	2.04×10^{-2}	3.25×10^{-4}
5.80×10^{-2}	1.63×10^{-1}	4.25×10^{-4}	2.04×10^{-2}	1.97×10^{-3}	3.50×10^{-4}
2.76×10^{-2}	1.05×10^{-2}	3.75×10^{-4}	2.63×10^{-7}	7.50×10^{-7}	9.64×10^{-6}
1.05×10^{-2}	5.80×10^{-2}	6.00×10^{-4}	7.50×10^{-7}	2.24×10^{-7}	1.02×10^{-5}

function of log (P_{O_2}), (2), this assumption is reasonable. The oxygen diffusion constant, D, so measured is equivalent to the phenomenological diffusion constant defined by Fick's first law.

It will now be demonstrated that the diffusional properties of oxygen in niobium pentoxide cannot be inferred from theory based on ideal solution of point defects exhibiting constant mobility. A $(P_{O_2})^{-1/4}$ pressure dependence of the electrical conductivity was found over four orders of resistance change, and in agreement with other workers (4, 9, 13) this is interpreted in terms of a vacancy model involving only singly ionized oxygen vacancies. Wagner (17) has shown that for an ionic solid

$$D = \frac{V_m RT}{8F^2\delta} \frac{K_{ion} K_e}{K_{ion} + K_e} \frac{d \ln (P_{O_2})}{d \ln \delta} \quad [2]$$

where, in this instance, K_{ion} and K_e would be the specific conductivities of the singly ionized oxygen vacancies ($\square\cdot$) and electrons (e), δ is the oxygen deficit represented by the formula $Nb_2O_{5-\delta}$, and V_m is the molar volume. These conductivities are related to the mobility, μ, of charged species by:

$$K_{ion} = \frac{F}{V_m} x_{\square} \mu_{\square}$$

and

$$K_e = \frac{F}{V_m} x_e \mu_e \quad [3]$$

where x represents the atom fraction of the respective point defect.

From the pressure dependence of the resistivity

$$\frac{d \ln P_{O_2}}{d \ln \delta} = -4 \quad [4]$$

If the Nernst-Einstein relation is invoked

$$D_{\square} = \mu_{\square} \frac{RT}{F} \quad [5]$$

Substituting Eq. [3], [4], [5] in Eq. [2] and in view of $K_{ion} << K_e$

$$D = \frac{D_{\square}}{2} \quad [6]$$

According to Eq. [4-6], the magnitude of the oxygen diffusion constant is not dependent on oxygen pressure or oxide stoichiometry providing that the activity coefficient and mobility of vacancies remains constant. In the case of α-Nb_2O_5, this behavior is valid over the pressure range 10^{-5}-1 atm. It is definitely invalid over the entire investigated pressure range because the values are much smaller at pressures less than 10^{-14} atm (Table I and Fig. 7). A similar behavior was exhibited by γ-Nb_2O_5 with the transition to lower values of the diffusion constant occurring at higher pressures. For this oxide modification, the diffusion constant is constant only over the pressure range 10^{-3}-1 atm (Table II).

Knowledge of diffusion in ionic solids is not sufficiently advanced for interpretation of this similar but complex oxygen diffusion behavior for both oxides. With increasing nonstoichiometry the point defects interact giving varying activity coefficients and mobilities. Furthermore, according to Wadsley (6) and Gatehouse and Wadsley (18), removal of oxygen from niobium pentoxide leads to compression of the structure by shear along certain planes, the unit ReO_3 type polyhedra being condensed upon each other. When these shear planes are ordered, a series of related oxides can be recognized as identified by Norin and Magneli (8), and when they are not they are retained in a disordered form difficult to recognize except as a berthollide. Since different x-ray diffraction lines occur and line intensities change when both oxides are changed from small to large nonstoichiometry, it is therefore more reasonable to consider the limiting rates of oxygen diffusion as the mobilities in particular structures.

Different rates of oxygen diffusion in particular bethollidic structures can account for the unusual oxygen pressure dependence of the parabolic oxidation rates for niobium. When only one ionic species such as oxygen diffuses in an oxide scale over a relatively narrow homogeneity range, the general expression given by Wagner (19) for the parabolic oxidation rate constant may be placed in the form

$$k_r = C_{eq} \int_{a_o^1}^{a_o^{11}} \frac{|Z_2|}{Z_1} D_o^* \, d \ln a_O \quad [7]$$

Here, C_{eq} is the oxygen concentration in equivalents per cm^3, Z_1 and Z_2 are the valencies of metal and oxygen, D_o^* is the self-diffusion constant for oxygen, and a_o is the oxygen activity. The integration would be carried out for the oxygen activity range to the oxide-gas interface from an inner surface of the oxide. Converting k_r to k_p (cm oxide)^2/sec and placing Eq. [7] in differential form

$$D_o^* = \frac{1}{9.21} \frac{d k_p}{d \log P_{O_2}} \quad [8]$$

Figure 1 of ref. (1) shows plots of the parabolic constants for niobium oxidation *vs.* the logarithm of oxygen pressure over the range 10^{-3}-1 atm at temperatures in the range 720°-825°C. If growth of the oxide scale is governed by volume diffusion, these linear plots demonstrate that the oxygen self-diffusion constant is essentially constant only over a small pressure range wherein the oxide composition remains close to stoichiometry, and that below approximately 10^{-3} atm the oxygen self-diffusion constant has a much smaller value. These and all other available oxidation data (20) for the temperature range 540°-840°C were analyzed according to Eq. [8] and an Arrhenius plot of the diffusion constant is shown in Fig. 10. The self-diffusion constant for oxygen in the γ-Nb_2O_5 scale is

$$D_o^* \ (cm^2/sec) = 1.0 \exp - 42600/RT \quad [9]$$

The self-diffusion constant for oxygen in the essentially stoichiometric oxide is related to the diffusion constant for vacancies by the relation

$$x_o D_o^* \simeq D_o^* \simeq x_{\square} D_{\square} \quad [10]$$

where x_o and $x_{\square}$ represent the mole fractions of occupied and vacant oxygen lattice sites. Substituting [6] into [14] gives

$$D_o^* = 2x_{\square} D \quad [11]$$

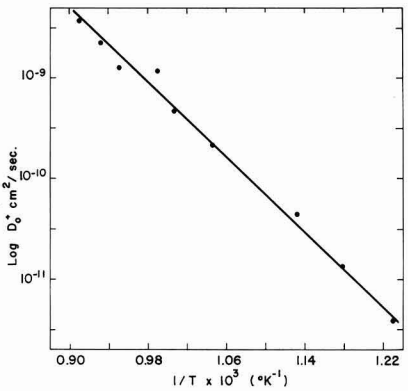

Fig. 10. Arrhenius plot of the oxygen self-diffusion coefficient for γ-Nb_2O_5 calculated from oxidation data for the pressure range 10^{-3} to 1 atm, references (1), (20).

According to Eq. [11] a large decrease in the magnitude of D_o^* for γ-Nb_2O_5 at oxygen pressures less than 10^{-3} atm would be primarily caused by the variation in D. The existence of this variation has been confirmed by the present measurements. Hence, the unusual pressure dependence of the parabolic oxidation kinetics is associated with the formation of a γ-Nb_2O_5 scale consisting of a series of structures changing with the oxygen potential. These structures would be distinct Magneli phases or blocks of a basic structure joined by regular discontinuities (18). If, as it has been suggested (6), the vacancy concentration in such berthollides is largely independent of composition, the observed decrease in oxygen diffusion rate in γ-Nb_2O_5 with stoichiometry would be sufficient to account for the decrease in oxidation rate of niobium with oxygen pressure. To determine the validity of these considerations, the self-diffusion coefficient of oxygen in γ-Nb_2O_5 must be determined as a function of both stoichiometry and structure.

Acknowledgments

This investigation was completed under the auspices of the U.S. Air Force Office of Scientific Research, Office of Aerospace Research, and the National Research Council of Canada.

Manuscript received March 3, 1967; revised manuscript received *ca.* Nov. 6, 1967.

Any discussion of this paper will appear in a Discussion Section to be published in the December 1968 JOURNAL.

REFERENCES

1. J. S. Sheasby, W. W. Smeltzer, and G. R. Wallwork, *This Journal*, **113**, 1255 (1966).
2. R. N. Blumenthal, J. B. Moser, and D. H. Whitmore, *J. Am. Ceramic Soc.*, **48**, 617 (1965).
3. P. Kofstad, *J. Phys. Chem. Solids*, **23**, 1571 (1962).
4. W. K. Chen and R. A. Swalin, *ibid.*, **27**, 57 (1966).
5. N. Terao, *Japanese J. Appl. Physics*, **2**, 156 (1963).
6. A. D. Wadsley, "Non-stoichiometric Compounds," p. 98, Academic Press, New York (1964).
7. G. Brauer, *Z. anorg. allgem. Chem.*, **248**, 1 (1941).
8. R. Norin and A. Magneli, *Naturwissenschaften*, **47**, 354 (1960).
9. E. H. Greener, D. H. Whitmore, and M. E. Fine, *J. Chem. Phys.*, **34**, 1017 (1961).
10. E. H. Greener and W. H. Hirthe, *This Journal*, **109**, 600 (1962).
11. E. H. Greener, F. J. Barone, and W. M. Hirthe, *J. Am. Ceramic Soc.*, **48**, 623 (1965).
12. R. F. Jannick and D. H. Whitmore, *J. Chem. Phys.*, **37**, 2750 (1962).
13. E. H. Greener, G. A. Fehr, and W. M. Hirthe, *J. Chem. Phys.*, **38**, 133 (1963).
14. P. Kofstad and P. B. Anderson, *J. Phys. Chem. Solids*, **21**, 280 (1961).
15. W. Jost, "Diffusion," p. 45, Academic Press, New York (1960).
16. *Ibid.*, p. 37.
17. C. Wagner, *Z. Physik Chem.*, (**B**)**21**, 25 (1933).
18. B. M. Gatehouse and A. D. Wadsley, *Acta Cryst.*, **17**, 1545 (1964).
19. C. Wagner, "Atom Movements," p. 153, American Society for Metals (1941).
20. J. S. Sheasby, Ph.D. Thesis, University of New South Wales, Australia (1963).

The Electrochemical Behavior of 4,4′-Azopyridine-1,1′-Dioxide

Joe L. Sadler and Allen J. Bard*

Department of Chemistry, The University of Texas at Austin, Austin, Texas

ABSTRACT

The electroreduction of 4,4′-azobispyridine-1,1′-dioxide (APDO) in dimethylformamide solutions was studied by polarography, cyclic voltammetry, controlled potential coulometry, and electron spin resonance, Voltammetric reduction showed two well-defined, reversible one-electron transfers. Coulometric reduction at a potential corresponding to the plateau of the first wave gave evidence of chemical reactions following the initial electron transfer producing intermediates which were also electroactive at the same potentials. Coulometry at the second wave gave an over-all value of six Faradays per mole for the complete reduction of APDO to the dianion of azopyridine (AP), identified by electrochemical and electron spin resonance techniques. A mechanism for the reduction process consistent with the experimental evidence is presented.

The polarographic behavior of a number of tertiary amine oxides in aqueous systems has been reported (1-9). Kubota and Miyazaki (6a) performed a polarographic study of pyridine N-oxide and its alkyl derivatives followed by a study (6b) of the effect of substituents on the polarographic reduction of pyridine N-oxide derivatives. Recently, Date (7a) reported a thorough polarographic investigation of dimethylaniline N-oxide, followed by an investigation of the relationship between the $E_{1/2}$ values of a series of similar compounds and the pKa's of their parent amines (7b). Chambers (8) studied the polarographic and adsorption behavior of dimethyldodecylamine N-oxide and Elving and Warner (9) have reported a study of the polarographic behavior of adenine 1-N-oxide.

In all of the above work, the amine oxide group gives a well-defined, irreversible polarographic wave between pH values of 1 to 6. Date proposed that the amine oxide group is reduced to the corresponding parent amine in a reaction involving two electrons, the first electron addition being rate controlling. This mechanism agrees quite well with his experimental data and is further supported by Chambers' work on N,N-dimethyldodecylamine N-oxide.

Recently Nasielski and co-workers (10) studied the polarographic reduction of pyridine N-oxide and other heterocyclic N-oxides in DMF solution. They proposed that the reduction involves a single, two-electron wave (composed of reduction to the anion radical, fast protonation, and further reduction, protonation, and dehydration), leading to the free base. We report here a study of the amine oxide 4,4′-azobispyridine-1,1′-dioxide (APDO) in DMF, in which a clear separation of the step leading to formation of the anion radical and to formation of the dianion is obtained.

* Electrochemical Society Active Member.

Results

Voltammetric methods. The polarographic reduction of APDO,

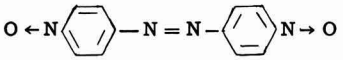

in a N,N-dimethylformamide (DMF) solution containing 0.1 *M* tetra-n-butyl-ammonium perchlorate (TBAP) showed two well-defined waves (Fig. 1) with half-wave potentials ($E_{1/2}$) of —0.73 and —1.35v *vs.* an aqueous saturated calomel electrode (SCE). The values of $E_{3/4}$—$E_{1/4}$ for the two waves (Tômes criterion for reversibility) 0.06 and 0.07v, respectively, suggested that the first wave involved a reversible, one-electron reduction and that the second wave may be complicated by a following chemical reaction. The diffusion currents of both waves were directly proportional to the square root of the height of the head of the dropping mercury electrode (dme). The diffusion current constants for the first and second waves were 2.97 and 5.45 $\mu a\text{-sec}^{1/2}\text{-mM}^{-1}\text{-mg}^{-2/3}$, respectively.

A cyclic voltammogram of APDO in DMF containing 0.1*M* TBAP at a hanging mercury drop electrode (hmde) is shown in Fig. 2. At all scan rates employed, the reverse scan clearly shows two anodic peaks, corresponding to the oxidation of APDO monoanion and dianion. The cyclic voltammogram obtained on a planar platinum electrode is illustrated in Fig. 3. The behavior of the first wave is essentially the same as that observed on a hmde; however, the second wave shows a much larger cathodic-to-anodic peak current ratio. Typical results of cyclic voltammetric (linear potential sweep chronoamperometry with reversal) experiments for both a hmde and platinum disk electrode are given in Table I. At both a platinum disk electrode and a hmde, the ratio of the peak current (i_{pa}) of the first anodic wave to the peak current of the corresponding cathodic wave (i_{pc}) is about 1, as would be expected for the formation of a radical species which is stable during the duration of the measurement. The value of E_{pc}-E_{pa} for this couple is very close to the value (0.057v) for a reversible, one-electron reaction. E_{pc} and E_{pa} for this couple are independent of scan rate v, and plots of the current function ($i_p/v^{1/2}$) and i_{pa}/i_{pc} *vs.* scan rate [diagnostic criteria given in the work of Nicholson and Shain (11) show this wave to be reversible].

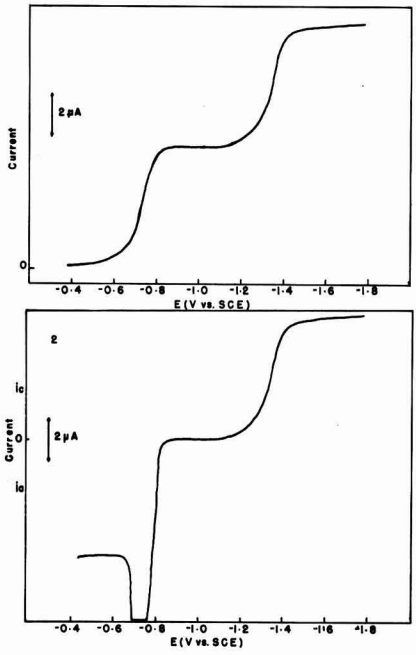

Fig. 1. Polarograms before and after reduction of a 1.32 mM APDO solution in DMF containing 0.1M TBAP at a mercury pool electrode: 1, before reduction; 2, after reduction at —1.0v vs. SCE.

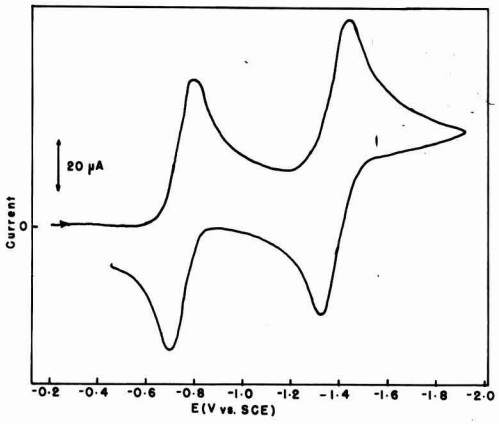

Fig. 2. Cyclic voltammetry of APDO at a HMDE. The solution contained 0.1M TBAP in DMF and was 1.32 mM in APDO.

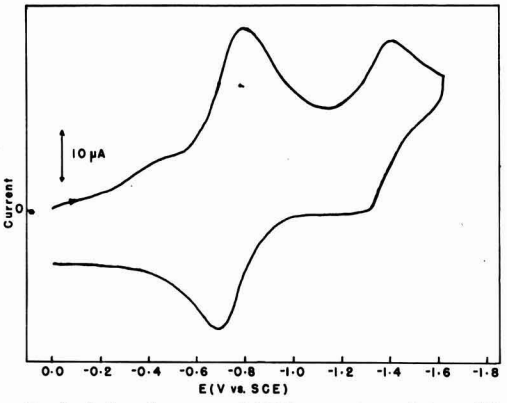

Fig. 3. Cyclic voltammetry of APDO at a planar platinum disk electrode. The solution contained 0.1M TBAP in DMF and was 1.32 mM in APDO.

The second reduction wave in cyclic voltammetric experiments utilizing a hmde shows some evidence of a chemical reaction following the reduction to give another electroactive species. The current function decreases about 20% for a 10-fold increase in scan rate, which indicates an ECE-type process (*i.e.*, an electron transfer reaction followed by a chemical reaction generating a species reducible at these potentials). A simple EC process is eliminated, because it is characterized by a change of only 10% in the current function for a 10-fold change in scan rate (11). The anodic-to-cathodic peak current ratios increase with increasing scan rate, as expected for an ECE process.

The results obtained in cyclic voltammetric experiments using a platinum disk electrode also give evidence for the presence of an irreversible chemical reaction following the second charge transfer step. At scan rates up to 657 mv/sec, however, essentially no corresponding anodic wave is seen for the second reduction wave. This suggests that either the following reaction is catalyzed at platinum or perhaps adsorption of the product at mercury occurs. This difference

Table I. Cyclic voltammetric data for the two-step reduction of 4,4'-azobispyridine-1,1'-dioxide[a]

Scan rate, mv/sec	First wave i_{pc}, μa	i_{pa}[b] μa	i_{pa}/i_{pc}	$-E_{pc}$ v vs. SCE	$-E_{pa}$ v vs. SCE	$i_{pc}/v^{1/2}$	Second wave i_{pc}[c] μa	i_{pa}[b] μa	i_{pa}/i_{pc}	$-E_{pc}$ v vs. SCE	$-E_{pa}$ v vs. SCE	$i_{pc}/v^{1/2}$
				Hanging mercury drop electrode;[d] conc. = 1.03 mM								
73	5.4	5.0	0.93	0.76	0.71	0.63	5.8	3.9	0.67	1.40	1.33	0.68
91	6.0	5.8	0.97	0.76	0.70	0.63	5.9	4.8	0.81	1.40	1.33	0.62
203	8.1	7.9	0.98	0.76	0.70	0.67	8.5	6.1	0.72	1.40	1.33	0.60
298	11.0	10.4	0.96	0.76	0.70	0.64	10.1	7.5	0.74	1.40	1.33	0.59
430	14.0	13.2	0.95	0.76	0.70	0.68	12.2	8.7	0.71	1.40	1.33	0.59
657	17.9	17.0	0.95	0.80	0.69	0.70	15.6	12.0	0.77	1.41	1.30	0.61
				Concentration = 1.29 mM								
73	6.5	6.0	0.93	0.76	0.70	0.77	6.1	4.4	0.72	1.42	1.35	0.72
91	7.7	6.5	0.85	0.76	0.70	0.80	6.5	4.4	0.68	1.42	1.35	0.68
203	11.0	10.0	0.91	0.76	0.70	0.77	8.5	6.3	0.74	1.42	1.35	0.60
298	13.3	12.5	0.94	0.76	0.70	0.77	10.4	7.9	0.76	1.42	1.34	0.60
430	15.8	15.0	0.95	0.76	0.70	0.76	11.7	8.9	0.76	1.42	1.34	0.57
657	19.5	18.5	0.95	0.80	0.67	0.76	14.4	9.3	0.65	1.42	1.32	0.56
				Concentration = 3.25 mM								
73	20.1	16.1	0.80	0.76	0.70	2.4	23.6	19.7	0.84	1.39	1.31	2.8
91	22.8	18.5	0.81	0.76	0.70	2.4	26.4	22.1	0.84	1.39	1.31	2.8
203	33.0	26.8	0.81	0.76	0.70	2.3	37.0	30.7	0.83	1.39	1.31	2.6
298	40.2	33.1	0.82	0.76	0.70	2.3	44.1	37.0	0.84	1.40	1.31	2.5
430	48.0	41.7	0.87	0.76	0.70	2.3	50.0	43.4	0.87	1.40	1.30	2.4
657	60.0	50.0	0.83	0.77	0.67	2.3	60.0	55.0	0.92	1.41	1.30	2.3
				Platinum disk electrode;[e] concentration = 1.74 mM								
73	8.0	6.5	0.81	0.77	0.71	0.94						
91	9.0	7.5	0.83	0.77	0.71	0.94						
203	13.0	13.0	1.00	0.77	0.71	0.91						
298	16.5	16.0	0.97	0.77	0.71	0.95						
430	18.0	17.5	0.97	0.78	0.70	0.97						
657	24.5	23.5	0.96	0.78	0.69	0.96						

[a] The solution was 0.1*M* TBAP in DMF.
[b] For scan reversed at a potential 100mv more negative than E_{pc}. Potentials given may also include some uncompensated iR drop.
[c] Measured using extrapolation of decreasing current of first peak as base-line.
[d] Electrode area = 0.088 cm².
[e] Apparent electrode area = 0.031 cm².

in behavior at platinum and mercury electrodes was not investigated further.

These results suggest that the following reactions occur during voltammetry

$$APDO + e \rightleftarrows APDO^{\cdot -} \quad \text{(first wave)} \qquad [1]$$

$$APDO^{\cdot -} + e \rightleftharpoons APDO^{=} \quad \text{(second wave)} \qquad [2]$$

$$APDO^{=} + HS \rightarrow APDOH^{-} + S^{-} \qquad [3]$$

where HS represents any source of protons and $APDOH^-$ is reducible at the potential of the second wave.

Coulometric experiments at a mercury pool electrode controlled at a potential on the diffusion plateau of both the first (—1.0v) and second (—1.8v) reduction waves were undertaken to study the electrochemical behavior of $APDO^{\cdot -}$ and $APDO^{=}$ and to obtain, via electron spin resonance (esr) techniques, further evidence for the above-postulated mechanism. Reduction of APDO at —1.0v gave values of n_{app} ranging from 1.40 to 1.92 faradays per mole (Table II). In all experiments the electrolysis current decayed to a value significantly higher than the corresponding background currents. For example, in the case of n_{app} = 1.70, the current decreased from an initial value of 38 ma to a steady value of 1.4 ma after 30 min, indicating that continued electrolysis does not bring about complete cessation of all reduction reactions. This behavior is indicative of a slow secondary process which produces a product that is electroactive at the same potential. Reversal coulometry at —0.20v *vs.* SCE gave n_{app} values for oxidation significantly lower than the corresponding initial reduction n_{app} values (Table II).

The solution resulting from reduction of APDO at —1.0v *vs.* SCE was a deep reddish-brown in color and gave an intense esr spectrum of about 75 lines. The spectrum was significantly nonsymmetrical about the center, indicating that the signal obtained was due to a mixture of two or more radical species. The presence of two radical species is also consistent with an ECE mechanism.

Voltammetry after Reduction

Polarograms for a APDO solution before and after reduction at —1.0v *vs.* SCE are shown in Fig. 1. The polarogram for a reduced APDO solution (Fig. 1, curve 2), shows an anodic wave with a large maximum which abruptly drops to near the expected diffusion current value at a potential (—0.68v) near the potential of the electrocapillary maximum for this medium, —0.70v. This behavior is similar to that observed by Santhanam and Bard (12) in their study of 9,10-diphenylanthracene and can probably be attributed to the anodic streaming mechanism proposed by them. The reduction of $APDO^{\cdot -}$ to $APDO^{=}$ occurs at the same potential as the second polarographic wave in the reduction of APDO (Fig. 1, curve 2). The diffusion current of the second wave is about the same before and after electrolysis at —1.0v. Cyclic voltammetry, utilizing a hmde, on a reduced solution of APDO is shown in Fig. 4, curve 2. The very large anodic current for the oxidation is attributed to the same stirring effect mentioned above. Cyclic voltammetry on a platinum disk electrode does not exhibit this stirring phenomena (Fig. 4, curve 4). The value of i_{pc} for the first wave at a platinum electrode decreases by about 20% after reduction of APDO at —1.0v (24.5 μa before *vs.* 19.4 μa after). Peak potentials (E_{pc} and E_{pa}) for the first reduction step are unchanged.

Further controlled potential reduction of the reduced solution at —1.80v, corresponding to the plateau of the second wave gave an additional 4.1 faradays

Table II. Controlled potential coulometric results[a]

Conc., mM	n_{app} Reduction at —1.0v	Oxidation at —0.20v	Reduction at —1.80v
0.90	1.63	—	5.92
1.05	1.92	—	—
1.32	1.92	—	—
1.73	1.40	0.47	—
3.25	1.70	0.70	—
1.05	—	—	5.84

[a] The solution was DMF containing 0.1*M* TBAP. The cathode was a mercury pool with an approximate area of 12 cm² and the anode was platinum wire, isolated by a fine-porosity, sintered glass disk. Potentials given above are *vs.* SCE. Electrolysis times were 0.5 to 1.5 hr.

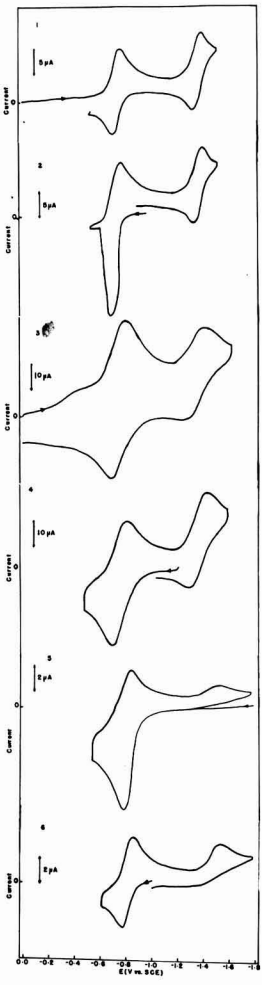

Fig. 4. Cyclic voltammetry of APDO on a hmde and platinum disk electrodes at various stages of reduction at a mercury pool working electrode. The solution was 1.73 mM in APDO in DMF containing 0.1M TBAP: 1, C.V. at hmde of original solution; 2, C.V. at hmde after reduction at —1.0 v; 3, C.V. at platinum disk electrode of original solution; 4, C.V. at platinum disk electrode after reduction at —1.0 v; 5, C.V. at a platinum disk electrode after reduction at —1.80 v; 6, C.V. at a platinum disk electrode of an authentic sample of azopyridine in the same medium as described above.

per mole for an over-all value of $n_{app} = 5.84$. Cyclic voltammetry, employing a platinum disk electrode, of an APDO solution after complete reduction at —1.80v, is shown in Fig. 4, curve 5. With the scan initiated in a positive direction from —1.80v, an oxidation wave occurs at —0.76v followed, on reversal, by two reduction steps at —0.84 and —1.53v. These peak potentials are significantly different from those observed for APDO itself.

Reversal coulometry (oxidation) at —1.0v resulted in no anodic current flow, indicating that the reduced species was not oxidizable at this potential. On changing the potential to —0.20v, however, this species was oxidized, giving a value of $n_{app} = 1.44$. Cyclic voltammetric reduction and oxidation of the species resulting from this oxidation showed waves at the same potentials as those observed for the completely reduced species as noted above; the first charge transfer was apparently reversible with a reduction wave at —0.84v and was followed by an irreversible reduction with a peak potential of —1.53v.

Controlled potential electrolysis of this product at a potential corresponding to the first reduction step (—1.0v) gave a value of $n_{app} = 1.30$. The solution was sampled at this stage for esr analysis. The resulting esr spectrum, containing approximately 40 lines, was significantly different from the spectrum of $APDO^{-\cdot}$ mentioned above.

The most logical product of the complete reduction of APDO, based on the behavior of other amine oxide systems, would involve the 4,4'-azobispyridine (AP) system; hence, the electrochemical behavior of AP was examined. Cyclic voltammetry, employing a platinum disk electrode, of AP is shown in Fig. 4, curve 6. The voltammetric behavior of AP is the same as that of the reduction product of APDO obtained by complete reduction at —1.8v. Controlled potential electrolysis of AP, using conditions identical to those employed for APDO, was performed at a potential of —1.0v, which corresponds to the plateau of the first reduction wave. An n_{app} value of 1.09 electrons per molecule was observed for this reduction. A sample was taken at this stage for esr analysis. The resulting esr spectrum was identical to that obtained from reversal coulometry reported in the previous paragraph.

Effect of Proton Donor

To gain some insight into the intermediate steps involved in the reduction of APDO, its electrochemical behavior in the presence of varying amounts of a proton-donating agent was studied. Hydroquinone (HQ), previously employed in a study of 9,10-diphenylanthracene (12) was used as the proton donor. The effect of varying amounts of HQ on the polarographic behavior of APDO is shown in Fig. 5. The first wave is unaffected by increasing concentrations of HQ; however, the second wave is shifted in an anodic direction and the diffusion current is increased as the HQ concentration is increased. The second reduction step changes from near reversible behavior, at zero concentration of HQ ($E_{3/4} - E_{1/4} = 65$ mv), to completely irreversible character ($E_{3/4} - E_{1/4} = 150$ mv) in the presence of excess HQ (HQ/APDO ratio = 8.0). The cyclic voltammetric behavior of APDO at a hmde in the presence of HQ is illustrated in Fig. 6. The first reduction step is unaffected by addition of excess HQ with the second reduction showing behavior analogous to that seen in polarography (i_{pc} increasing and E_{pc} shifting anodically with increasing HQ concentration). These results suggest that if the chemical reaction following the first reduction step involves protonation, its rate is still negligible during the duration of the voltammetric experiment. However, the rate of the reaction following the second reduction step is increased considerably. Controlled potential electrolysis at —0.80v was performed on the above-mentioned solution with a resulting n_{app} of 5.92 electrons, which is the same as the n_{app} found for the over-all reduction in the absence of proton donor.

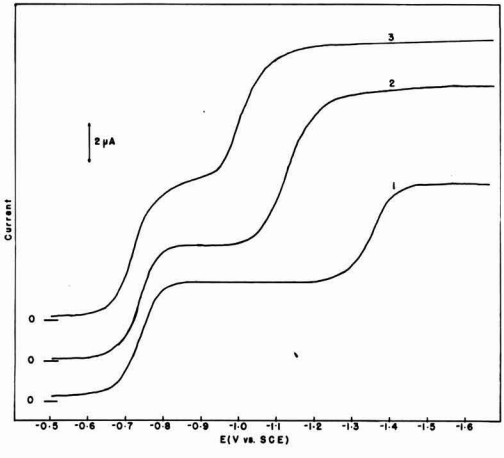

Fig. 5. Polarograms for reduction of 1.05 mM APDO in 0.1M TBAP in DMF in the presence of varying amounts of hydroquinone (HQ): 1, no HQ added; 2, HQ concentration is 1.77 mM; 3, HQ concentration is 8.10 mM.

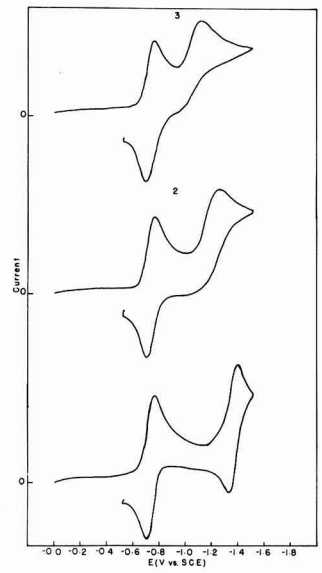

Fig. 6. Cyclic voltammograms for the reduction of 1.05 mM APDO at a hmde in 0.1M TBAP in DMF in the presence of varying amounts of hydroquinone (HQ): 1, no HQ present; 2, 1.77 mM HQ; 3, 8.10 mM HQ.

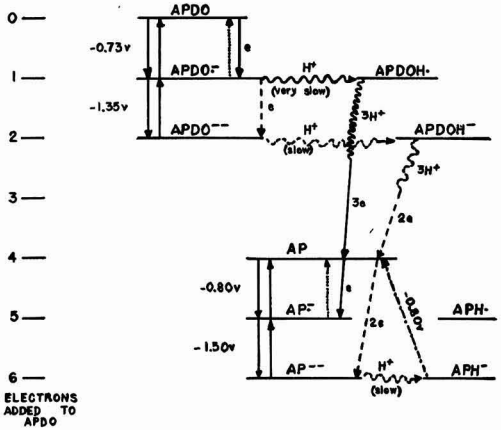

Fig. 7. Schematic diagram of mechanism of the electroreduction of APDO. Electron transfer processes at the electrode are indicated by straight lines (reductions downward and oxidations upward) and chemical reactions by wavy lines. The extent of reduction, in terms of electrons added to APDO, is indicated by the distance down from the APDO line. The potentials at which reactions occur ($E_{1/2}$, *vs.* SCE) are indicated near the appropriate couple, when known. Some qualitative measure of the rates of chemical reactions has been given ("slow" denotes a reaction which does not proceed to an appreciable extent during a time characteristic of voltammetric experiments but is appreciable on the coulometric time scale; "very slow" denotes a reaction which proceeds only partially even in coulometric experiments). ——— Reduction at —1.0v; ..... oxidation at —0.20v following this reduction; — — — — — — reduction at —1.8v; — ● — ● — ● oxidation at —0.2v following this reduction.

Discussion

The mechanism of the electrochemical reduction of APDO is shown in the schematic diagram in Fig. 7. In this diagram electron transfer processes at the electrode are indicated by straight lines and chemical reactions are shown as wavy lines. Compounds which are reduction products of APDO are shown as lines below the APDO line; these lines are spaced in increasing numbers of electrons added to the parent molecule. Where the appropriate electrode potentials are known, they are indicated next to the couple. Downward arrows show reduction and upward ones oxidations.

We proposed to explain the experimental results with the following mechanism:

At potentials corresponding to the first wave:

$$\mathrm{APDO} + e \rightleftarrows \mathrm{APDO}^{-\cdot} \qquad [4]$$

$$\mathrm{APDO}^{-\cdot} + \mathrm{HS} \rightarrow \mathrm{APDOH}\cdot + \mathrm{S}\ \text{(very slow)} \qquad [5]$$

$$\mathrm{APDOH}\cdot + 3\mathrm{H}^+ + 3e \rightarrow \mathrm{AP} + 2\mathrm{H_2O} \qquad [6]$$

$$\mathrm{AP} + e \rightleftarrows \mathrm{AP}^{-\cdot} \qquad [7]$$

At potentials corresponding to the second wave:

$$\mathrm{APDO}^{-\cdot} + e \rightleftarrows \mathrm{APDO}^{--} \qquad [8]$$

$$\mathrm{APDO}^{--} + \mathrm{H}^+ \rightarrow \mathrm{APDOH}^- \qquad [9]$$

$$\mathrm{APDOH}^- + 3\mathrm{H}^+ + 2e \rightarrow \mathrm{AP} + 2\mathrm{H_2O} \qquad [10]$$

$$\mathrm{AP} + 2e \rightarrow \mathrm{AP}^{--} \qquad [11]$$

$$\mathrm{AP}^{--} + \mathrm{HS} \rightarrow \mathrm{APH}^- + \mathrm{S}^- \qquad [12]$$

The polarographic and cyclic voltammetric results show that during the small duration of these experiments (3-20 sec), the results can be explained by reactions [1] to [3]. Only a small contribution of the following reactions [9] through [11] is found, resulting in the ECE-type behavior of the second voltammetric wave.

Controlled potential coulometric reduction at a potential corresponding to the plateau of the first wave gives n_{app} values significantly greater than one and evidence of production of an electroactive species (current not decaying to the background value). Reversal coulometry (oxidation at the foot of the first wave) gives a smaller value of n_{app}, for example (n_{app} reduction = 0.70, Table II). This behavior is ascribed to a very slow reaction of the anion radical $\mathrm{APDO}^{-\cdot}$ to form an electroactive species; a protonation reaction to APDOH· seems reasonable. Since the first reduction wave of APDO is unaffected by addition of a proton donor, this reaction must be slow, even in the presence of excess hydroquinone. Further reduction and protonation eventually leads to azopyridine (AP), which is reduced at these potentials to the stable anion radical $\mathrm{AP}^{-\cdot}$. Since APDOH· is reduced at these potentials in a series of steps involving 4 electrons, only a small amount of reaction of $\mathrm{APDO}^{-\cdot}$ will give an appreciable contribution to n_{app}. For example, the decomposition of about 20% of the $\mathrm{APDO}^{-\cdot}$ would account for these results. The fact that voltammetry of the reduced solution shows a cathodic peak current, on reversal, of about 80% of the original cathodic peak current, is also in agreement with this mechanism and suggests that some of the intermediates involved in [6] are not oxidizable. Since the second reduction wave is about the same after reduction as in the original solution, reduction of both products and intermediates is suggested. The esr spectra obtained following reduction at potentials of the first wave are probably those of $\mathrm{APDO}^{-\cdot}$, $\mathrm{AP}^{-\cdot}$ and perhaps some intermediates.

Reduction at a potential on the plateau of the second wave leads in a series of protonation and reduction reactions to APH^-, with $n_{app} = 6$ (within experimental error). The electrochemical behavior of the solution resulting from this reduction is identical with that obtained from reduction of AP itself.[1] After complete

[1] A complete study of the electrochemistry of azopyridine and other aromatic azocompounds in DMF has been completed (J. Sadler, Ph.D. Dissertation, The University of Texas at Austin, 1967) and has been submitted for publication elsewhere. The behavior of azopyridine shown in the lower part of Fig. 7 has been established in this study.

reduction, oxidation at —0.2v, and re-reduction, an esr signal which can unequivocally be ascribed to AP^- is obtained, giving further support to this mechanism.

Experimental

The cell and vacuum line used were essentially the same as reported by Santhanam and Bard (12). DMF purification and storage also followed the procedure outlined there. The filling of the electrochemical cell was accomplished by first evacuating the cell containing the supporting electrolyte and mercury pool, cooling with liquid nitrogen, then distilling DMF under vacuum into the cell. After the distillation had been completed, the cell and contents were allowed to warm to room temperature with continuous evacuation. The cell was then brought to atmospheric pressure by introducing helium through the vacuum line. The helium was obtained from the Matheson Company, LaPorte, Texas. It was passed successively through anhydrous magnesium perchlorate, copper turnings (heated to 350°C), activated charcoal cooled to liquid nitrogen temperature, and finally to the cell. A helium blanket over the solution was maintained throughout the experiment. The auxiliary electrode was a platinum wire. The reference electrode was an aqueous SCE connected via an agar plug and sintered glass disk to the test solution. Stirring was by a magnetic stirrer.

The voltammetric experiments were carried out using a multipurpose instrument employing operational amplifier circuitry with three-electrode configuration, similar to those discussed in the literature (13). Controlled potential coulometry was carried out using a previously described apparatus (14).

The APDO was from Aldrich Chemical Company. It was recrystallized twice from absolute ethanol and twice from benzene. The melting point of the resulting product was very sharp at 236.5°C (decomp.). AP was synthesized by reduction of APDO in ethanol with zinc dust and ammonia. The melting point of the product after recrystallization from petroleum ether, was 106.5°C as compared to a literature value of 107°C (15). The TBAP was obtained from Southwestern Analytical Chemicals, Austin, Texas. It was dried in a vacuum oven for 8 hr at 70°-80°C and stored in a desiccator until use.

A Varian Associates V-4502 spectrometer employing 100-kc field modulation was used for esr spectroscopy.

Acknowledgment

The support of this research by the Robert A. Welch Foundation and the National Science Foundation (GP 6688X) is gratefully acknowledged. The authors are indebted to Tom V. Atkinson and Larry O. Wheeler for aid in the esr spectroscopy and to K. S. V. Santhanam for helpful discussions during the work.

Manuscript received July 17, 1967; revised manuscript received *ca.* Nov. 23, 1967.

Any discussion of this paper will appear in a Discussion Section to be published in the December 1968 JOURNAL.

REFERENCES

1. A. Foffani and E. Fornasari, *Gazz. Chim. Ital.*, **83**, 1051, 1059 (1953).
2. A. Foffani and E. Fornasari, *Atti. Acad. Naz. Lincei*, Ser. 8, **23**, 62 (1957).
3. G. Horn, *Acta Chimica Acad. Hung.*, **27**, 123 (1961); **33**, 287 (1962).
4. L. V. Varyukhina and Z. V. Pushkareva, *J. Gen. Chem. USSR*, **26**, 1953 (1956).
5. O. N. Nechaeva and Z. V. Pushkareva, *ibid.*, **28**, 2721 (1958).
6. T. Kubota and H. Miyazaki, (*a*) *Bull. Chem. Soc. Japan*, **35**, 1549 (1962); (*b*) *ibid.*, **39**, 2057 (1966).
7. Y. Date, (*a*) *J. Chem. Soc. Japan (Nippon Kagaku Zasshi)*, **84**, 875 (1963); (*b*) *ibid.*, **84**, 964 (1963).
8. L. M. Chambers, *Anal. Chem.*, **36**, 2431 (1964).
9. P. J. Elving and C. R. Warner, *Coll. Czechoslov. Chem. Commun.*, **30**, 4210 (1965).
10. G. Anthoine, J. Nasielski, E. Vander Donckt, and N. Vanlautem, *Bull. Soc. Chim. Belges*, **76**, 230 (1967).
11. R. S. Nicholson and I. Shain, *Anal. Chem.*, **36**, 706 (1964).
12. K. S. V. Santhanam and A. J. Bard, *J. Am. Chem. Soc.*, **88**, 2669 (1966).
13. (*a*) W. M. Schwarz and I. Shain, *Anal. Chem.*, **35**, 1770 (1963); (*b*) W. L. Underkofler and I. Shain, *ibid.*, **35**, 1778 (1963).
14. A. J. Bard, *Anal. Chem.*, **35**, 1121 (1963).
15. H. I. den Hertog, C. H. Henkens, and J. H. Van Roon, *Rec. Trav. Chim.*, **71**, 1145 (1962).

The Cu/CuF_2 Couple in Anhydrous Hydrogen Fluoride

Brian Burrows* and Raymond Jasinski*

Tyco Laboratories, Inc., Waltham, Massachusetts

ABSTRACT

The electrochemical behavior of a Cu electrode was investigated in basic, anhydrous HF. Anodization of Cu established the Cu/CuF_2(s) couple. Micropolarization and bias tests indicated that this couple was reversible, and its potential *vs.* an H_2 electrode in the same solution agreed well with that predicted from thermodynamic data. Thus the couple is suitable for use as a reference electrode in basic HF. The formation of a relatively thick, insoluble anodic film at a copper electrode was demonstrated by cyclic voltammetry and chronopotentiometry. Anodic-cathodic cycling of an electrode gave rise to significant roughening of the electrode surface as shown by i-E curves, E-t curves, and differential capacitance measurements on cycled electrodes. X-ray analysis of the anodic film confirmed the presence of crystalline copper fluoride. The formation of CuF_2 appears to proceed via dissolution of Cu to form Cu^{2+} ions, followed by precipitation of the CuF_2 on the electrode surface. The polarization behavior of Cu electrodes in anhydrous HF solution containing added KF showed that anodic film formation can be approximated by Tafel lines with an apparent exchange current density of about 3×10^{-6} amp/cm^2. Properties of the anodic film of CuF_2 are quite similar to those observed for noncontinuous anodic films formed in aqueous solutions.

Very little work on the characterization of electrode reactions in anhydrous or aqueous HF has been reported. A small number of potentiometric investigations have been made (1-3); a brief report on the construction of a rotating nickel electrode for use in anhydrous HF is available (6), and a dropping mercury electrode using a Teflon capillary in aqueous HF

* Electrochemical Society Active Member.

has also been described (4, 5). The process of electrochemical fluorination of organic compounds has been known for some time (7, 8) and is a commercial operation. Recently, the anodic behavior of metals in HF has been examined, and an attempt was made to find an inert or passive anode at which the mechanisms of electrochemical fluorination could be studied (8). Monel, platinum, and nickel were least reactive; the anodic passivity of nickel in HF was studied in some detail (9).

The $Cu/CuF_2(s)$ couple has been used as a reference electrode of the second kind in anhydrous HF solutions (2, 3). The electrode was formed by anodizing a Cu plate in HF at + 1.0v against a Pt electrode. No direct evidence on the reversibility or composition of the electrode was given. A $Hg/Hg_2F_2(s)$ couple has also been used as a reference electrode of the second kind (1, 8, 9). Mention has been made (11) of a direct measurement of the potential of the cell $H_2/HF(KF)/F_2$ (E = 2.768v at 0°C). It was noted that the fluorine electrode was irreversible.

Cupric fluoride is of interest as a cathode in battery systems using aprotic organic solvents. One method for its preparation is by anodization of copper in anhydrous HF. This paper describes studies of the Cu/CuF_2 electrode and the mechanism of formation of CuF_2 at a copper electrode in basic, anhydrous HF.

Experimental

Experiments were carried out in a 1M solution of KF in anhydrous HF at 0°C and 25°C. The water content of the HF was nominally 0.04 m/o (mole per cent) corresponding to approximately 0.02M (19).

Apparatus and procedure.—A schematic diagram of the apparatus for handling anhydrous HF (Matheson Company, 99.9 m/o) is shown in Fig. 1. B_1, B_2, B_3, and B_4 are Teflon FEP bottles (4 oz capacity). The connecting tubing was of flexible Teflon (0.25 in. ID) and the stopcocks were of polyethylene. Kel-F wax (3M Company) was used to seal all the joints and inlets.

Since the ambient temperature was 25°C, HF was delivered from the cylinder in the gaseous state. Nitrogen was first flushed through the apparatus followed by HF vapor. An ice-bath was then placed around B_1 to condense HF. After about 40 cc of liquid HF had been collected, the ice-bath was removed and placed in position around B_2 (the electrochemical cell with counter, working, and reference electrodes already in position). An incandescent lamp was held under B_1 to warm the HF gently and distill it over to B_2. A small residual amount of liquid was left in B_1. An amount of KF (B & A, reagent grade) had previously been added to B_2 so that an ionically conducting solution, approximately (±10%) 1M in KF, would result. It was observed that KF dissolved quite readily in HF without mechanical stirring. Dry nitrogen was then bubbled through the cell for up to 2 hr until a current-voltage scan at a Cu electrode indicated the absence of impurities (see below).

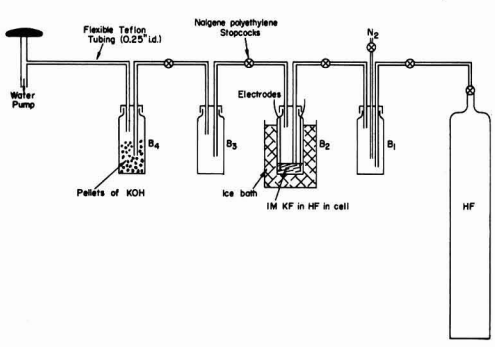

Fig. 1. Schematic representation of the apparatus used for handling anhydrous HF. B_1, B_2, B_3, B_4 were Teflon FEP bottles (4 oz capacity). The connecting tubing was flexible Teflon; the stopcocks were polyethylene.

At the end of an experiment the HF was transferred from B_2 by removing the ice bath, allowing the HF solution to warm up, and applying a gentle vacuum with a water pump. This vaporized the HF into B_4 which contained pellets of KOH. It was possible to remove a working electrode from B_2 during an experiment and replace it with a new one without overly contaminating the HF.

HF vapor could vent through the caustic trap (B_4) during cell measurements. However, the apparatus did provide a sufficient back pressure to make this leak rate negligible, even at 25°C where the vapor pressure of HF is slightly above 1 atm.

Electrodes.—Working electrodes were prepared from sections of electrolytic copper wire 1 mm diameter, covered with shrinkable Teflon (Rayclad Tubes, Inc.) which gave a tight, insulating layer. Sufficient Teflon was removed at the working end of the electrode to expose 1 cm of Cu. The working area (0.33 cm^2) was cleaned in dilute HNO_3 and washed in distilled water and acetone. The electrodes were placed in the cell (B_2) through small holes drilled around the lip of the bottle so that a close fit was obtained. The inlet holes were sealed with Kel-F wax. Electrodes of Ag (0.16 cm^2 in area), Pt (0.16 cm^2 in area), and Ni (0.20 cm^2 in area) were prepared similarly. The counter electrode was a coil of Ni wire; a 1 cm square piece of porous copper plaque (Clevite Corporation) was used to form the reference electrode.

The H_2 electrode was of the fuel cell type (15), consisting of Pt black (Engelhard Industries, Inc.) bonded with Teflon and supported on a Pt mesh screen of 2 cm^2 area. This electrode was placed in a Teflon tube (1 cm in diameter) with a hydrophilic porous Teflon frit (Chemplast, Inc.) at one end and held in place with Kel-F wax (3M Company).

Electrochemical measurements.—Potentiostatic current-potential curves (cyclic voltammograms) were obtained in the usual manner using a motor-driven, slow-function generator (maximum scan rate 800 mv/min). The output of the function generator was applied to a Wenking potentiostat (Model 61 RS). The i-v curve was recorded on an X-Y recorder (Houston Omnigraphic, Model HR-98T). Since the input impedance of the X-Y recorder was low (0.2 Mohm), a cathode follower was used in the potential-measuring circuit to avoid undue loading of the reference electrode-working electrode cell. The unity-gain follower was constructed from an operational amplifier (Philbrick Researches, Inc., Type P65AU); the input impedance of this device was 33 Mohm. Unless stated otherwise, all i-v curves were obtained using a scan rate of 800 mv/min.

Potential-time curves (chronopotentiograms) were recorded on the same X-Y recorder using the time base. A constant-current power source (Electronic Measurements, Model C623) was used to supply the current at voltages up to 400v.

Steady-state, constant current polarization curves were obtained by recording the change of potential with time on the X-Y recorder with a full scale deflection of 20 sec. The potential assumed a constant value within several seconds and steady-state potential values were read off the plateau. By using relatively short times to measure the activation polarization, convective and concentration polarization effects were minimized.

Micropolarization tests on the Cu plaque were carried out by passing a small constant current and measuring the potential with a differential d-c voltmeter (John Fluke, Model 825A).

The capacity measurements were based on a method in which a triangular wave of 100 cps and an amplitude of 25 mv (*i.e.*, a sweep rate of 5v/sec), biased by

a convenient d-c voltage, was fed into the signal input of the potentiostat (20). The d-c voltage was selected so that Faradaic currents were avoided. The small triangular potential wave (Exact Electronics, Inc., fast function generator, Type 255) was fed *via* a differential amplifier (Tektronix, Type 2A63 plug-in) into one axis of an oscilloscope (Tektronix, Type 561A). *Via* another differential amplifier of the same type, the voltage drop across a suitable precision resistor was fed into the other axis of the oscilloscope. The resulting trace on the oscilloscope screen was a rectangular box from which the peak-to-peak current was measured. The differential double layer capacity C_{dl} was then equal to $i/2(dE/dt)$.

X-ray analysis.—Qualitative identification of anodic films was obtained from analyses of Debye-Scherrer powder patterns using CuKα radiation with a Ni filter at 50 kv and 20 ma. The films were formed on 0.5 mm Cu wire in HF and then exposed to radiation up to 6 hr. The lines arising from Cu were determined during the analysis and eliminated.

Results and Discussions

The initial studies of the Cu/CuF_2 couple were complicated by the presence of an electroactive impurity. This impurity also reacted at Ag electrodes but not at Pt and Ni. An i-E curve taken at a Cu electrode in impure HF is shown in Fig. 2. The anodic wave beginning at 0 mv (*vs.* Cu/CuF_2) was diffusion controlled. After anodization, a black film was present on the Cu electrode; the same film was found on Cu electrodes left in contact with HF for some time. An x-ray analysis of this film showed the pattern of Cu_2S and possibly CuOHF; CuF_2 was not detected.

The impurity was removed by bubbling dry nitrogen (or argon) through the cell for periods of up to several hours. The absence of the impurity was indicated by the disappearance of the diffusion controlled anodic wave and the anodic peak current, as well as the absence of a black film after Cu had been standing in contact with HF. All electrochemical experiments described here were carried out in HF purified by N_2 bubbling.

In an attempt to identify the nature of the impurity, i-E curves were run at Cu electrodes in pure HF after bubbling SO_2 and H_2S through the solution for about 15 min in separate experiments. Neither of these impurities showed any anodic activity. Bubbling O_2 through the solution also decreased the impurity wave. The presence of dissolved O_2 was detected on a Pt electrode by a reduction wave at +0.5 to +0.6v *vs.* Cu/CuF_2. N_2 bubbling removed this reduction wave.

Ag was observed to dissolve anodically in the purified HF and no anodic film was formed. Figure 3 shows a background scan on a platinum electrode in anhydrous HF. The diffusion controlled anodic wave at +1.2 to +1.3v was presumably due to oxidation of traces of water. The limiting cathodic process was H_2 evolution. An order of magnitude calculation can be made of the concentration of water present. Using the equation given by Delahay (24) for the current as a function of potential scan rate with $\nu = 0.078$ v-sec^{-1}, $n = 2$, and taking $D = 10^{-6}$ cm^2 sec^{-1} for the diffusion coefficient of H_2O in HF, then C_{H_2O} calculates to 0.01M. This is close to the nominal impurity concentration of 0.02M.

As mentioned above, KF was added to HF in order to produce a solution with reasonable conductivity (10). In liquid HF, solutions of the alkali metal fluorides act as bases (10), so that the dissolution of KF may be formally represented as follows

$$KF + HF \rightarrow K^+ + HF_2^- \qquad [1]$$

Thus, the solvated fluoride ion acts as a base and its concentration is related to that of solvated protons through

$$3HF \rightleftharpoons HF_2^- + H_2F^+ \qquad [2]$$

with an equilibrium constant of approximately 2×10^{-12} (10). H_2O also acts as a base in liquid HF and the following equilibrium is established

$$H_2O + 2HF \rightleftharpoons H_3O^+ + HF_2^- \qquad [3]$$

with an equilibrium constant of 0.55 (3) at 0°C. Thus all HF_2^- ion concentrations should include the contribution from the solvolysis of impurity H_2O according to Eq. [3]. The concentration of H_2O in HF as taken from the cylinder is nominally 0.02M. Using the approach of Clifford *et al.* (3), the concentration of HF_2^- contributed from equilibrium [3] was calculated to be 0.01M.

Thus this additional concentration had an insignificant effect on the potential of the Cu/CuF_2 electrode potential in a solution already 1M in HF_2^- and, for the same reason, a negligible effect on the observed transition times for CuF_2 formation (see below). There may be, however, a specific chemical interaction between CuF_2 and undissociated H_2O, resulting in a slightly increased solubility of CuF_2, which would affect transition times. The magnitude of this effect would appear to be negligible since the solubility of CuF_2 in HF (containing about 0.01M H_2O) at 0°C was found to be less than 2×10^{-5}M (2). In the presence of 1M KF the solubility of CuF_2 may be even lower.

Reference electrode.—Copper electrodes immersed in a 1M solution of KF in HF at 0°C always had low differences (<5 mv) in rest potentials, which differences remained constant. The potential of a fresh Cu

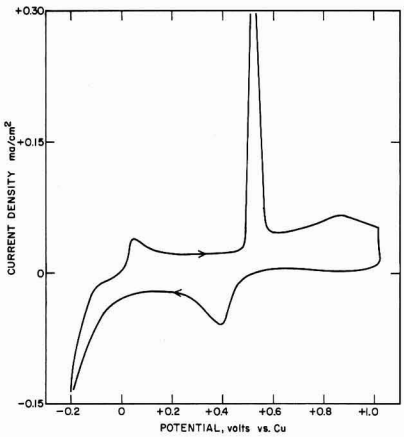

Fig. 2. Cyclic voltammogram at Cu electrode in impure HF (1M KF) at 0°C. Scan rate was 800 mv/min, and scan was started at 0 mv.

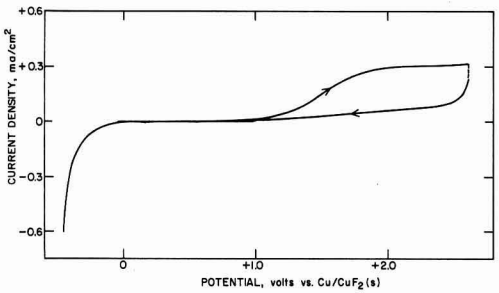

Fig. 3. Cyclic voltammogram at Pt electrode in purified HF (1M KF) at 0°C. Scan rate was 800 mv/min, and scan was started at 0 mv.

electrode placed in solution was less than 5 mv with respect to an electrode which had been immersed for several days. Furthermore, the potentials of fresh or aged electrodes were little different from those of electrodes previously anodized at +200 mv. This behavior suggested that a reversible couple was associated with the Cu electrode in a basic HF solution, namely

$$CuF_2 + 2HF + 2e^- \rightleftharpoons Cu + 2HF_2^- \quad [4]$$

To check the reversibility, a polarization test was carried out on a porous Cu electrode (geometric area 2 cm^2). Small constant currents were passed between the Cu electrode and a Ni counter electrode. The resulting polarization was measured with respect to an unpolarized Cu electrode as shown in Fig. 4. It can be seen that there was no significant hysteresis and only a small displacement of potential when several microamperes were flowing.

It is probable that some CuF_2 was formed at open circuit by corrosion involving trace amounts of reducible impurities in the solvent (12). As will be shown below, the quantity of CuF_2 formed in this manner is small compared with anodically formed CuF_2 at more positive potentials.

The composition of the film formed on copper after repetitive anodization was shown, by x-ray analysis, to be crystalline $CuF_2 \cdot 2H_2O$ (23). It is probable that CuF_2 formed in the cell hydrolyzed (23) upon exposure to the atmosphere during the x-ray measurements.

The potential of the Cu/CuF_2 couple at 25°C was measured with respect to a hydrogen electrode immersed in the same solution. A Teflon-bonded, high surface area platinum black electrode was introduced into the cell and was separated from the copper electrode and the bulk of the electrolyte by a junction of porous Teflon. The hydrogen electrode was only half immersed in the electrolyte so that a three phase contact could be maintained between the electrode, HF, and hydrogen gas. A flow of H_2 was sustained over the electrode rather than bubbling gas through the electrolyte during the measurements to keep the pressure of hydrogen close to one atmosphere and still avoid significant changes in HF content. The results of three such experiments are shown in Table I; the potentials were stable within ±3 mv for the duration of the experiments (approximately 30 min).

Table I. Potential of the Cu/CuF_2 couple vs. the hydrogen electrode at 25°C

Run	Potential, mv
1	+0.274
2	+0.278
3	+0.277
	Avg. +0.276 ± 5

In terms of the self ionization equilibria for HF described above, the half cell reactions are probably as follows

$$CuF_2 + 2HF + 2e \rightleftharpoons Cu + 2HF_2^- \quad [5]$$

$$H_2 + 2HF \rightleftharpoons 2H_2F^+ + 2e^- \quad [6]$$

The total cell reaction is thus

$$CuF_2(s) + H_2(g) \rightleftharpoons Cu(s) + 2HF(l) \quad [7]$$

with all components in their standard states. Equation [7] assumes that the activity of HF (approximately 50M) in 1M KF equals that of liquid HF. The data of ref. (25) implies that this assumption is valid within the limits quoted in Table I. Although the potentials for each half cell reaction (Eq. [5] and [6]) are dependent on the activity of the HF_2^-, the total cell potential (Eq. [7]) is independent of this factor because of equilibrium [2].

The theoretical cell potential is also independent of the activity of H_3O^+ arising from the presence of H_2O. Thus the two half-cell reactions in a solution containing H_3O^+ ions are probably [5] and

$$H_2 + 2H_2O \rightleftharpoons 2H_3O^+ + 2e \quad [8]$$

Adding [5] and [8] together results in the theoretical over-all cell reaction [7], which is independent of the HF_2^- activity as well as the H_3O^+ activity because of equilibrium [3]. The standard cell potential at 25°C can be computed from thermodynamic data and a value of +0.27v was obtained in this manner (13, 14) in reasonable agreement with the observed potential. This value at 25°C is in disagreement, however, with that of +0.52v given by Clifford and co-workers (3) for Cu/CuF_2 in HF at 0°C.

Polarization measurements.—A cyclic voltammogram for Cu in purified 1M KF-HF is shown in Fig. 5. The scan rate was 800 mv/min, scanning first from 0 to +200 mv *vs.* a Cu/CuF_2 reference electrode. The current scale in this figure is in terms of ma/cm^2 so that the small currents noted in Fig. 4 are not observable. The form of the curve is substantially different than that of the impure solutions. Apparently only one major process, presumably formation of CuF_2, is involved.

The i-E curve (Fig. 5) has two principal features: an anodic current peak and a less pronounced cathodic current peak. The anodic peak height was dependent on stirring, scan rate, and number of anodic-cathodic cycles to which the electrode had been subjected. In a quiescent solution the area under the anodic peak (between 0 to 200 mv) and the area under the corresponding cathodic peak (between 0 and —400 mv) was found to be equal at a scan rate of 800 mv/min. In cases when the anodic scan was taken to potentials more positive than +200 mv, the subsequent cathodic area was smaller. This may be attributed to partial dissolution of the film. Such behavior has been observed for anodic films in aqueous solutions (16).

When scan rates much slower than 800 mv/min (160 and 80 mv/min) were used, it was observed that the anodic peak areas were significantly larger than those at 800 mv/min, although the cathodic areas were unchanged. This indicates a loss by convection and diffusion of a soluble intermediate from the vicinity

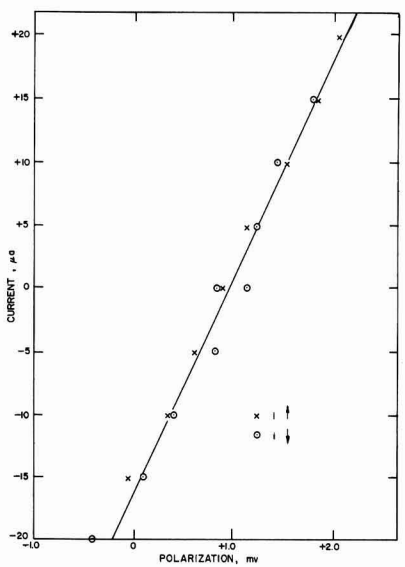

Fig. 4. Polarization (mv) as a function of current density (μa) for a porous Cu electrode (2 cm^2) in purified HF (1M KF) at 0°C.

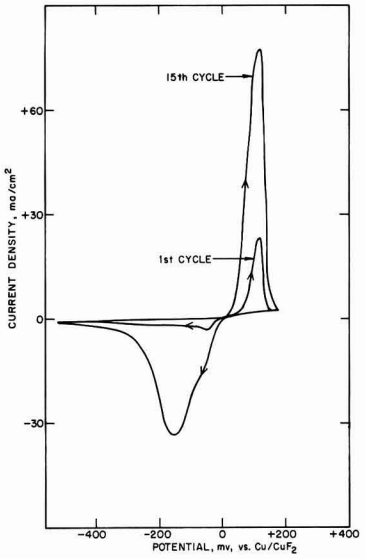

Fig. 5. Cyclic voltammograms at a Cu electrode in purified HF (1M KF) at 0°C. Scan rate was 800 mv/min, and scans were started at the open-circuit potential, *i.e.*, 0 mv.

of the electrode surface during the formation of the film of CuF_2. Similar behavior was observed in the chronopotentiometric experiments (see below).

With each subsequent anodic-cathodic scan, the anodic and cathodic peak heights (and areas) increased, suggesting that the electrode was progessively roughened (Fig. 5). The same behavior was observed with respect to transition times during repetitive constant-current cycling. In 2M KF, the anodic and cathodic peaks were considerably greater, indicating a proportionality between the basicity of the HF solution and the extent of CuF_2 formation.

A summary of the initial peak areas on fresh Cu electrodes and peak areas after 15 anodic-cathodic cycles in 1M and 2M KF solutions is given in Table II.

From the data in Table II, the initial average film thickness was estimated as 4×10^{-6} cm in 1M KF solution and 1×10^{-5} cm in 2M KF. Alternatively, using the data of Table II, one can estimate an apparent number of molecular layers of CuF_2 after the method of Hickling and Taylor (18). Thus the initial film thickness in 1M and 2M KF solution was calculated to correspond to 47 and 125 molecular units, respectively. These estimates of molecular units would, in the case of a compact film, correspond to the number of molecular layers. However, the fact that the initial film is as thick as it is suggests that the film has relatively poor protective powers; *i.e.*, the film is noncontinuous or porous. Hackerman, Snavely, and Fiel (8) concluded that Cu was intermediate in its corrosion resistance in HF. They placed Cu between metals such as Ta and Ag which corroded rapidly, and Pt and Ni which were quite stable.

Differential capacitance measurements.—Double layer capacitance measurements were made at −200 mv *vs.* Cu/CuF_2 before each anodic potential scan. The results are shown for the first five cycles in Table III, together with the total anodic charge passed to +200 mv (Q anodic) and with the ratio Q anodic/C_{dl}. It can be seen that the increase in anodic charge with cycling is primarily due to surface roughening. There is not, however, a direct proportionality between the increase of surface area and the anodic charge.

Table II. Anodic peak areas from i-E curves (scan rate 800 mv/min) recorded at Cu electrodes in HF at 0°C

	Basicity of HF	
	1M KF, mc/cm²	2M KF, mc/cm²
Initial scan	58	155
15th Cycle	421	531

Table III. Differential double layer capacitance of Cu electrode and charge associated with anodic film formation in HF (1M KF) at 0°C

	C at −200 mv (μf/cm²)	Q anodic (mc/cm²)	Q_a/C_{dl} (mc/μf)
1st Cycle	20	58	2.9
2nd Cycle	36	120	3.3
3rd Cycle	105	139	1.3
4th Cycle	138	176	1.3
5th Cycle	167	194	1.2

Chronopotentiometry.—A potential-time curve obtained for the formation and discharge of CuF_2 in 1M KF-HF is shown in Fig. 6 at a current density of 6.7 ma/cm² in an unstirred solution. The main feature is the equality of the anodic and cathodic transition times. This implies that an insoluble film is formed on anodization, in agreement with the observations from cyclic voltammetric scans (Fig. 5). These observations also imply that the effect of small amounts of water present (*ca.* 0.01M) on the anodic formation and cathodic reduction of CuF_2 was negligible. At lower current densities, it was observed that two poorly defined transition times actually were present on the reduction step. At current densities much higher than 20 ma/cm², the cathodic transition time became too distorted to measure.

The question of diffusion control was checked by observing the effect of stirring (N_2 bubbling) on the transition times. It was found that stirring increased the transition time for the oxidation step (τ_{ox}) by about 100% at 15 ma/cm², indicating some form of diffusion control, but τ_{red} was independent of stirring and approximately equal to the τ_{ox} at the same current density in an unstirred solution. This effect of stirring at short transition times is equivalent in terms of convection and diffusion to the effect of using slow scan rates (see below). These effects can be discussed

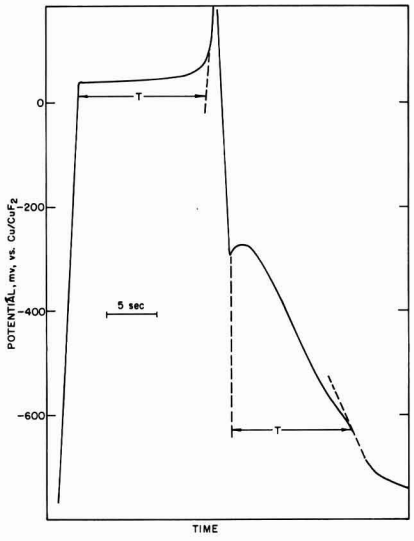

Fig. 6. Potential-time curve at a Cu electrode in purified HF (1M KF) at 0°C. Current density was 6.7 ma/cm².

in terms of the two possible general mechanisms of CuF_2 film formation.

One mechanism involves the dissolution of Cu to Cu^{2+} followed by precipitation of CuF_2 at the electrode surface, *i.e.*

$$Cu \rightleftharpoons Cu^{2+} + 2e$$

$$Cu^{2+} + 2HF_2^- \rightarrow CuF_2(s) + 2HF \qquad [10]$$

The other mechanism involves the direct formation on the electrode surface of CuF_2, *via* an adsorbed film of HF_2^-, *i.e.*

$$Cu + 2HF_2^-(ads) \rightleftharpoons CuF_2(s) + 2HF + 2e \qquad [11]$$

If [11] were the operative process, then stirring would enable the passive film to be formed more rapidly, shortening (or in any case not increasing) τ_{ox}. On the other hand with [10] as the process, stirring would have the effect of removing some of the Cu^{2+} ions from the vicinity of the elctrode surface or of removing some of the CuF_2 before it had precipitated on the surface. In either event the effect would be to increase τ_{ox}, as was observed. Thus the film of CuF_2 was most likely formed *via* the dissolution of Cu to Cu^{2+} ions. The same argument can be applied to explain the observed increase of anodic charge with decreasing scan rates.

The results of the galvanostatic charging experiments on individual electrodes are summarized in Table IV. The interesting points to note are that $i\tau$ decreases with increasing i, while $i\tau^{1/2}$ increases with increasing i. This indicates that processes controlled by diffusion become increasingly important at higher current densities. This is at variance with the usual observation that either $i\tau$ or $i\tau^{1/2}$ is constant with increasing i during the formation of porous (or noncontinuous) anodic films (16). Generally, at low i (large τ) diffusion is more important and $i\tau^{1/2}$ is constant. At large i (small τ) it is usually found that $i\tau$ is constant.

The explanation for the observed behavior in the present case probably involves the influence of a rate-limiting step associated with the crystallization of the precipitated CuF_2 (21).

Tafel parameters.—As shown in Fig. 6, the CuF_2 electrode comes to a steady potential within approximately 1 sec after the application of a constant current. At low current densities, *e.g.*, 2 μamp/cm^2, this potential was constant for over 1 hr. It was therefore possible to characterize the initial surface in terms of the Tafel parameters by exposing the surface to a series of constant current pulses of sufficient duration (*e.g.*, 2 sec) to establish a steady potential, but not so long as to consume a substantial portion of the surface. The anodic polarization behavior was determined first, followed by the cathodic behavior.

These Tafel parameters represent a complex combination of overpotentials involving the dissolution of copper metal, the potential dependence of nucleation and growth of the anodic CuF_2 film, and possibly other processes. Nevertheless, this representation is convenient for summarizing experimental data.

A Tafel plot is given in Fig. 7. Tafel behavior was obtained for both anodic and cathodic processes. It can be seen that the anodic and cathodic processes have

Table IV. Analysis of E-t curves recorded at Cu electrodes in unstirred 1M KF solution in HF at 0°C

i, ma/cm^2	τ, sec	$\tau^{1/2}$, sec$^{1/2}$	$i\tau$, mc/cm^2	$i\tau^{1/2}$, mc sec$^{1/2}$ cm^{-2}
9.1	9.25	3.0	85	27.6
15.5	5.25	2.3	79	34.9
21.2	3.63	1.9	76	40.3
30.4	1.90	1.4	58	42.0
33.4	2.00	1.4	67	47.0
39.5	1.60	1.3	63	50.0
45.5	0.88	0.9	39	42.7
51.5	0.94	1.0	49	50.0

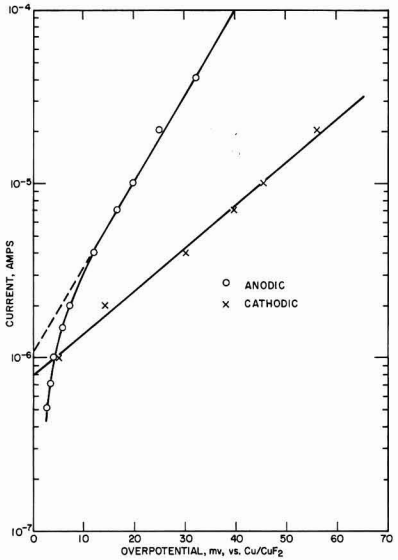

Fig. 7. Tafel plots for Cu electrode in purified HF (1M KF) at 0°C. Electrode area was 0.33 cm^2.

different intercepts on the current axis and hence different apparent exchange current densities. This is indicative of two different processes which may or may not be multistep processes (22). The apparent exchange current density for the anodic process is 3.0 x 10^{-6} amp/cm^2 and for the cathodic process, 2.4 x 10^{-6} amp/cm^2. The anodic Tafel slope is 20 mv and the cathodic Tafel slope 42 mv. The apparent exchange current density for the formation of NiF_2 at a nickel electrode in anhydrous HF containing 0.01M NaF is of the same order of magnitude (9), namely 3.7 x 10^{-6} amp/cm^2.

Conclusions

The Cu/CuF_2(s) couple is a reliable reference electrode in basic, anhydrous HF. The electrode meets the requirements of satisfactory polarization and has a meaningful thermodynamic potential *vs.* an H_2 electrode in the same solution. The value measured, +276 ±5 mv agrees well with that calculated from thermodynamic data at 25°C.

The formation of an insoluble anodic film at a Cu electrode in a 1M KF solution in HF at 0°C was demonstrated by cyclic voltammetry and chronopotentiometry. A film thickness of 4 x 10^{-6} cm (400Å) was estimated for the initial anodic formation of CuF_2. Anodic-cathodic cycling of Cu electrodes gave rise to a significant roughening of the electrode surface as shown by i-E curves, E-t curves, and differential capacitance measurements on cycled electrodes. X-ray analyses of these films confirmed the presence of crystalline copper fluoride.

Evidence from the chronopotentiometric and cyclic voltammetric experiments indicates that the anodic formation of CuF_2 proceeds *via* a soluble intermediate according to the following mechanism

$$Cu \rightleftharpoons Cu^{2+} + 2e$$

$$Cu^{2+} + 2HF_2^- \rightarrow CuF_2(s) + 2HF(l)$$

rather than through the surface reaction of Cu with adsorbed HF_2^-. During the formation of CuF_2, $i\tau$ decreased and $i\tau^{1/2}$ increased with increasing i over the range 10 to 50 ma/cm^2.

The polarization behavior of Cu electrodes in basic HF solution showed that film formation can be approximated by Tafel lines with an apparent exchange

current density for the anodic process of about 3.0 x 10^{-6} amp/cm^2 and a Tafel slope of 20 mv.

The properties of the anodic film of CuF_2 formed in basic HF solutions are similar to the properties observed for noncontinuous, anodic films formed in aqueous solutions (21). Thus such films tend to be thick ($>10^{-6}$ cm) and crystalline, have low resistance to current flow during film formation, and their formation leads to surface roughening.

Acknowledgment

The authors wish to acknowledge the support of the U. S. Navy Air Systems Command (NOw 66-0621-C).

Manuscript received Aug. 1, 1967; revised manuscript received Dec. 2, 1967.

Any discussion of this paper will appear in a Discussion Section to be published in the December 1968 JOURNAL.

REFERENCES

1. G. C. Koerber and T. De Vries, *J. Am. Chem. Soc.*, **74**, 5008 (1952).
2. A. F. Clifford and E. E. Zamora, *Trans. Faraday Soc.*, **57**, 1963 (1961).
3. A. F. Clifford, W. D. Pardieck, and M. W. Wadley, *J. Phys. Chem.*, **70**, 3241 (1966).
4. H. P. Raaen, *Anal. Chem.*, **34**, 1714 (1962).
5. H. P. Raaen, *ibid.*, **37**, 1355 (1965).
6. J. W. Sargent, A. F. Clifford, and W. R. Lemmon, *ibid.*, **25**, 1727 (1953).
7. J. H. Simons *et al.*, *This Journal*, **95**, 47 (1949).
8. N. Hackerman, E. S. Snavely, and L. D. Fiel, *Corrosion Science*, **7**, 39 (1967).
9. N. Hackerman, E. S. Snavely, and L. D. Fiel, *Electrochim. Acta*, **12**, 535 (1967).
10. H. H. Hyman and J. J. Katz, in T. C. Waddington, "Non-Aqueous Solvent Systems," Academic Press, London and New York (1965).
11. H. K. Fredenhagen and O. Kreft, *Z. Electrochem.*, **35**, 670 (1929).
12. J. H. Simons, in J. H. Simons, "Fluorine Chemistry," vol. 5, Academic Press, London and New York (1964).
13. O. Kubaschewski and E. L. Evans, "Metallurgical Thermochemistry," 2nd edition, John Wiley & Sons, New York (1956).
14. D. D. Wagman *et al.*, "Selected Values of Chemical Thermodynamic Properties," NBS Technical Note 270-1.
15. L. W. Niedrach and H. R. Alford, *This Journal*, **112**, 117 (1965).
16. T. P. Hoar, in J. O'M. Bockris, "Modern Aspects of Electrochemistry," No. 2, Butterworths, London (1959).
17. R. C. Weast, Editor, "Handbook of Chemistry and Physics," 45th Edition, Chemical Rubber Co., Cleveland, Ohio (1964).
18. A. Hickling and D. Taylor, *Trans. Faraday Soc.*, **44**, 262 (1948).
19. K. Fredenhagen and G. Cadenbach, *Z. physik. Chem.*, **A146**, 245 (1930).
20. F. Will and C. A. Knorr, *Z. Electrochem.*, **64**, 258 (1960).
21. D. A. Vermilyea, in P. Delahay, "Advances in Electrochemistry and Electrochemical Engineering," vol. 3, Interscience, New York, London (1963).
22. K. Vetter, "Electrochemical Kinetics," English ed., Academic Press, New York, London (1967).
23. J. M. Crabtree, C. S. Lees, and K. Little, *J. Inorg. and Nucl. Chem.*, **1**, 213 (1955).
24. P. Delahay, "New Instrumental Methods in Electrochemistry," p. 119, Academic Press, New York (1955).
25. G. Cady, *J. Am. Chem. Soc.*, **56**, 1431 (1934).

LEED Studies, Adsorption of Carbon Monoxide on the Tungsten (112) Face

Chuan C. Chang

Bell Telephone Laboratories, Murray Hill, New Jersey

ABSTRACT

Carbon monoxide adsorbs on the clean tungsten (112) face with an initial sticking probability of >0.9 at room temperature and desorbs with heat in three stages, the W(112)-α, $-\beta_1$, and $-\beta_2$ at 400°, 1000°, and 1200°K with about 5x10^{14} molecules/cm^2 in each state at maximum coverage. Room temperature adsorption is nondissociative and almost random. Heating a CO covered surface produces well defined C(6x4), P(2x1), C(2x4) and "Complex" structures. The α-CO does not contribute directly to any diffraction pattern. The β_1 is associated with the P(2x1) and C(2x4) structures, and an irreversible temperature activated conversion at about 1000°K produces β_2 molecules; these are responsible for the C(6x4) and Complex structures. Experiments with (112) substrates containing adsorbed oxygen show that CO does not react to produce CO_2, that CO does not adsorb onto an adsorbed oxygen atom and that in the presence of oxygen not all exposed tungsten atoms adsorb CO. The (112) surface is composed of two exposed (112) planes, and by covering only the second layer tungsten atoms with oxygen, it was found that CO adsorbs on the topmost layer as well as on the second layer. Molecules adsorbed on the top layer desorb as β_1 and the maximum number of β_2 molecules on the surface was proportional to the number of second layer tungsten atoms not covered by oxygen.

Low Energy Electron Diffraction (LEED) studies of carbon monoxide adsorption on the tungsten (112) face are of interest because of the possibilities of obtaining reliable values for sticking probabilities and coverages and of studying the atomistics of the adsorption process. Adsorption of CO on the (110) (1, 2) and (100) (3) faces of this bcc metal has been studied with LEED. The CO-W system has also been investigated by other methods, notably flash desorption (4-14), field microscopy (15-19), and calorimetry (20).

The present investigation is an extension of the work on the oxidation of the tungsten (112) face (21) and is part of a wider program in which the interaction of oxygen, carbon monoxide, and nitrogen with this face was studied (22). We are concerned here with adsorption of CO on the clean tungsten

surface, and also on surfaces previously exposed to oxygen.

Experimental Procedure

A tungsten crystal was cut to expose a (112) face to a precision of about 0.1°. The thickness was 0.15 mm and the surface area 4 x 14 mm. The ends of the crystal were welded to tungsten supports. The crystal was heated with a.c. and the temperature could be found from tungsten-rhenium thermocouple wires welded to the side not studied by electron diffraction. The studies were made in a Varian LEED chamber equipped with a gas handling system, a quadrupole gas analyzer, and an ion gauge. During exposure of the crystal to CO, the total amount of active residual gases could be maintained (22a) at below 1% for CO pressures above 2 x 10^{-8} Torr. The crystal was cleaned by repeated oxidation followed by flashing above 2200°K. Electron micrographs of the cleaned surface showed no discernible features down to a resolution of 70Å. Since large numbers of steps and other imperfections smaller than 70Å would have been detected with LEED, it is concluded that the surface was effectively atomically smooth.

Adsorption on the Clean Surface

The clean surface was found to have the ideal bcc (112) configuration (22b). A marble model of this surface is shown in Fig. 1. This surface consists of two exposed (112) planes; each plane is made up of parallel rows of close-packed atoms and the inter-row distance is a relatively large 4.46Å. Thus the $[\bar{1}\bar{1}1]$ close-packing direction (vertical in the photograph) and the $[1\bar{1}0]$ direction (horizontal) are "non-degenerate;" this, together with the fact that the unit cell vectors are orthogonal, make this a most appropriate surface for LEED work.

Flash desorption.—Much information not obtainable from LEED can be obtained from flash off experiments; these are presented first [for descriptions of flash off methods, see ref. (23, 24)].

Three pressure bursts were found in flash desorption, as shown in Fig. 2. These are the W(112)-CO-α, $-\beta_1$, and $-\beta_2$ with desorption temperatures of 400°, 1000°, and 1200°K. These temperatures correspond closely to those for the α, β_1, and β_2 peaks from polycrystalline tungsten (4, 9). Known desorption temperatures of various peaks from single crystal faces and from polycrystalline tungsten are shown in Table I.

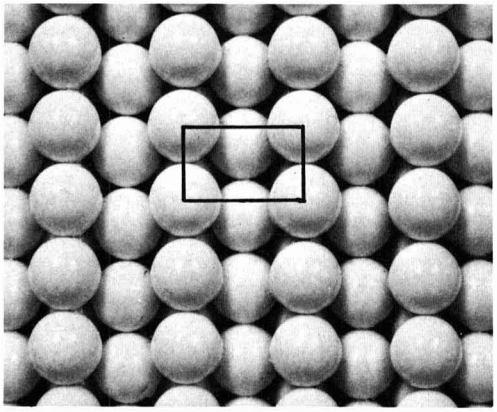

Fig. 1. Marble model of the bcc (112) face. The central rectangle outlines a surface unit mesh. The close packed rows of top layer atoms are separated by open channels or troughs. The asymmetric positioning of the second layer with respect to the topmost layer introduces an asymmetric intensity distribution in diffraction patterns observed at normal incidence.

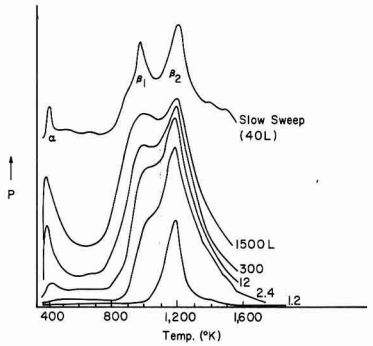

Fig. 2. Flash desorption from the (112) face after different exposures to CO (the exposure unit 1L = 10^{-6} Torr-sec). Heating rate 300°K/sec, except for the top trace. The zero of pressure has been changed for each curve to avoid overlapping.

It was found in the present experiments that most of the α-CO on the surface can be "pumped off" in good vacuum even after a heavy exposure. Also, the α desorption temperature falls from about 500°K to below 400°K with increasing coverage. These observations indicate that for this physisorbed component, there is a dynamic balance between adsorption and desorption. In contrast, β-CO molecules do not spontaneously desorb at room temperature. We can therefore conclude that a firmly bound state already exists after room temperature adsorption.

Others have also found that the α peak height and desorption temperatures are pressure and exposure dependent (8, 10), and in addition, that the β-CO adsorbs as an immobile layer (15, 16) and that CO does not dissociate upon adsorption (4, 15, 16, 26). For the (112), the β desorption temperatures are independent of coverage. At maximum coverage β_1 and β_2 contain equal amounts as measured by comparing areas under flash off curves.

Sticking probability and coverage.—Sticking probabilities and coverages were measured in three ways; flash desorption, gas uptake (22c), and analyses of changes in diffraction patterns. Results from the first two methods for the initial sticking probability S(O) and saturation coverage σ_0 are presented in Group A of Table II; this group lists results obtained from measurements of changes in CO pressure. The data for the present results are summarized in Fig. 3. Results from diffraction pattern studies (next section) are given in Group B of the table with results of several other workers; this group did not depend primarily on measurements of changes in CO pressure. In addition, they are concerned only with the β component.

Entries in Group B show remarkable agreement; in contrast, values in Group A show scatter and are consistently low, especially for S(O). The source of error for Group A is the well known wall desorption (and adsorption) of CO. This is why S(O) is affected more and workers who reduced these effects obtained the highest values for S(O), ref. (6, 7) of Table II. In the present experiments, wall desorption is known to be appreciable from the slow response of the pressure to

Table I. Temperatures (°K) of CO desorption peaks from tungsten

Surface	α	β_1	β_2	β_3	Reference
(110)	450	1100	None	None	1
(100)	—	None	1150	1380	3
(112)	400	1000	1200	None	This work
(114)	500	None	None	1300	25
(113)	—	—	—	—	7, 14
Polycryst.	500	1000	1200	1300	8
Polycryst.	400	1000	1300	1500	10

Table II. Initial sticking probability and final coverage, carbon monoxide on tungsten, 300°K

Surface[a]	Method[a]	S(O)	$\sigma_0(\theta_0)$[b]	Reference
Group A				
(112)	U, F	0.25	6	This work
(114)	U	0.36	6.5	25
(113)	U	0.62	5.8	7
(113)	U, F	0.2	7.5	14
P	U, F	0.62	6	6
P	U, F	0.5	9.5	8
P	U, F	—	10	13
P	U	0.27	10.1	27
P	F	0.5	4.8	4
P	F	0.3	—	5
P	F	—	5	10
Group B				
(110)	LEED	~0.9*	10 (0.71)*	1
(100)	LEED	~1	10 (1.00)	3
(112)	LEED	>0.9	10 (1.25)	This work
H	FEM	0.97	—	11

[a] P = polycrystalline (except for the single crystal Field Microscopy tip labeled FEM), U = uptake, F = flash desorption.
[b] Saturation coverage, σ_0, in units of 10^{14}/cm² and (θ_0), in monolayers, where a monolayer equals the density of atoms in one (hkl) plane.
* Not values given in ref. (1), as those were "normalized" to agree with some of the results of Group A above; values presented here were obtained by comparing areas under flash off curves from the (110) and (112) faces, since LEED observations on the (110) do not readily give coverages as for the (100) and (112).

sudden changes in CO leak rate, as compared to the rapid response for oxygen.

LEED observations.—CO adsorbed at room temperature produces a diffuse diffraction pattern with no well defined extra spots and with high background intensity. The bright background is indicative of disorder. This is very different from the sharp patterns with high contrast seen after oxygen adsorption (21). Sharp diffraction patterns are, however, seen after heating.

In experiments involving heating, the crystal was given various exposures to CO at room temperature and then heated to progressively higher temperatures in good vacuum. Well defined C(6x4), P(2x1) and C(2x4) patterns were found with this treatment; in addition, a "Complex" pattern was found which has no well defined symmetry. These are displayed in Fig. 4. Much of the data can be summarized in a temperature-exposure diagram showing the conditions under which each pattern is observed; this diagram is shown in Fig. 5. Significant findings about the surface structures are presented in Table III.

The two most important results are that each structure can be associated with a particular gas burst observed in flash desorption and that for three of the structures, their coverages have been found.

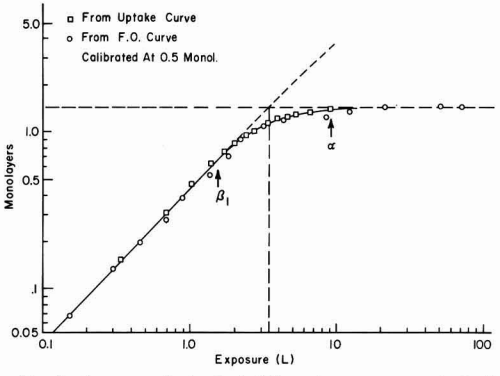

Fig. 3. Amounts of absorbed CO against exposure, obtained from uptake and flash off curves. Arrows show the minimum exposures at which the β_1 and α peaks appear on the flash off curves. Calibrated using LEED results by assigning the value of ½ monolayer to the amount absorbed after 1.2L.

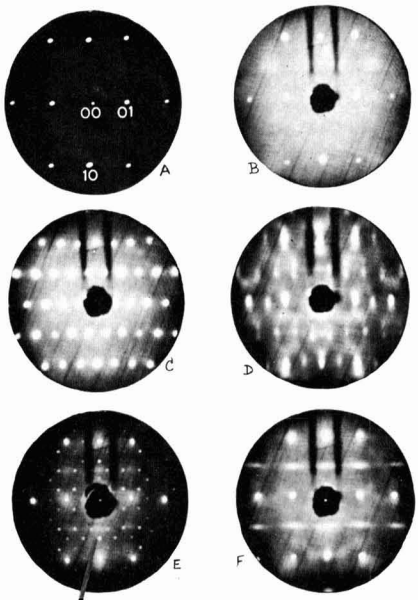

Fig. 4. Diffraction patterns from CO adsorption. (A) clean surface, Miller indices shown on some of the spots. (B) after saturation exposure at room temperature. (C) to (F), the C(2x4), Complex, C(6x4) and P(2x1) patterns. All taken at 80v except (E) and (F), at 81v, normal incidence.

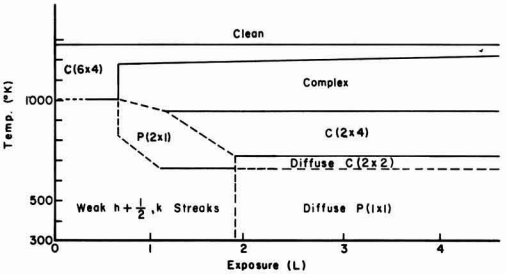

Fig. 5. Temperature-exposure ranges in which various CO patterns appear for initial room temperature exposures shown on the abscissa followed by heating to progressively higher temperatures in good vacuum.

As an example of how the entries in the table were obtained, consider the P(2x1). This pattern will develop to its best if the crystal is heated to about 750°K after an exposure of 1.2L (1L = 10^{-6} Torr-sec), see Fig. 5. Since a P(2x1) symmetry represents multiples of ½ monolayer of scatterers (1 monolayer = 8 x 10^{14}/cm² on this face) and 1.2L represents 0.57 monolayer of molecular collisions with the crystal, the coverage must be ½ monolayer. The average sticking probability up to ½ monolayer is then about 0.9. The P(2x1) is stable up to about 1000°K (Fig. 5) when it changes to a weak Complex pattern with no detectable gas evo-

Table III. CO structures on the (112) face

Pattern	Exposure, L	Coverage, monolayer	Destruction temperature, °K	Associated F. O. peak
C(6 × 4)	0.6	1/4	1200	β_2
P(2 × 1)	1.2	1/2	1000	β_1
C(2 × 4)	>1.4	5/8 to 10/8	1000	β_1
Complex	>1.5	5/8	1200	β_2

lution and then to a C(6x4) at about 1200°K with loss of some CO. Because the destruction temperature of the P(2x1) coincides with the β_1 desorption temperature, we are led to associate the P(2x1) with the β_1-CO.

It is unmistakable that β_2 molecules are responsible for the C(6x4) and Complex structures since all the β_1 molecules have been desorbed when either of these patterns is seen. However, the β_1 can only be loosely associated with its structures. Strong supporting evidence that β_1 molecules produce the P(2x1) and C(2x4) comes from the fact that the β_1 desorption temperature is the same as the destruction temperature for these structures. Further evidence will be presented in the section on LEED observations and surface structures.

The C(2x4) pattern first appears at a coverage of about ⅝ monolayers. Additional molecules, up to full coverage, do not substantially affect the diffraction pattern. This is one example of the many possible pitfalls wherein coverage estimates based on diffraction patterns alone can go wrong. Fortunately, for the P(2x1), a unique value could be found so that the flash off data could be calibrated at ½ monolayer. This calibration is, therefore, all important and a separate check of its correctness will be provided in the section on LEED observations and surface coverage.

The Complex pattern was so named because it has no well defined symmetry. It is nevertheless interesting, as adsorbed nitrogen produces a practically identical pattern (22d). Note that this unusual pattern (Fig. 4D) consists of streaky features quite unlike the spot patterns normally observed in LEED. It is therefore surprising that two gases give this same strange pattern. A little investigation shows, however, that these gases have much in common. First, CO and N_2 are iso-electronic. Second, they have been associated with the concept of surface complexes which arose out of attempts to account for the kinetics of the nitrogen-tungsten system (28, 29) and the results from isotopic mixing experiments with CO (13) and N_2 (30, 31).

Conditions under which isotopic mixing becomes appreciable correspond to conditions for the formation of the Complex structures for both CO and N_2. Under these same conditions it is generally believed that both atoms of the nitrogen molecule are in contact with the metal. Since the CO-Complex pattern indicates that CO has the same configuration, it is concluded that both atoms of this molecule also contact the substrate in the β_2 state.

Diffraction pattern studies do not give direct information on the coverage for the Complex structure as it has no well defined symmetry. The coverage was estimated to be about ⅝ monolayer by comparing the flash desorption amount with that from ½ monolayer coverage.

Surface structures.—Of the four CO structures on the clean surface, the P(2x1) is simplest. It is like the oxygen P(2x1) ½ monolayer structure so that every trough site h,k with h even is occupied by a CO molecule. Accordingly, the intensity-voltage curves from these two P(2x1) patterns are quite similar. Although the tungsten surface is undisturbed in the P(2x1) structure, the possibility of reconstruction (32, 33) has not been ruled out for the other three structures. Note, however, that because of the simplicity of the P(2x1) structure and the large minimum distance of 4.46Å between scatterers, the conclusion that this structure requires ½ monolayer of adsorbates is expected to remain valid whether the surface is reconstructed or not.

The C(2x4), C(6x4), and Complex patterns show a diversity of behavior which indicates that not enough is as yet known about them for a meaningful structure analysis.

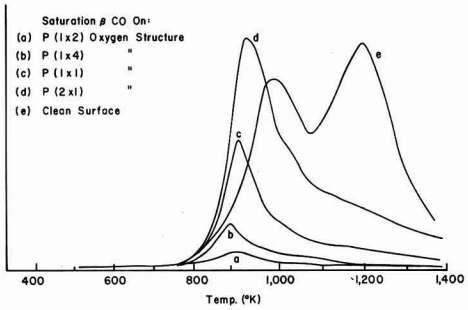

Fig. 6. CO flash off from oxygen structures after saturation exposure at room temperature. Heating rate 300°K/sec. (a) to (e) in order of decreasing oxygen content.

A simple model that can account for all of the present results is the one in which β_1 molecules adsorb at room temperature undissociated, with only the carbon contacting the metal. A temperature activated transformation to the β_2 occurs after heating to about 1000°K and in this state both carbon and oxygen contact the metal. In the Complex structure, β_2 "molecules" agglomerate into surface stabilized complexes that can be studied at room temperature.

Adsorption onto Oxygen Structures

Experiments in which CO is adsorbed on a surface previously covered by oxygen might seem to have special interest because of this bearing on the catalytic formation (2) of CO_2. These experiments could also provide a check for the CO coverage estimates because the oxygen coverages are quite reliably known. In carrying out such experiments, the oxygen surface structures (21, 22e) were used as substrates. These are the facet structures produced by exposing a hot crystal to oxygen and five nonfacet structures.

Flash desorption.—No CO_2 was observed to flash off from any of the oxygen structures and repeated adsorption and desorption of CO left the surface oxygen content undiminished. In most cases, the original oxygen structure remained apparently undisturbed, as reported earlier (2). Thus no oxygen could be removed by CO from these structures.

The flash off data of Fig. 6 shows that only one β peak desorbs from the oxygen structures. These structures, together with their oxygen coverages and their per cent of tungsten atoms still uncovered, are listed in Table IV. The amounts of β-CO that adsorb are shown in row 4 as a per cent of the maximum that adsorbs on the clean surface.

Figure 6 shows that the β_2 peak is suppressed by pre-adsorption of oxygen and that the observed β desorption occurs essentially at the β_1 temperature [actually, almost 100°K lower, as also happens in the case of CO on W(110)-O[½] structure; compare Fig. 5 of ref. (1) with Fig. 3B of ref. (2)]. Accordingly, we shall see below that the β_2 structures are never seen.

Table IV shows that the per cent of adsorbed CO decreases faster than the per cent of exposed tungsten atoms as more of the surface is covered with oxygen.

Table IV. β-CO flash off from the oxygen structures

1.	Clean	P(2 × 1)	P(1 × 1)	P(1 × 4)	P(1 × 2)	P(1 × 3)	Facet
2.	0	½	1	1¼	1½	1-2/3	~2
3.	100	75	50	38	25	17	0
4.	100	80	40	15	3	0	0
5.	100	75	50	13	0	0	0

1. Oxygen structures; 2. oxygen coverage in monolayers; 3. per cent of exposed tungsten atoms; 4. per cent of β-CO observed to flash off; and 5. amounts of adsorbed β-CO as predicted from diffraction pattern observations (section on LEED observations and surface structures).

LEED observations and surface structures.—The above flash off experiments show that adsorbed oxygen inhibits CO adsorption. We now examine this in more detail as the (112) face is gradually covered with more and more oxygen atoms.

We start by covering half of the second layer tungsten atoms with oxygen. This is accomplished by using the oxygen P(2x1) structure which is constructed by placing an oxygen atom into every other trough site, thus exposing 75% of the original 2 monolayers of surface tungsten atoms.

Adsorption of CO on the P(2x1) results in a P(1x1) pattern so that the spaces between oxygen atoms have become filled with CO. Heating this P(1x1) produces a C(2x4) as with adsorption on the clean surface. This C(2x4) is destroyed near 900°K with desorption of about ⅜ monolayer of CO, leaving a second, much sharper, P(1x1). If we hypothesize that CO does not stick to an adsorbed oxygen, then all the CO desorbed during the formation of this P(1x1) was initially adsorbed on the top layer tungsten atoms. Here is a second evidence that molecules adsorbed on the top layer desorb essentially as β_1 and that these molecules produce the C(2x4) pattern. We are now ready to perform a very important experiment, since all the excess CO has now been removed so that the remaining P(1x1) must be a monolayer structure.

When all the CO is flashed off from this second P(1x1), the area under the flash off curve is equal to that from the P(2x1)-CO structure. This serves as a check for the ½ monolayer calibration of the CO flash off, as the only other calibration used the extremely streaky P(2x1)-CO pattern (Fig. 4F) which could not be made as sharp and bright as the oxygen P(2x1). Unlike the case with CO, the ½ monolayer estimate for the P(2x1) oxygen structure could be checked with the uptake method, and most important, it was shown that the P(2x1) oxygen structure covered the entire surface. Moreover, a deviation from ½ monolayer of only 5% would be easily detectable for the P(2x1) oxygen pattern (22f).

In the above P(1x1)-O[½] + CO [½] structure, the CO is lodged into the spaces between adsorbed oxygen atoms so that the CO molecule has an effective diameter of less than about 2.8Å, much smaller than the 3.2-4.1Å obtained from several other methods.

Next we use the P(1x1)-O[1] structure in which the troughs are completely filled with a monolayer of oxygen atoms so that only the close packed rows of top layer tungsten atoms are exposed. With this substrate, the C(2x4) is observed, but not the P(2x1). This again shows that the β_1 and C(2x4) are associated with the top layer tungsten atoms and that molecules responsible for the P(2x1) are located above the second layer tungsten atoms. All these conclusions, however, depend on the hypothesis that CO does not adsorb onto the oxygen atoms. This is quite clearly shown in the following experiment in which an oxygen structure with the next higher coverage, the P(1x4)-O[1¼], is used.

The P(1x4) is constructed by covering every fourth top tungsten row on the P(1x1)-O[1], say rows 0, 4, 8, . . ., with oxygen. Upon adsorption of CO, this pattern changes to a P(1x2) so that rows 2, 6, 10, . . . become covered with CO, leaving 1, 3, 5, . . . still bare. Thus about 13% of the original surface tungsten atoms adsorb CO.

Adding more oxygen, we use the P(1x2)-O[1½] structure in which only every second top row is bare, and the P(1x3)-O[1-2/3] structure in which only every third row is bare. Since CO does not adsorb on these surfaces, not all exposed tungsten atoms can accept CO although these actively adsorb oxygen.

Finally, the oxygen faceted surface exposes to the CO only (110)-type planes covered with a monolayer of oxygen atoms. Failure to find any CO adsorption on faceted surfaces again confirms the hypothesis that CO does not stick to an adsorbed oxygen.

Enough was described above so that entries in row 5 of Table IV can be found from a knowledge of the oxygen structures and the diffraction pattern changes accompanying CO adsorption. A tacit assumption was made throughout that adsorbates scatter slow electrons sufficiently to produce the observed patterns. That this assumption is valid is most dramatically illustrated by the close match in Table IV between the observed flash off amounts in row 4 and the predicted values in row 5, since the predictions were based on models arrived at from diffraction pattern analyses.

Acknowledgment

The author would like to thank Dr. L. H. Germer for his support and encouragement and for reading the manuscript.

This work was performed at Cornell University, Ithaca, New York, supported by the Advanced Research Projects Agency through the Cornell Material Science Center.

Manuscript received Sept. 22, 1967; revised manuscript received *ca.* Nov. 13, 1967. This paper was presented at the Dallas Meeting, May 7-12, 1967, as Abstract 177.

Any discussion of this paper will appear in a Discussion Section to be published in the December 1968 JOURNAL.

REFERENCES

1. J. W. May and L. H. Germer, *J. Chem. Phys.*, **44**, 2895 (1966).
2. J. W. May, L. H. Germer, and C. C. Chang, *ibid.*, **45**, 2383 (1966).
3. J. Anderson and P. J. Estrup, *ibid.*, **46**, 563 (1967).
4. G. Ehrlich, *ibid.*, **34**, 39 (1961).
5. G. Ehrlich, *ibid.*, **36**, 1171 (1962).
6. R. E. Schlier, *J. Appl. Phys.*, **29**, 1162 (1958).
7. V. M. Gavrilyuk and V. K. Medvedev, *Sov. Phys., Solid State*, **4**, 1737 (1963).
8. P. A. Redhead, *Trans. Faraday Soc.*, **57**, 641 (1961).
9. P. A. Redhead, Proc. Symp. on Electron and Vac. Phys., Hungary (1962).
10. L. J. Rigby, *Can. J. Phys.*, **42**, 1256 (1964).
11. A. A. Bell and R. Gomer, *J. Chem. Phys.*, **44**, 1065 (1966).
12. T. W. Hickmott and G. Ehrlich, *ibid.*, **24**, 1263 (1956).
13. T. E. Madey, J. T. Yates, and R. C. Stern, *ibid.*, **42**, 1372 (1965).
14. J. Eisinger, *ibid.*, **27**, 1206 (1957).
15. R. Gomer, *ibid.*, **28**, 168 (1958).
16. R. Klein, *ibid.*, **31**, 1306 (1959).
17. L. W. Swanson and R. Gomer, *ibid.*, **39**, 2813 (1963).
18. E. Menzel and R. Gomer, *ibid.*, **41**, 3329 (1964).
19. A. A. Holscher, Doctoral Thesis, Univ. of Leiden, Netherlands, (1967).
20. D. Brennan and F. J. Hayes, *Phil. Trans. Roy. Soc., London*, No. 1089, **258**, 325 (1965).
21. C. C. Chang and L. H. Germer, *Surface Sci.*, **8**, 115 (1967).
22. C. C. Chang, Doctoral Thesis, Cornell Univ., Ithaca, N. Y., (1967).

22a *Ibid.*, chap. II. 1.
22b *Ibid.*, chap. III.
22c *Ibid.*, Appendix III.
22d *Ibid.*, chap. VI.
22e *Ibid.*, for descriptions of the oxygen structures, see chap. IV. 2d.
22f *Ibid.*, chap. IV. 2b.

23. P. A. Redhead, *Vacuum*, **12**, 203 (1962).
24. G. Ehrlich, *J. Chem. Phys.*, **32**, 4 (1961).
25. J. A. Becker, *Solid State Phys.*, **7**, 379 (1958).
26. W. J. M. Rootsaert, L. L. von Reijen, and W. H. M. Sachtler, *J. of Catalysis*, **1**, 416 (1962).
27. F. Ricca, A. G. Nasini, and G. Saini, *ibid.*, **1**, 458 (1962).
28. W. K. Warburton, M. S. Thesis, Cornell Univ., Dept. Engineering Physics, Ithaca, N. Y. (Sept. 1965).
29. J. L. Robins, W. K. Warburton, and T. N. Rhodin, *J. Chem. Phys.*, **46**, 665 (1967).
30. J. T. Yates and T. E. Madey, *ibid.*, **43**, 1055 (1965).
31. T. E. Madey and J. T. Yates, *ibid.*, **44**, 1675 (1966).
32. L. H. Germer, *Surface Sci.*, **5**, 147 (1966).
33. E. Bauer, *ibid.*, **5**, 152 (1966).

Environmental and Reaction Studies on Electrochemical Cells Based on Solid Charge-Transfer Complexes

F. Gutmann,[1] A. M. Hermann,[2] and A. Rembaum

Jet Propulsion Laboratory, California Institute of Technology, Pasadena, California

ABSTRACT

Solid state electrochemical cells using metal anodes with charge transfer complexes as cathodes which were previously reported have been further studied. The presence of the I^- ion has been verified in cells with iodine as the acceptor. Quantitative recovery of the reaction product in amounts proportional to the total charge delivered, substantiates the originally proposed reaction mechanism. Long time decay data under a steady load as well as under a pulsed load, extending over periods of up to nine months, are presented. It is shown that the performance of the cells is considerably improved by the admission of vapors of high permittivity liquids into the anode-electrolyte interface. Evidence is presented that the effect is primarily due to improved availability of reactant at the electrode surface.

We have previously reported (1) data on solid state electrochemical cells using metal anodes and a charge transfer complex as cathode. In the present communication, we wish to present further results on cells of the type Mg/Phenothiazine-I_2/Pt. The well-known phenothiazine-iodine charge transfer complex (2) has the advantage of high electronic conductivity; however, donors other than phenothiazine have also been employed yielding similar results.

Experimental

The cells were assembled in the holders previously described (1); the complex was produced by intimately mixing reagent grade phenothiazine and iodine as received in the stoichiometries indicated below.

The currents and voltages were measured by means of a Hewlett Packard 412A-VTVM unless stated otherwise.

Reaction Mechanism

We have proposed a reaction mechanism (1) involving the I^- ion. In order to support this contention, MgI_2 was recovered thus:

A cell was prepared using a 1:2 phenothiazine: iodine complex and then continuously discharged in ambient atmosphere and at room temperature over a period of nine months into a constant 31.6 ohm load; *i.e.*, for this cell, virtually a short circuit load. The integration of the area under the current *vs.* time curve showed that a total of 216 coulombs had been delivered by this cell. The cell was then dismantled and analyzed for MgI_2 (the electrolyte) by extracting the contents with distilled water. This solution was stirred, filtered, and the filtrate was treated with aqueous ammonia and an excess of $(NH_4)_2HPO_4$ was then added. The precipitate formed was filtered, dried, and analyzed for Mg and for phosphate. The recovery was 190 mg of $MgNH_4PO_4$ corresponding to the passage of 282 coulombs. Thus, the difference of 66 coulombs must have been consumed in a side reaction. This reaction is most likely an internal corrosion process at the Mg anode, probably associated with traces of water present in the ambient atmosphere.

The above data, therefore, support the reaction mechanism which was based on the formation of MgI_2 (1).

Long Time Decay Curves. Effect of Solvent Vapors

The above test commenced with the rather low short circuit current density of 560 $\mu a/cm^2$; after two days, the short circuit density was of the order of 30 $\mu a/cm^2$; after nine months, the current density had dropped to about 4 $\mu a/cm^2$. The initial open circuit voltage was 1.7v; after one week, it recovered to a value of 1.5v after removal of the load for a few seconds. This recovery voltage was maintained to $\pm$ 0.1v for seven months of the total test period. After nine months, the recovery open circuit voltage had dropped to 1.2v. The results of a further decay test are shown in Fig. 1. These data refer to another cell of the type Mg/phenothiazine: iodine 1:2/Pt, but in an atmosphere saturated with acetonitrile vapor. The cell had an initial open circuit voltage of 1.7v. Its voltage under a continuous load of 5000 ohm was recorded over a period of 415 hr. The voltage is seen to keep substantially constant over about 10 hr whence it commences to decay approximately linearly at a rate of about 7 mv/hr. This rate is then maintained over about 70 hr.

A further series of discharge tests was performed using an electromechanical oscillator (3) as the load. A typical oscillogram is reported in Fig. 2. This oscillator draws a current pulse of 200-300 μa of 6-8 msec duration at a repetition frequency of 6 sec^{-1}; its impedance is partly inductive, causing the transient waveshape of the sharp spikes. The discharge test was carried out at room temperature in (uncontrolled) laboratory atmosphere. The cell, with initial open circuit voltage 1.62v and short circuit current 3.4 ma, operated in a room atmosphere with the oscillator load for 480 hr. At this point, the open circuit voltage

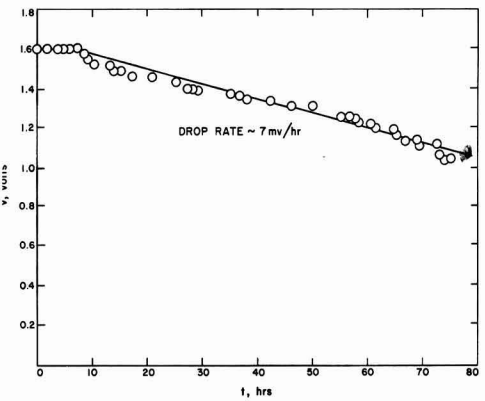

Fig. 1. Decay of the terminal voltage for the system Mg/phenothiazine; I_2 1:2/Pt. The test was conducted in saturated vapors of acetonitrile under a constant load of 5000 ohm.

[1] Present address: Institute for Direct Energy Conversion, University of Pennsylvania, Philadelphia, Pennsylvania 19104.
[2] Present address: Physics Dept., Tulane University, New Orleans, Louisiana 70118.

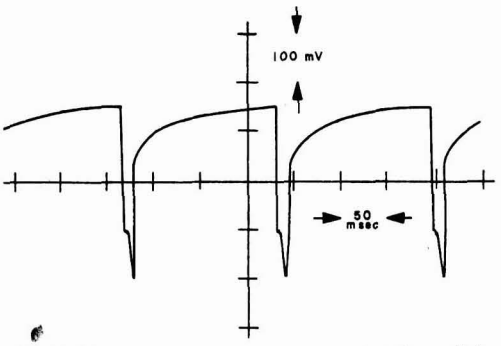

Fig. 2. Pulsed oscillogram depicting the time dependence of the terminal voltage for the cell Mg/phenothiazine; I_2 1:2/Pt. Current was drawn for 6-8 msec at a repetition frequency of 6 sec^{-1} causing the terminal voltage drop shown.

had dropped to 0.5v. Upon exposure without load to a high humidity atmosphere for 24 hr, the open circuit voltage recovered completely. Continuing the test under load in the high humidity environment, 550 hr were required for the voltage to drop to 0.5v. The difference ΔV between open circuit and loaded voltage remained fairly constant, even though the open circuit voltage itself dropped. Total operating time was 1032 hr (43 days) of which 552 hr occurred in a humid atmosphere. Another cell was tested with a purely resistive load of 4700 ohm, which was periodically connected to the battery by a switching circuit (8 msec "on", 172 msec "off"). The open circuit voltage was 1.59v, and the current through a 10 ohm load was 4.2 ma. In room temperature, an open circuit voltage of 0.5v was reached after 192 hr. The cell was then subjected for 24 hr to the humidity treatment described above. Only an additional 48 hr of operation in room atmosphere were obtained before the open circuit voltage again dropped to 0.5v. Recharging with 500 μa for 72 hr did not restore the cell. Total accumulated operating time was 250 hr, all in laboratory atmosphere.

In this experiment, carried out in uncontrolled laboratory atmosphere, ΔV increased significantly with time.

In the experiment carried out in a controlled, humid atmosphere, the wave forms obtained remained constant and showed no variation with time, *i.e.*, there was no difference in the shape nor in the amplitude of the voltage pulses as measured by connecting an oscilloscope across the cell throughout the duration of the test.

The difference ΔV between the terminal voltage under a load R_L and the voltage V' to which the cell recovers just before the start of the following pulse thus remains constant though the recovery voltage itself decreases approximately linearly during the test. We shall now investigate the conditions under which one could expect ΔV to be constant with time. ΔV represents the voltage drop across the internal resistance due to the current pulse

$$\Delta V = \frac{V'}{\dfrac{\partial V}{\partial I} + R_L} \frac{\partial V}{\partial I} \qquad [1]$$

Since the decay of V' is approximately linear[3] with time t, we may write an explicit decay function in terms of an open circuit voltage V

$$V' = V(1 - \alpha t) \qquad [2]$$

where α is a decay constant. Since ΔV is independent of time

$$\left| \frac{\partial}{\partial t} \Delta V \right|_I = 0 \qquad [3]$$

Hence

$$(1-\alpha t)\left(\frac{\partial V}{\partial I} + R_L\right)\frac{\partial^2 V}{\partial I \partial t} - \alpha \frac{\partial V}{\partial I}\left(\frac{\partial V}{\partial I} + R_L\right) - \frac{\partial V}{\partial I}(1-\alpha t)\frac{\partial^2 V}{\partial I \partial t} = 0 \qquad [4]$$

Since this must hold for all values of t, the terms containing t explicitly must vanish

$$(1-\alpha t) R_L \frac{\partial^2 V}{\partial I \partial V} = 0 \qquad [5]$$

$$\therefore \frac{\partial}{\partial t}\frac{\partial V}{\partial I} = 0 \qquad [6]$$

Thus the dynamic internal resistance must remain constant with time. This leaves only one term remaining in Eq. [4]

$$\alpha \frac{\partial V}{\partial I}\left(\frac{\partial V}{\partial I} + R_L\right) = 0 \qquad [7]$$

so that

$$\frac{\partial V}{\partial I} = -R_L \qquad [8]$$

The second condition for the time independence of ΔV (Eq. [8]) therefore is the requirement that the load resistance matches the internal dynamic resistance of the cell. The latter quantity is, of course, negative since the cell is an active circuit element; an increase in current is accompanied by a drop in cell voltage. To the extent that this very simplified analysis holds—see footnote—the constancy of the voltage drop ΔV during the tests in a humid atmosphere is thus seen to be associated with the dynamic internal resistance of the cell remaining constant, plus the rather fortuitous approximate equality between the values of the load resistance and the dynamic internal cell resistance. We note that the latter quantity remains constant in the humid environment though not in the uncontrolled laboratory atmosphere. Since the dynamic internal resistance $(\partial V/\partial I)$ is the sum of a constant ohmic series resistance plus a polarization or diffusion resistance term, it follows that the diffusion resistance is held constant in the presence of a vapor of high permittivity liquid, but not in its absence. Hence the admission of solvent, although not necessarily water, vapor tends to assist the diffusion processes, causing a substantially constant and improved rate of diffusion of I^- ions into the reaction site. The decay involves the shift of the entire polarization curve to lower voltage values, parallel to itself, without a change in its slopes.

Further experiments aimed at determining the influence of gases and vapors on the performance of these cells showed that the complete removal of all solvent and water vapors reduces the short circuit current by 2 to 3 orders of magnitude below the value recorded in ambient laboratory atmosphere (1) (see Fig. 3). Likewise, the introduction of benzene or CCl_4 vapor into the otherwise dry and solvent free system causes no increase in the short circuit current density. However, dry vapors of acetone, methylalcohol, or acetonitrile cause the current density to rise to values of up to several 100 ma/cm^2, higher by about an order of magnitude than the best current densities obtainable in an uncontrolled room atmosphere. Water vapor has a similar effect. In brief, it appears that the presence of vapors of liquids of high permittivity improves

[3] Prima facie one would expect the decay to be exponential; the linear decay characteristic observed during a limited time interval thus might well be the equivalent to taking only the first, linear, term in an exponential series. Since Fig. 1 indicates that such a linear approximation does hold for the time interval considered, the following analysis will apply to the same degree of approximation.

the performance of these cells while vapors of low permittivity liquids do not affect the short circuit current densities available as compared to those under vacuum or dry conditions.

Thus, e.g., a cell prepared and tested in air gave a short circuit current of 4.0 ma which, upon drying out with $CaCl_2$ dropped to 50 μa. Introduction of methanol vapor raised the current to 70 ma. Likewise, admission of acetonitrile vapor into a dried and solvent-free cell raised the current from 50 μa to 50 ma.

Moreover, the open circuit voltages of cells kept in a solvent-free environment produced by either evacuating or exposure to a drying agent such as $CaCl_2$, drop from the thermodynamical value of 1.85v to values in the vicinity of 1.2v. There is no increase in open circuit voltage nor short circuit current on admission of vapors of benzene or CCl_4.

Figure 3 illustrates the effect of admission of acetonitrile vapor on the short-time decay of the current into a constant 5000 ohm load, with vapor pressure as the parameter: the cells were kept in an evacuated glass vessel and acetonitrile vapor at controlled pressures was then admitted.

The beneficial effect of a high permittivity solvent vapor atmosphere must be due to the permeation of the vapors into the anode-electrolyte interface. This contention is supported by the following observations: (*i*) corrosion of the electrode surface starts at the edges and thence penetrates inwards; (*ii*) assembly of a complete cell under high pressure in a hydraulic press yields cells with characteristics essentially those of cells maintained in a completely solvent free environment; (*iii*) insertion of a semipermeable membrane, say a thin sheet of cellulose or of polypropylene-acrylic acid graft copolymer, between the Mg anode and the solid, tends to raise the value of the short circuit current considerably; the open circuit voltage likewise is brought even closer to its thermodynamical value of 1.87v. Insertion of such a separator anywhere else but directly into the anode-solid interface causes both open circuit voltage and short circuit current to decrease. It appears that the separator acts as a wick assisting the penetration of solvent vapor into the interface. Cells assembled with the separator extruding beyond the electrode and then wetted with acetonitrile produced current densities of the order of hundreds of ma/cm^{-2}, significantly in excess of the performance of untreated cells; (*iv*) the constancy of the polarization resistance in the presence of vapors, discussed above, indicates that such vapors are effective in assisting processes within the reaction zone near the anode.

The introduction of vapor of a high permittivity solvent may either increase the reaction rate in the energy producing reaction (1)

$$\begin{aligned} 2[Mg + I^- &\rightarrow MgI + e^-] \\ 2MgI &\rightleftarrows MgI_2 + Mg \\ \hline Mg + 2I^- &\rightarrow MgI_2 + 2e^- \end{aligned} \qquad [9]$$

or it may retard poisoning of the electrode surface by assisting in the removal of the reaction product, *viz.*, MgI_2. However, the voltage pulse waveforms obtained are considerably different from those expected in a regime in which poisoning of the electrode surface is the main effect. Such waveforms have been reported, *e.g.*, by Schuldner and Hoare (4). The time constants involved here (see Fig. 2) are too long, by at least a factor of a hundred, to be entirely caused by electrode poisoning. Moreover, the admission of such vapors into a solvent-free cell causes an immediate and sudden rise in the current density, far too fast for an effect associated with the dissolution of the MgI_2.

Thus, it appears that this effect involves an increase in the rate of the first step of the above reaction sequence, which is the rate-determining step. More specifically, the energy of the activated complex MgI^- must be substantially lowered: this may occur by solvation or, perhaps more likely, by an increase in the polarization energy of the activated complex, since only highly polarizable molecules enhance the current.

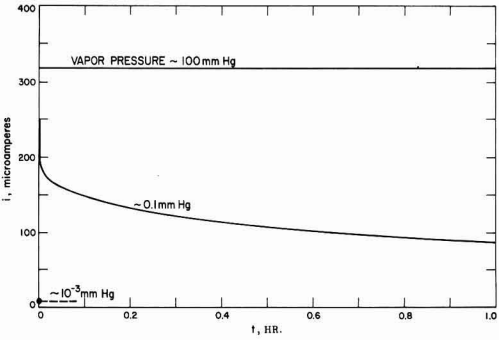

Fig. 3. Current decay curve for the system Mg/phenothiazine; I_2 1:2/Pt. The cell was operated into a constant load of 5000 ohm at various vapor pressures of acetonitrile.

This suggestion is supported by the work of Hale and Mehl (5) who ascribe current limitation in a Redox organic electrolyte system to either diffusion limitation or to a reorientation of the solvation shell of the reactant. Thus, the vapor in the present case might well form an adsorbed liquid thin film yielding sufficient surface solvation energy (6) to facilitate the reaction: the solvated ion then becomes isoenergetic with an appropriate energy band of the solid (5).

Another contributing factor to such a "flat-band condition" would be changes in the work function and electron affinity of both the metal anode and of the charge transfer complex: high permittivity media are known (7) to be active in this respect; thus an adsorbed water layer changes the work function of a solid polymer by several hundred millivolts (8).

During each current pulse of the pulse experiment, 1.3 x 10^{13} electrons were consumed. At the anode surface, even assuming complete coverage, about 6 x 10^{11} I^- ions are available. Thus, these data refer to a regime of diffusion control. Furthermore, consider a cell discharged continuously into a matched load, corresponding to a reaction rate (1) of 1.5 x 10^{15} ions cm^{-2} sec^{-1}, and a calculated diffusion layer (1) of 0.05 cm thick containing 2.7 x 10^{16} ions. At these current densities, diffusion would be rate determining.

In the solid system, it is to be expected that diffusion limitation sets in at lower overvoltages already than in a corresponding liquid system: indeed, the exchange current density i_o obtained (1) for the present, solid, system is of the order of 10^{-5} amp-cm^{-2}, while Vetter (9) reports values of the order of 10^{-2} to 10^{-3} amp-cm^{-2} for a liquid iodine/iodide Redox system. Since (9)

$$\left(\frac{\partial \log i_o}{\partial \log [I^-]} \right)_{E=\text{const}} \cong 1 \qquad [10]$$

it appears that it is the exhaustion of the I^- supply at the anode surface which causes the current to become diffusion limited.

Thus, at the higher current densities, where the current tends to become diffusion controlled, the introduction of vapor also involves an improved diffusion rate. At least in part, this is due to the increased diffusion gradient caused by the increase in reaction rate discussed above. However, it may well be that a liquid layer at the interface as such substantially assists in the diffusion processes.

Acknowledgment

The continued interest and constructive criticism of Professor Pierre van Rysselberghe, Stanford University, are gratefully acknowledged.

This paper represents one phase of research performed by the Jet Propulsion Laboratory, California Institute of Technology, sponsored by the National Aeronautics and Space Administration, Contract NAS7-100.

Manuscript received July 12, 1967; revised manuscript received Nov. 24, 1967.

Any discussion of this paper will appear in a Discussion Section to be published in the December 1968 JOURNAL.

REFERENCES

1. F. Gutmann, A. M. Hermann, and A. Rembaum, *This Journal*, **114**, 323 (1967).
2. Y. Matsunaga, *Helv. Phys. Acta*, **36**, 800 (1963); F. Gutmann and L. E. Lyons, "Organic Semiconductors," p. 726, John Wiley & Sons, Inc., New York (1967).
3. *See*, for example, R. J. Brodd, *This Journal*, **106**, 471 (1953).
4. S. Schuldner and J. P. Hoare, *J. Chem. Phys.*, **26**, 1771 (1957).
5. J. M. Hale and W. Mehl, *Surface Science*, **4**, 221 (1966).
6. D. O. Raleigh, *J. Phys. Chem.*, **71**, 1785 (1967).
7. F. Gutmann and L. E. Lyons, *op. sit.*, p. 197.
8. V. B. Margulis, L. I. Boguslavskii, and N. A. Bakh, *Elektrokhimiya*, **3**, 329 (1967).
9. K. Vetter, *Z. Physik. Chem.*, **195**, 337 (1950); **199**, 285 (1952); *Z. Elektrochem.*, **55**, 123 (1951).

Oxidation of Hydrogen on a Passive Platinum Electrode

Sigmund Schuldiner*

Naval Research Laboratory, Washington, D. C.

ABSTRACT

Under potentiostatic, steady-state conditions and at anodic potentials above 0.7v (NHE), the rate of oxidation of molecular hydrogen decreases at a high activity Pt electrode in 1M H_2SO_4. It is shown that this decrease is not owing to the formation of oxygen species on the electrode surface. It is believed that this passive behavior of Pt is due to anion adsorption, at least between 0.7 and 1.2v. Depending on potential and previous potential sequence, passivity in this region is evidently sensitive to the amount of sulfate ion adsorbed, its heat of adsorption, and the presence of dermasorbed oxygen. At higher potentials both sorbed oxygen species and sulfate ion may be present and may contribute to the passivity. In the 0.7-1.2v passive region, hydrogen oxidation is electrochemical. There is no significant chemical oxidation via an oxygen intermediate.

A steady-state electrochemical investigation (1) in a high-purity closed system (2) showed very slow oxidation of water on Pt in helium-saturated 1M H_2SO_4 in the potential region from 0.46 to 1.6v (*vs.* NHE). That work (1) established the solvent (water) reaction rates in this potential region. Since the oxidation of water occurs at such slow rates, it appears that on the addition of an easily oxidizable species to the system, the oxidation of this added species would predominate.

Several papers (3, 4) by Wroblowa *et al.* demonstrated that even though the rate of hydrocarbon oxidation is increased as the potential is increased to about 0.9v, the rate of oxidation decreases at higher potentials. They postulated that this decrease in reaction rate was caused by the formation of a Pt oxide which passivated the surface. Even though the work was done at 80°C, compared to the previously mentioned study (1) on water oxidation, which was at 26°C, there is a question as to why an oxide should be formed in the presence of an oxidizable species in the potential region of interest.

The answer to this question is, of course, a matter of mechanisms. If water oxidation is rate-controlling, then in the presence of a species which is electrochemically inert but which is chemically oxidized rapidly by the oxidation product of water on Pt, the rate of water oxidation may be increased. However, in such a case the accumulation of the oxidation product of water would not occur and could not cause passivation of the surface. If the oxidizable species is electrochemically oxidized faster than water and a significant accumulation of an oxygen species from water occurs the reaction may be retarded. However, it is difficult to conceive of an oxidation product of water on a Pt surface which would not be very easily reduced, so that chemical reaction of water oxidation products with added oxidizable species is very likely. In any case, if the current density is much greater at a given potential in the presence of an added oxidizable species, the very slow oxidation of water plus the high reactability of resulting oxygen species makes the passivation of the surface by an oxide or oxidation product of water hardly feasible.

Anodic passivation of a surface has been explained in another possible way by Frumkin (5). He believes that passivation could be caused by the saturation of the free valencies of the electrode surface by chemisorbed anions. Anodic passivation of Pt for the hydrogen reaction has been repeatedly observed by many investigators [see review by Frumkin (6)]. Aikazyan and Fedorova (7) and Wicke and Weblus (8) attributed this passivation to either adsorption of anions or the appearance of surface oxides. Frumkin (6) claims that at high disk-electrode rotation rates the drop in the current maxima can occur at potentials of about 0.05v, which is much too low for an oxide formation and he believes must be due to anion adsorption. Frumkin and co-workers believe that passivation by oxygen occurs at potentials of about 0.8v.

Kazarinov and Balashova (9) showed that as the potential of platinized Pt became more positive, the concentration of adsorbed sulfate ion increased linearly until a potential of 0.8v was reached. At higher potentials the sulfate ion concentration decreased. They interpreted this decrease as due to the formation of an oxygen species on the surface (their work was done in N_2-saturated solutions of H_2SO_4) which caused a partial displacement of $SO_4^=$. On smooth Pt they found that at potentials above 1.5v that there was a sharp increase in adsorbed $SO_4^=$ which they attributed to the incorporation of these anions in the oxides on the surface. Here one can ask

* Electrochemical Society Active Member.

the question: "If an oxidizable species (other than water) is present will it, under steady potentiostatic conditions, interfere with the formation of oxygen species on the surface and influence the adsorption of the sulfate ion?"

To try to answer the question of water oxidation in the presence of other oxidizable species and to try to gain some further insight into the passivation of Pt, it was decided to study further the oxidation of hydrogen in the passive Pt region. Hydrogen was selected because it is easily oxidized on active Pt and its maximum rate of oxidation of 2×10^{-3} amp/cm^2 (true area basis) in H_2SO_4 is from 2 to 7 orders of magnitude greater than water oxidation (1) in the same potential region. Use of the high-purity closed system (1, 2) developed at this Laboratory would permit long-time steady-state measurements where relatively slow sorption phenomena could affect electrode behavior. This system also allowed a determination of the hysteresis, when high potentials are decreased, noted by Frumkin and Aikazyan (10).

Experimental and Results

The experimental setup and conditions were the same as described in ref. (1), except that a constant flow of hydrogen, purified by flowing through heated Pd-Ag tubes and saturated with pure water, replaced helium. It was found that an N_2 atmosphere in the environment box was unnecessary and part of the data was taken with the front panel removed. The hydrogen flow into the cell remained at about 40 ml/min until a constant current was reached under potentiostatic control. The time required ranged from a quarter of an hour to many hours, depending both on the set potential and the previous sequence of potentials. The hydrogen flow rate was then increased to well over 1000 ml/min and the constant current recorded. Potentiostatic control was by a Pt/H_2 wire electrode in the cell. The sulfuric acid solution was one molar, the temperature 25° ± 2°C, and the true (11) area of the three Pt bead working electrodes used were each close to 0.2 cm^2.

The experimental results, which are steady-state values, are shown in Fig 1. Figure 1 is for the case of very rapid stirring with H_2 and gives potentiostatic current density *vs.* potential relations under conditions where diffusion effects in solution are minimized. For the slopes shown, $b = \Delta E/\Delta \log i$. The $b = -0.025$ and 0.025 values shown are the well-known Tafel slopes (12) in the cathodic and anodic polarization regions, respectively. At anodic potentials above 40 mv, a limiting current density of 2×10^{-3} amp/cm^2 is observed up to a potential of about 0.7v. A potentials above this value, the current density decreases, at first slowly up to 1.0v, then rapidly along the slope designated as $b = -0.11$ down to a second limiting current density of about 1.5×10^{-5} amp/cm^2. At potentials above 1.6v ($b = 0.13$ slope) the normal oxygen evolution reaction is observed. The diamond-shaped symbols show that potential reversal within a given region gave the same current densities.

After the oxygen evolution region was reached, a subsequent decrease in potentials gave the hysteresis shown. The time required to obtain steady-state for each point in this region ranged from a few hours to a day. The scatter of points and especially the two paths shown in the potential range from 1.16 to 0.88v appeared to be real. Using the same electrode a consistent set of points on either path was followed for a particular run. The path shown by the solid line, however, was favored over the dotted line. The broken line shown in Fig. 1 comes from Fig. 1 of ref. (1) and represents the potential *vs.* current density relation found in a pure helium-saturated solution.

Discussion

A comparison of Fig. 1 with the data shown by Frumkin and Aikazyan (6, 10) for hydrogen ionization

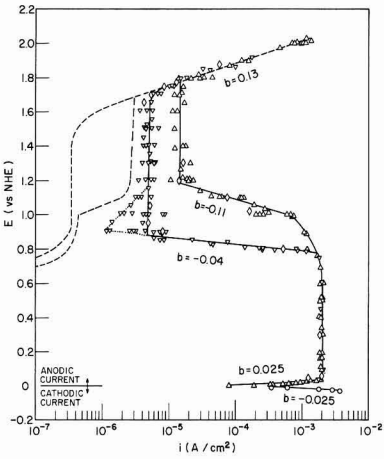

Fig. 1. Steady-state potentiostated current density *vs.* potential relation on Pt in hydrogen-saturated 1M. $H_2SO_4 \cdot H_2$ flow rate > 1000 ml/min: ○ cathodic current, △ anodic current, increasing applied potentials; ▽ anodic current, decreasing applied potentials; ◇ anodic current, intermediary reversal of applied potential values. Broken line is relation in helium-saturated solution (1), where hysteresis line to the right is for increasing applied potentials, to the left for decreasing applied potentials. See text for meaning of dotted line.

on a smooth Pt disk electrode in 1*N* H_2SO_4 at a rotation speed of 20,000 rpm shows some important differences. Figure 1 shows a maximum current density from 0.04 to 0.7v of 2 ma/cm^2 (since this current density is on a true area basis it is equivalent to about 4 ma on a geometric area basis). This limiting current density is essentially the same as the Frumkin and Aikazyan value of 3.8 ma/cm^2 (geometric area). In the Frumkin and Aikazyan case, however, the current density maximum is at 0.05v and there is a continuous dropping off of current density with increasing potential up to 1.2v. Figure 1 shows a constant current density at 2 ma/cm^2 up to 0.7v (for both the increasing and decreasing sequence of potentials) followed by a slow decrease and then a linear log decrease in current density up to 1.2v.

The essentially equivalent maximum current densities found by Frumkin and Aikazyan and this work show that the Pt electrodes were of equal activity. The important difference is that Frumkin and Aikazyan anodically and cathodically pre-electrolyzed their electrode just before taking measurements, which were then taken in a matter of minutes at each potential setting. With the high purity system, long time steady-state measurements were possible because poisoning of the electrode did not occur (as, for example, evidenced by the constancy of the maximum current density for long periods of time). Whether the Frumkin and Aikazyan decrease in current density (from 0.05 to 0.7v) was due to impurity adsorption or a lack of true steady-state conditions at the electrode is uncertain.

Considering Pt passivation above 0.7v, the possibility of a stable oxygen species remaining on the surface is remote. In the first place, the oxidation of water, which appears to be limited by slow discharge (1), occurs at rates from about five to one order of magnitude slower. In addition, Schuldiner and Warner (13) have shown that oxygen chemisorbed on Pt reacts rapidly with molecular hydrogen. Warner and Schuldiner (14) have shown also that the reaction rate is potential independent and zero order in both hydrogen and chemisorbed oxygen when the initial fractional coverage with chemisorbed oxygen is less than 0.8. Reaction rates of chemisorbed oxygen with hy-

drogen in this particular system for the three different working electrodes used were 0.4, 1.2, and 8 ma/cm^2. All three electrodes gave virtually the same potential *vs.* current density results.

The chemical rate of reaction of any oxygen which may be formed on the surface with hydrogen would with a few exceptions always be faster than the rate of anodic hydrogen oxidation. Hence, there is little possibility that chemisorbed oxygen or an oxygen species exists on the surface at least up to a potential of 1.2v. This analysis does not, of course, prove that an oxygen species may not be formed which rapidly oxidizes the hydrogen and that the rate-controlling process depends either on the rate of formation of this oxygen species or its reaction rate with hydrogen. However, it is very unlikely that the anodic hydrogen reaction under these conditions would be slower than the oxidation of water. (It will subsequently be shown that in this region a chemical oxidation of H_2 with an oxygen intermediate does not occur.) These results show that the oxidation of Pt or the formation and adsorption of oxygen species are not the cause of the Pt passivation and retardation of the anodic hydrogen oxidation reaction at least up to 1.2v.

The cause of passivation is much more likely the anion adsorption explanation as given by Frumkin (5); specifically, the adsorption of sulfate ion as was demonstrated by Kazarinov and Balashova (9). In the Kazarinov and Balashova paper a dropping off of the amount of sulfate ion adsorbed above 0.8v was observed. However, this was done in a nitrogen-saturated solution where formation and adsorption of an oxygen species and the partial replacement of sulfate are possible. In a hydrogen-saturated solution, a residue of oxygen would not remain on the surface so that as the potential increased beyond 0.8v, an increase in the amount of sulfate would be expected. And, in fact, as was shown by Kazarinov and Balashova, at higher potentials the coverage with sulfate ion can increase even in the presence of oxygen. With the elimination of a chemisorbed oxygen species, or Pt oxide, the bonding and coverage of the surface with sulfate ion should increase and is a reasonable explanation of the increased passivity shown in Fig. 1. The limiting current density from 1.2 to $\approx$ 1.8v can be due to a saturation of the surface with sulfate ion.

It should be noted that the $b = -0.11$ and -0.04 slopes in Fig. 1 are not Tafel slopes. The fact that the rate of hydrogen oxidation decreases with increasing potential demonstrates that the rates are not controlled by the exponential overvoltage term in the kinetic equation. The controlling term is obviously in the free energy of activation for the oxidation of hydrogen. As the potential increases, the free energy of activation can increase because of the increased coverage with sulfate ion and because of the increase in bonding of the sulfate ion with the surface.

In the oxygen generating region ($b = 0.13$) the presence of hydrogen has no apparent effect on the rate of oxidation of water. There is no "so-called" depolarization effect. This must be because the combined sulfate and oxygen sorption in this region is so extensive that significant anodic oxidation of hydrogen is virtually completely blocked. The data also show that the oxidation of water is primarily under charge transfer control. Otherwise, the chemical reaction of hydrogen with oxygen on the surface could influence the rate. In this region current densities were independent of stirring rate which also indicates virtually complete kinetic control.

The effects of dermasorbed oxygen (15) can be seen in the Fig. 1 data. Once the potential exceeds 1.8v, extensive dermasorption occurs and hysteresis results. In the potential range from 1.7 to 1.2v, the rate of hydrogen oxidation is reduced by about one-half. From about 1.16 down to 0.88v either the solid or dotted line was followed. Evidently the amount or distribution of dermasorbed oxygen may vary from run to run and may markedly influence the passivity behavior of the electrode. This influence of dermasorbed oxygen is evinced also by the scatter of points, which were, however, consistent for a particular run, in the entire region from 1.7 to 0.88v.

Something remarkable occurs in the $b = -0.04$ region. At current density values greater than 1.5×10^{-5} amp/cm^2, the potential required for the oxidation of hydrogen at a given current density can be as much as 0.3v less than in the $b = -0.11$ region. In the $b = -0.04$ region most of the dermasorbed oxygen would be removed, but a trace must remain because one can go up and down in potential in this region and remain on the $b = -0.04$ line. Once the intersection at about 0.8v is reached, increasing potentials will follow the path leading to the $b = -0.11$ slope. This eliminates the possibility of an impurity in the region of decreasing potential. However, at the same potentials on the increasing potential arm of the curve, the current densities are considerably higher. The lower current densities in the $b = -0.11$ region are evidently due to increased sulfate ion adsorption. Hence in the $b = -0.04$ region, the presence of dermasorbed oxygen plus the lower sulfate ion adsorption reduces the activation energy (potential) required to oxidize hydrogen at a given rate. However, at a given amount of sulfate ion adsorption the rate of hydrogen oxidation would always be lower in the presence of dermasorbed oxygen.

Another interesting consequence of this region is that the previous work (1) in helium-saturated solution showed that in the presence of dermasorbed oxygen a given rate of oxidation of water to an oxygen species (which was not retarded by increased sulfate ion adsorption) always occurred at a higher potential. If the oxidation of hydrogen took place via an intermediate oxygen species, then in the presence of dermasorbed oxygen a given rate of hydrogen oxidation should never occur at a lower potential. Since in the $b = -0.04$ region oxidation of hydrogen at a given rate can occur at a lower potential than in the $b = -0.11$ region [which is free of dermasorbed oxygen (1)] the oxidation cannot be through an oxygen intermediate, but must involve a direct electrochemical oxidation of hydrogen. Another conclusion is that pulsing or other electrochemical activation procedures of electrodes may do more than just clean the surface.

The catalytic properties of platinum are strongly affected by adsorbed sulfate ions and by dermasorbed oxygen. The relationships are very complex, but it appears that a narrowing down of possibilities is resulting. Since information is available concerning very slow solvent oxidation and relatively fast oxidation of the ideal fuel, hydrogen, similar studies made with organic fuels of intermediate oxidizability should be revealing.

Manuscript received Sept. 28, 1967; revised manuscript received Nov. 20, 1967. This paper will be presented at the Boston Meeting, May 5-9, 1968, as Abstract No. 185.

Any discussion of this paper will appear in a Discussion Section to be published in the December 1968 JOURNAL.

REFERENCES

1. S. Schuldiner, T. B. Warner, and B. J. Piersma, *This Journal*, **114**, 343 (1967).
2. S. Schuldiner, B. J. Piersma, and T. B. Warner, *ibid.*, **113**, 573 (1966).
3. H. Wroblowa, B. J. Piersma, and J. O'M. Bockris, *J. Electroanal. Chem.*, **6**, 401 (1963).
4. J. O'M. Bockris, H. Wroblowa, E. Gileadi, and B. J. Piersma, *Trans. Faraday Soc.*, **61**, 2531 (1965).
5. A. N. Frumkin, *This Journal*, **107**, 461 (1960).
6. A. N. Frumkin, in "Advances in Electrochemistry and Electrochemical Engineering," vol. 3, pp. 340-358, Paul Delahay, Editor, Interscience Publishing Co., New York (1963).

7. E. A. Aikazyan and A. I. Fedorova, *Dokl. Ak. Nauk, SSSR*, **86**, 1137 (1952).
8. E. Wicke and B. Weblus, *Z. Elektrochem.*, **56**, 169 (1952).
9. V. E. Kazarinov and N. A. Balashova, *Dokl. Ak. Nauk, SSSR*, **157**, 1174 (1964); *Dokl. Phys. Chem.*, **157**, 795 (1964).
10. A. N. Frumkin and E. A. Aikazyan, *Dokl. Ak. Nauk, SSSR*, **100**, 315 (1955).
11. S. Schuldiner and R. M. Roe, *This Journal*, **110**, 332 (1963).
12. S. Schuldiner, *ibid.*, **107**, 452 (1960).
13. S. Schuldiner and T. B. Warner, *ibid.*, **112**, 212 (1965); T. B. Warner, S. Schuldiner, and B. J. Piersma, *ibid.*, **114**, 1120 (1967).
14. T. B. Warner and S. Schuldiner, *ibid.*, **115**, 28 (1968).
15. T. B. Warner and S. Schuldiner, *ibid.*, **112**, 853 (1965).

Technical Notes

The Li/Li^+ Reference Electrode in Propylene Carbonate

Brian Burrows* and Raymond Jasinski*

Tyco Laboratories, Inc., Waltham, Massachusetts

Recent investigations of the $Li(Hg)/Li^+$ electrode couple in LiCl-DMSO solutions (1) indicate that the electrochemical reaction

$$Li^+ + e \rightleftharpoons Li$$

has a relatively high exchange current density, thereby making the system suitable for use as a reference electrode. It is reasonable to expect that the exchange current density of the same electrode couple in $LiClO_4$-PC solutions would also be high enough to allow its use as a reference electrode. However, for simplicity in use, a solid electrode would be preferred.

The evaluation of a reference electrode of the metal-metal ion type (in absence of a liquid junction) involves showing that (*i*) potential differences between pairs of the same electrodes in the same electrolyte solution are reproducibly small and constant over long periods; (*ii*) the electrode potential responds to varying cation concentrations in accordance with the Nernst equation; (*iii*) the passage of small amounts of current (microamperes) through the electrode does not permanently polarize it.

Experimental

All electrochemical measurements and associated materials handling were carried out in a water and oxygen free (<1 ppm) argon-atmosphere dry box at 28°C (Vacuum Atmospheres Corporation).

Both "anhydrous" $LiClO_4$ (K&K Laboratories 99.9%) and dried $LiClO_4$ (Anderson Physics Laboratories) were used to make up solutions. The purified $LiClO_4$ was prepared from 99.9% $LiClO_4$, recrystallized three times from water, and heated to just below the melting point in a vacuum over a period of several days to remove water. Finally, the sample was fused in vacuum and sealed in an argon atmosphere. This crystalline $LiClO_4$, obtained from Anderson Physics Laboratories, contained approximately 0.0015% water (15 ppm) and less than 0.0005% chloride. Both "as-received" PC (Matheson, Coleman and Bell) and distilled PC were used to make up 1M solutions with the dried $LiClO_4$.

A conventional three-compartment Pyrex glass cell was used, except where stated otherwise. The test lithium electrode was placed in the middle compartment, the reference compartment contacted the middle compartment through a Luggin capillary, and the counter electrode was in the third compartment. A cathode follower was employed to avoid undue loading of the reference electrode-working electrode cell. The unity-gain follower was constructed from an operational amplifier (Philbrick Researches, Inc., Type P65AU); the input impedance of this device was 33 Mohm.

Results

An electrodeposited Li (on a Pt-metal substrate)-Li^+ ion couple was first investigated for use as a reference electrode. Initially, experiments were carried out in 1M solutions of $LiClO_4$ in distilled PC, in a beaker using Pt foil counter and pseudoreference electrodes. Under these conditions, it was found that the residual current was <60 $\mu a\ cm^{-2}$ up to $-3.0v$ *vs.* Pt foil electrode. At -3.6 to $-3.8v$ *vs.* Pt, a deposit of lithium became visible with the concurrent evolution of gas. Gas evolution during the electrodeposition of lithium was also reported by Selim *et al.* (2). The bias potentials between four of the electroplated lithium electrodes were $\pm$ 80 mv for periods of time up to 2 hr.

The next set of experiments was carried out in a 1M solution of $LiClO_4$ in distilled PC, which had been passed over lithium powder. Currents of 60 $\mu a\ cm^{-2}$ were observed up to $-2.4v$ *vs.* Pt and a Li deposit became visible at about $-3.2v$. No gassing was observed during the deposition of lithium; however, no significant improvement in the potential difference between electroplated lithium electrodes was observed.

Up to this point no effort had been made to separate the counter electrode and the reaction products arising at this electrode from reaching the working electrode. When this was done by the use of a fritted glass plug in a three-compartment cell, lithium was deposited on Pt wire electrodes (area 0.2 cm^2) from the same solution. For example, when a current of >1 ma cm^{-2} was used to form a relatively thick and coherent deposit of Li without gassing, a stable potential difference of ± 15 mv was obtained.

Lithium was then deposited onto two platinum foils (area = 1 cm^2) from a 1M solution of $LiClO_4$ in PC at current densities of 1 ma/cm^2, and the potential difference was monitored in a fresh solution. After about 3 hr a stable difference of 23 mv developed and remained steady for a period of 10 hr before the experi-

* Electrochemical Society Active Member.

ment was discontinued. Polarization tests indicated that the electrodes had a very poor response; considerable hysteresis was observed.

Electrodes were then prepared from Li powder with a copper wire forming the contact to the external circuit. The electrode consisted of a glass tube 0.5 cm in diameter and drawn to a tip of 0.1 cm at one end. A plug of glass wool was placed in the contracted end, and powdered lithium was poured over the plug to a depth of about 0.5 cm. A copper wire spiral contact was inserted and another plug of glass wool pressed over the top of the lithium. Two electrodes of this type, when immersed in a 1M solution of $LiClO_4$ in PC, had a potential difference of 1 mv, which remained steady for 10 hr.

Polarization tests were carried out on the lithium powder electrodes by applying a small constant current from a constant current power supply (Electronic Measurement Model C623). The polarization was measured on a differential d-c voltmeter (John Fluke Model 825A). The results are shown in Fig. 1.

The linear relation between overpotential and current as well as the absence of significant hysteresis indicate that the electrodes were behaving reversibly. It will be noticed, however, that the inverse slope has a value of 2.4×10^6 ohms. This large value of resistance is probably due in large part to a poor contact between the lithium powder and the copper.

Finally, reference electrodes based on bulk lithium ribbon as a substrate were investigated. The Li ribbon (K&K Laboratories, Inc., 99.9%, approximately 3 mm diameter) was cleaned with acetone before being passed into the dry box. Inside the box the surface was scraped with a spatula until it was bright and metallic in appearance. Three electrodes were then placed in a cell containing distilled PC (1M $LiClO_4$). The potential differences between these three electrodes were then monitored over a period of several days. It was found that the potential difference between any pair was always <1 mv. Furthermore, it was found that when a fresh electrode was added to the solution after those already present had been submerged for several days, the potential differences were still <1 mv.

A Li electrode in "wet" $LiClO_4$ solution rapidly developed a dark gray film on its surface, accompanied by visible gassing. After the gassing subsided, the potential difference with respect to a fresh Li electrode was always <1 mv. The gray film dried to a white color after the electrode was removed from the solution.

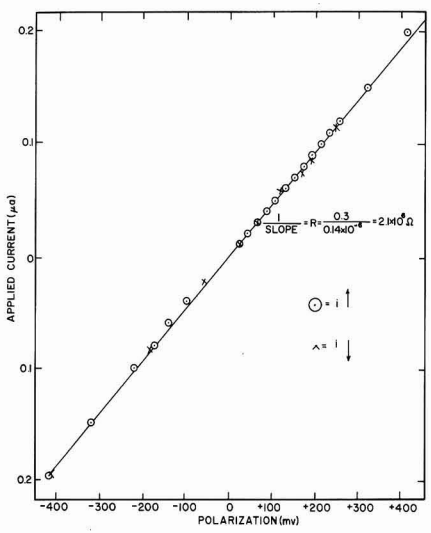

Fig. 1. Micropolarization test on a lithium powder reference electrode in $LiClO_4$/PC solution at 28°C.

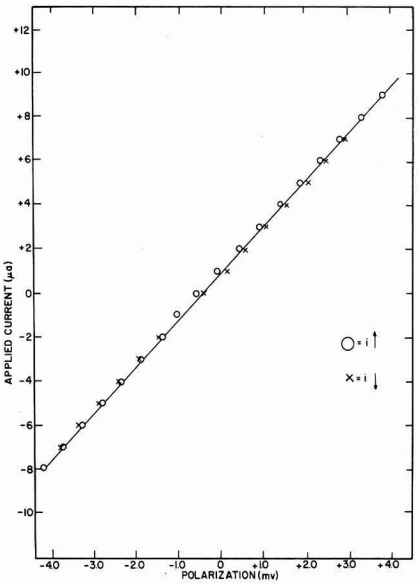

Fig. 2. Micropolarization test on a Li wire electrode (area approx. 2 cm^2) in $LiClO_4$/PC solution at 28°C.

Having established that the bias potentials were small and reproducible, we next carried out polarization tests on the solid Li electrodes. It can be seen (Fig. 2) that there is a linear relation between overpotential and current, indicating that the electrodes were behaving reversibly; there was no significant hysteresis. The fact that the line does not go through the origin is due to the slight bias in potential between two lithium rods. A comparison of Fig. 1 and 2 shows that the Li ribbon electrode structure is a considerable improvement over the Li powder structure and is also much simpler to set up.

Summary

Three forms of Li/Li^+ electrodes were evaluated as reference electrodes in 1M lithium perchlorate-propylene carbonate solutions. Electrodeposited lithium proved to be very susceptible to poisoning by impurities in the electrolyte and by those generated at the counter electrode. An electrode constructed from lithium powder in a glass tube was stable over prolonged periods of time and showed little hysteresis in the micropolarization tests. However, the ohmic resistance was high, due presumably to poor contact with the copper lead wire.

A lithium ribbon electrode, scraped clean before immersion in solution, was satisfactory for most work and was quite simple to prepare. Hysteresis in the micropolarization tests was negligible (<1 mv). Replicate electrodes gave potential differences less than 1 mv for extended periods of time (days). The electrode potential was also quite stable in the presence of sufficient water impurity to give visible gassing. The Nernst behavior of the Li/Li^+ couple in PC has been established by others (3).

Acknowledgments

The authors wish to acknowledge the support of the U.S. Naval Air Systems Command (Contract Now 66-06212).

Manuscript received Oct. 23, 1967.

Any discussion of this paper will appear in a Discussion Section to be published in the December 1968 JOURNAL.

REFERENCES

1. D. Cogley and J. N. Butler, *This Journal*, **113**, 1074 (1966).
2. R. Selim, K. Hill, and M. Rao, Final Rept. Contract No. NAS 3-6017 (Dec. 1965).
3. D. Boden, H. Buhner, and V. Spera, First Quart. Rept. Contract DA-28-043-AMC-01394(E), (Oct. 1965).

A New Technique for Studying the Rate of Gas Evolution Reactions

N. Marincic*

P. R. Mallory & Co., Inc., Laboratory for Physical Science, Burlington, Massachusetts

Low rate gassing processes were found difficult to study, whenever the amount of gas, consumed or liberated by chemical reaction, was used as an indicator of the reaction rate. The proper choice of the gas measuring technique is of particular importance in the case when the control of the gaseous reaction participant stands as the only practical alternative. A typical example of this kind is the corrosion reaction of a zinc electrode in battery systems, in an alkaline electrolyte containing an appreciable concentration of dissolved zinc (1). A significant quantity of gas is evolved in this corrosion reaction before the change of the zinc concentration in solution becomes measurable. The reaction rate measurement through the depletion of the metallic zinc, as one of the possibilities, is of no practical value in this case due to an undefined distribution of the corrosion products between the liquid and the solid phase.

Gassing also occurs in rechargeable battery systems during charging processes. The quantity of gas produced in the latest phase of charging (or overcharging) is of crucial importance for the battery performance, particularly when a sealed structure is employed. The participation of the gassing processes in the overall energy consumption during the charging could easily be estimated, provided an accurate method was available for measuring the amount of gas evolved. A more convenient and eventually more accurate method is needed for this type of study than the usual gas coulometry with direct volume reading of the quantity of gas collected (2).

The two examples mentioned above dictated the design of the technique for the gas measurement described in this paper.

A very detailed study of the gas coulometer has been done in the past (3) as a part of general effort to establish the true value of the Faraday. The weight of mercury displaced by the hydrogen-oxygen mixture evolved in an electrolysis reaction was measured. A balance of a remarkable high capacity-accuracy relation was used in this method among other precautions undertaken to maximize the accuracy of the measurement. A limitation of the method, however, rested on the fact that the displaced mercury was being collected in drops coming out of a capillary with the single drop weight being anywhere between 1 and 20 mg.

Several other basic studies have been done on coulometric technique dealing either with the problem of the impurities incorporated in silver deposits in the silver coulometer (4, 5) or with the other experimental conditions concerning the accuracy of the measurement (6, 9). The hydrogen-oxygen coulometer was thoroughly re-examined (10, 11) long after the basic study of the instrument has been done (3). It was found to be a sensitive instrument, if all the influencing factors were under control. No major change in the *modus operandi* was suggested, apart from the very careful evaluation of the performance determining factors.

The method employed in this work was designed for the determination of small amounts of gas produced either in a corrosion reaction in solution or as a by-product of an electrochemical reaction. It is based on the measurement of the change of buoyancy due to the gas collected under a glass bell, immersed in the solution. The method can be applied in any reaction rate study, whenever gas is involved, either as a reaction product or one of its participants.

Theoretical

A schematic representation of the technique employed is shown in Fig. 1. An increase of the volume of gas, generated under the bell $(V-V_o)$ will result in a buoyancy change (ΔG) under constant pressure and temperature.

$$\Delta G = (V - V_o)u_o \qquad [1]$$

if u_o is the density of the liquid in which the bell is immersed. The total quantity of gas under the bell at the beginning of the experiment can be expressed as

$$n_o = (P_{bo} + \Delta H u_o)\, V_o/RT \qquad [2]$$

where n_o is the number of moles, P_{bo} is the initial barometric pressure $\Delta H u_o$ is the hydrostatic component of the total pressure of the gas. With the number of moles of n_g of the gas generated during the experiment, n_v moles of vapor will be formed over the liquid in order that constant vapor pressure be preserved. These two quantities are related to each other as follows

$$n_v = n_g P_v/(P_b + \Delta H u_o - P_v) \qquad [3]$$

where P_v is the vapor pressure of the liquid and P_b

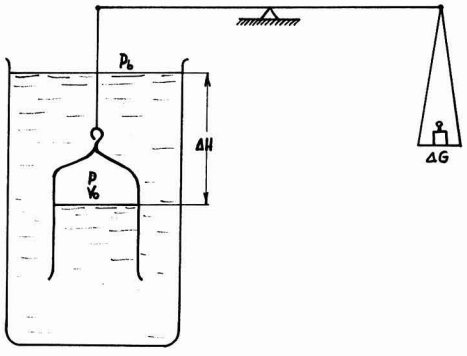

Fig. 1. Schematic representation of the gas measuring technique.

* Electrochemical Society Active Member.

is the actual barometric pressure at the moment of the measurement. Since the total quantity of gas under the bell is related to the volume of the gas in the manner

$$V = (n_o + n_g + n_v)RT/(P_b + \Delta Hu_o) \quad [4]$$

Eq. [2] and [3] with Eq. [4] lead to the expression

$$V = V_o\,(P_{bo} + \Delta Hu_o)/(P_b + \Delta Hu_o) + n_g RT/ (P_b + \Delta Hu_o - P_v) \quad [5]$$

Equation [5] gives with Eq. [1] after rearranging a final expression relating the moles of the gas generated at the measured buoyancy change

$$n_g = \Delta G(P_b + \Delta Hu_o - P_v)/u_o RT + V_o(P_b + \Delta Hu_o - P_v)\,(P_b - P_{bo})/(P_b + \Delta Hu_o)RT + V_1C \quad [6]$$

The V_1C—member of the right-hand side of Eq. [6] is added to the expression afterward in order to provide the correction for gas solubility (C) in a given volume of liquid (V_1).

Certain correction factors can be eliminated from the general expression (6) depending on the conditions of the experiment and the accuracy requirements.

(*a*) The barometric pressure change during the course of the experiment ($P_b - P_{bo}$) becomes irrelevant in high reaction rate measurements, when the experiment is completed in a short period of time, or when the barometric pressure is otherwise stable during the experiment. In such a case no calibration of the initial volume is necessary.

(*b*) The initial volume of the gas (V_o) can be eliminated from the expression if the bell is completely filled with the solution at the beginning of the experiment. This also eliminates the need for barometric pressure change correction, (P_{bo}) and *vice versa*.

(*c*) The hydrostatic pressure (ΔHu_o) depends on the design of the bell and can be made negligibly small for the majority of the experimental requirements particularly when low density solutions are used. A 100 mm difference between the inside and the outside liquid level means 1% difference in pressure reading under standard pressure and temperature conditions.

(*d*) The correction for the gas solubility is of some importance depending on the nature of the gas. Since hydrogen evolution occurs in a majority of metallic corrosion processes, its low solubility in a variety of the electrolytes (12) has no significant influence on the results of the measurement.

(*e*) The vapor pressure of the solution has to be known in order to estimate its influence on the results of the measurement. It is well-defined for a large number of solutions and can also be calculated for dilute solutions.

The general expression (6) is reduced to

$$n_g = \Delta GP_b/u_o RT \quad [7]$$

when a high degree of accuracy of the measurement is not required, *i.e.*, under the conditions described above. Reduced Eq. [7] shows the direct transfer of each ml of the gas generated into 1g difference in the buoyancy recorded on the balance.

Experiments and Results

The validity of the experimental technique was tested in a cell similar to the one represented in Fig. 2.

Two platinum electrodes were used to generate hydrogen electrolytically with the anode situated outside the bell. The central tube with the stopcock at the end was used for bleeding the bell in order to flood the electrode. It also provided the means for removal of the gas collected under the bell without dismounting the cell. The testing was done with 3M KOH and the results are shown in Fig. 3.

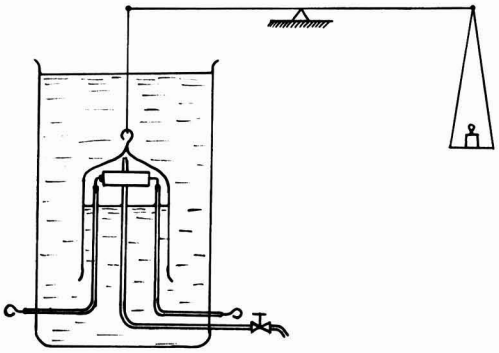

Fig. 2. Experimental set-up for the cell gassing measurement

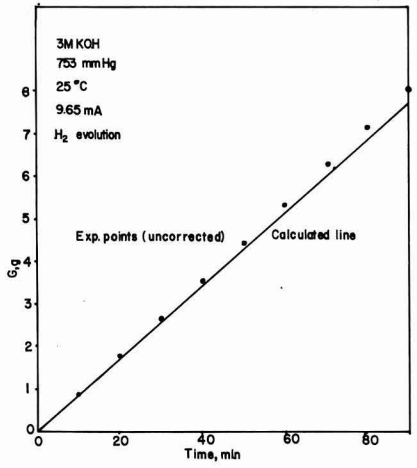

Fig. 3. Comparison of the results with the theoretical hydrogen evolution rate.

The discrepancy between the experimental points and the theoretical line illustrates the effect of the correction factors, summarized in general Eq. [6]. The accuracy of the measurement is proved to be higher than required for the experimental conditions given.

The set-up shown in Fig. 2 was used for the evaluation of experimental galvanic cells, *i.e.*, for gas evolution measurement in the course of charging of rechargeable cells. The platinum electrodes were used only as leads to the cell electrodes in this type of measurement. They were, obviously, not flooded in this case. The initial free volume in the bell had to be calibrated (V_o) for an accurate gas quantity calculation. A typical charging curve for an alkaline MnO_2-zinc cell is represented in Fig. 4 accompanied with the corresponding gas generation curve. The charging process was continued beyond the practical voltage cut-off point in order to follow the gas evolution curve all the way to water electrolysis. The ultimate slope of the gassing curve represents a gas evolution rate of 1.07 ml/min and is in good agreement with the theoretical gas evolution rate of 1.05 ml/min for the given set of the experimental conditions.

Conclusion

The measurement method described above is found to be reliable for gas evolution studies. In fact, an accuracy of the measurement can be achieved beyond that required for the majority of practical problems. It offers a means of registering the gas bubbles as they are generated with no need to collect the gas at

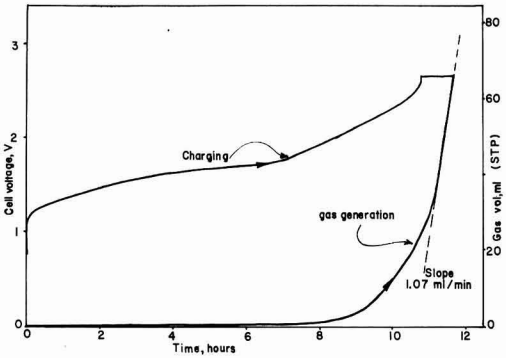

Fig. 4. Typical charging curve for an alkaline MnO_2-zinc system with the corresponding gas generation curve.

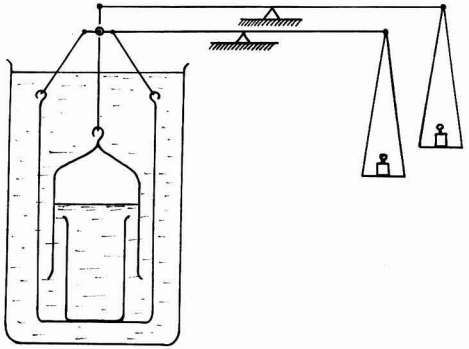

Fig. 5. Proposed set-up for the simultaneous recording of the gas evolution rate and the solid-state transformation rate.

certain particular section of the measuring device. This seems to be very convenient in the study of porous electrodes where the collection of the gas generated represents the major obstacle to reliable quantity measurements.

A recently published paper (13) describes the technique for the study of the rechargeable electrodes by measuring the buoyancy change of the electrode material during the metal-metal oxide transformation. That technique combined with the gas measuring technique described in this work could be utilized for a simultaneous recording of the solid-state transformation rate and the accompanying gas evolution rate in more detailed studies of electrode and/or the corrosion processes. The schematic representation of the set-up proposed is illustrated in Fig. 5.

Two analytical balances (or recording balances) could be used; one for the gas measurement, and one for the solid electrode transformation measurement. The corrosion of the electrodes in practical galvanic cells could be studied by this combined method in order to establish the corrosion product distribution between the liquid and the solid phase. The simultaneous gas evolution measurement could be an additional means of a net corrosion rate measurement in a system metal/electrolyte in the absence of oxygen.

The usefulness of the method in coulometric measurements can be illustrated by comparison with the electrogravimetry with copper as an example. A 1 amp-sec equivalent of copper amounts to 0.33 mg weighed directly on the balance. When the equivalent quantity of hydrogen is measured as in the present method, 1 amp-sec results in a change of buoyancy of 116 mg. This represnts the increase in the sensitivity of the measurement by factor of 350.

Acknowledgment

The author is indebted to Dr. P. Bro for stimulating discussions and to P. R. Mallory & Co. Inc. for permission to publish this work.

Manuscript received Aug. 17, 1967. This paper was presented at the Chicago Meeting, Oct. 15-19, 1967, as Abstract 44.

Any discussion of this paper will appear in a Discussion Section to be published in the December 1968 JOURNAL.

REFERENCES

1. N. Marincic and P. Bro, To be published.
2. P. Ruetschi, *This Journal* **114,** 301 (1966).
3. R. A. Lehfeldt, *Phil. Mag.*, (6) **15,** 614 (1908).
4. F. E. Smith, Report of Nat. Phys. Lab. 1910, p. 32.
5. T. W. Richards, *J. Am. Chem. Soc.*, **37,** 20 (1915).
6. G. W. Vinal and S. J. Bales, *U. S. Bur. Standards,* **Bull. 10,** 425 (1914).
7. E. B. Rosa, G. W. Vinal, and A. S. McDaniel, *ibid.*, 475 (1914).
8. E. B. Rosa and G. W. Vinal, *U. S. Bur. Standards,* **Bull. 9,** 151 (1913).
9. E. B. Rosa, G. W. Vinal, and A. S. McDaniel, *ibid.*, 493 (1913).
10. J. J. Lingane, *J. Am. Chem. Soc.*, **67,** 1916 (1945).
11. J. J. Lingane, Discussion Faraday Soc., **1,** 203 (1947).
12. R. D. Walker, Report to NASA on Grant 10-005-022, March 1966.
13. A. Langer and J. T. Patton, *This Journal,* **114,** 113 (1967).

Influence of Thin Noble Metal Films on Zirconium Oxidation

A. Fiegna[1] and P. Weisgerber

EURATOM-CCR, Ispra, Italy

Attempts were made for several years to measure electrical properties of oxides on metal surfaces during the oxide forming reaction between metal and gas phase (1-5). In those cases where the current density or the dielectric capacitance were investigated, the area of current flow was limited by a suitable contact. Some investigators (4,5) used noble metal films deposited by evaporation techniques on the metal surfaces. Joergensen (4) observed that thin films of platinum, deposited by cathodic sputtering, did not alter the reaction rate of zinc single crystal faces in oxygen.

In order to find suitable contacts for the measurements of electrical properties of zirconium oxide on zirconium metal during the oxide forming reactions,

Key words: Reaction kinetics, oxidation, zirconium, metal films, gold, silver, platinum, cathode sputtering, markers.

[1] Present address: Centro di Studi sulla Corrosione—Instituto Chimico dell'Università di Ferrara—Ferrara—Italy.

the influence of the metallic deposits on the reaction rate had to be investigated. At first sight a possible decrease of the reaction rate was expected, assuming that the noble metals blocked the access of the oxidant to the zirconium.

Experimental Procedure

Sheets 0.1 x 15 x 50 mm were made from crystal bar zirconium by repeated rolling, cleaning of the surface by electropolishing, and annealing at 750°C in vacuum ($p < 10^{-5}$ Torr).

Different series of samples were coated on both sides with uniform films of platinum, gold, silver, palladium, iridium, or rhodium by cathodic sputtering in high-purity argon. The thickness of the noble metal film deposits could be roughly estimated between 100 and 300Å from the transparency of the underlying glass plates, which served as target supports during the sputtering process. This was confirmed by later measurements carried out with a quartz crystal monitor.

Thickness control during the sputtering process was achieved by resistance monitoring between silver paint contacts of 1 cm length and 1 cm distance. All Pt and Au deposits were stopped at a resistance of 100 ohm and those of Ag at 30 ohm.

Thermogravimetric experiments were carried out in a continuously recording thermobalance. The oxygen atmosphere in the balance was established by filling the preevacuated system with high-purity oxygen to a pressure of 10 Torr. The water vapor atmosphere was made from distilled water, degassed by boiling in vacuum in a glass flask. The latter was then held at 11.2°C by a cryostat and connected to the preevacuated system. The temperature regulation of the cryostat maintained the pressure in the system automatically at 10 Torr.

For every experiment a series of 6 specimens, corresponding to a total surface area of 90 cm², was inserted on a platinum specimen holder into the thermobalance. The reaction temperature was in all cases 450°C and the duration of the experiments between 100 and 120 hr.

Experimental Results

Weight gains for the experiments in oxygen atmosphere are plotted in Fig. 1 on double logarithmic scale. Values for noncoated zirconium were in reasonable agreement with the literature (6). The reproducibility between series of specimens from the same preparation lot was within the precision of the thermobalance. After the oxidation process the specimens were covered with the usual black oxide.

The weight gain of the platinum coated specimens was about two times higher than that of the uncoated zirconium while the order of the reaction did not change considerably. After the oxidation the surface of the specimens were metallic, brilliantly reflecting, and only slightly darker than platinum coated, but nonoxidized specimens. It can therefore be concluded that at least the greater part of the deposited platinum remained unaltered at the oxide-gas interface.

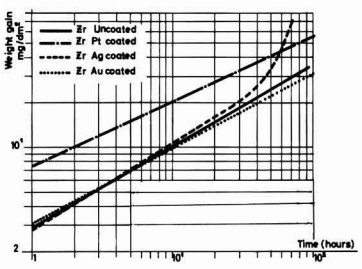

Fig. 1. Oxidation in dry oxygen at $P_{O_2} = 10$ Torr and $T = 450$°C.

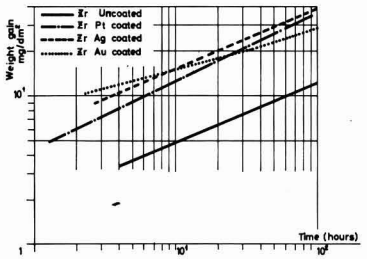

Fig. 2. Oxidation in water vapor at $P_{H_2O} = 10$ Torr and $T = 450$°C.

The weight gain of the gold coated specimens differed only slightly from that of uncoated specimens. The surface after oxidation was that of the normal black oxide with a few isolated small areas of a slight gold tint. Here the original metal deposit had almost completely disappeared, probably by diffusion into the zirconium oxide.

The weight gain of the silver coated specimens agreed with that of the uncoated specimens for the first 24 hr of the oxidation process. Afterward a rapid increase in the reaction rate took place, approaching linearity with time. The oxidized specimens looked brilliantly metallic, but at several places aggregates of white powdery material were found. This is similar to the "post transition corrosion" observed during the aqueous corrosion of zirconium. Obviously the same phenomenon occurred here as an effect of the silver film.

The results of the oxidation experiments in water vapor are plotted in Fig. 2. Recently experiments in water vapor of 10 mm Hg were carried out (8). Results are not comparable because that work concerned the early stages of the oxidation process, and observation times and temperatures differ too much from our conditions. Despite the lack of literature values for the oxidation of zirconium in water vapor at pressures lower than 1 atm, the weight gains found seem to be reasonable. Compared with weight gains at 100 and 1 atm at 450°C which differ by a factor of about 40 (6), these values at 0.001 atm differ by a factor of 38 from those at 1 atm.

In water vapor all noble metal coated specimens had an increased reaction rate.

The surface of the platinum and silver covered specimens were brilliantly metallic and only slightly darker than before oxidation. "Break-away" phenomena were not found. The gold again disappeared leaving only a few gold tinted spots at some places.

The reaction constants followed Eq. [1]

$$m^n = (k\,t) \qquad [1]$$

where m = mass of oxide formed in g/cm², t = time in sec, and n and k are reaction constants given in Tables I and II. The time during which these constants are valid is also indicated.

The hydrogen uptake of the specimens oxidized in water vapor was analyzed, and the data are given in Table III. The yield was calculated from the total weight gain, assuming 100% uptake for the case that all hydrogen formed from the water would be absorbed. The relatively low yield in the case of platinum may be due to the fact that, during this experiment,

Table I. Reaction constants for the oxidation at 450°C in dry oxygen ($P_{O_2} = 10$ Torr) following equation $m^n = k\,t$

	n	k[(g cm^{-2})^{n}sec^{-1}]	Validity (hr)
Uncoated	2.18	$1.4 \cdot 10^{-13}$	1-100
Silver coated	2.03	$5.2 \cdot 10^{-13}$	1-30
Gold coated	2.31	$0.51 \cdot 10^{-13}$	1-100
Platinum coated	2.42	$0.81 \cdot 10^{-13}$	3-100

Table II. Reaction constants for the oxidation at 450°C in water vapor (P_{H_2O} = 10 Torr) following equation $m^n = k\,t$

	n	k[(g cm^{-3})^{n}sec^{-1}]	Validity (hr)
Uncoated	2.51	$12 \cdot 10^{-13}$	3-100
Silver coated	2.46	$3.4 \cdot 10^{-13}$	3-100
Gold coated	2.62	$0.51 \cdot 10^{-13}$	32-100
Platinum coated	2.15	$19 \cdot 10^{-13}$	3-100

Table III. Hydrogen uptake from oxidation in water vapor at P_{H_2O} = 10 Torr and 450°C

Specimen	H_2 (ppm)	Yield Mol %
Uncoated	80	13
Platinum coated	69	4.5
Gold coated	73	10.2
Silver coated	251	15.5

a vacuum pump was connected to the system with a needle valve. The water vapor was drawn off continuously at a constant pressure of 10 Torr in the system, but had the effect of keeping the partial pressure of hydrogen envolved from the reaction at a lower value. Because of the failure of the pump the other experiments were carried out in the static system, *i.e.*, with increasing partial pressure of hydrogen during reaction.

Oxidation of specimens coated with palladium, rhodium, and iridium were expected to form the stable noble metal oxides (7).

Conclusions

Thin noble metal film deposits of 100-300Å thickness on zirconium did not block the surface from reaction with oxygen and water vapor at 450°C. This is not surprising if one takes into account that film deposits in that thickness range are not uniform, but consist of isolated nuclei. Instead of blocking oxygen, a catalytic effect was observed which resulted in an increase of the reaction rate for platinum and silver coated samples in water vapor, and for platinum coated samples in oxygen. Silver coating did not influence the rate in oxygen in the initial phase, but later on transition to "breakaway corrosion" began.

The catalyzing effect could be explained by different assumptions:

1. The metal deposits increase the adsorption of oxygen or water at the oxide-gas interface.
2. The metal deposits catalyze the ionization of adsorbed oxygen or water at the oxide-gas interface.
3. The metal deposits produce stresses in the underlying oxide influencing the number and mobility of dislocations.
4. Small fractions of noble metal ions diffusing into the oxide increase the number of oxygen ion vacancies and thereby the mobility of oxygen.
5. The metal deposits emit electrons into the oxide increasing the oxygen vacancy concentration and the mobility of oxygen.

Whichever of these explanations is right, the influence of the deposits on the oxide has to be taken into account when measuring electrical properties. Because there is little hope of eliminating these effects, and their magnitude in the case of zirconium is within the limits known to result from different surface treatments or specimen preparations, platinum seems to be the most suitable contact material.

The behavior of the gold deposits excludes application at reaction temperatures on zirconium.

On the other hand, care has to be taken in the choice of noble metals for inert marker experiments to determine the mobile ion species during oxide forming reactions. It is shown here, that different noble metals could lead to contradictory conclusions.

Manuscript received Oct. 4, 1967; revised manuscript received Dec. 18, 1967.

Any discussion of this paper will appear in a Discussion Section to be published in the December 1968 JOURNAL.

REFERENCES

1. L. D. Kirkbride and D. E. Thomas, WAPD-T-308, Feb. 1956.
2. R. D. Misch and F. H. Gunzel, Jr., *This Journal*, **106** 15 (1959).
3. D. W. Shannon, *Corrosion*, **19**, 414 (1963).
4. P. J. Joergensen, *This Journal*, **110**, 461 (1963).
5. D. K. Dawson and R. H. Creamer, *Brit. J. Appl. Phys.*, **16**, 1643 (1965).
6. Lustman and Kerze, "The Metallurgy of Zirconium," p. 623, McGraw-Hill Publishing Co., New York (1953).
7. J. C. Chaston, *Platinum Metals Rev.*, **9**, [2], pp. 51-6, [4], pp. 126-8.
8. J. K. Dawson, U. C. Baugh, and F. T. White, *Electrochem. Technol.*, **4**, 137 (1966).

Multiple Twin Structures in Electrodeposited Silver Dendrites

J. Smit, F. Ogburn,* and C. J. Bechtoldt

National Bureau of Standards, Washington, D. C.

The structure of electrodeposited dendrites of FCC metals, particularly of silver, has been the subject of several communications (1-7). These investigations have been conducted on dendrites produced from both fused salt and aqueous systems. The dendrites are described as being usually in one of two forms, *i.e.*, acicular and growing in the <110> direction or planar and growing in the <112> direction. Twinning in these dendrites has not been uniformly reported. With respect to silver dendrites formed in fused salt systems, Bockris (2), on the basis of x-ray diffraction and metallographic evidence, reports twinning in the planar form dendrites. Reddy (7) also reports twinning, but on the basis of metallographic evidence alone, as does Faust and John (8) in their examination of dendrites supplied by Hudson (3). In aqueous systems Kikuchi (6) has observed twinning in planar form dendrites growing in the <112> direction. Wranglen, however, does not report twinning (1, 4). Faust *et al.* (9) report observing twinning in the form of crossed lamella within the matrix of a single orientation. In the last case the lamella are each in twin relation to the matrix but not in twin relation to each other. In no case has multiple twinning, *i.e.*, more than three orientations about a common zone axis, been reported in silver.

Faust and John (10) describe multiple twinning configurations in semiconductor FCC materials deposited from the melt. They classify twinning modes or configurations as follows: (*i*) Class I twinning, in which {111} composition planes appear to radiate from a central point and are 70°32′ apart. The orientations are pie shaped and mutually exclusive. (*ii*) Class II twinning, in which {111} composition planes are parallel. In this case one orientation is minor to another

* Electrochemical Society Active Member.

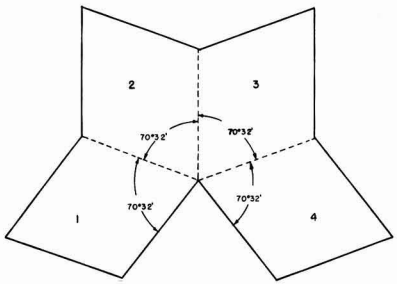

Fig. 1. Class I twinning. Four orientations. Dashed lines indicate {111} composition planes. <110> direction normal to paper.

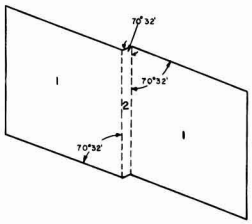

Fig. 2. Class II twinning. Two orientations. Dashed lines indicate {111} composition planes. <110> direction normal to paper.

and contained within it in the form of a band or lamella.

Figures 1 and 2 are sketches of idealized cases of both classes of twinning.

It is the purpose of this communication to report experimental observations of the structure of silver dendrites electrocrystallized from aqueous solutions with reference to the classes of Faust and John. This investigation was undertaken to supplement our fragmentary knowledge of the roll of growth twins in the formation of electrodeposited dendrites.

Description of Apparatus and Techniques

Electrocrystallization was conducted in Pyrex vessels 44 mm in diameter and 80 mm high. The dendrites were produced on silver wire cathodes in 70 ml of 0.5M $AgNO_3$. The solution was prepared from reagent grade $AgNO_3$ and distilled water. A silver wire in a Luggin capillary was used as a reference electrode. The tip of this electrode was positioned approximately halfway between the two active electrodes and was used to maintain potentiostatic control of the system during deposition. The potential values reported here include the IR drop between the reference electrode and cathode, which varies substantially as the dendrite grows toward the anode. Dendritic growth was induced at cathode potentials of at least 300 mv and then maintained potentiostatically at approximately 160 mv. Growth was permitted to proceed until the dendrites attained a length of at least 1 cm. Dendritic growth often proceeded at a rapid pace and has been observed here at rates up to 1.2 mm/min. After growth termination the dendrites were removed carefully from the electrolytic solution, washed in distilled water, air dried, and mounted with the base end secured in clay plugs fixed to the inner surface of polyethylene bottle caps. These caps were then secured to 4 or 6 dram vials. The dendrites were now fully enclosed and protected against mechanical shocks and corrosion. The dendrites remained thus secured until such time as detailed optical goniometric, x-ray diffraction, and metallographic examinations were undertaken.

Observations

In the course of this investigation 38 dendrites were examined. The dendrites ranged from one-fourth to one millimeter thick and were at least one centimeter long. All specimens contained bright shiny well-defined facets. Preliminary two circle optical goniometric surveys and x-ray diffraction examinations (precession alignment and rotating crystal patterns) indicated the dendrites to be fundamentally twin crystals with composition planes and growth axis parallel to the <110> direction. Although the full extent of multiple twinning is not necessarily revealed by the use of optical equipment alone, the optical data did indicate in all cases the existence of twinning. All dendrites examined were of acicular form and were clearly faceted, mainly on the <110> zone. The most frequently observed facets on this zone were the {111} facets, then the {100} and {112} facets; {110} facets were seen also, but only rarely. As many as six orientations in twin relation were identified in this manner. Low orders of twinning, that is, two and three orientations in twin relation, are exhibited generally in those crystals having relatively large smooth bright surfaces. These crystals frequently appeared x shaped in cross section with crevasses extending down the entire crystal length. High orders of twinning, that is, four and more orientations in twin relation, are characteristic of crystals having jagged appearing surfaces containing many nodes or knobby protuberances.

Zero level <110> Weissenberg patterns of the dendrites confirmed and, in some cases, expanded on the preliminary findings. The extent of twinning was determined from the number and position of the {111} spots. The <110> zone of a single orientation (FCC) contains in a 180° interval two {111} spots, providing the interval does not start on a spot. Each additional orientation in twin relation generates one new {111} spot. The {111} spot common to two orientations represents the composition plane. Up to eight orientations in twin relation were revealed in this way. Figures 3, 4, 5, and 6 are zero level <110> Weissenberg patterns showing 2, 4, 6, and 7 orientations, respectively. The film translation is approximately 100 mm (200 degrees). K_α molybdenum radiation was used to produce the patterns. This radiation was selected principally because of the atomic number and irregular thickness of the dendritic material. In photographs 5 and 6 some streaking is observable between {111} spots 3.6 mm (7.4 degrees) apart. It is slight and has been enhanced by both over exposure of the original photo-

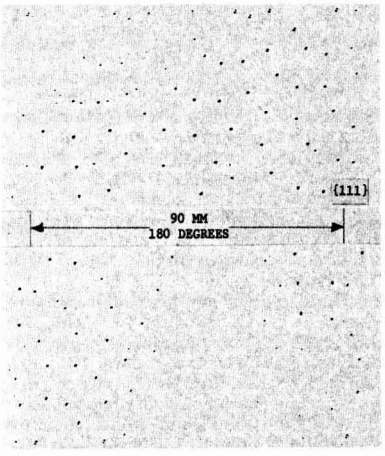

Fig. 3. Zero level. {110} Weissenberg diffraction pattern showing two orientations in twin relation.

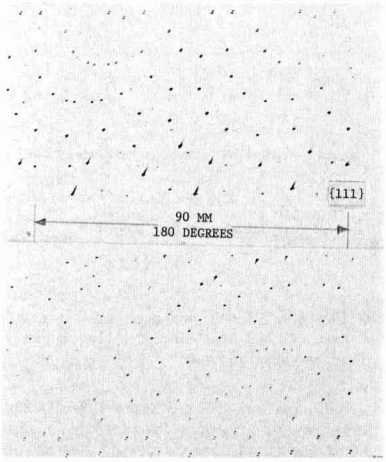

Fig. 4. Zero level. {110} Weissenberg diffraction pattern showing four orientations in twin relation.

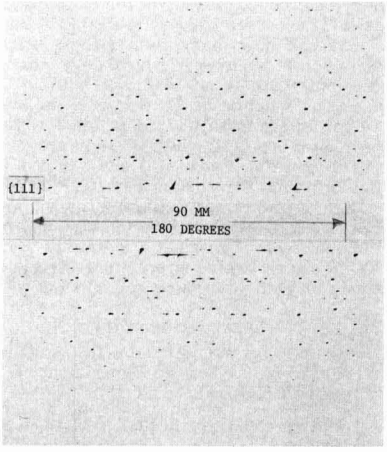

Fig. 5. Zero level. {110} Weissenberg diffraction pattern showing six orientations in twin relation.

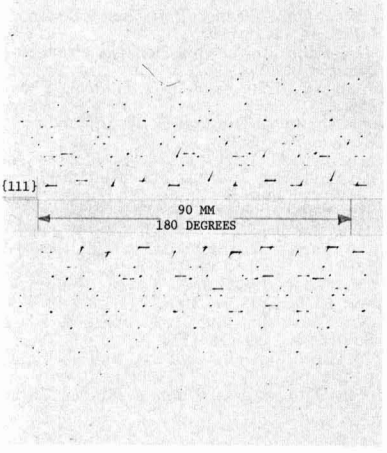

Fig. 6. Zero level. {110} Weissenberg diffraction pattern showing seven orientations in twin relation.

graphs and by reproduction. Nonetheless it may be indicative of strains in the orientations involved.

In the majority of cases the number of orientations discerned optically was the same as the number of orientations as determined from the Weissenberg patterns. This was particularly so for the low orders of twinning. The majority rule held for the higher orders of twinning as well except that in several cases more orientations were revealed on the Weissenberg patterns than were displayed optically.

A determination of the consistency of twinning through a dendrite was made by examining some dendrites at two positions along the growth axis. Weissenberg {110} zero level patterns were obtained of these dendrites near the growth tip and in the base region. In each case the number and position of the orientations at the tip agreed with the number and position at the base.

The classes of twins as described by Faust and John (10) and detailed here in the introduction were observed in metallographic sections taken normal to the growth axis of dendrites electrodeposited during this investigation.

Figure 7 is an example of Class I twinning showing five orientations about an axis. The observations here reported were made on specimens mounted, ground, and polished according to standard metallographic practices. The details of the structure were most often, though not consistently, brought out using an etchant prepared by combining, just prior to use, at a ratio of 1:1 a 5% solution of KCN in distilled water with a 5% solution of $(NH_4)_2S_2O_8$ in distilled water. However, no etching system and schedule used produced good results consistently. It appeared that simple twin boundaries could not be clearly developed consistently. The maximum number of related orientations observed in Class I type specimens was six. This was in agreement with both the optical and x-ray data for that specimen. The maximum number of orientations observed in Class II type specimens was three. This also was in agreement with optical and x-ray data. In the latter specimen two orientations appeared as 10μ wide crossed lamella in a third predominant orientation. This same specimen showed only one orientation on a 27-hr exposure Weissenberg pattern taken using a Mo target tube at 50 kv and 15 ma. An increase of exposure time to 90 hr at the same conditions brought out faintly the two orientations of the lamella forms.

Dendrites containing both classes of twins simultaneously were also observed. This is illustrated in Fig. 8 and 9.

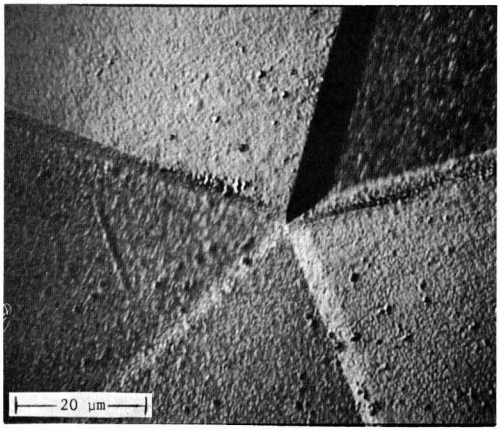

Fig. 7. Class I twinning showing five orientations about a central axis. X1500 before reduction.

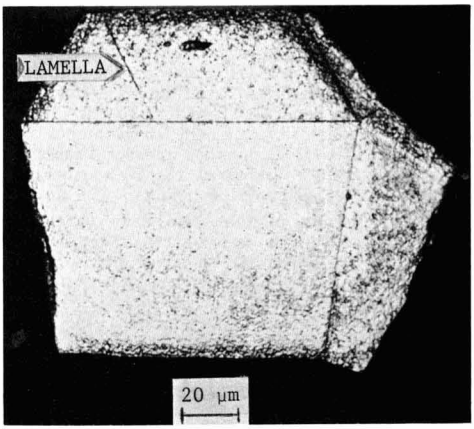

Fig. 8. Combination of Class I and II twinning. X500 before reduction.

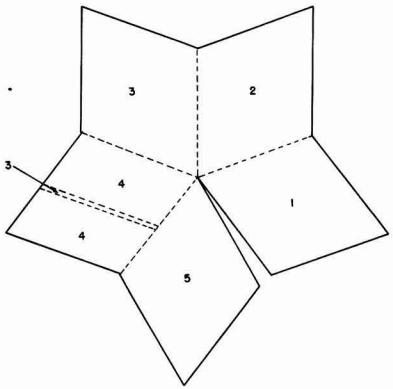

Fig. 9. Combination of Class I and II twinning. Five orientations. Dashed lines indicate {111} composition planes. <110> direction normal to paper.

Discussion

This note has brought to attention modes of multiple twinning as encountered in the electrocrystallization of silver from aqueous solution. Multiple twinning involving up to eight orientations is reported. No exception to twinning was uncovered among the 38 silver dendrites examined during this study. Every one was made up of two or more crystals in twin relation with all the composition planes parallel to the growth axis. Our observations were, of course, limited to a specific set of conditions and to rapidly growing dendrites. Hence, we cannot make any generalized statement concerning all dendritic growth. The inference here, however, is that the twinned structure is involved in the growth mechanism. We are also impressed by the fact that in the literature, wherever dendritic growth by electrodeposition has been rapid, i.e. mm/hr, a twinned structure has been present. This has been reported by Barton and Bockris (2) (silver), Reddy (7) (silver), Ogburn *et al.* (5) (lead), and Bechtoldt *et al.* (11) (molybdenum). From these and other experimental observations it is evident that twinning plays an important role in the growth process. It exerts a profound influence on the shapes of dendrites, on their directions of growth, and on the

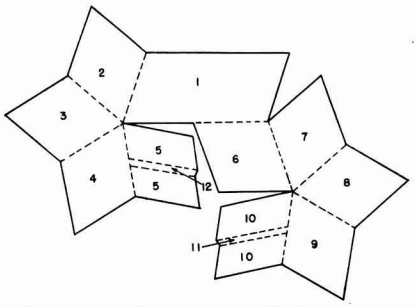

Fig. 10. Composite Class I twinning. Twelve orientations. Two axes of twinning. Dashed lines indicate {111} composition planes. <110> direction normal to paper.

cathodic polarization. Where twin lamella occur, the twin plane re-entrant-edge mechanism of Faust and John seems adequate. The same mechanism may also be applicable to the radiating twin structure, although it remains to be shown that faceting suitable for re-entrant edges occurs. {111} Faceting is suitable for twin lamella, but not for radiating twin structures. However, electrodeposited silver develops other facets, such as {571} observed by von Dauber (12) and by us.

One may ask how many twin related orientations are possible in a dendrite. We have detected eight and no more, but there is no reason to think that more than eight could not occur. At this time the only rules that we can apply to this twinning are (*i*) the composition planes are {111} and (*ii*) they are parallel to the growth axis. Faust *et al.* (9) show that in the case of radial twinning, a mismatch boundary or void must occur. With no more restrictions, it is very easy to conceive of a variety of twin configurations, many of which include more than eight orientations. For example, Fig. 10 shows twelve orientations associated with two centers for radial twinning and lamella.

Acknowledgment

This research was supported by the Advanced Research Projects Agency of the Department of Defense under Project DEFENDER.

Manuscript received Oct. 5, 1967; revised manuscript received Dec. 14, 1967.

Any discussion of this paper will appear in a Discussion Section to be published in the December 1968 JOURNAL.

REFERENCES

1. G. Wranglen, *Trans. Roy. Inst. Technol. Stockholm*, **94**, 13-15 (1955).
2. J. L. Barton and J. O'M Bockris, *Proc. Royal Soc.*, **268**, 494 (1962).
3. L. Yang, C. Chien, and R. G. Hudson, *This Journal*, **106**, 632 (1959).
4. A. M. Shams El Din and G. Wranglen, *Electrochim. Acta*, **7**, 79 (1962).
5. F. Ogburn, C. Bechtoldt, J. B. Morris, and A. de Koranyi, *This Journal*, **112**, 574 (1965).
6. M. Kikuchi and R. Yamazaki. *Denki Kagaku*, **33**, 283 (1965).
7. T. B. J. Reddy, *This Journal*, **113**, 117 (1966).
8. J. W. Faust, Jr., and H. F. John, *ibid.*, **108**, 109 (1961).
9. J. W. Faust, Jr., Daniel Kahan, Fielding Ogburn, and A. W. Ruff, Jr., *ibid.*, **114**, 1311 (1967).
10. J. W. Faust, Jr., and H. F. John, *J. Phys. Chem. Solids*, **25**, 1409 (1964).
11. C. J. Bechtoldt, F. Ogburn, and J. Smit, To be published.
12. H. von Dauber, *Ann. Chem. & Pharm.*, **78**, 68 (1851).

JOURNAL OF THE ELECTROCHEMICAL SOCIETY

SOLID STATE SCIENCE

APRIL 1968

Journal of The Electrochemical Society is the fundamental research journal serving the interdisciplinary interests of chemistry, physics, electronics, biology, medicine, and engineering as they pertain to electrochemistry and to electrochemical phenomena. Written for the research scientist in industry, government, the independent laboratory and the university, it publishes contributed Technical Papers, Technical Notes and Brief Communications describing current basic research of original character, and is edited in two sections: 1) ***Electrochemical Science*** including such areas as batteries, fuel cells, corrosion and corrosion mechanisms, electrothermics and metallurgy, electrodeposition, electroorganic reactions and phenomena, and allied work of theoretical electrochemical nature. 2) ***Solid State Science*** including such areas as dielectrics and insulation, electrothermics and metallurgy, semiconductors, luminescence and related solid state investigations.

Time-Temperature Superposition Theory for Electrets

Bernhard Gross

National Nuclear Energy Commission of Brazil, Rio de Janeiro, Brazil

ABSTRACT

The previous theory applies to isothermal behavior of dielectrics. It correlates current transients and dielectric loss curves obtained at different, but constant temperatures. A theory of nonisothermal effects is, however, needed to describe the conductivity glow curves during heating or the current transient during the thermal release of a "frozen-in" charge. The outline of such a theory is developed in the present paper. It is based on the principles of linearity and of charge invariance. Charge invariance means that the amount of charge which can be released by reheating a dielectric containing a frozen-in charge is a state variable depending only on the state of the system at the time when the reheating begins. The relaxation time can then be expressed in terms of a time- and temperature-independent distribution parameter. The generalized distribution function, which corresponds to the distribution of relaxation times of the isothermal system, is a function only of the distribution parameter and therefore independent of temperature. The formalism of rate theory is used to obtain an explicit expression for the relaxation time in terms of temperature and of activation energy. A simple mathematical model is obtained using an empirical expression for the distribution function. To account for the extremely strong temperature dependence of the current one must assume that states with high activation energies are much more frequent than states with low energies.

The isothermal behavior of dielectrics under different types of stress, in the time and frequency domains, has been investigated extensively. At an early stage of the theory, Wagner (1) formulated his "Law of Corresponding States" by which he was able to correlate discharge current and dielectric loss curves at different, but constant temperatures. In the analogous case of linear viscoelasticity a similar method has yielded "master" curves which correctly describe the behavior of systems over wide ranges of time, frequency, and temperature (2). The method is now called time-temperature superposition theory. The behavior of electrets is, however, characterized by nonisothermal transitions to which the theory in its present form does not apply (3). The lack of an adequate analytic theory of nonisothermal effects makes it difficult to obtain a systematic presentation of experimental results. In the present paper an attempt is made to formulate such a theory. For numerical applications an explicit expression for the distribution of relaxation times must be given. It is shown how such an expression can be obtained under rather general conditions and how it leads to a simple mathematical model.

Charge Invariance

The theory is based on the postulate of charge invariance: The amount of charge which can be released by reheating an electret containing a "frozen-in" charge is a constant which depends only on the state of the system at the time when the reheating begins, not on subsequent heating rate and temperature. This assumption is by no means trivial although it seems to have been made implicitly by most authors on the subject. Thus it seems worth while to present here the experimental evidence (4) in some detail and subsequently to give a mathematical formulation.

Experimental.—Experiments were made with samples of filtered yellow prime carnauba wax with painted-on silver electrodes, of 1 mm thickness and 20 cm^2 area, under a voltage of 118v.

Figure 1 gives heating transients for different heating rates. Samples were first polarized at room temperature for 24 hr; subsequently the temperature was raised as shown in the bottom part of Fig. 1. The voltage was applied during the heating period. Currents increased strongly with increasing heating rate and reached peak values when the temperature became constant. The final constant value of the current represents the ohmic conductance. Thus when the heating rate was very low, the transient became obliterated by the ohmic current. The current transients indicated that the polarization of the system increased due to the increase in temperature although the applied voltage remained constant.

Figure 2 gives current as a function of temperature, during heating and during cooling. The heating curves are derived from the corresponding curves of Fig. 1. During all measurements, *i.e.*, during heating and during cooling, the same constant voltage was applied. For the cooling curves, samples were charged at 60.5°C during 13 hr before the temperature was reduced. All cooling curves are identical although cooling rates varied within a wide range of values. This absence of any current transient during cooling, contrasting strongly to what happens during heating, proves that the polarization of the sample remains constant if the temperature is reduced while the voltage remains applied. Obviously if there was any change in polarization this would have to manifest

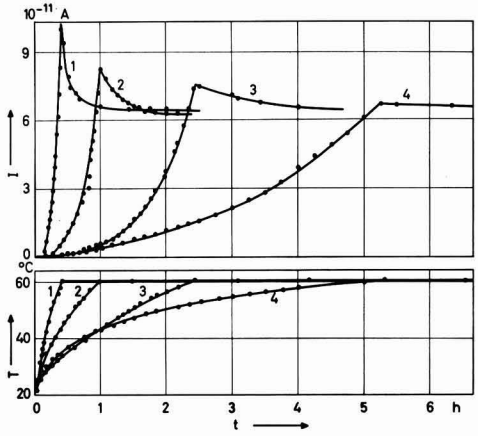

Fig. 1. Polarization currents as a function of time for different heating rates. Top: currents as a function of time; bottom: corresponding temperatures.

Key words: Electrets; dielectric theory (nonisothermal); linear superposition theory; electrical relaxation systems.

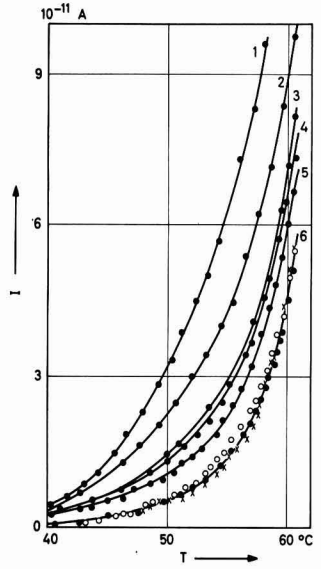

Fig. 2. Current as a function of temperature. Curves 1 to 5: heating curves. (Curves 2 to 5 of this figure correspond to curves 1 to 4 of Fig. 1). Average heating rates were: curve 1, 1.35°C/min; curve 2, 1.25°C/min; curve 3, 0.5°C/min; curve 4, 0.21°C/min; curve 5, 0.095°C/min. Curve 6: Cooling curves. Average cooling rates were: open circles 0.6°C/min; solid circles, 0.23°C/min; crosses 0.05°C/min.

itself by a depolarization or discharge transient in the same way as the polarization of the sample gives a charging transient.

Figure 3 gives depolarization curves in short-circuit following polarization experiments during which charge was "frozen-in" under different cooling conditions. Samples were charged at 60.5°C during 3 hr, cooled to room temperature with different cooling rates, and shorted. They were kept in short-circuit and subsequently reheated under identical conditions. Depolarization curves, as shown in Fig. 3, are approximately identical and indicate no systematic dependence on cooling rate.

These experiments show that the storage capacitance is independent of temperature during cooling. Further direct evidence has been obtained by Murphy (5). He found that the time integral over the depolarization current of a series of identically polarized samples was independent of the rate of reheating in short-circuit between 0.19 and 0.75°C/min.

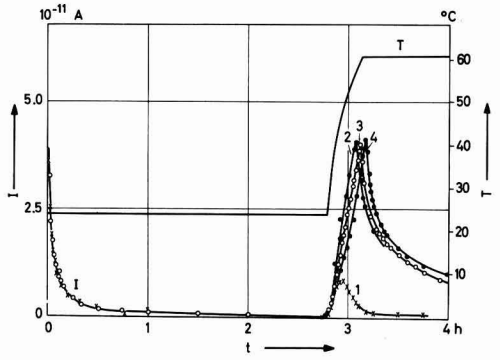

Fig. 3. Depolarization curves. Polarization time: 3 hr at 60.5°C. Average cooling rates (with voltage applied): for curve 2, 0.22°C/min; for curve 3, 0.55°C/min; for curve 4, 0.48°C/min. For curve 1 the sample was charged at room temperature.

Theoretical.—An absorptive dielectric which has been polarized at a given (high) temperature and subsequently cooled and shorted, contains at the moment of the short-circuit (taken as $t = 0$) a frozen-in or stored charge $q(0)$. This charge is defined as the time-integral over the transient component of the charging current. Thus it depends on the electrical and thermal treatment for $t < 0$, but is always the same for a given polarization process. The system is discharged by reheating in short-circuit. The temperature during this period is an arbitrary function of time $T(t)$. The discharge current $J(t,T)$ is a function of time and temperature, different temperature functions giving different discharge currents. The released charge is defined as the time integral over the discharge transient, *i.e.*, as $\int_0^\infty J\,ds$. There is no *a priori* reason to assume that the released charge is always the same, independently of the temperature function $T(t)$ and that a unique value can be assigned to it. But in the case of charge invariance, the released charge is a constant which depends only on the initial state of the system at the moment of the short-circuit, not on subsequent heating rate and temperature. Under these conditions the released charge is equal to the stored charge and one has

$$\int_0^\infty J[s,T(s)]ds = q(0) \qquad [1a]$$

where $q(0)$ is a constant which depends only on the values of the system parameters at $t = 0$. If t_o is an arbitrary time $0 < t_o < \infty$ one has also

$$\int_{t_o}^\infty J[s,T(s)]ds = q(0) - \int_0^{t_o} J[s,T(s)]ds = q(t_o) \qquad [1b]$$

$q(t_o)$ is the charge released between the arbitrary time t_o and infinity; according to Eq. [1b] this depends only on the thermal treatment prior to t_o, not on what might happen afterward. Therefore if charge invariance applies at the time $t = 0$, it applies also for any later time t_o. Since t_o is arbitrary we shall write briefly

$$\int_t^\infty J(s)\,ds = q(t) \qquad [2a]$$

$$J = -dq/dt \qquad [2b]$$

q is a state variable which depends on the state of the system at time t, Jdt is a total differential.

We shall exclude the case of resonance absorption. Thus we consider systems containing only two types of parameters, a dissipative (ohmic) one and a charge-storing (capacitive) one, *i.e.*, pure relaxation systems. Transformation of electrostatic into electromagnetic energy is excluded. Under these conditions the released charge has always the same polarity, is uniformly decreasing, bounded, and disappears for $t \to \infty$. This gives the relations, for $t > 0$,

$$M \geq q(t) \geq 0;\ dq/dt \leq 0;\ q(\infty) = 0;\ J \geq 0 \qquad [2c]$$

where M is finite.

Superposition Theory

Linearity.—In this paper the electret is treated as a linear electrical system, in line with the author's theory which considers the nonisothermal charging and discharging transients of solid dielectrics in the context of the general theory of dielectric anomalies (6). The application of the principle of linearity has already been successful in the treatment of dielectric absorption, open-circuit behavior of absorptive dielectrics (7) and electret polarization (8) at different, but constant temperatures. It appears also as a convenient basis for the discussion of the nonisothermal transient currents characteristics of electret behavior.

Linear systems are defined as systems which can be described by means of linear differential equations. Systems with a finite or infinite number of lumped parameters correspond, respectively, to a finite or an infinite set of total differential equations; systems with continuously distributed parameters correspond to partial differential equations. The knowledge of the linearity of these equations provides one with important information without a knowledge of the detailed structure of the physical system. Linear systems are conveniently discussed in terms of electrical network analogues. The network analogue of an electret is a two-terminal, passive, pure relaxation system. The current transient produced by a unit voltage step is called indicial admittance. The purpose of this paper is, therefore, to give an expression for the nonisothermal indicial admittance.

Isothermal.—System parameters change with temperature, but are constant, *i.e.*, time-independent, for all measurements performed with constant temperature throughout. Thus under isothermal conditions a linear system theory applies in its conventional form. Consider a system composed of a finite number of lumped parameters. This is described by a set of total differential equations, of the first order, containing mesh currents and applied voltage. The relation between the applied voltage $V(t)$ and the external current $J(t)$ is obtained by the elimination of all other currents. This gives (9) the linear differential equation with constant coefficients

$$\sum_{m=0}^{n} a_m d^m J/dt^m = \sum_{m=0}^{n'} b_m d^m V/dt^m \qquad [3a]$$

The short-circuit current, for $V \equiv 0$, is the solution of the homogeneous equation

$$\sum_{m=0}^{n} a_m d^m J/dt^m = 0 \qquad [3b]$$

the solution of which is

$$J = \sum_{i=1}^{n} (q_i/\tau_i) \exp(-t/\tau_i) \qquad [4]$$

The τ_i are the relaxation times, the q_i are the integration constants giving the initial charges of the individual systems, and $\tau_i > 0$, $q_i \geq 0$. The open-circuit voltage, from which the potential of the unshielded electret could be obtained, is given by the differential equation in $V(t)$ obtained by putting $J \equiv 0$.

A system with continuously distributed parameters has a continuous distribution of relaxation times. The short-circuit current is obtained by a generalization of Eq. [4], replacing the sum by an integral and q_i by $dq(\tau)$, where τ now is a continuous variable. This gives the integral transform

$$J = \int_o^\infty \phi(t,\tau) \frac{dq}{d\tau} d\tau \qquad [5]$$

where $dq/d\tau$ is the distribution function of relaxation times τ. The kernel

$$\phi(t,\tau) = (1/\tau) \exp(-t/\tau) \qquad [6a]$$

is the solution of the differential equation

$$d\phi/dt + \phi/\tau = 0 \qquad [6b]$$

that satisfies the normalization condition

$$\int_o^\infty \phi(t,\tau)\, d\tau = 1 \qquad [6c]$$

Nonisothermal lumped parameter system.—The electret effect is typically nonisothermal. During the course of the experiment the temperature is a function of time; therefore the system parameters are time-dependent. This obliges one to generalize the theory and to reformulate the expressions for the distribution function and the kernel of the integral-transform representation for the current.

The time-dependence of the system parameters does not affect the linearity of the system. Therefore the relation between J and V has the same form as before, but the coefficients of the differential equation are now functions of time. The same applies to the differential equation for the short-circuit current. Thus it is sufficient to replace the constant coefficients a_m by time-dependent coefficients $k_m(t)$. This gives for the current the equation

$$\sum_{m=0}^{n} k_m(t)\, d^m J/dt^m = 0, \quad t > 0 \qquad [7]$$

The time $t = 0$ is taken as the moment when the applied voltage is removed and the system is short-circuited. The solution has the form

$$J = \sum_{i=1}^{n} A_i \phi_i(t) \qquad [8]$$

where the ϕ_i are linearly independent particular solutions of Eq. [7]. A_i are the integration constants which define the state of the system for $t = 0$. This is supposed to be always the same, *i.e.*, the system shall have been completely polarized with a given constant voltage before the stored charge is released. Now we consider two depolarization experiments, corresponding to two temperature-time functions $T^{(1)}(t)$ and $T^{(2)}(t)$ which shall be identical for $0 \leq t \leq t_o$, but different for $t_o < t < \infty$.

Thus

$$T^{(1)}(t) = T^{(2)}(t) \qquad 0 \leq t \leq t_o \qquad [9a]$$

$$T^{(1)}(t) \neq T^{(2)}(t) \qquad t_o < t < \infty \qquad [9b]$$

The coefficients k_m will therefore also be identical for $0 \leq t \leq t_o$ and different for $t > t_o$. Under these conditions one has two solutions

$$J^{(1)} = \sum_{1}^{n} A_i \phi_i^{(1)}(t) \qquad [10a]$$

$$J^{(2)} = \sum_{1}^{n} A_i \phi_i^{(2)}(t) \qquad [10b]$$

$$t_o < t < \infty$$

$$J^{(1)}(t) = J^{(2)}(t) \qquad 0 \leq t \leq t_o \qquad [10c]$$

The functions $\phi_i^{(1)}$ and $\phi_i^{(2)}$ in the interval $t_o < t < \infty$ are different because they correspond to different temperature-time functions, but the integration constants A_i are the same in both cases because the initial state of the system is the same (Fig. 4). The released charge as a function of time is given by

$$q^{(1)}(t) = \sum_{1}^{n} \int_t^\infty A_i \phi_i^{(1)}(t)\, dt \qquad [11a]$$

$$q^{(2)}(t) = \sum_{1}^{n} \int_t^\infty A_i \phi_i^{(2)}(t)\, dt \qquad [11b]$$

Charge invariance requires that

$$q^{(1)}(t) = q^{(2)}(t) = q(t), \quad 0 \leq t \leq t_o \qquad [12]$$

or

$$\sum_{1}^{n} A_i \int_t^\infty \phi_i^{(1)}(t)\, dt - \sum_{1}^{n} A_i \int_t^\infty \phi_i^{(2)}(t)\, dt = 0, \qquad 0 \leq t \leq t_o \qquad [13]$$

Since the A_i are arbitrary constants, it follows that

$$\int_t^\infty A_i \phi_i^{(1)}(t)\, dt = \int_t^\infty A_i \phi_i^{(2)}(t)\, dt = q_i(t), \quad 0 \leq t \leq t_o, \quad i = 1,2,\ldots n \qquad [14]$$

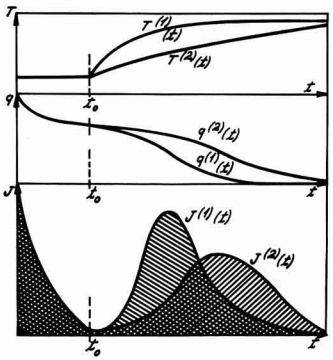

Fig. 4. Temperature, charge, and current for different heating rates.

independent of the particular temperature-time function $T(t)$, and

$$A_i\phi_i(t) = -dq_i/dt \qquad [15a]$$

$$q(t) = \sum_1^n q_i(t) \qquad [15b]$$

So far the two "test" functions $T^{(1)}$ and $T^{(2)}$ were arbitrary for $t \geq t_o$. Now consider a function $T^{(2)}$ which is constant for $t_o < t < \infty$. The corresponding isothermal relaxation current is given by a series of real exponentials with positive amplitudes. The integral over each term is also positive and equals $q_i(t)$ since relation [14] is valid for any function $T(t)$, in particular the function $T = \text{const}$. It follows that

$$M_i > q_i(t) \geq 0; \quad q_i(\infty) = 0 \qquad [16]$$

Since t_o was arbitrary, charge invariance applies to each particular solution $A_i\phi_i(t)$ in the whole discharge interval.

Any function subject to these conditions can be written as

$$q_i(t) = q_i(0) \exp [-F_i(t)] \qquad [17]$$

where F_i is a continuous function and $q_i(0)$ is positive. Writing $dF_i/dt = 1/\tau_i$ this gives

$$J(t) = \sum_1^n [q_i(0)/\tau_i(t)] \exp \left[-\int_o^t ds/\tau_i(s)\right] \qquad [18]$$

The integration constants A_i have been replaced by the initial charges $q_i(0)$.

The case of an infinite number of lumped parameters does not present any difficulty, the series in Eq. [18] then extending from 1 to infinity.

Relaxation times as state variables.—If the temperature is constant, equal to T_o, the isothermal current is

$$J = \sum_1^n [q_i(0)/\tau_i(T_o)] \exp [-t/\tau_i(T_o)] \qquad [19]$$

in accordance with Eq. [3] and [5], the τ_i being the relaxation times for the temperature T_o.

If the temperature is not constant, the functions τ_i might depend on the temperature and its derivatives and, in addition, explicitly on time. If τ_i depends explicitly on time, an instantaneous variation of T is followed by a delayed variation of τ_i. If τ_i depends on the heating and cooling rates, the same value of T gives different values of τ_i. Here we shall exclude these effects and assume that the τ_i depend only on the value of T itself. The functions τ_i of the nonisothermal system at any given temperature are then identical with the relaxation times of the isothermal system at the same temperature; since the latter are always positive, the τ_i are always positive and $dq_i/dt \leq 0$. With this assumption we postulate the existence of relaxation times as state variables. This is justified within the context of rate theory, as discussed below. It is, however, not a necessary consequence of the assumption that the system parameters, or network elements in the case of the electrical network analogue, are state parameters, because the coefficients $k_m(t)$ of the differential Eq. [7] in general contain the values of the system parameters at a given temperature and their temperature derivatives.

Network representation.—It is easy to find an electrical network model which represents Eq. [18] when all τ_i are positive. Consider the parallel arrangement of independent "relaxators" of Fig. 5. The differential equation for the short-circuit current in branch i is

$$dJ_i/dt + J_i [(1/R_iC_i) + d \ln (R_iC_i)/dt] = 0 \qquad [20]$$

which gives

$$J_i(t) = [q_i(0)/R_iC_i] \exp \left[-\int_o^t ds/R_iC_i\right] \qquad [21]$$

where $q_i(0)$ is the charge of the capacitor C_i at $t = 0$. Equation [21] becomes identical with Eq. [19] if one takes

$$\tau_i = R_iC_i \qquad [22]$$

The network elements R_i and C_i are always positive. Equation [22] can, therefore, be satisfied only if τ_i is positive. This condition is fulfilled according to the previous discussion. Therefore any system whose current is given by expression [19] with $\tau_i > 0$ can be represented by the network of Fig. 5. A more detailed discussion of network representations will be given in a subsequent paper. Here it might be mentioned in passing that any "impulsive" network (10) is charge-invariant. A charge-invariant system, whose polarization current contains a steady-state component, can therefore always be represented by an impulsive network connected in parallel with a pure resistance.

The two types of parameters appear in the equations only in the form of the product R_iC_i. Therefore short-circuit measurements do not allow one to discover whether both are temperature-dependent or only one of them, *i.e.*, R_i. The situation is different when an external voltage is applied. Consider a sample which has been polarized at temperature T_2 with the constant voltage U_o. At the end of the polarization period the total charge is $q_2 = U_oC_o(T_2) + U_o \sum_1^n C_i(T_2)$. Subsequently the temperature shall be reduced to T_1. The corresponding final charge is $q_1 = U_oC_o(T_1) + U_o \sum_1^n C_i(T_1)$. If the C's depend on temperature, $q_2 \neq q_1$, the charge difference $\Delta q = q_2 - q_1$ flows through the external circuit and a current results. A distinction must be made between the effects of a temperature dependence of C_o and of the C_i, $i \geq 1$. C_o, which rep-

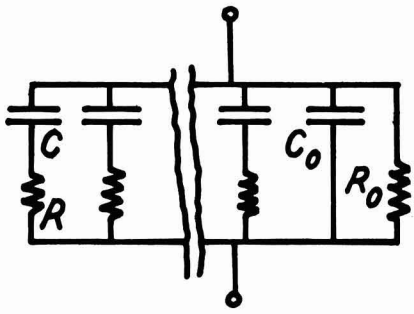

Fig. 5. Network representation

resents the high-frequency dielectric constant, is not connected in series with a resistive element. If it is a function of temperature, the corresponding current $U_o(dC_o/dT)dT/dt$ is proportional to the rate of temperature change, but it is an "in-phase" current. Like the "ohmic" current $U_oR_o(T)$ it becomes constant when the temperature becomes constant. The C_i, $i \geq 1$, are in series with resistive elements. Their temperature dependence is associated with an "out-of-phase" current which extends beyond the period during which the temperature changes with time, *i.e.*, a transient current. In our experiments the current was found to be independent of the rate of temperature change during cooling and became constant at the same time as temperature. Therefore within the precision of these experiments all capacitive elements remained constant and the temperature effect was due entirely to the dissipative elements.

Continuous Systems

Distribution function.—The transition to continuous systems is made by considering a dense distribution of infinitesimal elements each characterized by a relaxation time and an amplitude factor dq, the latter being the contribution of that system to the polarization charge. In the isothermal case one could associate dq directly with τ, writing $dq = (dq/d\tau)d\tau$, and thus obtain an integral of type [3]. When τ is a function of temperature, and thus implicitly of time, this procedure makes the spectrum time-dependent and would lead to a violation of charge invariance unless limiting conditions are introduced subsequently. The difficulty is avoided by introducing a time- and temperature-independent parameter U. The relaxation time is a function of both U and $T(t)$, while the amplitude factor is a function of U alone, *i.e.*

$$\tau = \tau[U,T(t)] \qquad [23a]$$

$$dq = (dq/dU)dU \qquad [23b]$$

Replacing in Eq. [18] $q_i(0)$ by $dq(U)$, τ_i by $\tau(U,T)$, and the series by an integral one obtains the integral transform

$$J(t) = \int_o^\infty \phi(t,U)\,\frac{dq}{dU}\,dU \qquad [24a]$$

$$\phi(t,U) = \frac{1}{\tau[U,T(t)]}\exp\left[-\int_o^t \frac{ds}{\tau[U,T(s)]}\right] \qquad [24b]$$

The condition of charge invariance is fulfilled because the amplitude factor dq/dU is independent of time and

$$\int_t^\infty \phi(t,U)\,dt = \exp\left[-\int_o^t \frac{ds}{\tau[U,T(s)]}\right] \qquad [25]$$

Equation [25] expresses the integral over the interval t to ∞ on the left side in terms of an integral over the interval 0 to t on the right side. The kernel itself is the integral of the differential equation

$$d\phi/dt + \phi/f(t) = 0 \qquad [26a]$$

$$1/f(t) = (1/\tau) + d\ln\tau \qquad [26b]$$

These relations generalize the corresponding relations [3]-[6]. A heuristic method of derivation could, therefore, start with Eq. [23], [24a], and [26a], with the additional conditions (a) that the differential Eq. [26a] for the kernel ϕ transforms into the isothermal Eq. [5] and (b) that ϕ is charge-invariant. These conditions give for $f(t)$ the relation [26b] and for ϕ the expression [24b].

Distribution parameter.—To get an explicit expression for ϕ one can use the formalism of rate theory (11) writing

$$\tau = (h/kT)\exp[F/RT] \qquad [27]$$

where F is the molar free energy increase for the activated system, R the gas constant, k the Boltzmann constant, h Planck's constant, and T the absolute temperature. Since $F = U - TS$, where U is the molar activation energy and S the entropy increase one has

$$\tau = \tau_o \exp U/RT \qquad [28]$$

with

$$\tau_o = (h/kT)\exp(-S/R) \qquad [29]$$

A distribution of relaxation times corresponds to a system of energy states with different activation energies and entropy increases. In the general case (12) one would have to introduce distributions for both U and S. The usual treatment considers, however, only a single distribution of energy levels. Paralleling this treatment we consider only a distribution of activation energies, identifying activation energy with the parameter U in Eq. [23] and taking a single value S, an average value.

One might object that Eq. [28] does not lead to a law of corresponding states as has been found by many authors. Such a law is obtained if the temperature dependence is the same for all values of τ, *i.e.*, $\tau = \tau_o U$. Here U is a dimensionless parameter, the temperature function $\tau_o(T)$ is usually assumed to be exponential. This alternative will, however, not be discussed in this paper.

It is worth noting that for a single relaxation time and uniform heating rate the system of Eq. [24] and [28] becomes identical with the function that has been used to describe current glow curves and thermoluminescence with monomolecular kinetics (13).

Model Distribution Function

Froehlich (14) has considered a model assuming a dilute solution of dipolar molecules in an amorphous solid, each molecule having two equilibrium positions with opposite dipole directions and equal energy in the ground level. He assumed the potential barrier between the two positions to have different heights equally distributed between two extreme values, or what is equivalent an equal distribution of the number of molecules over the energy interval. This gives a continuous distribution of energy levels with activation energies between a minimum value U_1 and a maximum value U_2 and a population of dipolar molecules $N(U)$ independent of U. Then $dq = eN_o dU/(U_2 - U_1)$ where N_o is the total number of molecules and e the electron charge. This expression can be generalized by abandoning the restriction $N(U) = \text{const}$ and writing

$$dq = neN_o U^{n-1}\,dU/(U_2^n - U_1^n) \qquad [30]$$

where $n \geq 1$ is a constant coefficient. This Eq. [30] is more general than the above model. It also applies for instance to the case where one has a number of charge carriers with equilibrium positions in potential wells separated by barriers of different heights. For $n = 1$ one has Froehlich's expression. Equation [30] satisfies the normalization condition $q = \int_{U_1}^{U_2} dq = eN_o$. Since from Eq. [28], $U = RT\ln\tau/\tau_o$, one has also

$$dq = \frac{neN_o(RT)^n}{U_2^n - U_1^n}\ln^{n-1}(\tau/\tau_o)\,d\ln(\tau/\tau_o) \qquad [31]$$

Substitution into Eq. [24] gives for $T = \text{constant}$

$$J = \frac{neN_o(RT)^n}{U_2^n - U_1^n}\int_{\tau_1}^{\tau_2} \frac{\exp[-t/\tau]}{\tau}\ln^{n-1}(\tau/\tau_o)\,d\ln(\tau/\tau_o) \qquad [32]$$

where

$$\tau_i = \tau_o \exp[U_i/RT] \qquad i = 1,2 \qquad [33]$$

The logarithmic term in Eq. [32] is slowly varying compared with the rest of the integrand. For an approximate evaluation of the integral this term will

be taken out of the integral, with that value of τ for which $\exp(-t/\tau) = 1/e$, *i.e.*, for $\tau = t$. This gives

$$J = \frac{neN_o(RT)^n}{U_2^n - U_1^n} \ln^{n-1}(t/\tau_o) \int_{\tau_1}^{\tau_2} \frac{\exp(-t/\tau)}{\tau} d\ln \tau/\tau_o \quad [34]$$

and after integration

$$J = \frac{neN_o(RT)^n}{U_2^n - U_1^n} \frac{\ln^{n-1}(t/\tau_o)}{t} [\exp(-t/\tau_2) - \exp(-t/\tau_1)] \quad [35]$$

This expression satisfies the condition of charge invariance. The factor in square brackets is approximately a "unit box" function, *i.e.*, it equals unity for $\tau_2 \geq t \geq \tau_1$ and 0 for t outside the interval. Therefore one has

$$q = \int_o^\infty J\,dt = \frac{neN_o(RT)^n}{U_2^n - U_1^n} \int_{\tau_1}^{\tau_2} \ln^{n-1}(t/\tau_o)\, d\ln(t/\tau_o) = eN_o \quad [36]$$

For $n = 1$ one obtains correctly Froehlich's formula

$$J = \frac{eN_oRT}{U_2 - U_1} \frac{[\exp(-t/\tau_2) - \exp(-t/\tau_1)]}{t} \quad [37]$$

To discuss Eq. [35] consider first the time dependence. According to what has been said about the square bracket term, the current at any temperature is given by

$$J = \begin{cases} 0 & t > \tau_2 \\ c(1/t)\ln^{n-1}(t/\tau_o) & \tau_2 > t > \tau_1 \\ 0 & \tau_2 > t \end{cases} \quad [38]$$

Within a limited interval of time J decreases approximately like $1/t$, while over a wider range the influence of the logarithmic factor makes J decrease with time somewhat slower than $1/t$. This behavior is in agreement with most experiments which give $J \sim (1/t^m)$ with m slightly less than 1.

Currents at different temperatures differ by a constant factor $(RT)^n$. To assure charge conservation, the increase in current amplitude must be compensated by a decrease in width of the interval $\tau_1 - \tau_2$, as is shown by Eq. [38]. This is again in qualitative agreement with experiment.

The temperature dependence of the current is certainly much stronger than would be given by a linear term, as in Eq. [37]. Therefore the exponent n must be considerably greater than unity, and the generalization $dq \sim U^{n-1}dU$ with $n > 1$ is in the right direction, although possibly an exponential increase would fit better the observed data. Since $dq = edN(U)$, one has also $N(U) \sim U^n$ and, instead of an equipartition of energy, one has a much higher occupation of states with high activation energy than with low activation energy. The power law, however, does not give the right increase; a function $N \sim \exp(cU)$ should give a better representation of the experimental situation.

Conclusions

The discussion has been in terms of electrets. Electret behavior is a general property of solid dielectrics, like dielectric absorption and dielectric loss, and caused by the same mechanism as these effects. Froehlich's theory and its generalization, as presented here, are charge-invariant and refer to dielectrics in general. The principle of charge invariance might not be rigorously valid in all cases, but in most is a good approximation. The conclusions of the present paper are, therefore, of interest to dielectric theory in general. Some consequences will be examined in following papers.

SYMBOLS

T = absolute temperature, °K
t = time, sec
J = current, amp
q = charge, coul
τ = relaxation time, sec.
ϕ = kernel of integral transform
R_i = resistance, ohms
C_i = capacitance, F
h = Plank's constant, J sec
R = gas constant, $J\ °K^{-1}\ mol^{-1}$
k = Boltzmann constant, $J\ °K^{-1}$
F = molar free energy, $J\ mol^{-1}$
S = entropy, $J\ °K^{-1}\ mol^{-1}$
U = molar activation energy, $J\ mol^{-1}$

Manuscript received Sept. 22, 1967; revised manuscript received Jan. 3, 1968. This paper was presented at the Electrets Symposium at the Chicago Meeting, Oct. 15-19, 1967, as Abstract 121.

Any discussion of this paper will appear in a Discussion Section to be published in the December 1968 JOURNAL.

REFERENCES

1. K. W. Wagner, *Elektrotechn. Z.*, **36**, 135, 163 (1915).
2. J. Ferry, "Viscoelastic Properties of Polymers," p. 201, John Wiley & Sons, Inc., New York (1961).
3. Cf. B. Gross, "Charge Storage in Solid Dielectrics," p. 86, Elsevier Publishing Co., Amsterdam (1964).
4. B. Gross and L. F. Denard *An. Brasil. Acad. Cienc.*, **14**, 349 (1942).
5. P. V. Murphy. Information Storage by Persistent Electric Polarization Systems, Report No. 1, June 1, 1963-Dec. 15, 1963, Panoramic Research Inc., Palo Alto, Calif. presented at the Symposium on Electrets, Chicago Meeting, Oct. 15-19, 1967; The Electrochem. Soc., Dielectrics and Insulation Division, Extended Abstracts J-2, Vol. 4, No. 2, p. 90.
6. B. Gross, Universidad Nacional de Tucuman (Argentina), *Revista* **A1**, 35 (1940); *An. Acad. Brasil Cienc.*, **17**, 219 (1945); *J. Chem. Phys.*, **17**, 866 (1949).
7. B. Gross. *Z. Phys.*, **107**, 217 (1937); *Phys. Rev.*, **57**, 57 (1940); **62**, 683 (1942).
8. B. Gross *An. Acad. Brasil. Cienc.*, **17**, 219 (1945); G. Wiseman and G. R. Feaster, *J. Chem. Phys.*, **3**, 521 (1957); M. M. Perlman and J. L. Meunier, *J. Appl. Phys.*, **36**, 420 (1965); D. E. Tilley, *ibid*, **38**, 2543 (1967).
9. B. Gross and W. Guttinger, *J. Appl. Sci. Res.*, **B16**, 189 (1956).
10. For physical representation of relaxation systems see for instance H. W. Bode, "Network Analysis and Feedback Amplifier Design," p. 177, D. Van Nostrand Co., New York (1945); B. Gross, *J. Polymer Sci.*, **20**, 371 (1956); *Nuovo Cimento*, Vol. 3, Serie X, Supplemento No. 2, p. 235 (1956).
11. W. Kauzman, *Rev. Mod. Phys.*, **14**, 1 (1942).
12. J. R. MacDonald, *J. Appl. Phys.*, **34**, 538 (1963).
13. C. Bucci and R. Fieschi, *Phys. Rev.*, **148**, 148 (1966).
14. H. Froehlich, "Theory of Dielectrics," p. 90, Oxford Clarendon Press (1949).

Electret Behavior and Ionic Thermal Currents in Alkali Halides

N. Januzzi

Physics Department, Faculdade de Ciencias, Rio Claro, Sao Paulo, Brazil

and S. Mascarenhas

Physics Department, Escola Engenharia, Sao Carlos, Sao Paulo, Brazil

ABSTRACT

The behavior of alkali-halide electrets of KCl/Sr and double doped KCl/Ca, OH is investigated by the glow peak discharge method of Fieschi, Bucci *et al.* (1) (ionic thermal conductivity method or ITC). In this case a complete analysis of the trapped polarization is possible quantitatively. The electret polarization is due to impurity vacancy dipoles. It is shown that the electret behavior in this case can be used as a very powerful tool to investigate the motion of defects in the solid matrix. As an application, the dipole diffusion to form higher aggregates is studied by a thermal annealing technique. By studying the variation of the electret released charge for various temperatures it is shown that trimers (3 dipole aggregates) are formed. The reaction is found to be of third order, and the activation energy for defect motion is (0.71 ev). The dipole relaxation frequency at 0°K is 10^{-13} sec^{-1}. All data agree very well with that obtained by other techniques and confirms the results of Dryden and Cook (2). In the case of double-doped systems, it is shown that the ITC method allows a quantitative determination of the solid-state reaction between OH and Ca. A correlation between F center formation by x-irradiation and electret behavior is also found, showing that the reaction is probably the precipitation of $Ca(OH)_2$ in the matrix leading to dipole destruction and quenching of the color center production. This is perhaps the only case in which the electret behavior is completely understood in a quantitative way, and, used as a tool, to obtain important solid-state parameters such as relaxation times, number of defects in the matrix, activation energies, and to investigate defect production and reactions in the solid state.

In a series of very complete and fundamental papers Fieschi Bucci *et al.* (1) established the foundations of the ITC (ionic thermal conductivity) method. The present paper is an application of their method using electret behavior and ITC as a tool to investigate solid-state problems. The electret trapped polarization arises in this case from the well-established presence of dipoles in the solid matrix. These dipoles are associated with impurity-vacancy complexes. In Fig. 1 this is indicated for the case of a fcc lattice such as that of KCl. It is seen that the addition of the divalent impurity (indicated by a double-charge in Fig. 1) such as Ca, Sr, Mg, Cd is associated with the presence of an additional positive ion vacancy to satisfy charge conservation in the matrix. This impurity may be added to the melt when the crystal is grown by techniques such as the Kyropoulus technique, or can be diffused into the material at temperatures near the melting point (3). Depending on the temperature and association energy the vacancy may be in a nearest neighbor position to the divalent impurity. In the case of the fcc lattice this will correspond to a dipole oriented in a general 110 position. Because of ionic diffusion this dipole can change its orientation. It is found that the reorientation is due mainly to positive ion mobility, or if we want, to vacancy jumps around the more or less fixed divalent impurity. To this process we can associate of course a thermal activation energy (related to the potential function seen by the vacancy in its neighborhood), a relaxation time, and eventually even an activation energy connected with the motion of the entire entity. In the physics of defects in solids this is a classical problem which has been extensively investigated (4). Other configurations of the IV (impurity vacancy complex) are also possible, in which the vacancy is at a next-neighbor distance (n^2 complex), or next-next-neighbor distance (n^3 complex), and these also have associated dipole moments, relaxation times and other corresponding parameters, and in some phenomena may play a prominent role. The presence of the IV complex has also been detected by lattice expansion effects (5), by the use of the photoelastic technique of color center investigation (6), by dielectric relaxation measurements (7), by magnetic resonance (8), by dielectric absorption measurements (9) as well as by internal friction measurements (10). The ITC technique is however the most powerful one in our opinion. It is also very straightforward experimentally. The detection limit for dipoles is surprisingly small, in some cases concentrations as low as 10^{15} dipoles/cm^3 can be detected.

The essential points related to the theoretical interpretation of the peaks have been discussed by Fieschi, Bucci *et al.* (1), and we will only summarize here the main results that are needed for the objectives of the present paper.

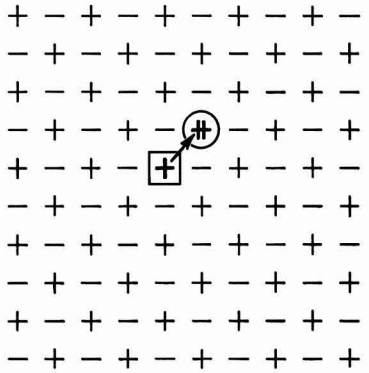

Fig. 1. Divalent impurity and associated positive ion-vacancy in a fcc alkali halide. The dipole moment (arrow) is along a (100) direction.

The electret polarization and depolarization by the glow peak obtained while heating the sample is conducted in the same way as first introduced by Gross in his now classical papers (11). In the case of the alkali-halides doped with divalent impurities, we know however that (*a*) by applying the polarization field we are orienting at the polarization temperature, T_p, a certain fraction of the IV dipoles in total number per unit volume N_d. If the temperature is high enough, we can suppose these dipoles to be rotating freely in the matrix. If the concentration is not too high, we can safely assume that these dipoles do not interact with each other. The relaxation time for dipole reorientation will be given by

$$\tau = \tau_o \exp E/kT \qquad [1]$$

(*b*) When we cool the electret under the applied field to a lower temperature T_1 the relaxation time may change drastically (see Eq. [1]), and the oriented dipole configuration and its associated polarization will be frozen in the matrix.

If we now switch off the external field, we shall be left with the frozen polarization due to the orientation of the IV dipoles. If we then warm the electret, the relaxation time of the dipoles will gradually decrease and a displacement current will be observed in the external circuit because of the polarization change. This current $i(t)$ is a function of temperature T and time t (we assume a constant heating rate) and is given by [see ref. (1)]

$$i(t) = N_d \frac{p^2 E_p}{3kT_p}\left[\tau_o \exp\left\{\frac{E}{kT}\right\}\right]^{-1} \times \exp\left(-\int_o^T \left[b\,\tau_o \exp\left\{\frac{E}{kT'}\right\}\right]^{-1} dT'\right) \qquad [2]$$

This follows directly from the unimolecular nature of the dipole orientation process. The factor 1/3 is due to the hypothesis of freely rotating dipoles of moment. As expected intuitively this $i(t)$ will present a maximum at a certain temperature T_m, the glow peak function being asymmetric in time (or temperature). The maximum peak position in temperature is related to the activation energy, E, heating rate, b, and relaxation time in the following way

$$T_m = \left\{\frac{bE\tau(T_m)}{k}\right\}^{1/2} \qquad [3]$$

It is very interesting to observe that the maximum peak position temperature is independent of the polarization temperature T_p and of the polarization field E_p. The activation energy can be obtained from the glow-peak in two independent ways. The easiest and most direct way is to calculate it from the initial rise in current. The low temperature tail of the band, at temperatures away from T_m, is given by

$$i(T) = i_o \exp(-E/kT) \qquad [4]$$

The other way to obtain E is by a global analysis of the whole band, which is much more difficult and requires a pure band form. That is, no overlapping bands may be present, so that Eq. [1] is valid during all of the charge release process.

When these conditions are satisfied we can apply the following relation

$$\ln\left[\int_t^\infty i(t')\,dt'\right] - \ln i\,(T) = \ln \tau_o + E/kT \qquad [5]$$

The equation above expresses the ln of the relaxation time $\tau(T)$ as a function of the observed glow in an integral form. By plotting the latter as a function of $1/T$ a straight line is obtained that furnishes directly the activation energy and τ_o. This process is more cumbersome because several graphical integrations of the band have to be performed. It is, however, independent of the heating rate. Bucci and Fieschi (1) have shown in the case of overlapping bands that the bands can be properly "cleaned" by a proper choice of the polarization temperature T_p, and by letting the lower temperature bands discharge and subsequently recooling to obtain the next band.

Finally, the total number of dipoles in the electret can also be found with good precision from the area of the band. At saturation the total polarization P_o is given by the following relation

$$P_o = N_d\,(1/3\,p^2 E_p)/kT_p \qquad [6]$$

Thus by measuring P_o from the underlying area of the band N_d the total number of dipoles per unit volume can be obtained, if their dipole moment is known. In the case of the IV complex this is known. E_p and T_p as above are the polarizing field and temperature.

Equation [6] above is important if we wish to investigate the variation of the number of dipoles associated with some particular phenomenon like a solid-state reaction or defect production that may be dependent on the dipole sources.

Experimental

The samples used were grown in our Laboratory at S. Carlos by the pulling or Kyropoulos technique from the melt. In the case of doped samples the impurity was added to the melt in the desired concentration. In some cases where necessary the direct analysis of the impurity in the solid was made by spectrophotometric or activation analysis techniques and will be described when appropriate. The samples were cleaved in thin plates of thickness approximately 1 mm and area of circa 1 cm^2 along a (100) plane. Aquadag or alcoholdag electrodes were painted to obtain good electrical contact with the electrodes. The field was applied to the sample in vacuum or in a controlled atmosphere of dry N_2, and the electrodes were held together by magnetic attraction so that no dielectric was present at the site where the temperature would be cycling. The current was measured with a Keithley 603 electrometer. The warming rate was kept constant and of the order of 0.1°K/sec, which was found to be the ideal rate for the quantitative and reproducible measurements obtained. Reproducibility for the currents and peaks was of the order of 5% or better. The activation energies could be measured to within 0.05 ev.

For the radiation damage of the samples to produce color centers, a 100 kv tungsten tube was used with proper filtration to ensure uniformity of defect production. The experimental sequence was the following. The sample was polarized at a desired temperature T_p for a certain time t_p (usually a few minutes) under a certain polarizing field E_p. The temperature was then lowered by pouring liquid nitrogen into the Dewar which contained the whole experimental assembly. After the crystal attained the lower temperature T_1 the field was switched off, and the crystal warmed at a constant rate. The current due to the dipole relaxation which appeared in the form of glow peaks was then continuously recorded as well as the temperature. For convenience two recorders were used. One a X-Y recorder for $i(T)$ and the other a recorder for the temperature as a function of time, so that the warming rate was directly observed during the experiments. The temperature was measured with an iron-constantan thermocouple situated in one of the electrodes. It is important in this work that the samples receive the proper thermal treatment. As shown in this paper the dipoles can aggregate to form dimers, trimers, or the divalent metal may precipitate in various sites like grain boundaries, dislocations, and other favorable places. It is then essential with an old sample, or a sample that is cleaved from a certain block which received no special thermal treatment, to

warm it to a temperature where the dipoles and the impurities will be dissolved properly in the matrix. This was done in an oven under controlled temperature and atmosphere conditions. The crystal was then quenched to room temperature or slowly cooled, depending on the type of experiment to be performed as will be described below. The optical measurements were made using a Beckman DK-2 double-beam automatic recording spectrophotometer in the range of 200 nm to 3μ.

Results

Dipole aggregation in KCl/Sr.—It was shown by Cook and Dryden using a dielectric loss method that the IV dipoles in KCl/Sr aggregated to form trimers. Because of this aggregation process the resulting trimer has a negligible dipole moment, and thus the total polarization in our samples should decrease with their formation. This should be a temperature dependent process because of the thermal activation energy involved in the diffusion mechanism. In our ITC measurements the total area under the glow corresponding to isolated dipoles should then diminish with the aggregation process. We thus measured the polarization P_o as a function of time t. We kept the samples at different temperatures T. This polarization aging diminished, as expected, with time, as is shown in the results of Fig. 2. The particular way in which we plotted our results is related to the equations of the association process that will be discussed below. The results of Fig. 2 were obtained by polarizing the crystal always at the same temperature T_p for the same polarization time t_p. After the desired thermal treatment the polarization P was measured under the same field for all experiments. The crystal was then taken to a constant-temperature oven for the required length of time (days, hours, or minutes, depending on the temperature). After this time a new ITC measurement was made and the sample returned to the oven to continue with the aging process at a constant temperature.

Ca *Precipitation with* OH *in* KCl.—The OH impurity is now one of the more important defects in the physics of alkali halides. Luty *et al.* (12), Feher *et al.* (13), and Kanzig *et al.* (14) studied important paraelectric, paraelastic, and cooling effects of the OH dipole in alkali halides. Kuhn and Luty were the first to explain the apparent paradoxical behavior of the electrical conductivity of some of these solids as a function of temperature, by assuming a solid state reaction between Ca and OH ions. The same argument was used by Ikeya to explain the absence of F center sensitization in Cd containing samples. In the present work we give direct experimental evidence for this reaction

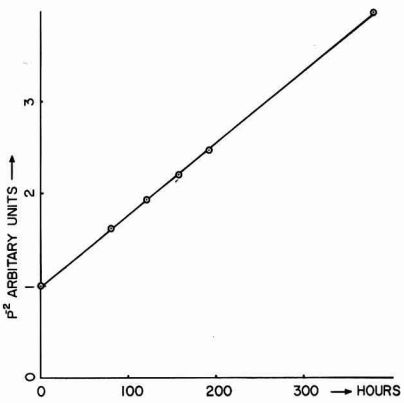

Fig. 2. Decay of polarization for a fixed temperature (293°K) as a function of time (KCl:Sr).

Table I. Results

Sample	$CaCl_2$(10^{-3}M)	KOH(10^{-3}M)	Polarization (arbitrary units)
A	1.0	2.0	0.2
B	1.0	1.0	20.0
C	1.0	0.5	40.0

using the electret behavior. For this, we doubly doped KCl with Ca and OH in different proportions. We then measured the ITC band corresponding to the Ca IV complexes as a function of their different concentrations. Results are shown in Table I.

It is seen that we used concentrations corresponding to partial $(OH)_2Ca$ formation and complete reaction stoichiometry. While it was possible to detect directly the total amount of Ca in the solid by chemical analysis, the presence of free Ca was inferred in the following indirect way: The OH ion has an electronic absorption band in the uv region of the spectrum when substitutionally dissolved in the alkali halide. This OH absorption was extensively studied by many workers (15), and its oscillator strength is well known. The OH ion also has a vibrational absorption band in the near infrared portion of the spectrum. The precipitation of OH by Ca destroys the electronic absorption, but the vibrational band is still present. By measuring in both regions of the spectrum, we were able thus to distinguish between "free" OH and the precipitated OH.

Discussion and Conclusions

Dipole aggregation in KCl/Sr.—The reaction for trimer formation is that of a third order reaction

$$\frac{dc}{dt} = -Kc^3 \qquad [7]$$

where c is the dipole concentration, t is the time, and K a proportionality rate parameter. The polarization P that is proportional to dipole concentration is then obtained as a function of time by integration of Eq. [7] above as

$$P^{-2} = P_o^{-2} + 2\,\alpha^2 Kt \qquad [8]$$

where α is a proportionality factor between P and the number of dipoles per unit volume, and P_o is the polarization immediately after thermal quenching. Following Cook and Dryden we assume the reaction is diffusion controlled and set

$$K = A_d \exp(-E_d/kT)$$

Using Eq. [7] with this value for K, we get

$$C^{-2} - C_o^{-2} = 2\,A_d t \exp(-E_d/kT)$$

We can now define a half-life $t_{1/2}$, for the reaction at the time where $C = C_{o/2}$. This is given by

$$t_{1/2} = \frac{3}{2\,C_o^2 A_d} \exp(E_d/kT) \qquad [9]$$

We can thus determine $t_{1/2}$ from Eq. [8]. That Eq. [8] is followed is shown by the results of Fig. 2. If we get $t_{1/2}$ as a function of temperature from Eq. [9], we can obtain the relevant quantities A and E_d. At the same time a new check of the whole model is provided. In Fig. 3 we show the results for several temperatures.

Our values for A_d and E_d and those determined by Cook and Dryden are in excellent agreement with each other.

The reaction is thus of third order, the process is diffusion controlled, and the electret polarization P and its quantitative analysis provided all the relevant conclusions in excellent agreement with other techniques.

Ca *precipitation with* OH *in* KCl.—It is clearly seen that polarization P increased from sample A to C, that

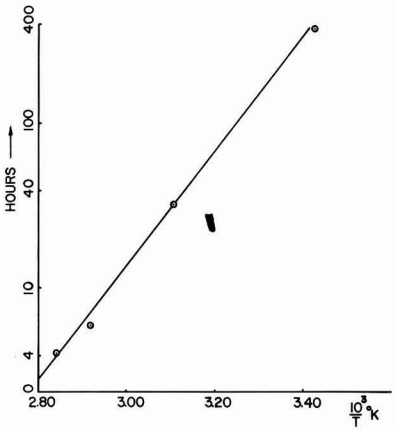

Fig. 3. Polarization half-life in hours as a function of the inverse of the absolute annealing temperature. Activation energy is 0.71 ev (KCl:Sr).

is, in the expected direction, if the $(OH)_2$ Ca compound stoichiometry is considered. In order to understand further and discuss this result we decided to make another experiment: It is known that the "free" Ca ion sensitizes F-center production. In a recent paper Ikeya (16) has shown in part that the presence of OH in Cd crystals hindered the F-center sensitization by precipation. We thus make an experimental analysis of the F-center growth curves and 100 kv x-ray irradiation for the different doubly doped samples. Ikeya showed that the square of the extrapolated optical density at zero time was proportional to the free Ca content in the samples. In order to discuss our results further we plotted this magnitude as a function of the electret polarization P as measured by the glow-peak technique

If the precipitation reaction was really being followed by the electret polarization, there should be a direct proportionality between the free Ca as measured by the F-center growth curves and P.

The results of the experiments are shown in Fig. 4. These results taken together with those of Table I

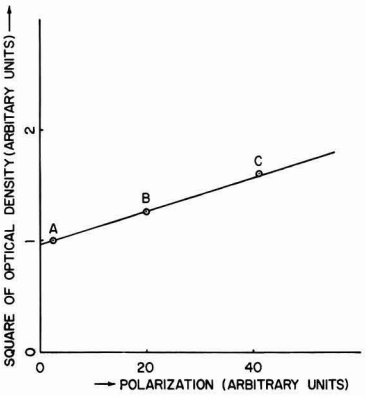

Fig. 4. Square of extrapolated optical density for the F band as a function of polarization for sample A (KCl + $1x10^{-3}$M $CaCl_2$ + $2x10^{-3}$M KOH); B ($1x10^{-3}$M $CaCl_2$ + $1x10^{-3}$M KOH); and C ($1x10^{-3}$M $CaCl_2$ + $0.5x10^{-3}$M KOH).

show that we have detected the defect reaction directly from the electret behavior.

We think this paper exemplifies that in the case of the alkali-halides the electret behavior is not only very well understood quantitatively but can even be used as a powerful tool to investigate solid-state physics and solid-state chemistry phenomena. We are now in the process of investigating new phenomena using alkali-halide electrets, such as: (*a*) action of an electric field to break dipole aggregates; (*b*), action of the internal electric field of the electret on defects like the F center; (*c*) presence of negative ion vacancy divalent negative-ion dipoles in alkali halides; and (*d*) investigation of electret behavior due to impurity-vacancy dipoles in other inorganic materials like ZnO and MgO.

We hope that this paper will encourage other investigators in the field of electrets to join efforts in this very promising area.

Acknowledgments

The authors are deeply grateful to Dr. C. Bucci and Dr. M. Ferreira de Souza for helpful and valuable discussions and experimental suggestions; to all our colleagues at S. Carlos and especially to Dr. G. Leal Ferreira for several discussions; to C. Bicegli, Sebastiao Pereira, Carlos Trombella, and Salvador Sanchez Vera for technical help, and to Bartyra de Oliveira for secretarial help during the preparation of this paper.

This work was done under ONR contract and partial support of C. N. Pq. and Fapesp.

Manuscript received Sept. 7, 1967; revised manuscript Dec. 6, 1967. This paper was presented at the Electrets Symposium at the Chicago Meeting, Oct. 15-19, 1967, as Abstract 123. Part of this work was done to fulfill the requirements for the Ph.D. degree of one of the Authors (N. J.) at the University, S. Paulo, S. Carlos.

Any discussion of this paper will appear in a Discussion Section to be published in the December 1968 JOURNAL.

REFERENCES

1. C. Bucci and R. Fieschi, *Phys. Rev. Letters*, **12**, 16 (1964); M. Beltrami, R. Capelletti, and R. Fieschi, *Phys. Letters*, **10**, 3 (1964); C. Bucci, R. Fieschi, and G. Guidi, *Phys. Rev.*, **148**, 816 (1966).
2. Dryden and Cook, *Proc. Phys. Soc.*, **80**, 479 (1962).
3. Milton Ferreira de Souza, Ph.D. Thesis, University Sao Paulo, Brazil (1966).
4. A. Lidiard, in Handbuch der Phyzik, Vol. XX, p. 246.
5. See for instance J. Schulman and D. Compton, Color Centers in Solids," Pergamon Press, New York.
6. Milton Ferreira de Souza and G. Leal Ferreira, *Bull. Am. Phys. Soc.*, **12**, 3,351 (1967).
7. R. W. Dreyfus, *Phys. Rev.*, **121**, 1675 (1961).
8. G. Watkins, *ibid.*, **113**, 91 (1958).
9. Y. Haven, *J. Chem. Phys.*, **21**, 171 (1953).
10. R. Dreyfus and R. Leibowitz, *Phys. Rev.*, **135**, A1413 (1964).
11. See for instance B. Gross and S. Denard, *Phys. Rev.*, **67**, 253 (1945).
12. H. Hartel and F. Luty, *Phys. Stat. Solidi.*, **12**, 347 (1965); U. Kuhn and F. Luty, *Solid State Comm.*, **2**, 281 (1964); B. Fritz, F. Luty, and J. Anger, *Z. Phys.*, **174**, 240 (1963).
13. G. Feher, I. Shepherd, and H. Shore, *Phys. Rev. Letters*, **16**, 500 (1966).
14. W. Kanzig, *J. Phys. Chem. Solids*, **23**, 479 (1962).
15. H. Etzel and D. Patterson, *Phys. Rev.*, **112**, 1113 (1958).
16. H. I. Keya and N. Itoh, *J. Phys. Soc. Japan*, **20**, 1284 (1965).

Studies on HF-Doped Ice Thermoelectrets

S. Mascarenhas

Physics Department, Escola Engenharia, Sao Carlos, Sao Paulo, Brazil

and C. Arguello[1]

Faculdade de Ciencias, Rio Claro, Sao Paulo, Brazil

ABSTRACT

Pure and doped ice thermoelectrets were prepared at different polarization temperatures (—10° to —135°C). Stored charge was then investigated by the glow peak method. A main band was observed at —50°C, with a total charge of 10^{-6} to 10^{-8} coulombs/cc depending on doping. The total charge released by the glow varied with the square root of HF concentration indicating that the OH^- and H_3O^+ ions are responsible for the effect. Space charge formation was also shown to be associated with the electret behavior by investigating the influence of sample thickness on the polarization and of the temperature of the glow peak maximum on polarization temperature.

In recent papers (1) Gellin and the present authors reported observations on the ice thermoelectret. Riehl and co-workers (2) also reported recently on the behavior of ice subjected to thermal changes under electric fields and claimed to have observed ferroelectric behavior in ice. Pinatti and Mascarenhas (3) described the behavior of ice crystals during growth from the melt and reported strong electrical effects. In the present work we report on the ice thermoelectret, using the glow peak discharge method, and demonstrate that the effect is strongly dependent on or related to the HF doping of the samples. The nature of the trapped polarization that is released during the thermal glow was investigated by the analysis of the variation of the charge with concentration of the dopant as well as by changing the thickness of the sample and the polarization temperature. In view of the claim for ferroelectric behavior of ice made by Riehl and collaborators this is a very important question to be decided. Our investigations on the Costa Ribeiro effect in ice and its possible importance for the explanation of atmospheric electricity also stimulated the present investigations.

Experimental

We have designed and constructed a special Dewar in which the ice single crystals were grown and the electret was prepared and measured. This is shown in Fig. 1. Initially, the bottom electrode E was positioned with the desired separation from the top electrode M by means of a ring stopper R, movable through the vacuum seal S. Both the bottom electrode E and the top one contained small Alnico magnets M so that the bottom one was maintained in position by magnetic attraction. This was a very convenient way of obtaining variable interelectrode distance and of avoiding any insulator in this part of the Dewar where the temperature would be cycling. The top electrode was the ground connection for the electrometer and the lower one was the high insulation electrode. The lead from E came out of the Dewar through a Teflon insulator I. V are vacuum connections. LS are leveling screws and W are windows through which the ice single crystal could be observed under polarized light with an optical system. Liquid nitrogen or any proper coolant was introduced inside the stainless steel tube T. The whole system was enclosed in a metal cylinder C. The liquid to be solidified (either pure water or HF solution) was initially placed between the two electrodes. At this time the ring-stopper would still be maintaining the proper electrode separation. A coolant was then introduced inside T causing solidification of the liquid. After complete solidification the ring R was raised. The quality of the single crystal was then ascertained with the polarized light system. In this way we were able to grow very good single crystals of thicknesses ranging from 0.5 to 2 mm. The current was measured with a Keithley 603 electrometer and a 10^9 ohm grid resistor. The electrodes were platinum or palladium covered and their area approximately 3 cm^2. What we call pure water in this paper is doubly distilled water from a quartz still of conductivity circa 10^{-6} mhos/cm. Nitrogen gas was introduced in the Dewar in order to maintain good thermal contact to the sample during the warm up and cooling.

Results

A typical experimental sequence would be as follows: The electric field E was applied to the sample

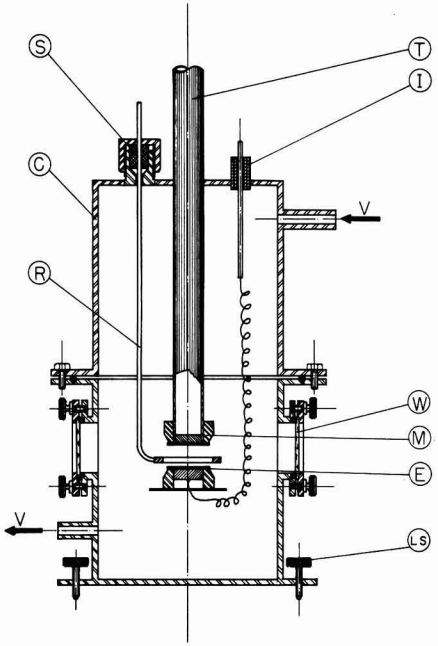

Fig. 1. Apparatus for single-crystal growth and electret preparation and measurement. T, stainless steel tube; I, Teflon insulator; S vacuum seal; C, external metal cylinder; R, ring-stopper; W, optical window; M, magnet; E, electrode (platinum or palladium); LS, levelling screws; V, vacuum outlets.

[1] Present address: University of Southern California, Los Angeles, California.

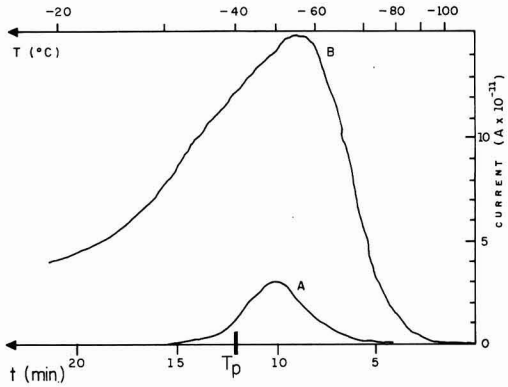

Fig. 2. Electrical glow-peaks due to charge release in the ice thermoelectret. A, pure ice; B, HF-doped ice.

for a specified time at the chosen polarization temperature *Tp*. The crystal was then cooled under the electric field to *circa* —100°C. The electric field was then switched off and the crystal warmed up to —10°C again. During the warm up the current was constantly monitored and both the temperature and the current were recorded on a X-Y recorder so that the glow peaks could be directly observed.

Immediately after formation the ice single crystal would present some charge, probably due to the Costa Ribeiro effect. When this charge had dissipated the external field was applied. The discharge of the electret under its own field to produce the glow peaks was first used by Gross (4). A very well-defined and reproducible discharge was observed here peaking at around —50°C, as is shown in Fig. 2. In the same figure the larger peak is connected with HF doping. After observing the discharge with pure water, we decided to investigate the possible influence of defects on the electret behavior, and also to look for possible ferroelectric behavior. We decided to dope the samples with HF. Much larger peaks were then observed with HF doped ice in concentrations ranging from 2.5×10^{-6} to 10^{-4}M. The total integrated charge under the glow peak is shown as a function of concentration in Table I.

One can see that the effect of doping is rather large and that the integrated charge may change by two orders of magnitude in the range of concentrations used. The polarization time *tp*, the polarization temperature *Tp*, the thickness and the applied voltage *Vp*, were kept constant in these experiments.

We have also investigated, due to reasons mentioned in the discussion section of this paper, the influence of the thickness of the sample on the total measured charge *Q* of the glow. The results shown in Fig. 5 were obtained for a constant field of 335 v/cm for all samples. The linear behavior of *Q* with thickness will help us to clarify the nature of the trapped charge.

Discussion

As is discussed below, in order to decide on the nature of the phenomenon, or more specifically on the nature of the trapped polarization of the ice thermoelectret the HF doping proved to be very important. It is known from previous theories on the physics of ice (5) that HF doping will change the concentration of d and l defects (Bjerrum defects) as well as the concentration of ionic states (OH^- and H_3O^+). From thermodynamic arguments it is expected that the d and l defects will change their concentration in a linear way with HF doping, while the ionic states will change with the square root of HF concentration. If we were dealing with orientation of dipoles which would be directly related to d and l defects our effect might be expected to depend on a linear way on HF doping.

Table I. Integrated charge under the glow peak

HF concentration	Q coul.
10^{-7}	6.0×10^{-8}
2.5×10^{-6}	3.5×10^{-7}
5.0×10^{-6}	7.2×10^{-7}
1.0×10^{-5}	8.5×10^{-7}
5.0×10^{-5}	10.5×10^{-7}
10^{-4}	1.75×10^{-6}

The results of Table I are plotted on a double logarithmic scale in Fig. 3. From it we clearly see a square root dependence was found. This indicates that probably we are dealing with an effect related to OH^- and H_3O^+ ionic carriers. This would tend to indicate that we are not dealing with a dipole orientation effect, or in fact, with any collective dipole effect that might even lead us to think of ferroelectric behavior. On the other hand, we are led to conclude that space-charge effects due to the motion of ionic carriers (specially the more mobile OH_3^+) may be the main cause of the electret behavior.

In order to investigate this point further we did one more experiment. It is known that space-charge glow-peaks do not present a constant peak-position temperature, but rather this is strongly dependent on the polarization temperature (6). Keeping the warming rate cycle reproducible, because this is known to affect slightly the peak-position, we obtained several electret glows by varying the polarization temperature from —88° to —26°C. We found large changes in the corresponding peak position as shown in Fig. 4. Again this indicates space-charge behavior.

Finally, the experiment described by Fig. 5, in which we found a linear dependence of the charge *Q* on thickness seems to us to rule out any possibility of uniform polarization and thus reinforces very strongly the case for space charge as the main cause for the electret behavior.

When we tried to apply the Fieschi and Bucci dipole model (6) to our results, applying their expression for the total charge, we calculated an absurd concentration of 10^{25} dipoles/cm^3, assuming a dipole moment of one Debye. The peaks also do not allow the determination of any single activation energy *E*.

We thus conclude that: the electret effect in ice is greatly enhanced by HF doping; the electret charge can be released by glow peaks around —50°C depending on the polarization temperature; the nature of the electret charge is related to space-charge effects; the nature of the space charge is connected to H_3O^+

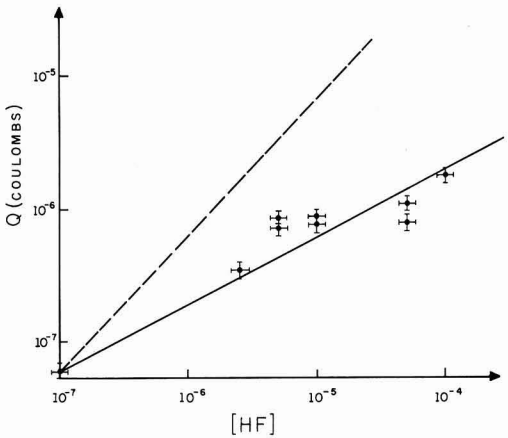

Fig. 3. Dependence of released charge *Q* on HF doping. A square root-dependence is found. The dashed line indicates a linear function (see text for discussion).

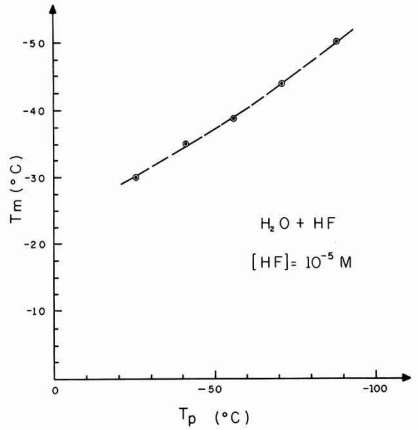

Fig. 4. Dependence of temperature of maximum peak position T_m on polarization temperature T_p for a HF doped sample (10^{-5}M).

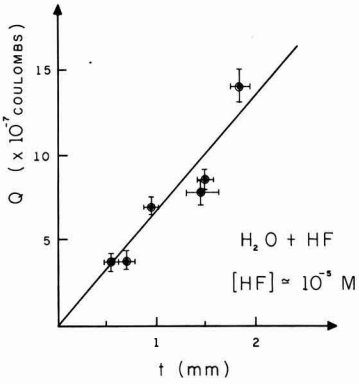

Fig. 5. Dependence of the released charge Q on the sample thickness t, indicating a space-charge effect.

and OH^- ionic states. We also found that a claim for ferroelectric behavior of ice (2) cannot be substantiated. Explanation of the present effects using dipoles would require an enormous number, indicating the absence of a collective effect.

It is our opinion that any claim for ferroelectricity would have to include a very careful study of the influence of sample thickness and possibly doping to check for possible space-charge effects.

Finally, we think that the present results may be important for the understanding of the Costa Ribeiro effect in ice (3), in which large currents and voltages appear during phase changes. The fields at the solid-liquid interface may be effective in producing space-charge effects similar to those described here. In this respect it is interesting to point out that a large change in the freezing potentials due to the Costa Ribeiro effect has in fact been reported in the literature (7). We are proceeding with our investigations, trying to detect directly the presence of the space charge by doping the ice with chemical dye indicators.

Manuscript received Sept. 7, 1967; revised manuscript received *ca.* Dec. 6, 1967. This paper was presented at the Electrets Symposium at the Chicago Meeting, Oct. 15-19, as Abstract 126. The work was done under ONR contract and partial support of C.N. Pq. and Fapesp.

Any discussion of this paper will appear in a Discussion Section to be published in the December 1968 JOURNAL

REFERENCES

1. H. Gellin and R. Stubbs, *J. Chem. Phys.*, **42,** 967 (1965); see also C. Arguello and S. Mascarenhas, *Bull. Am. Phys. Soc.*, **12,** 4, 558 (1967).
2. H. Engelhardt and N. Riel, *Phys. Letters*, **14,** 20 (1965); O. Dengel, U. Eckener, H. Plitz and N. Riel, **9,** 291 (1964).
3. D. Pinatti and S. Mascarenhas, *J. Appl. Phys.*, **38,** 2648 (1967).
4. B. Gross and S. Denard, *Phys. Rev.*, **67,** 253 (1945).
5. Granicher, Jaccard, Scherrer, and Steineman, *Discussions Faraday Soc.*, **23,** 50 (1957).
6. C. Bucci, R. Fieschi, and G. Guidi, *Phys. Rev.*, **148,** 816 (1966).
7. E. Workman and S. Reynolds, *ibid.*, **78,** 254 (1950).

Glow Peak Analysis of Pure and Doped Naphthalene Thermoelectret

M. Campos, G. Leal Ferreira, and S. Mascarenhas

Physics Department, Escola Engenharia, Sao Carlos, Sao Paulo, Brazil

ABSTRACT

Polarization current for pure and doped naphthalene thermoelectrets is investigated. The thermal depolarization of the electret is used as a technique to investigate trapped polarization. Doped crystals with alpha and beta naphtol present new independent peaks in addition to the pure matrix peaks. The peaks are analyzed quantitatively for total integrated charge and activation energy by the initial rise method. The OH vibrational band of the impurities was used as an optical probe to detect their presence in the solid. Charges trapped in the dielectric absorption process corrected for the released charge at the low-temperature depolarization, compare satisfactorily with the total integrated glow peak charge for both pure and doped samples. It was possible to differentiate between alpha and beta naphtol through the electret behavior using the glow peak position and activation energy of the peaks. The electret state is shown to be due to electronic carriers, trapped in a set or sets of exponentially distributed traps, as indicated by the at^n dependence of the polarization current on time.

Naphthalene is a very important example of a pure substance, an organic molecular semiconductor, exhibiting electret behavior. Naphthalene was first reported to present natural electret behavior by Costa Ribeiro (1) and Tavares (2). Baldus (3), and, later, Mascarenhas (4) also reported on its electret properties. Extensive photoconductivity studies on this substance were carried out by Tavares in a very in-

teresting series of papers (5). Its general semiconductivity properties were investigated by Pick (6) and Riehl (7). Mascarenhas and Freitas reported (8) anisotropic electrical properties of the material during phase changes. In many ways naphthalene is an excellent system for electret studies. It forms very good single crystals from the melt (9), it is easily orientable (10); it can be purified by several techniques such as zone melting, chromatography and sublimation (11); it has a very well-known electronic and molecular structure (12); and is a known electronic organic semiconductor (13). The conduction mechanism in the dark is still somewhat obscure, but this is a general question still to be solved for most molecular solids, where it is very difficult to distinguish among tunneling, hopping, or a trap-controlled mechanism (14). In this work we make an analysis of the electret state in oriented naphthalene crystals by the glow peak technique. For the first time, to our knowledge, controlled doping is introduced in an organic semiconductor electret system and independent glows obtained due to the specific dopant. Furthermore, the presence of the dopant can be monitored by optical analysis. For this purpose we availed ourselves of the presence of a very well-defined and prominent vibrational absorption band of OH radicals in the dopant, in our case alpha and beta naphthol.

Experimental

Single crystal plates were grown by the Tavares (2) technique from double sublimed C. P. naphthalene. From a large plate, analyzed by polarized light, good single crystal areas were chosen and cut. The samples all had the same orientation, that of the cleavage plane in the plane of the plate. The samples were polished to an optical finish with alcohol. We used crystals of approximately 0.5 mm thickness and areas varying from 4 to 9 cm^2. In the case of the doped samples, alpha or beta naphthol were added to the melt, and the presence of the dopant was ascertained from optical analysis in a Beckman DK 2 automatic spectrophotometer. These substances present an absorption band in the near infrared due to the presence of an OH radical, as shown in Fig. 1. The spectrum of pure naphthalene is also shown for comparison.

The crystals were painted with conducting silver on both faces. One one of the faces a guard ring was used. This is essential because of the high specific bulk resistance of naphthalene. Spurious or undesirable surface effects are thus avoided.

A special system was built for preparing the electret and for the measurement of the release of charge. This permitted the measurement of conductivity, electret preparation, glow peak investigations, and dielectric absorption measurements at variable or constant

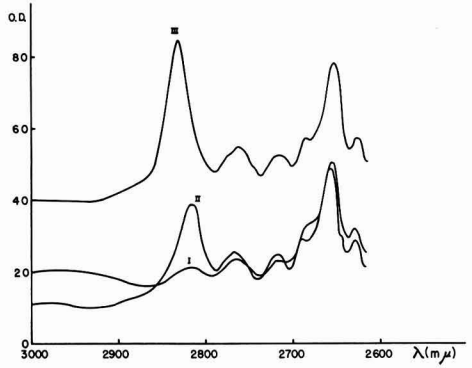

Fig. 1. Optical absorption of pure naphthalene, (curve I); doped with alpha naphthol, (curve II); and doped with beta naphthol (curve III).

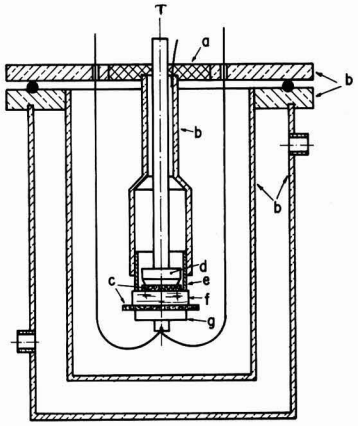

Fig. 2. System for electret production and measurements: a, Teflon insulation; b, brass walls; c, graphite electrodes; d, magnets for electrode assembly; e, guard ring; f, crystal (see text).

temperature in a vacuum or in a controlled atmosphere (Fig. 2).

The crystal (f) was placed between two graphite electrodes and the guard ring. The electrodes and the crystal were held together by the attraction of two small magnets (d) and (g). The guard ring was connected to an outer metal tube insulated by Teflon on the top plate of the system (see Fig. 2). The top central electrode was grounded, and the guard ring and the lower measuring electrode were insulated practically at the same potential, so that surface currents were negligible. The whole assembly was shielded by a metal case. An outer jacket (b) allowed water circulation from a precision Haake thermostat. The temperature of the sample was maintained constant to within 0.2°C during polarization. A liquid coolant could be introduced into tube T and the crystal brought to a low temperature. The temperature was measured by a properly insulated thermocouple placed in the lower electrode which also served as a lead for the electrometer. Electrical measurements were made using a Cary 31 vibrating reed electrometer with a 10^{11} ohm resistor. The current was recorded with a Brown potentiometer. Dry nitrogen gas was used inside the inner container to avoid sublimation of the samples and insure good thermal conductivity.

The measurements comprised the following three steps: (a) During polarization, the exponential current decay was recorded as a function of time at a chosen temperature, T_P, until it approached a constant value. (b) While maintaining the field, the sample was cooled to a lower temperature, T_1. Then the field was removed, and the depolarization current recorded as a function of time. (c) Finally, the crystal was heated at a constant rate, and this depolarization current recorded. The whole sequence was very reproducible, and it was found that the proper stabilization of the polarization temperature to 0.2° was essential for this purpose.

Results

We usually performed the whole sequence decribed above after previous warming of fresh samples to 60°C to empty all traps and release all accumulated charges due to growth, polishing, and handling. Results for the polarization current for pure naphthalene are shown in Fig. 3. Typical depolarization behavior for two different temperatures is also shown. The polarization current approached a constant current asymptotically under the applied field, and in the case of depolarization the current decayed to zero under no field. Similar results were found for the doped samples and are discussed below in more detail. Samples were then warmed under a constant rate. Very prominent

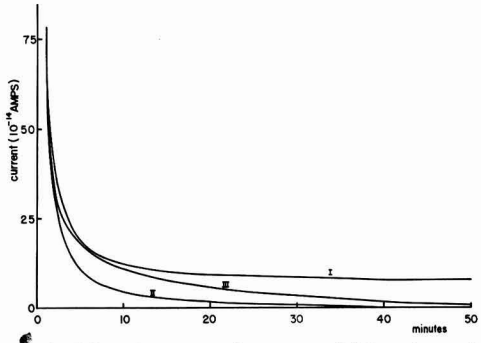

Fig. 3. Polarization current for pure naphthalene (curve I: 305°K); depolarization current at 305°K (curve II), and 280°K curve III).

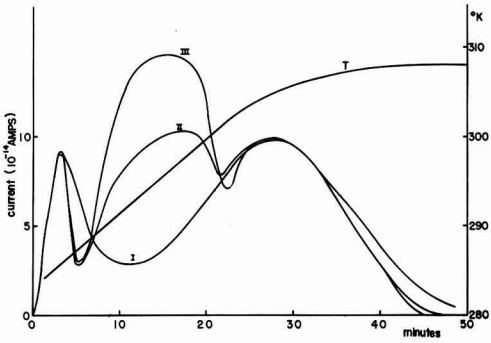

Fig. 4. Glow peaks obtained with pure naphthalene (I), doped with alpha-naphthol (II), and doped with beta-naphthol (III). Also shown is temperature T as a function of time during warm-up.

peaks were found for all samples. Figure 4 shows glow peaks obtained for both pure and doped samples. It is seen that the pure matrix peaks are present in the doped samples and that a new peak appears at an intermediate temperature. This peak was found to depend on the presence of the dopant.

Discussion

With the quantitative results of the polarization, depolarization, and glow peaks in our possession, we can now proceed to a quantitative analysis of the electret behavior. As a first step we should try to understand, at least partially, the polarization mechanism. To do this the data were analyzed in a log plot of the total current minus the constant final direct current *vs.* time j to investigate the dielectric absorption current. From this figure two straight lines are obtained. The total charge Q_p trapped in the dielectric via the dielectric absorption mechanism can also be determined.

From the lower temperature depolarization current as a function of time (Fig. 3) a value for the charge Q_d released from the dielectric at this temperature can be found. Finally, from the glow peak curves the total integrated charge Q_g that was released from the dielectric during warm up is calculated. Table I shows the values of Q_p, Q_d and Q_g for pure naphthalene. Within the experimental errors common for this type of experiment (order of 5-10%) the relation

$$Q_g = Q_p - Q_d$$

is satisfied. A similar analysis was done for the doped samples. The polarization behavior of these samples showed the same general behavior as that of the pure

Table I. Charges due to impurities

Kv/cm	Type	Q_p 10^{-10} coul.	Q_D 10^{-10} coul.	Q_G 10^{-10} coul.	Q_t 10^{-10} coul.
1.08	doped with α naphthol	1.24	0.96	0.23	1.19
0.54	doped with β naphthol	1.08	0.81	0.31	1.12
1.08	pure	6.24	5.07	1.06	6.13

samples. Again depolarization currents at the low temperature and the glow peak allowed us to obtain Q_p, Q_d, and Q_g. These magnitudes are shown in Table I. The glow peaks were also analyzed to determine the activation energy in the following way: If the internal field is approximately constant for temperatures well away from the maximum peak position, the initial rise method may be applied to determine a trap depth. In this case the current, at the initial rise of the peak, is given by

$$i = i_0 \exp -E/kT$$

This analysis was applied to the main pure naphthalene band (peaking at 308°K) and consistent and reproducible values of the activation energy obtained. Good results were also obtained for the impurity peaks of alpha and beta naphthol. Experimental difficulties prevented a proper analysis of the lower temperature pure naphthalene peak. We hope to do this in the near future. The activation energies found were reproducible to within 0.05 ev. Since the field is not constant during the glow, especially near the maximum, other methods will have to be used to analyze the peak for trapping cross section, activation energy, and other parameters. The complete analysis of the functional form of the peak depends on a model for the trapped polarization of the electret and the way in which the internal field varies with time.

It is interesting to observe that the alpha and beta naphthol maximum temperatures are slightly different, and that the activation energies for the corresponding glow peaks are also different. This shows the sensitivity of the glow discharge method of analysis of the electret. The results above can be summarized in the following way:

1. The naphthalene thermoelectret can be analyzed very conveniently by the glow peak technique. Two bands are present for the range of temperatures studied, the main band being situated at 308°K.

2. Activation energies can be obtained consistently from the glow by an initial rise method of analysis. The total charge associated with the glows is of the order of 10^{-10} coulombs for fields of the order of 1 kv/cm. The activation energy for the main band is 0.75 ev, the same as that found for the thermal activation energy of the conductivity itself.

3. Controlled doping of the naphthalene thermoelectret with alpha and beta naphthol resulted in the appearance of independent peaks for each impurity. The total charge under the new glow was found to add to the dielectric absorption and to be of the same order of magnitude as that of the pure naphthalene main band for concentrations of 10^{-2} molecules of impurity per molecules of naphthalene in the melt. The presence of the impurity in the matrix was monitored by the vibrational absorption band of the OH radical of the naphthol. No oscillator strength is available for this band so the concentration cannot be quoted. The activation energies for both peaks were measured and found to be noticeably different (Table II). This indicates that the method may constitute in the future a very sensitive technique for the investigation of impurities in solids.

We would like now to present some possible inferences from the above results. It seems that in the present case the electret behavior cannot be ascribed to dipoles or ions, but rather to electron or hole carriers trapped in defects or impurity levels in the solid. Considering a charge per unit volume of 10^{-11}

Table II. Activation energies (in ev)

Pure	Doped with α naphthol	Doped with β naphthol
0.75	0.65	0.47

coulombs/cm in our electret samples about 10^8 to 10^9 carriers/cm^3 are associated with the effect. This exceedingly small number points out the following: (a) the enormous sensitivity of the glow peak analysis of the electret to detect defects or impurities, compared to other methods used in physics like E.P.R., optical analysis or electrical conductivity; only luminescence effects can probably be compared with the present technique; (b) that practically any way of purifying the matrix will be useless, because no purification method is available for this range of concentration. Besides, the number of structural or thermodynamical defects in the solid is probably much larger than the above number. Thus an essential and perhaps unique way to proceed with investigations of this type is to dope the solid in a controlled manner, as we have done.

From the results presented here one cannot decide whether electrons or holes are the predominant mechanism. Nothing can be said concerning the nature of the trapping levels introduced by alpha or beta naphthol. New experiments, in which selective filling of electron and hole trap is possible, are now being carried out (15). With this new technique we hope to clear up the latter questions. To measure the concentration of the dopants in the solid a determination of the oscillator strength of the optical absorption of the OH ion is necessary.

Finally, using Tavares' data on natural naphthalene electrets, it was shown that these samples also followed the same polarization behavior as the thermoelectret. It is perhaps appropriate to point out that similar (at^n) behavior was found for ice electrets (16), carnauba wax electrets (17), our pure and doped naphthalene thermoelectrets and, as mentioned above, for natural electrets (10) obtained from the Costa Ribeiro effect. In the case of naphthalene, this tends to show that the same traps or sets of traps are involved in both phenomena. The anisotropy of the thermoelectret could then be expected, in view of the anisotropy of the Costa Ribeiro effect as found by Mascarenhas and Freitas (8). This is also being investigated in our laboratory.

This problem brings into discussion the question of the mobility of the carriers in naphthalene. Our samples showed the same activation energy for conductivity as that found by Riehl. Since we found the definite presence of trapping centers as revealed by the polarization and glow peak behavior of the electret, it would seem that the mobility is also trap-controlled. The fact that the thermal activation energy for the conductivity coincided with the glow peak activation energy for the case of pure naphthalene (0.75 ev) is in agreement with the above observation. Finally the possible space-charge nature of the phenomenon is being investigated

Acknowledgments

The authors would like to thank Carlos Biscegli, S. Bastos Pereira, Carlos Trombella, and S. Sanchez Vera of the technical staff of our Laboratory. Special thanks are due to Professor Milton Ferreira de Souza for extensive discussions and experimental suggestions. Thanks are also due to Bartyra de Oliveira for secretarial help on the present paper.

This work was done under ONR contract and partial support of C.N. Pq. and Fapesp.

Manuscript received Sept. 7, 1967; revised manuscript received Dec. 7, 1967. This paper was presented at the Chicago Meeting, Oct. 15-19, 1967, as Abstract 127.

Any discussion of this paper will appear in a Discussion Section to be published in the December 1968 JOURNAL

REFERENCES

1. J. C. Ribeiro, Thesis, University of Brazil (1945); see also *An. Brazil. Acad. Ci.*, **22**, 325 (1950).
2. A. D. Tavares, *An. Acad. Brasil. Ci.*, **25**, 53 (1953); **25**, 357 (1953); see also A. D. Tavares and H. Marques da Fonseca, **37**, 201 (1965).
3. W. Baldus, *Z. Angew. Phys.*, **6**, 481 (1954).
4. S. Mascarenhas, *An. Acad. Brazil. Ci.*, **31**, 395 (1959).
5. A. D. Tavares, Thesis, University of Rio de Janeiro (1960); see also Boletim de Física, August 1953.
6. H. Pick and W. Wissman, *Z. Physik*, **138**, 436 (1954).
7. N. Riehl, *Ann. Phys.*, **20**, 93 (1957).
8. S. Mascarenhas and L. G. Freitas, *J. Appl. Phys.*, **31**, 1685 (1960).
9. A. D. Tavares and H. Marques da Fonseca, *An. Acad. Braz. Ci.*, **37**, 201 (1965).
10. F. Lipsett, *Can. J. Phys.*, **35**, 284 (1957).
11. H. Inokuchi and H. Akamatu, "Solid State Physics," Vol. 12, Seitz and Turnbull, Editors, Academic Press, New York.
12. S. Abrams, J. Robertson, and J. White, *Acta Cryst.*, **2**, 233 (1949).
13. S. Glarum, *J. Phys. Chem. Solids*, **24**, 1577 (1963).
14. D. Gibbons and Spear, *ibid.*, **27**, 1917 (1966).
15. F. S. Sinencio, S. Mascarenhas, and B. Royce, *Bull. Am. Phys. Soc.*, **12**, 1048, (1967).
16. H. Gellin, *J. Chem. Phys.*, **42**, 967 (1965).
17. R. Gerson and J. Rhorbaugh, *ibid.*, **23**, 2381 (1955)).

Effect of Low Pressure on Surface Charge of Electrets

Robert A. Draughn and Avery Catlin

Department of Materials Science, School of Engineering and Applied Science, University of Virginia, Charlottesville, Virginia

ABSTRACT

Electrets prepared from Mylar and a polystyrene material were exposed to low pressure. The effective surface charge of the electrets decreased as the pressure was lowered. It is proposed that the charge decrease is due to either desorption of charge sources from the electret surfaces or spark breakdown on the electret surface.

When electrets are exposed to pressures less than atmospheric, the magnitude of the effective surface charge is reduced. Previous investigators (1-3) have suggested that this effect is due to neutralization of a portion of the surface charge by ions formed by spark breakdown in the air gap between the electret surface and adjacent electrodes. This paper presents experimental evidence which shows that this is not a suitable explanation for the observed charge decrease. The data show that the charge decrease is due to either

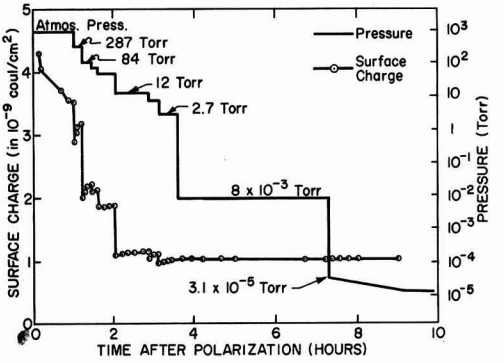

Fig. 1. Relationship of effective surface charge and pressure of surrounding air. Forming field: 140 kv/cm for 30 sec at 23°C.

desorption of ions from the electret surface or spark breakdown on the electret surface.

Experimental

The electret materials used in this study were a commercially obtained polystyrene material[1] and Mylar.[2] Infrared, x-ray, and chemical analysis of the polystyrene material showed it to be polystyrene containing 10% by weight TiO_2. The polystyrene sheet was 5 x 10^{-2} cm thick and the Mylar thickness either 2.6 x 10^{-2} cm or 1.3 x 10^{-2} cm. The dielectric constants, measured at 1 kc were: polystyrene, 3.2; Mylar, 3.3.

The electrets were formed by positioning the specimens between guarded machined brass electrodes of 20 cm^2 area and applying a voltage of 5-7 kv across the electrodes. Most of the electrets were prepared by applying the high field for 30 sec at room temperature (23°, ±1°C) and room relative humidity (25%, ±3%).

The movable electrode of the dissectible capacitor used to measure the effective surface charge was of machined brass with a surface area of 5 cm^2. Surface charge measurements were made both at reduced pressures and at atmospheric pressure following exposure of the electret to reduced pressure.

All specimens were stored with their surfaces exposed to the environment, *i.e.*, in the unshielded condition.

Results and Discussion

Figure 1 shows the behavior of the effective surface charge when a polystyrene electret was formed at atmospheric pressure, then exposed to low pressure. The charge measurements were made at the pressures indicated. The dissectible capacitor arrangement employed allowed the specimen to be stored between measurements with both of its surfaces freely exposed to the vacuum. During storage, the measuring electrode was positioned 5 cm above the electret surface. All specimens formed at atmospheric pressure exhibited a homocharge which was maintained throughout the period of observation. The data shown are taken from the negatively charged side of the electret. For graphic clarity, all data are shown as positive numbers. All effects reported in this paper were observed for both surfaces of the electrets.

As is shown in Fig. 1, the effective surface charge (Q) of the electret decreased as the pressure was lowered. Below 2.7 Torr, no further changes of Q occurred as the pressure was lowered to a minimum of 2 x 10^{-5} Torr.

Following each sudden drop in the magnitude of Q, the charge partially recovers. The recovery results from the response of the internal polarization to a decrease in the internal field of the electret. The removal of a portion of the surface charge at low pressures causes a reduction in the internal field of the electret thereby allowing a partial decay of the internal polarization. Since the contribution of internal polarization to effective surface charge is opopsite in sign to the real charge on the electret surface, the decay of internal polarization appears as a growth of effective surface charge. The response of internal polarization to changes in internal field has been treated phenomenologically by other authors (4-6). A theory of dielectric aftereffect (7, 8) has been applied to the polarization decrease by one of the present authors (9).

There are two apparent explanations for the drop in Q as a function of pressure. The drops could be due to neutralization of surface charge by ions produced by spark breakdown of the air in the vicinity of the electret. This breakdown could occur in the gap between the measuring electrode and the electret surface or it could possibly occur on the electret surface between regions having different charge intensity. Also, desorption of ions from the electret surface could produce the observed effects.

For experiments in which the dissectible capacitor is used to measure Q at reduced pressure (as in Fig. 1), the occurrence of spark breakdown between the electret surface and the measuring electrode seems quite feasible. However, the following analysis of the experimental conditions shows that such sparking probably does not occur.

Figure 2 compares a plot of the voltage between the measuring electrode and the electret surface with the voltage required to initiate spark breakdown. The external voltage of the electret was calculated using the expression (3, 10)

$$E_1 = \frac{-Q_1}{\epsilon_1\left[\frac{\epsilon(d_1\epsilon_2 + d_2\epsilon_1)}{\epsilon_1\epsilon_2 L} + 1\right]}$$

where: E_1 = field between the electret surface and the movable induction electrode of the dissectible capacitor (in volts/m); Q_1 = effective surface charge of the electret (in coul/m^2); d_1 = distance between the electret surface and the induction electrode (in m); d_2 = distance between the electret surface and the stationary electrode (in m). d_2 is taken as 0.01 cm in this calculation; L = thickness of electret (in m); ϵ = permittivity of the electret material (in coul²/Newton-m), ϵ_1, ϵ_2 = permittivities of the media adjacent to the electret surfaces. In these experiments, $\epsilon_1 = \epsilon_2 = \epsilon_0$, where ϵ_0 is the permittivity of free space.

The voltage (V_1) between the electret surface and the induction electrode is given by

$$V_1 = E_1 d_1$$

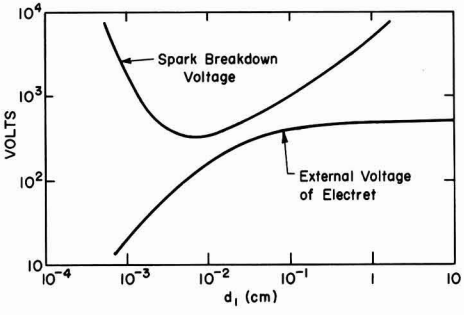

Fig. 2. Comparison of external voltage of electret and voltage required to initiate spark breakdown. Closest approach of the curves occurs at d_1 = 2 x 10^{-2} cm where the difference between voltage required to initiate spark breakdown and electret voltage is 200v.

[1] Cadillac Plastics and Chemical Company, Detroit, Michigan.
[2] Mylar is a registered trademark of E. I. du Pont de Nemours & Company.

The value of Q is taken from the large charge drop (Q decreasing from 3.2 x 10^{-9} coul/cm^2 to 2.0 x 10^{-9} coul/cm^2) of Fig. 1. The spark voltage curve is taken from the literature (11) with the assumption that the observed drop in Q occurred at the minimum pressure of 84 Torr. As Fig. 2 shows, the spark breakdown voltage curve and the electret voltage curve do not intersect for any value of d_1. Thus no breakdown could occur to produce the observed charge drop. This same analysis was applied to many charge-pressure conditions at which Q drops were observed, and it was found that the spark voltage curve and the electret voltage curve never intersected.

Another series of experiments showed that the effective surface charge of Mylar and polystyrene electrets decreased with decreasing pressure when the electrets were positioned in the vacuum bell jar in such a way that the distance between the electret surfaces and any conductor ranged from 4.5 to 40 cm. With these separation distances, the external electret field which could act to produce spark breakdown was quite small. The electrets were evacuated to a given pressure, then returned to atmospheric pressure, where the effective surface charge was measured. The charge measurements were made at atmospheric pressure in order to insure that breakdown could not occur during the measurement. Even though the possibility of spark breakdown between the electret surface and a nearby conductor was eliminated in these experiments, the effective surface charge still decreased as a function of pressure. The charge decreased slightly as the pressure was lowered from atmospheric and underwent a large decrease in the pressure range of 1-10 Torr.

The occurrence of spark breakdown between an electret surface and nearby metal depends on the pressure of the surrounding air, the length of the available discharge path, and the magnitude of the external electric field of the electret. The external field in turn depends on the magnitude of the effective surface charge, according to expression [1]. The data shown in Fig. 3 show that the occurrence of the charge drops do not depend on the magnitude of the external field of the electret. These data were obtained from a polystyrene electret formed by application of 140 kv/cm for 4 hr at 105°C. These forming conditions produce a large internal polarization of the electret. On removal of the forming field, the effective surface charge (Q) of the unshielded electret initially increased due to relaxation of the internal polarization. When Q equalled 4.6 x 10^{-9} coul/cm^2, the electret was evacuated to 43 Torr and then returned to atmospheric pressure. Measurement of Q at atmospheric pressure showed that the evacuation had caused a charge drop. Q resumed its slow increase in magnitude as the electret was held in room atmosphere with its surfaces exposed. When Q had grown to 4.7 x 10^{-9} coul/cm^2, the bell jar containing the electret was evacuated to 41 Torr, again returned to atmospheric pressure and Q measured. It was found that the charge had not been affected by the second evacuation. The process was repeated as Q continued to increase, and no further reduction of the charge was observed until the electret was evacuated to 26 Torr. Evacuation to 26 Torr produced the second charge drop shown in Fig. 3. The process was then continued to lower pressures. If the charge drop on the initial evacuation was due to spark breakdown between the electret surface and nearby conductors, then another charge drop should have occurred on the second evacuation where the external field of the electret was slightly higher and the pressure slightly lower. The fact that no further charge drop was observed until the pressure was lowered to 26 Torr, even though the external field of the electret was continuously increasing, appears to support an ion desorption mechanism for the charge drops. If a desorption mechanism is active, then Q should not drop on the second evacuation because the initial evacuation would desorb all ions which could be desorbed in that pressure range. According to this theory, further ion desorption did not occur until the pressure was reduced to 26 Torr.

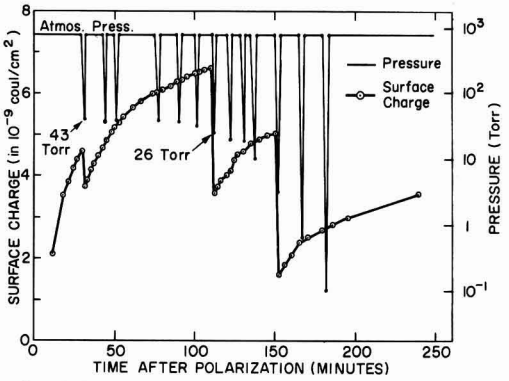

Fig. 3. Effect of reduced pressure on effective surface charge of polystyrene electret.

It would be expected that the forming conditions employed for electrets of this paper would produce an uneven distribution of surface charge, thus the charge decreases might be due to spark breakdown between regions of different charge intensity on the electret surface. However, an uneven distribution of surface charge would provide a continuous distribution of possible spark distances, thus for the electret of Fig. 3, for pressures between 43 and 26 Torr, there should exist some distance for which the potential would be sufficient to initiate spark breakdown and thereby cause charge drops. The absence of any indication of charge decrease between the pressures where large charge drops are observed apparently opposes spark breakdown along the electret surface as the source of the charge drops.

Figure 4 depicts the behavior of the effective surface charge when electrets are exposed to gases other than air. Both Mylar and polystyrene electrets were formed in room atmosphere and placed in oxygen, nitrogen, and helium at atmospheric pressure. The results for polystyrene electrets are shown in Fig. 4. The surface charge of Mylar electrets behaved similarly. Exposure of the electrets to oxygen and nitrogen caused small drops in Q, and exposure to helium caused a more drastic charge decrease. When the electrets were rapidly evacuated to 10^{-2} Torr, the charge dropped further. The potential required to initiate spark breakdown in these gases is less than that required in air. The sparking potential is significantly lower in helium, where for a distance of 10^{-2} cm sparking will occur at a potential of 170v, while in air at atmospheric pressure, 900v are required (11). In view of this, spark

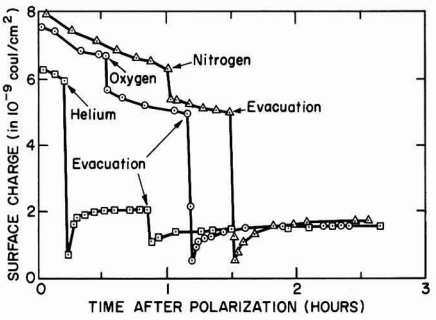

Fig. 4. Effect of oxygen, nitrogen, and helium on effective surface charge of polystyrene electrets.

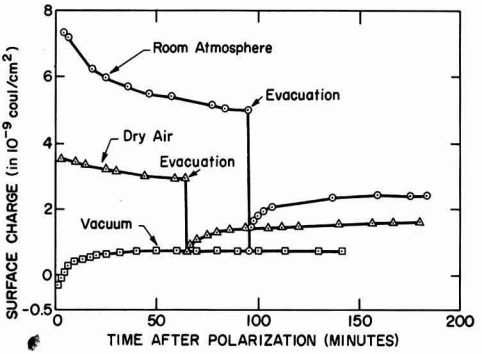

Fig. 5. Effective surface charge of polystyrene electrets formed in various environments. Forming field: 140 kv/cm for 30 sec at 23°C.

breakdown on the electret surface might account for the initial charge drops of Fig. 4. However, spark breakdown by itself does not adequately explain the later drops in surface charge. One of the authors has proposed a theory of ion desorption to account for the drops in surface charge when electrets are exposed to reduced pressure (9). According to this theory, it appears that ion desorption is a significant contributor to the second charge drops of Fig. 4.

That oxygen, nitrogen, and water are primary sources of electret surface charge is shown by the data of Fig. 5. Here is shown the effective surface charge of polystyrene electrets formed in room atmosphere, dry air, and a vacuum of 2×10^{-5} Torr. Since the charge is less for the electret formed and stored in dry air than for the electret formed and stored at 23% relative humidity, water vapor must be a significant source of the surface charge. Similarly, the low (in fact initially negative) value of charge for the vacuum formed electret shows that the components of air are major sources of surface charge.

Summary

Experiments reported in this paper yielded the following results:

1. The magnitudes of external fields of the electrets studied are not sufficient to initiate spark breakdown.
2. The occurrence of charge drops does not depend on the distance between the electret surface and nearby conductors.
3. The charge drops are not controlled by the magnitude of the effective surface charge (and hence the external field) of the electret.
4. Charge decreases occur at atmospheric pressure in environments other than air.
5. Oxygen, nitrogen, and water are primary sources of electret surface charge.

The results lead to the conclusion that the decrease in effective surface charge observed when electrets are exposed to low pressure is not the result of spark breakdown between the electret surface and nearby conductors. The data indicate that the charge drops are due to ion desorption. However, the experiments do not definitely distinguish between the mechanisms of ion desorption and spark breakdown on the electret surface as sources of the charge drops. There are apparently no previously reported studies of conditions present in the experiments of this paper, *i.e.*, the room temperature exposure to reduced pressure of a polymer having a significant concentration of gaseous ions on its surfaces. In view of this lack of available information, further investigations are required in order to show the relative importance of the surface breakdown and desorption processes in causing the observed charge decrease.

Acknowledgment

This work was supported by the National Institute of Dental Research, Grant DE-2111-02.

Manuscript received Sept. 8, 1967; revised manuscript received Dec. 18, 1967. This paper was presented at the Electrets Symposium at the Chicago Meeting; Oct. 15-19, 1967, as Abstract 135.

Any discussion of this paper will appear in a Discussion Section to be published in the December 1968 JOURNAL.

REFERENCES

1. G. E. Shepherd and J. D. Stranathan, *Phys. Rev.* **60**, 360 (1941).
2. J. W. Wild and J. D. Stranathan, *J. Chem. Phys.*, **27**, 1055 (1957).
3. A. N. Gubkin and G. I. Skanavi, *Sov. Phys.—Solid State*, **3**, 215 (1961).
4. G. G. Wiseman and G. R. Feaster, *J. Chem. Phys.*, **26**, 521 (1957).
5. M. M. Perlman, *J. Appl. Phys.*, **31**, 356 (1960).
6. M. M. Perlman and J. L. Meunier, *ibid.*, **36**, 420 (1965).
7. D. Kuhlmann, *Z. Physik.*, **124**, 468 (1947).
8. D. Kuhlmann, G. Masing, and J. Raffelsieper, *Z. Metallkde.*, **40**, 241 (1948).
9. R. A. Draughn, Doctoral thesis, University of Virginia (1968).
10. A. N. Gubkin, *Sov. Phys.—Tech. Phys.*, **2**, 1813 (1957).
11. "Tabellen der Elektronenphysik, Ionenphysik, and Ubermikroskopie," M. von Ardenne, Berlin: VEB Deutscher Verlag der Wissenschaften (1956).

Measurement of Quantum Efficiencies of Eu^{3+}-Activated Phosphors Using Excitation to Selected Eu^{3+}-Levels

A. Bril, G. Blasse, and J. A. A. Bertens

Philips Research Laboratories, N. V. Philips' Gloeilampenfabrieken, Eindhoven-Netherlands

ABSTRACT

A method to determine the efficiency of the red Eu^{3+}-fluorescence of phosphor powders using excitation of the $^5D_1$-, $^5D_2$-, and $^5L_7$-levels is described. These efficiencies were compared with those found with short-wave ultraviolet excitation, in order to study the transfer of the absorbed energy to the europium ion.

The quantum efficiency of a fluorescent substance is generally defined as the ratio of the number of emitted quanta to the number of absorbed exciting quanta, while the radiant efficiency (energy-conversion efficiency) is defined as the ratio of the corresponding radiant powers. The measurement of quantum efficiency is simple in principle but sometimes rather difficult in practice (1, 2)! One of the difficulties in measurement of efficiencies of powders is the determination of the absorption of the exciting radiation. Phosphors such as are used in fluorescent lamps gives the least difficulties because they have both a high light output and a high absorption in the host lattice or in the activators (2). This means that small spurious absorptions (*e.g.*, absorptions in contaminations which do not give rise to fluorescence) play only a minor role. Problems arise when activator absorptions are low in comparison with absorptions of the host or of contaminations. This is the case in the rare earth activated phosphors when they are excited in the narrow energy levels of the rare earth ions themselves.

In this paper a method is described for the measurement of efficiencies of Eu^{3+}-activated phosphor powders when excited in the $^5D_1$-, $^5D_2$-, and $^5L_7$-levels (see Fig. 1) which are very narrow (about 10 cm^{-1}) and for which the absorption is only some per cent. (The absorption at the $^5D_3$-level is generally too weak, in accordance with the selection rules, for the determination of the efficiency.) It is of interest to determine these efficiencies for phosphors which have a low efficiency under short-wave u.v.- and cathode-ray excitation to see where the exciting energy is lost. Excitation at the $^5D_0$-level has not been considered because fluorescence and absorption cannot be easily separated in the case of powders. Moreover, the absorption at the $^5D_0$-level is very weak. Measurements of this type with selective excitation at Eu^{3+}-levels have been performed for liquids (Eu-chelates) by Dawson, Kropp, and Windsor (3).

Apparatus and Method

The experiments are carried out by use of a Perkin-Elmer grating spectrophotometer model 13G, which we modified slightly and used in single beam mode. The Nernst filament with mirror was replaced by a tungsten-iodine lamp in combination with a quartz lens, so that more energy was obtained in the short wavelength region. A Bausch and Lomb grating, blazed at 500 nm and with 600 grooves/mm, was used.

The phosphor was placed behind the exit slit (see Fig. 2), so that it was irradiated monochromatically. To reduce stray light to a still lower level a Schott VG 12 filter was placed in the exciting beam, to absorb energy in the longer wavelength region.

Two measurements were carried out for each Eu^{3+}-absorption region of every phosphor:

1. The excitation spectrum. The fluorescent radiation emitted by the phosphor was collected and measured as a function of the exciting wavelength with a photomultiplier tube (EMI, Type 9558 Q), in front of which a filter was placed (4 mm Schott OG 5) which transmitted only the orange and red fluorescent energy while absorbing the exciting energy. A curve of the type given in Fig. 3a was then obtained.

2. The diffuse reflection spectrum. In this measurement only one thing was different from the previous measurement: The OG 5 filter is replaced by a VG 12 filter, which transmitted only the exciting energy and absorbed the fluorescence. Everything else remained the same (lamp curent, photomultiplier voltage, *etc.*). Then the absorption curve as a function of wavelength was obtained, as shown in Fig. 3b.

The width of the peaks in the excitation spectrum are found to be equal to the corresponding peaks in the reflection spectrum. We have described earlier (2) that for powder phosphors the angular distribution of the reflected radiation is the same as that of the fluorescence (nearly Lambertian distribution).

As has been said in the introduction, the radiant efficiency is the ratio of the emitted power and the power absorbed from the exciting radiation. The emitted power is determined by the maximum ordinate U_{em} of the peak in the excitation spectrum with two corrections: (*i*) The transmission τ_{OG5} of the filter used is not unity and moreover it varies as a function of the wavelength of the emission. (*ii*) The response $G(\lambda)$ of the photomultiplier, given in $\mu a/\mu w$, varies as a function of wavelength. Therefore the total emitted power is

$$E = U_{em}\frac{\int_{em}\rho(\lambda)\,d\lambda}{\int_{em}\rho(\lambda)\,G(\lambda)\,\tau_{OG5}(\lambda)\,d\lambda}$$

where $\rho(\lambda)\,d\lambda$ is the relative emitted power in a region $d\lambda$ at wavelength λ, derived from the spectral energy distribution curve. The integration has to be extended over the total spectral region of the emission.

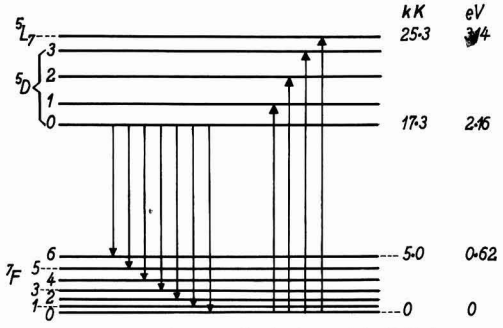

Fig. 1. Part of the energy level scheme of the Eu^{3+}-ion

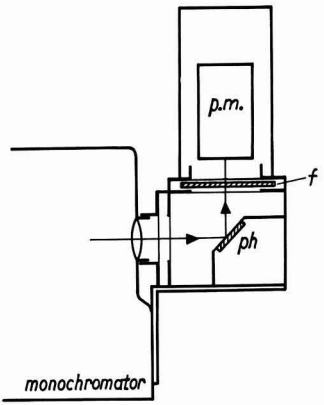

Fig. 2. Schematic diagram of experimental arrangement: p.m., photomultiplier; ph, phosphor; and f, filters.

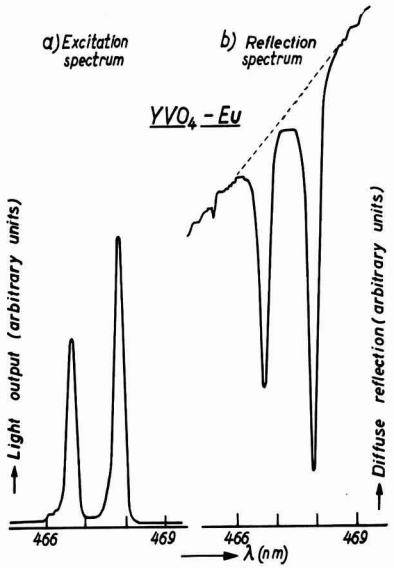

Fig. 3. Relative light output of Eu^{3+}- emission (curve a) and diffuse reflection (curve b) as a function of wavelength for YVO_4-Eu. For curve b the zero line is suppressed (the absorption peak has a depth of about 13%).

The radiant energy absorbed from the excited beam is determined by the peak height U_{abs} of the diffuse reflection spectrum, corrected in a similar way for (*i*) the transmission $\tau_{VG\,12}$ of the filter used, and (*ii*) for the response G of the photomultiplier in the excitation region. Because the width of the excitation peak is only a few angstrom units, we can take here the transmission and response at the peak wavelength λ_{exc}. Thus the absorbed power is proportional to

$$A = U_{abs}/G(\lambda_{exc}) \cdot \tau_{VG\,12}$$

The radiant efficiency η is then determined by

$$\eta = \frac{E}{A} = \frac{U_{em} \cdot \tau_{VG12} \cdot G(\lambda_{exc}) \cdot \int_{em} \rho(\lambda)\, d\lambda}{U_{abs} \cdot \int_{em} \rho(\lambda)\, G(\lambda)\, \tau_{OG5}(\lambda)\, d\lambda}$$

The quantum efficiency q is found by multiplying the radiant efficiency with

$$q/\eta = \frac{\int_{em} \lambda\rho(\lambda)\, d\lambda}{\lambda_{exc} \int_{em} \rho(\lambda) d\lambda}$$

being the ratio of the energy of the exciting and the emitted quanta. The response of the photomultiplier was determined by comparing its output with that of a photocell calibrated by the National Physical Laboratory in Teddington (England). The spectral energy distributions for most phosphors were measured up to $\lambda \approx 720$ nm. Those of Gd_2O_3-Eu and YVO_4-Eu were measured up to 900 nm. We found that the intensities of the $^5D_0 \rightarrow {}^7F_5$ and $^5D_0 \rightarrow {}^7F_6$ lines located in this region were negligible, in accordance with theoretical considerations of Ofelt (4). Therefore we ignored these lines in the case of the other phosphors, too.

The error in this type of measurement will be of the order of 25%. This large error is caused by the very low value of the absorption, as has been already mentioned in the introduction.

Results and Discussion

When exciting in the $^5D_2$ (λ = 465 nm) and $^5D_1$ (λ = 535 nm) Eu^{3+}-levels quantum efficiencies of about 100% were measured for Gd_2O_3-Eu, Y_2O_3-Eu, and YVO_4-Eu with the method described in the previous section. This is in agreement with the high efficiency figures found for these phosphors when excited with cathode rays or short wave u.v. radiation (quantum efficiency q = 70%) (5). For YVO_4-Eu the spectral energy distributions were measured for excitation with λ = 525 nm, λ = 465 nm, λ = 395 nm and for short wave u.v. radiation (λ = 254 nm). No differences between these distributions were found, within the limits of experimental accuracy.

It is assumed that this is valid for all phosphors. The same correction (see previous section) is applied in determining the radiant efficiencies for different excitations. The emission peaks in the regions near 595, 610-620, and 700 nm are all taken into account.

There are other phosphors which have a lower quantum efficiency for short wave u.v. excitation, *e.g.* $Y_{0.8}Eu_{0.2}Al_3B_4O_{12}$ with q = 35%. When excited in the selected Eu^{3+}-levels, however, $Y_{0.8}Eu_{0.2}Al_3B_4O_{12}$ and even $EuAl_3B_4O_{12}$ have a quantum efficiency near 100%.

In the phosphors mentioned above and many others evidently practically no radiationless processes occur from the $^5D_1$ and $^5D_2$ levels.

Excitation in the $^5L_7$-level (λ = 395 nm) gives also quantum efficiencies near 100% in many cases: $YAl_3B_4O_{12}$-Eu, Gd_2O_3-Eu, YPO_4-Eu, $YNbO_4$-Eu. However, difficulties arise when the $^5L_7$-absorption is superimposed on the host lattice absorption or a tail of this absorption, as is the case in substances like YVO_4-Eu, Y_2WO_6-Eu, and Gd_2WO_6-Eu (see the survey spectrum of Y_2WO_6-Eu in Fig. 4. This curve has not been used for the calculation of the efficiency; for that purpose higher resolved spectra with suppressed zero line are determined as given in Fig. 3). If we take as absorption the area of the narrow absorption peak as is done for the $^5D_2$ and $^5D_1$ absorption (see Fig. 3, the area under the dashed line), apparent efficiencies of about 200% are obtained. Since there is no reason to expect quantum efficiencies higher than 100%, our method seems not to work, if the rare earth absorption coincides with the host lattice absorption. This can be explained at least partly by the fact that the procedure used is not valid in cases where there is considerable absorption in the host lattice: To determine U_{abs} of the narrow peak the dashed line, connecting the host lattice reflection at both sides of this peak, is considered as a separation between activator absorption (narrow band) and host lattice absorption. However, following common absorption rules, in the presence of additional absorption, the host lattice cannot absorb as many photons as would be the case without it. Hence the activator absorption, as has been determined in this way, is underestimated leading to quantum efficiency figures which are too high.

An interesting case is the comparison of the efficiencies of Gd_2WO_6-Eu and Y_2WO_6-Eu. We found for

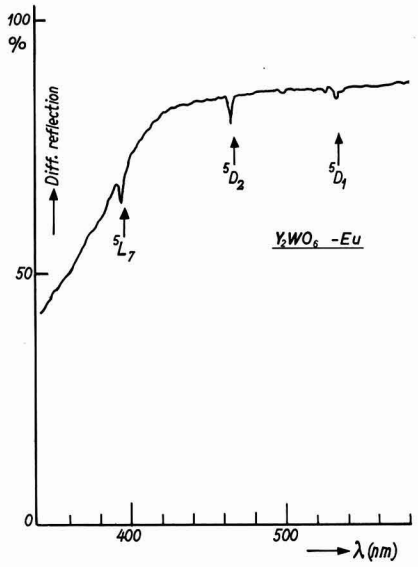

Fig. 4. Reflection spectrum of Y_2WO_6-Eu (survey spectrum with low resolving power).

both phosphors quantum efficiency values near 100%, when they are excited in the selected $^5D_2$ and $^5D_1$-levels. When excited in the broad u.v. excitation band Y_2WO_6-Eu is a reasonably efficient phosphor (q = 55%), while Gd_2WO_6-Eu is not (q = 10%). These results are in agreement with our earlier given explanation concerning the different energy transfer efficiency from the host lattice to the Eu^{3+} centers (7). The transfer from the tungstate group to the Eu^{3+}-ion is efficient, if the angle Eu-O-W is about 180° as is the case in Y_2WO_6-Eu, whereas it is not efficient when this angle is 90° as in Gd_2WO_6-Eu. Our measurements confirm this difference in energy transfer efficiency, since both phosphors show efficiencies near 100%, when the Eu^{3+} ions are directly excited in the selected $^5D_2$ and $^5D_1$ levels.

The difference between the results of Dawson, Kropp, and Windsor (2) for Eu-chelates and ours for oxides is that we generally find no increase of efficiency from the $^5L_7$- to lower excitation levels, whereas they do find such an increase. Apparently the population of the $^5D_0$-level from the higher levels is not much different in our phosphors.

Acknowledgments

The authors wish to express their thanks to the Reviewer of this Journal for suggesting an explanation for the apparent efficiencies higher than 100%. Further they are greatly indebted to Dr. W. L. Wanmaker and Mr. J. Broos for the preparation of some of the phosphors and to Dr. W. C. Nieuwpoort for stimulating discussions.

Manuscript received Aug. 3, 1967; revised manuscript received Oct. 16, 1967.

Any discussion of this paper will appear in a Discussion Section to be published in the December 1968 JOURNAL.

REFERENCES

1. M. H. Bhaumik and C. L. Telk, *J. Opt. Soc. Am.*, **54**, 1211 (1964).
2. A. Bril and W. Hoekstra, *Philips Research Reports*, **16**, 356, (1961).
3. W. R. Dawson and J. L. Kropp, *J. Opt. Soc. Am.*, **55**, 822 (1965); W. R. Dawson, J. L. Kropp, and M. W. Windsor, *ibid.*, **45**, 2410 (1966).
4. G. S. Ofelt, *J. Chem. Phys.*, **37**, 511 (1962).
5. A. Bril and W. L. Wanmaker, *This Journal*, **111**, 1363 (1964), **112**, 111 (1965); A. K. Levine and F. C. Palilla, *Appl. Phys. Letters*, **5**, 118 (1964); F. C. Palilla, A. K. Levine, and M. Rinkevics, *This Journal*, **112**, 776 (1965).
6. G. Blasse, *J. Chem. Phys.*, **46**, 2583 (1967).
7. G. Blasse and A. Bril, *ibid.*, **45**, 2350 (1966); G. Blasse, *ibid.*, **45**, 2356 (1966).

Kinetics of Hydrolysis of Single Crystal CaF_2 from 1000° to 1120°C

D. R. Messier[1]

Argonne National Laboratory, Argonne, Illinois

ABSTRACT

The kinetics of the reaction $CaF_2(s) + H_2O(g) = CaO(s) + 2HF(g)$ were determined on single crystal CaF_2 specimens by a gravimetric technique in the temperature range from 1000° to 1120°C at water vapor partial pressures from 1 to 20 Torr. Paralinear rate behavior was observed; *i.e.*, the reaction rate, which is initially parabolic, eventually becomes linear. The parabolic and linear rates were both found to be dependent on the partial pressure of water vapor. Activation energy values of 63.6 and 38.4 kcal/mole, respectively, were obtained for the parabolic and linear reaction periods. The complexity of the reaction mechanism prohibits assigning the activation energy values to specific processes.

A literature survey reveals considerable interest in the role of oxygen and hydroxyl ion impurities in producing optical effects in calcium fluoride (1-6). Bontinck (1) reported the only measurements which have been made on the kinetics of the hydrolysis of CaF_2. He showed that the net reaction responsible for the rapid oxidation of CaF_2 in air at high temperatures is

$$CaF_2(s) + H_2O(g) = CaO(s) + 2HF(g)$$

Bontinck's measurements were made on powder specimens in air containing a low but unspecified partial pressure of water vapor. The present measurements were undertaken to provide kinetic data on single crystal specimens in atmospheres containing known partial pressures of water vapor.

[1] At the time the experimental work was done, the writer was Graduate Research Assistant in the Inorganic Materials Research Division, Lawrence Radiation Laboratory and in the Department of Mineral Technology, University of California at Berkeley. He is now Assistant Ceramic Engineer, Metallurgy Division, Argonne National Laboratory, Argonne, Illinois.

Experimental Procedure

Specimens were fabricated from single crystal CaF_2 (Harshaw Chemical Company). Specimen blanks in the form of thin plates were made by cleaving the crystals along parallel [111] planes. The blanks were then diamond-sawed parallel to [110] and [112] planes to form square plates. The plates were ground to their final dimensions in a slurry of 600 mesh silicon carbide and water. Although CaF_2 reacts readily with water vapor at elevated temperatures, it is unreactive with water at room temperature. The approximate dimensions of the specimens were 9 x 9 x 2 mm. The dimensions of each specimen were determined to within 0.01 mm with a micrometer.

The kinetics of the hydrolysis reaction were determined by following the weight loss of a specimen as a function of time. The quartz spring weight-loss apparatus that was used is described elsewhere (7).

A run was initiated by heating a specimen to the desired reaction temperature in flowing, dry argon. The reaction was started by introducing water vapor at the desired partial pressure. A gas flow rate of 400 cc/min was used for all of the runs. At the end of a run the atmosphere was again changed to dry argon and the furnace power was shut off.

Results

Figure 1 is a schematic representation of a typical section from a quenched, reacted specimen. The outer region, labeled zone 1, contained precipitate particles of uniform size and concentration in a transparent matrix. Zone 2 represents the fluorescent region shown by Adler and Kveta (2) to contain dissolved oxygen. Zone 3 contains unreacted CaF_2. Under no circumstances was a single phase product layer observed.

X-ray diffraction patterns showed that the precipitate was CaO. Although $Ca(OH)_2$ is another possible reaction product (4), none was observed.

Figure 2 shows the results of all but two of the reaction runs. The latter duplicate two of the runs shown, and were omitted for the sake of clarity. Figure 2 illustrates the typical paralinear rate behavior that obtained in every run.

Figure 3 shows plots of weight-loss *vs.* the square root of time for the initial period assuming that a parabolic rate law applies. Although data from four runs at high water vapor pressures were arbitrarily selected for Fig. 3, the fit was equally good for all of the data.

Table I contains the rate data for runs made at various water vapor partial pressures in the temperature range from 1000° to 1120°C. The parabolic rates, R_p, were obtained from the slopes of plots of weight loss *vs.* the square root of time. The linear rates, R_l, were calculated from the slopes of the linear portions of the weight-loss plots. Both sets of rates were normalized for surface area. The surface area, which was assumed to be equal to the initial surface area, was calculated from measured dimensions.

Discussion

The results of this and earlier studies (2, 3, 8) indicate that oxygen is highly soluble in CaF_2 at elevated temperatures. Existing evidence also indicates that oxygen can be substituted for F^- as O^{--} (with the formation of anion vacancies) (2, 3, 5, 6) and as OH^- (3, 4, 6). It is therefore evident that the mechanism of the hydrolysis process is more complex than

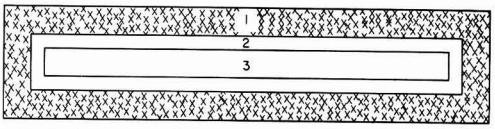

Fig. 1. Appearance of the cross section of a typical CaF_2 specimen after hydrolysis.

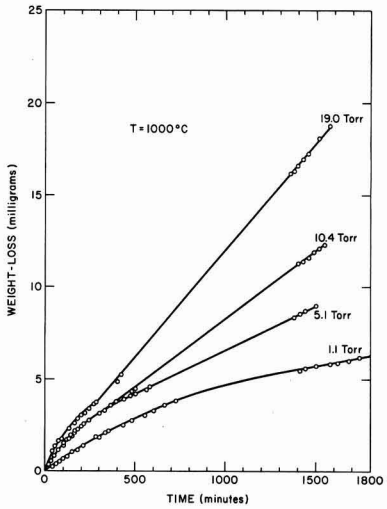

Fig. 2A. Weight-loss *vs.* time curves for the hydrolysis of single crystal CaF_2 specimens at 1000°C.

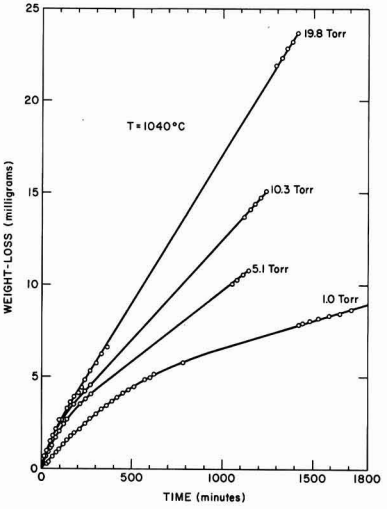

Fig. 2B. Weight-loss *vs.* time curves for the hydrolysis of single crystal CaF_2 specimens at 1040°C.

was previously thought (1) and that a detailed description of the process requires more experimental data than are presently available. The following discussion attempts to point out some of the complexities involved in the interpretation of the results, and to suggest the existence of possible reaction mechanisms not heretofore considered.

The qualitative observation that the precipitate particles found in quenched specimens in this and a previous investigation (8) were uniform in size and distribution suggests that the precipitate formed only on quenching. If the precipitate had existed at the temperature of reaction, one would expect the precipitate particles to be larger in the region of higher oxygen concentration near the surface of the specimen. One might also expect such a size gradient to result from slower cooling which would allow more time for growth of the precipitate. Indeed, Bruch *et al.*, (5) observed just such a gradient in specimens that were cooled slowly.

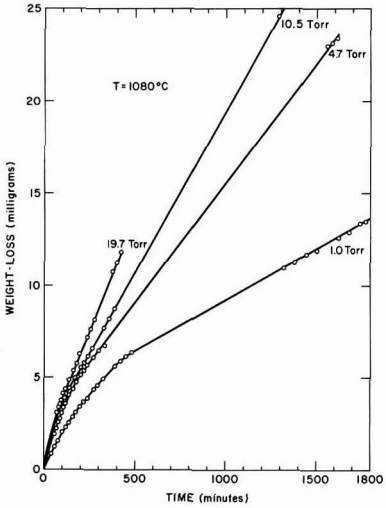

Fig. 2C. Weight-loss *vs.* time curves for the hydrolysis of single crystal CaF_2 specimens at 1080°C.

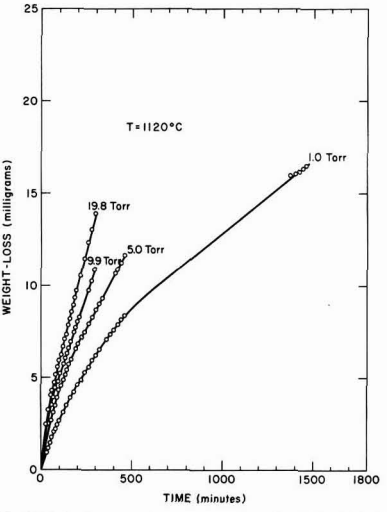

Fig. 2D. Weight-loss *vs.* time curves for the hydrolysis of single crystal CaF_2 specimens at 1120°C.

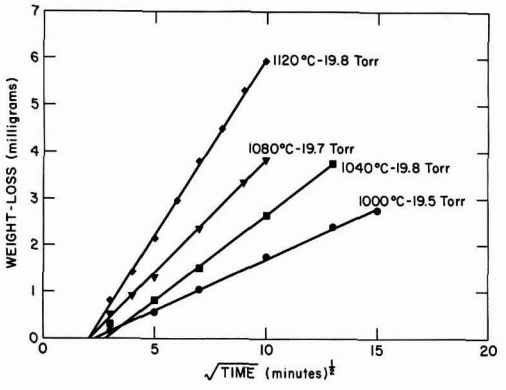

Fig. 3. Plots of weight-loss *vs.* $t^{1/2}$ for the initial portion of the hydrolysis reaction.

Table I. Collected rate data

Temp, °C	P_{H_2O}, Torr	$R_l \times 10^6$, g cm^{-1} min^{-1}	$R_p \times 10^4$, g cm^{-2} min$^{-1/2}$
1000	1.1	0.750	0.440
1000	5.1	1.94	0.898
1000	10.4	3.04	0.978
1000	19.0	4.45	1.05
1000	19.5	4.69	0.913
1040	1.0	1.25	1.14
1040	1.0	1.47	0.988
1040	5.1	3.26	1.32
1040	10.3	4.60	1.43
1040	19.8	6.78	1.46
1080	1.0	2.26	1.48
1080	4.7	5.25	1.92
1080	10.5	7.36	2.02
1080	19.7	9.70	1.99
1120	1.0	3.34	1.78
1120	5.0	7.78	2.55
1120	9.9	11.5	2.93
1120	19.8	15.7	3.03

If, for the purpose of calculation, it is assumed that all of the oxygen was dissolved as O^{--}, minimum values for the solubility of oxygen in CaF_2 can be estimated from the maximum observed weight losses. These values are in the range from 5 to 20 m/o (mole per cent).

The paralinear rate behavior demonstrated by the curves in Fig. 2 was also observed by Bontinck (1) in experiments on the hydrolysis of CaF_2 powder specimens over a similar temperature range. Bontinck ascribed the parabolic to linear rate transition to saturation of the specimen with oxygen and formation of a precipitate. The present results, however, are inconsistent with this interpretation because they indicate that the transition is dependent on the partial pressure of water vapor, while the solubility limit should be independent of pressure. Furthermore, one would expect the growth of precipitate particles to exhibit nonlinear kinetics (9) instead of the linear kinetics actually observed.

It is evident from Fig. 2 that the extent of reaction at the transition point is dependent on both temperature and water vapor pressure. Unfortunately, the breaks in the curves cannot be established with sufficient precision to deduce quantitative relationships. One can see qualitatively, however, that the transition point weight-loss is inversely proportional to pressure under isothermal conditions, and directly proportional to temperature under isobaric conditions.

Bontinck (1) suggested that the initial stage of the hydrolysis process involved the substitution of OH^- for F^- at the crystal surface with the formation of one molecule of HF gas. He also interpreted his measurements as indicating that the OH^- disappeared after several hours of heating and that the final net reaction was

$$CaF_2(s) + \delta H_2O = (1-\delta)CaF_2\delta CaO + 2\delta HF \quad [1]$$

or

$$H_2O = \delta O^{--} + \delta\square^- + 2\delta H^+ \quad [2]$$

However, Wickersheim and Hanking (4) presented clear evidence that OH^- exists in the CaF_2 even after prolonged heating. They reported that the OH^- absorption band at 3650 cm^{-1} was at least as strong after 6 hr of heating as it was after 4 hr of heating at 1020°C, and that the disappearance of the peak observed by Bontinck was actually a result of an increase in background. The ESR and EPR measurements of Sierro (3, 6) on gadolinium doped CaF_2 also indicate the presence of OH^- within CaF_2 crystals after hydrolysis. Sierro's measurements further indicate that OH^- decomposes within the crystal to form O^{--} Presumably, the decomposition process results in the formation of anion vacancies and HF along with O^{--}.

The magnitudes of the weight losses obtained in this study indicate that decomposition of OH^- must be

occurring throughout the course of the reaction. The mere substitution of a hydroxyl ion (M.W. = 17) for a fluoride ion (A.W. = 19) could not account for the large weight changes which were observed.

On the basis of existing data, one can list a number of rate processes that may be involved in the over-all hydrolysis reaction. Some of these are: (*i*) chemisorption of water vapor and desorption of HF; (*ii*) surface reaction to form OH^- and HF; (*iii*) surface reaction to form O^{--}, anion vacancies and HF; (*iv*) diffusion of O^{--}, OH^-, and anion vacancies into the crystal; (*v*) diffusion of F^- toward the surface by the interstitial mechanism proposed by Ure (10); (*vi*) internal decomposition of OH^- to yield O^{--}, anion vacancies, and HF; and (*vii*) diffusion of HF out of the crystal.

The following discussion deals with the parabolic and linear portions of the reaction with respect to the possible rate-controlling mechanisms listed above.

The parabolic character of the initial reaction period suggests that a diffusion process is rate controlling; if a surface-reaction process were rate controlling, a linear rate law would be observed (11). Interpretation of the parabolic weight-loss rates therefore requires relating the weight loss data to a diffusion coefficient and identifying the diffusing species.

The parabolic rate exhibited a strong dependence on the partial pressure of water vapor with a tendency toward a limiting value at the higher pressures. Similar pressure dependencies have been observed for reactions in which a chemisorption equilibrium step precedes the rate-controlling one. (7, 12). If the rate is assumed to be proportional to the extent of surface coverage by the reacting gas, and if the surface concentration is expressed by the Langmuir adsorption isotherm, the applicable rate expression is (7)

$$-\frac{P}{R_p} = \frac{kT}{k_p K_c \sigma_o} + \frac{P}{k_p \sigma_o} \qquad [3]$$

where P is the partial pressure of water vapor, R_p is the parabolic reaction rate, k is Boltzmann's constant, T is the absolute temperature, k_p is the parabolic rate constant, K_c is the chemisorption equilibrium constant, and σ_o is the concentration of reactive surface sites. Equation [3] predicts that a plot of P/R_p *vs.* P should yield a straight line of slope equal to $1/k_p\sigma_o$ Figure 4 shows that the parabolic rate data fit Eq. [3].

If it is assumed that the parabolic period corresponds to steady-state diffusion in a semi-infinite medium, the applicable rate expression is (13)

$$R_p = \left(\frac{D_i}{\pi t}\right)^{1/2} C_i \qquad [4]$$

where D_i is the diffusion coefficient, C_i is the concentration per unit volume of the diffusing species adjacent to the surface, and t is the time. As Eq. [3] was derived from the expression $R_p = k_p(\sigma/t^{1/2})$, D_i can be related to k_p by

$$k_p\sigma = (D_i/\pi)^{1/2} C_i \qquad [5]$$

When the surface is saturated with chemisorbed water vapor, $\sigma = \sigma_o$, and C_i is the concentration of the diffusing species present at saturation.

Values of $k_p\sigma_o$ (arbitrary units) were obtained from the reciprocal slopes of the lines given in Fig. 4. It was assumed that σ_o was constant. Figure 5 shows a semilog plot of $(k_p\sigma_o)^2$ *vs.* $1/T$. According to Eq. [3], $(k_p\sigma_o)^2$ should be proportional to $D_iC_i^2$. If it is assumed that $D_i = D_o \exp(\Delta H_D/RT)$, and $C_i = C_o \exp(\Delta H_e/RT)$, the activation energy obtained from Fig. 5 is the sum of terms for diffusion and carrier concentration. It was calculated that $(\Delta H_D + 2\Delta H_e) = 63.6$ kcal.

Although, in principle, values for K_c are obtainable from Fig. 4, the intercepts could not be established with sufficient precision to do so.

An unambiguous identification of the diffusing species is not possible by evaluation of the parabolic rate data. If one assumes that the surface concentration of carriers is independent of temperature, the activation energy of 63.6 kcal/mole obtained here is close to the value of 67 kcal/mole for interstitial diffusion of argon in CaF_2 obtained by other investigators (14, 15). This correlation would suggest that the interstitial diffusion of HF out of the crystal is rate-controlling. On the other hand, if the diffusion of OH^- or O^{--} and anion vacancies were rate controlling, one would expect an activation energy close to that for self diffusion of F^- in CaF_2, *i.e.*, 46 kcal/mole (10, 15, 16). Because the value obtained is a composite one, the latter possibility is not ruled out.

The dependence of the linear reaction rate on the partial pressure of water vapor is clearly different than

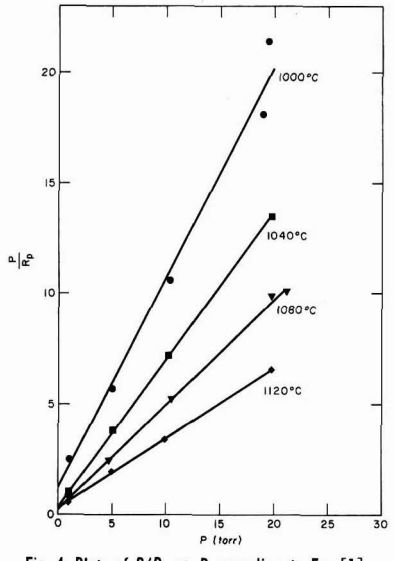

Fig. 4. Plots of P/R_p *vs.* P according to Eq. [1]

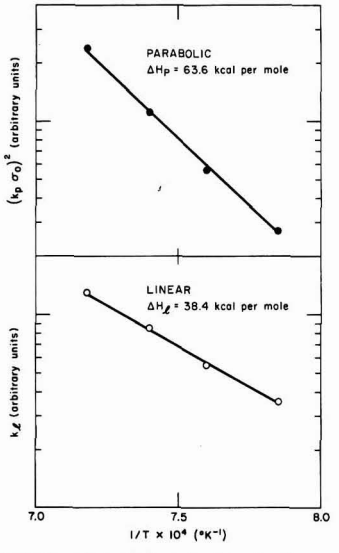

Fig. 5. Arrhenius plots of the rate data for the parabolic and linear reaction stages.

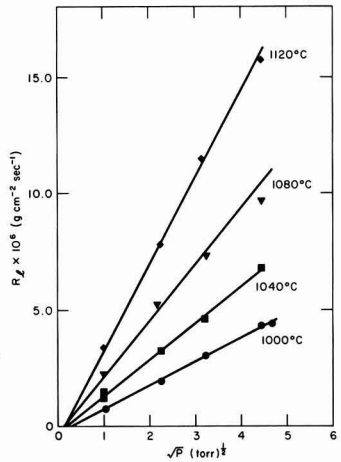

Fig. 6. R_1 vs. $P^{1/2}$ according to Eq. [5]

the dependence of the parabolic rate. As shown in Fig. 6, the linear reaction rate is proportional to the square root of the partial pressure of water vapor. Assuming a rate expression of the form

$$R_l = k_l P^{1/2} \qquad [6]$$

rate constants were calculated from the lines in Fig. 6. The Arrhenius plot shown in Fig. 5 yielded a value of 38.4 kcal/mole for the apparent activation energy.

The interpretation of the linear reaction period is uncertain. It could correspond to rate control by a surface reaction process of the type given in Eq. [1] and [2], *i.e.*, reaction at the surface to form substituted oxygen and anion vacancies. If such were the case, Eq. [2] indicates that the concentration of dissolved oxygen would be proportional to the square root of the partial pressure of water vapor. An enthalpy of 38 kcal/mole that was obtained by Mollwo for the formation of F centers in CaF_2 was quoted by Bontinck (1). It appears, however, that detailed speculation about the mechanism that gives linear kinetics is unwarranted at the present time.

Acknowledgments

The author is deeply indebted to Joseph A. Pask for his generous support in this work. He also thanks Marcus P. Borom for many helpful criticisms and Barry R. Rossing for useful comments. This work was done under the auspices of the United States Atomic Energy Commission.

Manuscript received Sept. 28, 1967; revised manuscript received Nov. 22, 1967.

Any discussion of this paper will appear in a Discussion Section to be published in the December 1968 JOURNAL.

REFERENCES

1. W. Bontinck, *Physica*, **24**, 650 (1958).
2. H. Adler and J. Kveta, *Osterr. Akad. Wiss., Math, naturw. Kl., Sitzer. Abt. II*, **166**, 199 (1957).
3. J. Sierro, *J. Chem. Phys.*, **44**, 2183 (1961).
4. K. A. Wickersheim and B. M. Hanking, *Physica*, **25**, 569 (1959).
5. H. Bruch, P. Gorlich, H. Karras, and R. Lehmann, *Phys. Stat. Sol.*, **4**, 685 (1964).
6. J. Sierro, *Helv. Phys. Acta.*, **36**, 505 (1963).
7. D. R. Messier, *J. Am. Ceram. Soc.*, **48**, 452 (1965).
8. W. L. Phillips, Jr., and J. E. Hanlon, *ibid.*, **46**, 447 (1963).
9. W. E. Garner, "Chemistry of the Solid State," Butterworths, London (1955).
10. R. W. Ure, Jr., *J. Chem. Phys.*, **26**, 1363 (1957).
11. W. Jost, "Diffusion in Solids, Liquids, Gases," Academic Press, New York (1960).
12. J. N. Ong, Jr., M. E. Wadsworth, W. M. Fassell, Jr., *Trans. AIME*, **206**, 257 (1956).
13. J. Crank, "*The Mathematics of Diffusion*," Clarendon Press, Oxford (1956).
14. T. Lagerwall, *Nukleonik*, **6**, 179 (1964).
15. Hj. Matzke, *J. Nucl. Mat.*, **11**, 344 (1964).
16. Hj. Matzke and R. Lindner, *Z. fur Naturforsch.*, **19a**, 1178 (1964).

Low-Temperature Silicon Epitaxy

R. G. Frieser*

Research and Development Laboratories, Sprague Electric Company, North Adams, Massachusetts

ABSTRACT

Highly oriented large-area silicon films have been deposited onto single crystal Si, <111> substrates. Illumination of the substrates with a mercury vapor lamp during deposition appeared to be essential for obtaining oriented films. The deposition was accomplished by an H_2 reduction of Si_2Cl_6. The energy of activation for this reaction was found to be 35.7 kcal/mole ± 5%. Utmost chemical cleanliness of the substrate surface is essential and more critical than for high temperature deposition.

The objective of this work was to explore the possibility of growing single crystal films of silicon by a simple chemical vapor phase deposition at temperatures considerably below those presently employed (< 900°C). Such a technique would supplement and extend existing semiconductor technology and would permit the manufacture of devices with properties presently not feasible with existing techniques. The following examples will illustrate these points. Low temperature silicon films would permit formation of abrupt, almost perfect step junctions on silicon, by reducing migration of impurities from the substrate into the epitaxial layer during formation of the film. Another possibility would be the prevention of junction movements, if such are already present in the substrate, while depositing new semiconductor material. The same technology would permit formation of metal base- or metal gate-transistor structures in one apparatus in a continuous operation. This is not possible at present, because temperatures needed to obtain single crystal silicon are high enough to form silicides, thus destroying the thin (~ 400Å) metal layer (base).

Prior technology.—Reports of low temperature silicon (Lot Si) deposition in the literature usually

* Electrochemical Society Active Member.

deal with temperatures of about 850°C (1). These results have been achieved by sputtering, evaporation, or sublimation. A few investigators, however, reported deposition temperatures below 850°C (1-4).

All these techniques involve cumbersome, expensive, and especially sophisticated equipment. For these reasons, such techniques limit the depositions usually to small area films. Deposition rates are quoted as correspondingly slow if mentioned at all.

Therefore, chemical vapor deposition (CVD) seemed to be a more promising technique to achieve the goal of a simple, flexible, open tube, flow process of depositing single crystal silicon at low temperatures. However, no oriented, much less single crystal, silicon films are reported in the literature below 900°-1000°C by CVD (6). The one exception is Nakanuma (7), who deposited silicon epitaxially at 850°C after having deposited a 0.2μ layer of silicon at 1200°C. This makes Nakanuma's technique less generally applicable than one wherein the total deposition occurs at the lower temperature.

Experimental

Substrate—Silicon substrates used were <111> oriented, 0.007 ohm-cm, p-type, ~ 3 cm diameter. Conductivity and type were chosen in order to easily measure thickness by infrared spectroscopy and more readily see the junction after angle lapping and staining. Because the source material (Si_2Cl_6) was not doped, deposited silicon layers were expected to be n-type, as is usually the case with $SiCl_4$ or $SiHCl_3$.

Reagents—Pure line nitrogen was used for flushing the apparatus. Bottled hydrogen was passed through a palladium hydrogen purifier (Surfass Model L-15-D) prior to use. Anhydrous HCl as well as $SiHCl_3$ (electronic grade purity) were supplied by Pittsburgh Materials and Chemical Company. $SiCl_4$ used, was obtained from Sylvania and (1%) SiH_4 in H_2 from Matheson Company. Disiliconhexachloride (Si_2Cl_6) was supplied by K and K Chemicals.

Si_2Cl_6 was chosen as the source material for several reasons. This compound has an extended liquid range (−1° to 144°C). Control of the vapor pressure, and, therefore, of the concentration of Si_2Cl_6 in H_2 carrier gas, becomes simply a matter of controlling the source temperature. If the Si-Si bond remains intact, and there are indications it may (8, 9), and if film growth is by way of a two-dimensional nucleation process (10), then Si_2Cl_6 may have an advantage over monosilicon compounds as a source material. Furthermore, Si_2Cl_6 has been reported to be readily decomposed at 450°C to Si, $SiCl_4$, and Cl_2 (12). This reaction is presumed to be surface catalyzed.

Light source.—To supply other than thermal energy to the substrate, ultraviolet light was a reasonable choice. While it would not increase the deposition temperature, it would aid in the decomposition of the Si_2Cl_6 molecule. This expectation seemed justified, because u.v. light of 3160Å corresponding to 92 kcal should strip the chlorines from the molecule. The bond energy of the Si-Cl bond is 91 kcal/mole for $SiCl_4$. Furthermore, the u.v. illumination may be expected to have an effect on the surface nucleation as well since the energy of 3160Å radiation corresponds to about the work function of Si (4.1 ev = 95 kcal).

A Hanovia Utility Model Lamp (100w) was used as a light source. This lamp employs a U shaped quartz mercury-arc tube. To achieve selectivity of wavelength, a set of 8 monopass u.v. interference filters from Optics Technology were used. These filters covered the range of 230-370 mμ. Their half width was rated at 6-10% of peak wavelength, transmission at peak was 10-22%. Two additional blocking filters were employed, one blocking u.v., the other visible light.

System.—The deposition apparatus was of the conventional upright, one-slice quartz reactor. A silicon pedestal with a molybdenum insert was used instead of graphite to eliminate possible carbon contamination, which could cause spurious nucleation during deposition. Evidence of this has been reported in the literature (10). Deposition temperatures were measured with an Ircon IR pyrometer directly on the surface during deposition.

Substrate preparation.—Lustrox-polished silicon substrates were further subjected to the following routine: The substrates were first degreased in hot organic solvents. To remove any polishing compound embedded in the surface (*i. e.*, alumina, zirconia) the substrates were subjected to a copper displacement plating step and the copper was subsequently removed (11). Since this left a pitted surface, the substrates were chemically polished (5-20 min in 5% HF in HNO_3) to a smooth mirror finish by removing a total of 3-10 mils from both surfaces. The final thickness of substrates was ~ 8 mils. Immediately after chemical polishing, these substrates were quenched in a solution of anhydrous methanol saturated with iodine (12). The substrates were placed wet in the reactor and iodine was sublimed off at temperatures below 600°C in a stream of H_2.

HCl etching was performed in situ at 1175°C using a 6% (vol.) mixture of anhydrous HCl and H_2, about 3 mils of material were removed.

All substrates were handled with Teflon tweezers to minimize mechanical damage.

Characterization.—Deposited silicon films were characterized visually, electrically and crystallographically. Surface structure and roughness were examined on the Leitz metallograph, or under the Reichert microscope, using a Nomarski polarization interferometer. Occasionally, the surface smoothness was studied using the "Talysurf." Thickness measurements of deposited films were determined either by angle lapping on a 3° block, staining, and using an interference fringe technique (13), or directly by IR spectrophotometry (Beckman, IR 10).

The electrical properties were observed in the customary manner with a four-point and hot-point probe.

Low angle reflection electron diffraction techniques were used to study the degree of orientation of the films.

Results

Films having a high degree of orientation were achieved when Si_2Cl_6 was used as a source at a deposition temperature of 700°C in the presence of u.v. illumination. This conclusion was based on reflection electron diffraction studies as shown in Fig. 1a. The films were also evaluated by angle lapping and staining as shown in Fig. 1b. This 3.4μ thick film is seen to be well defined and uniform in depth.

Possible evidence that the interface is abrupt is shown in Fig. 2. This picture shows two IR interference fringe curves of Si films of comparable thickness on similar substrates. Their only difference is that one was deposited at 700°C from a Si_2Cl_6 source in the presence of u.v., the other at 1100°C from $SiCl_4$ with no illumination. The fact that the Lot Si film shows many more distinct absorption peaks can be interpreted to mean an abrupt "interface" between film and substrate. In the absence of u.v. illumination, the deposition rate is about ½ of that with u. v. light (1 μ/hr) and the resulting films were polycrystalline in nature (Fig. 1c).

Preferred conditions.—The above experiments are taken as evidence that highly oriented Si films can be deposited at 700°-800°C under the following conditions: source Si_2Cl_6, source temperature 10°C (2 Torr), H_2 flow rate 1.5 l/min, and u. v. illumination of substrate during deposition. All subsequent information will refer to these conditions unless otherwise specified.

Table I summarizes the observations made when using various silicon halides as source materials, such as doped (n- and p-) as well as undoped $SiCl_4$,

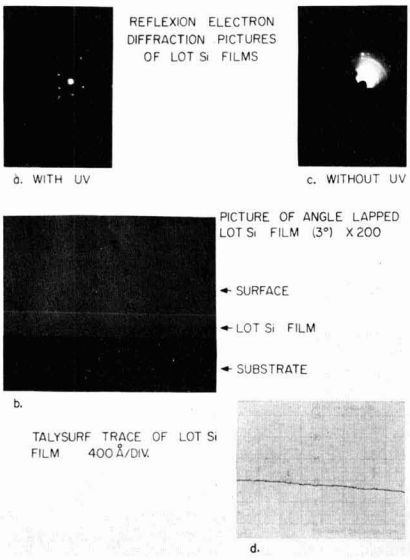

Fig. 1a. Reflection electron diffraction picture of Lot Si film (with u.v.). Fig. 1b. Picture of angle lapped (3°) Lot Si film. Fig. 1c. Reflection electron diffraction picture of Lot Si film (without u.v.). Fig. 1d. Talysurf trace of a representative Lot Si film.

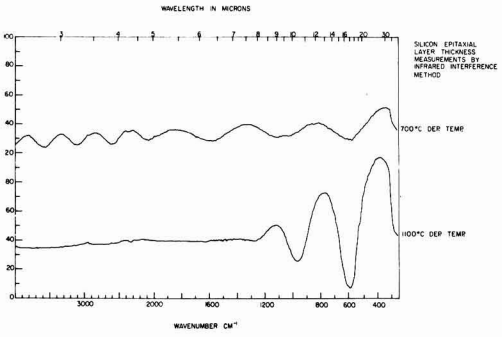

Fig. 2. Comparison of IR interference fringe measurement of Lot Si film and high temperature deposited silicon film.

$SiHCl_3$, and SiH_4. H_2 flow rates and source temperatures were varied to result in a gas stream composition that would correspond (assuming the Si-Si bond breaks) to the preferred concentration of Si_2Cl_6.

A recent report (14) describes single crystal films of Si on Si at temperatures as low as 740°C using $SiCl_4$ as a source (0.6% in H_2) and u.v. illumination. No flow rates were indicated. This experiment was repeated at two flow rates (0.5 and 1.5 l/min), but continuous films were not observed, only occasional isolated crystallites.

Either no deposits at all or polycrystalline films were obtained at deposition temperatures of 700°C when source material was used containing one Si atom only. At higher temperatures, oriented and single crystal films were obtained as was expected from previous published accounts.

General appearance of lot Si films.—The quality of the surface varied greatly; the higher the deposition temperature the greater was the aggregation, and the rougher the final surface. At 700°C, the surfaces were consistently smooth with a surface roughness of about 100Å according to Talysurf measurements (Fig. 1d). The surfaces were metallic and highly reflective,

Table I. Effect of source material on structure of epitaxial films

Source	Dep. temp.	Film Structure: With u.v.	Film Structure: No u.v.
$SiCl_4$	700	No dep.	
	900	No dep.	
	1000	Oriented	
$SiCl_4$ (n-type)	(5 ppm $AsBr_3$)		
	700	No dep.	
	900	Polycrystalline	Polycrystalline
	1000	Oriented	Polycrystalline
	1100	Oriented	Single crystal
$SiCl_4$ (p-type)	(30 ppm BBr_3)		
	1100	Isolated crystals on surface	Single crystal
$SiHCl_3$	700	No dep.	No dep.
	1000	Polycrystalline	Polycrystalline with some orientation
SiH_4	700	Polycrystalline	Polycrystalline
Si_2Cl_6	700	Oriented	Polycrystalline

although they showed a milky white, but still specular appearance.

General information.—The resistivity of the deposited films varied greatly (from 0.04 to 0.8 ohm-cm). All deposits were found to be n-type. The only exceptions were those which were HCl etched (*in situ*) as a final surface preparation step. These surfaces were all p-type.

Deposition rates, also, varied greatly (0.4—2.5 μ/hr), but were reasonably constant for each batch of Si_2Cl_6 and varied linearly with the deposition temperature (Fig. 3) in the range of 600°-1000°C. From this data, a tentative activation energy of 35.7 kcal/mole ± 5% was calculated.

Substrate predeposition treatment.—Various substrate treatments prior to deposition under preferred conditions were evaluated by reflection electron diffraction techniques of deposited films. Unbroken diffraction rings were considered evidence of polycrystallinity, segmented rings indicated orientation; the closer the "arc pattern" was to a "spot pattern" the higher the orientation assigned to the film in question. Using these criteria, the following observations were made:

Omission of the copper displacement plating step would invariably result in unequivocal polycrystalline

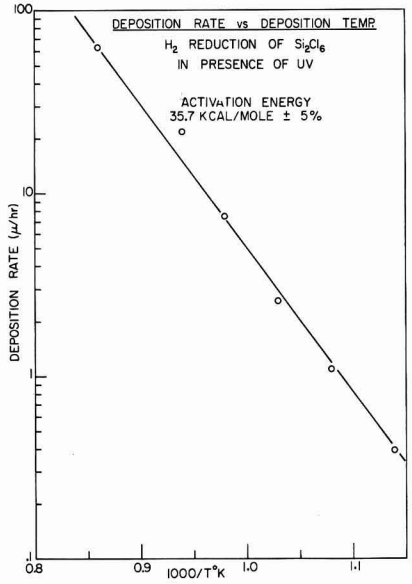

Fig. 3. Deposition rate vs. deposition temperature of Lot Si films

films, regardless of other surface preparation. Even a final HCl etching step did not prevent the formation of polycrystalline films. This may indicate that particles of polishing compound left behind after chemical or HCl etching still contaminated the surface and were apparently only removed by copper displacement plating. Finishing the substrate preparation with an alcohol quench (without I_2) gave ambiguous results; resulting films might be completely polycrystalline or a mixture of oriented and polycrystalline materials. However, when the alcohol was permitted to dry prior to insertion in the reactor, only polycrystalline films were noted. These observations were not changed if the alcohol step (dry or wet) were followed by HCl etching in situ. On the other hand, it appears that a consistently high degree of orientation was obtained free from any polycrystalline material when the substrate was treated in the following manner: copper displacement plating, chemical polishing, quenching in I_2-saturated methanol, insertion wet in the reactor in an argon atmosphere, and removal of I_2 by heating the substrate to below 600°C (~ 550°C) in H_2.

Effect of Wavelength.—Using the above surface preparation and the preferred deposition conditions, the best oriented films with no evidence of polycrystallinity were observed when a 230 mμ narrow band pass filter was employed. Judging by the electron diffraction pictures, the orientation decreased and polycrystallinity increased with an increase in the passing wavelength of the optical filter. Figure 4 shows two representations of reflection electron diffraction pictures of films deposited with the aid of a 230 mμ filter in one case and, in the other, with the aid of a 360 mμ filter. The inference from these pictures is that wavelengths below 230 mμ may even be more advantageous.

Summary and Conclusions

It is obviously too early to draw any firm conclusions concerning the mechanisms of this reaction. However, certain inferences can be made on the basis of the above work and the following facts emerged:

a. Highly oriented silicon films can be deposited on single crystal silicon substrates at deposition temperatures of ~ 650°-800°C provided u.v. illumination is employed during the deposition and the silicon source is Si_2Cl_6.

b. Surface treatment of substrates appears to be more critical when depositing at 700°C than at 1000°C. Therefore, lapping debris must be removed. Marked improvement in crystalline perfections was obtained by copper displacement plating that was not observed with wet chemical etching or in situ HCl high temperature etching. Elimination of a polishing step using oxides other than SiO_2 should eliminate this problem.

To prevent formation of an oxide layer prior to deposition, quenching the chemically polished substrate in an alcohol solution saturated with I_2 was found to be necessary.

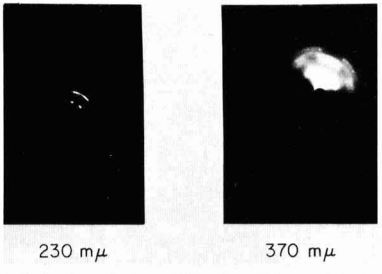

Fig. 4. Reflection electron diffraction pictures of Lot Si films deposited under 230 and 370 mμ illumination.

c. The relatively large variations in electrical and physical properties expressed in the variation of resistivities and deposition rates indicate that the source material was not sufficiently pure and varied from batch to batch. For this reason, inferences about the kinetics are very tentative.

d. Oriented epitaxial films were obtained only when: (*i*) the substrate was illuminated (with u. v. light) during the deposition, and (*ii*) Lot Si oriented films were obtained only when Si_2Cl_6 was used as the source. No deposit was obtained at 700°C using $SiCl_4$ or $SiHCl_3$ sources and only polycrystalline films were obtained using SiH_4 at 700°C. One might expect that the Si-Si bond (42 kcal/mole) would break easily when illuminated with u. v. light. Yet the dissociation energy for Si_2Cl_6 is reported to be 85 kcal/mole (9). Indications from organic reactions with Si_2Cl_6 are that the Si-Si bond is not as easily broken as one might expect from thermodynamic considerations alone. A large activation energy could account for the observed stability of the Si-Si bond. Steric hindrance of the Cl atoms as well as electronic effect from this (p → d)π bond could account for this high activation energy. It appears then that the Si-Si bond may survive and thus play an important part in the oriented growth of the nuclei.

Furthermore, the effect of the light indicates that the reaction is surface catalized. In view of the fact that the energy is almost the same as that of the work function (4.1 ev or 95 kcal/mole) of Si, it appears that this could be further evidence for the surface model for Si proposed by Chung and Haneman (15). The light quanta may indeed draw electrons to the surface and produce a surface which may, for all intents and purposes, appear to the oncoming atoms like a plane through the crystal. In other words, on a statistical basis the effect of the light may be that each surface atom has now a "dangling bond" most of the time as compared to one for every five surface atoms (15). Thus, the oncoming Si atoms do not have to search about for a favorable site, but could stay where they land. If all sites are equivalent, growth is then oriented at all nucleation sites in the same manner.

Acknowledgments

The author would like to express his appreciation to J. J. Casey, R. P. Auty, and F. W. Anderson for stimulating discussions and for their interpretations of the electron diffraction data. The assistance of T. Horner and C. Sweeney must be acknowledged for their help in the preparation of the epitaxial layers, and the electron diffraction data, respectively. And, finally, thanks are due to W. Bracht for his advice on the substrate preparation.

Manuscript received Sept. 6, 1967; revised manuscript received *ca.* Nov. 7, 1967. This paper was presented at the Philadelphia Meeting, Oct. 9-14, 1966, as Abstract 191.

Any discussion of this paper will appear in a Discussion Section to be published in the December 1968 JOURNAL.

REFERENCES

1. a. A. J. Mountvala and G. Abowitz, *Vacuum*, **15,** 359 (1965); b. H. Widmer, *Appl. Phys. Letters*, **5,** 108 (1964); c. K. L. Chopra, *J. Appl. Phys.*, **37,** 3405 (1966).
2. J. D. Filby and S. Nielsen, *Microelectron. Rel.*, **5,** 11 (1966).
3. R. Kikuchi a.o., Technical Report AFML-TR-66-326, p. 48, Wright-Patterson Air Force Base, Ohio.
4. F. Jona, a. Abstract BDlo; *Bull. Am. Phys. Soc.*, 1966 (Annual Meeting at New York City, 1966; b. *Appl. Phys. Letters*, **9,** 235 (1966).
5. E. T. Handelman and E. I. Povilonis, *This Journal*, **109,** 201*C* (1962).
6. a. J. Bloem and J. W. Scholte, *ibid.*, **112,** 1211 (1965); b. Hewlett-Packard, Annual Summary

Report, 1965 Contract No. AF 33 (615)-2035, Air Force Avionics Laboratory.
7. S. Nakanuma, *IEEE Trans.*, Electron Devices ED **13**(7), 578-589 (1966).
8. W. C. Steele and F. G. A. Stone, *J. Am. Chem. Soc.*, **84**, 3599 (1962).
9. E. A. V. Ebsworth, Volatile Silicon Compounds, Int. Series of Mongraphs on Inorg. Chem., pp. 91-92 (1963).
10. S. Nielsen and G. J. Rich, *Microelectron. Rel.*, **3** 165 (1964).
11. D. L. Klein, U. S. Patent 3,224,902 (1965).
12. D. L. Klein, Personal communication.
13. W. L. Bond and F. M. Smits, *Bell Syst. Tech. J.*, **35**, 1209 (1956).
14. M. Kumagana, H. Sunami, and J. Nishizawa, RIEC. Tech. Rep., TR-23 (1967) Tohoku Univ., Japan.
15. M. F. Chung and D. H. Haneman, *J. Appl. Phys.*, **37**, 1879 (1966).

Influence of Substrate Temperature on GaAs Epitaxial Deposition Rates

Don W. Shaw

Texas Instruments Incorporated, Dallas, Texas

ABSTRACT

The effects of substrate temperature on the GaAs deposition rates were studied for {111}A, {112}A, {113}A, {115}, {100}, {113}B, {112}B, and {111}B substrate orientations. An open tube chloride transport system with elemental gallium and arsenic sources was employed. This apparatus allowed independent control over the gallium monochloride, arsenic, and hydrogen chloride partial pressures. The sensitivity of the deposition rate to substrate orientation is observed to be strongly temperature dependent. Experimental evidence is provided which indicates that the deposition rate is kinetically limited in the temperature range from 725° to 800°C.

Recent stress has been placed on improved material quality in order to realize the numerous potential applications for gallium arsenide. At present, vapor phase epitaxial deposition is the most successful method for production of such high quality material. However, continued material improvements have become increasingly difficult due to the need for fundamental information concerning the deposition process itself. In order to partially satisfy this need, a fundamental study concerning the influence of substrate temperature on the GaAs deposition rate was carried out. An investigation of this nature is a logical initial step toward understanding the basic nature of an epitaxial process.

Numerous investigators have studied GaAs epitaxial deposition processes. However, detailed studies concerning the effects of a single variable are rare. Magomedov and Sheftal (1) studied the effect of substrate temperature on the GaAs deposition rate using an open tube iodide process. The deposition rate was found to pass through a maximum as the substrate temperature was raised from 570° up to 690°C. Taylor (2) observed a similar effect with a chloride transport system. In the present study, an effort was made to isolate the substrate temperature as a single variable and study its effect on the deposition rate. The effects of substrate orientation and flow rate on the deposition rate were then related to the rate-temperature data.

Experimental

The apparatus shown in Fig. 1 was employed throughout the study. It was designed to allow independent control of the partial pressures of the gallium and arsenic species. The arsenic partial pressure was controlled by the flow rate of hydrogen over the elemental arsenic source and the temperature of the source. Transport experiments were carried out to establish empirically the arsenic transport rate as a function of the source temperature and hydrogen flow rate. The results indicated complete saturation of the hydrogen stream with arsenic up to the maximum flow rate studied (300 ml/min). The HCl used for gallium transport was obtained by reduction of $AsCl_3$ with hydrogen at a temperature > 900°C. Transport experiments established that one gram atom of gallium was transported for each mole of HCl entering the gallium source chamber. This indicated complete formation of GaCl at the temperature of the gallium source (900°C). Additional experiments established that complete reduction of $AsCl_3$ occurred in the reduction tube. The arsenic obtained from $AsCl_3$ reduction was condensed on the reduction tube walls and did not enter the main reaction tube with the HCl. These transport experiments enabled calculation of the initial gallium monochloride partial pressure from the vapor pressure of $AsCl_3$ at the bubbler temperature and the hydrogen flow rate through the bubbler. The purity of the elemental source materials was rated at 99.9999%. Redistilled arsenic trichloride was utilized. In all of the experiments to be described the initial vapor composition was $P^o_{GaCl} = 7.9 \times 10^{-3}$ atm and $P^o_{As4} = 3.7 \times 10^{-3}$ atm. Unless otherwise specified, the total flow rate was constant at 0.383 l/min.

Care was taken to prevent extraneous deposition of GaAs on the tube walls between the substrate holder and the source material as well as on the substrate holder itself. Prevention of this deposition was essential because such wall deposits would deplete the gas

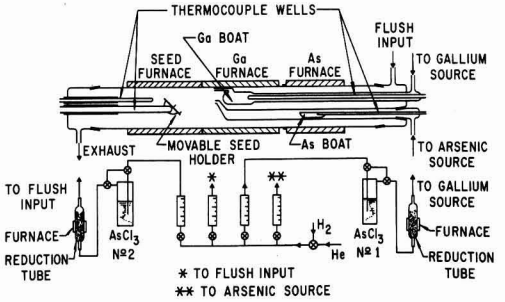

Fig. 1. Experimental apparatus for epitaxial deposition

stream of reactants before reaching the substrate region. The wall deposition was prevented by adding HCl to the gas stream. This HCl, which was also obtained by reduction of $AsCl_3$, entered the flush input of the reaction tube and did not react with the gallium source. In all of the experiments the HCl initial partial pressure was 3.0×10^{-3} atm. Since growth occurred only on the GaAs substrate, the deposition process may be treated as a special case of heterogeneous catalysis. However, unlike ordinary heterogeneous catalysis a considerable amount of information concerning the nature of the single crystal catalyst surface is available.

Usually four substrate orientations were simultaneously subjected to deposition in each run. Preliminary experiments established that the deposition rates were independent of the relative positions of the substrates on the holder. The substrates were vapor etched prior to deposition by raising the substrate temperature to 850°C. All temperatures were controlled to ± 1°C. Initial experiments established that the deposit thicknesses were linear functions of time up to 90 min. Thus 1 hr runs were employed and the rate was computed from the deposit thickness. Thickness measurements for the thicker deposits were obtained from measurement of cleaved cross-sections after the interface was revealed by anodic oxidation. For the thinner specimens angle-lapping and anodic oxidation were employed. The thickness was checked on the angle-lapped samples by interferometry. The reproducibility of the deposition rates for a given set of conditions was approximately 10%.

Chromium doped and tin doped substrates, oriented to within 0.5° of the desired direction, were used in all runs. Generally, with large area substrates growth in the direction perpendicular to the substrate surface is actually the result of the lateral propagation of steps across the surface. These steps may be inherent in the substrate prior to deposition (because of small errors in orientation), or they may result from a two-dimensional nucleation process. Accordingly, in an investigation of chemical transport epitaxial growth, the concept of surface steps must be considered. This may be accomplished by intentionally introducing steps whose nature and number could be resolved theoretically. For example, a {112} GaAs surface may be considered to be composed of {100} unit steps together with twice as many {111} steps (3). Likewise, the {113} surface consists of equal numbers of {100} and {111} steps and the {115} has a {100}:{111} ratio of 2:1. Accordingly, a self-consistent series was chosen for study which consisted of {100}, {115}, {113}, {112}, and {111} orientations. However, the polarity of the {111} planes must be considered. Polarity effects should decrease in the order: {111}, {112}, {113}, and {115}; with the {100} surface being essentially nonpolar. Indeed, the {115} was sufficiently nonpolar that no differences were observed in deposition rate between the front and back surfaces of a {115} substrate when both surfaces were polished. The following eight substrate orientations were employed: {111}A, {112}A, {113}A, {115}, {100}, {113}B, {112}B, {111}B. The "A" designation indicates the gallium face or the surface terminating in more gallium than arsenic atoms. Arsenic rich surfaces are designated as "B" orientations.

All substrates were polished with sodium hypochlorite on a rotating Pellon cloth in the manner described by Reisman and Rohr (4). After final polishing, the substrate orientation was again checked to determine if any failed to meet the 0.5° misorientation limitation.

Results and Discussion

Figure 2 shows the results obtained as the temperature is varied at constant vapor composition for {100}, {115}, {113}A, and {112}A substrates. The rates for all four orientations increase with increasing temperature up to a maximum at approximately 800°C. Further increases in temperature resulted in sharply reduced deposition rates until etching occurred near 850°C. The {111}A deposition rate exhibited a similar temperature dependence with the exception that, in general, the rate was much greater than for the other orientations. This dependence is shown in Fig. 3. Finally, the deposition rate variations as a function of temperature for {100}, {112}B, and {113}B substrates are shown in Fig. 4. The {100} was studied together with the {111}B orientations as well as with the {111}A in order to provide a reference. In addition, this permitted a check on reproducibility of the data, since the B orientations were studied several weeks after completion of the A series. Comparison of Fig. 2 and 4 reveals that similar results were obtained for both experiments. However, good quantitative agreement was obtained only in the low temperature regions before the peaks on the {100} rate-temperature curves. For this reason quantitative comparison of deposition rates between the {111}B and {111}A orientations was limited to the low temperature region (725°-775°C). In general, the B orientations exhibited the same temperature dependence as the A series. The {111}B orientation behaved anomalously in comparison with the others. Its rate never exceeded 6 μ/hr over the entire temperature range.

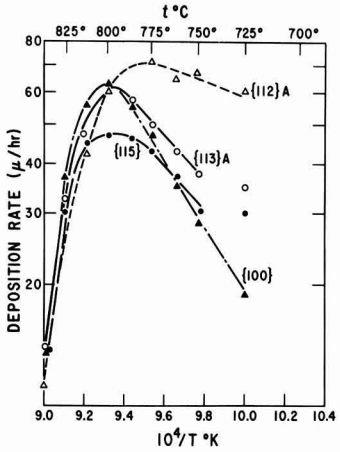

Fig. 2. Effect of substrate temperature on the {112}A, {113}A, {115}, and {100} deposition rates.

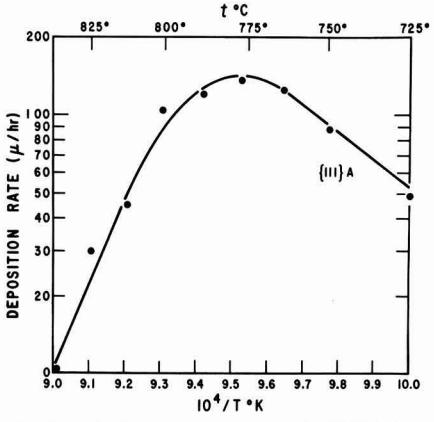

Fig. 3. Effect of substrate temperature on the {111}A deposition rate.

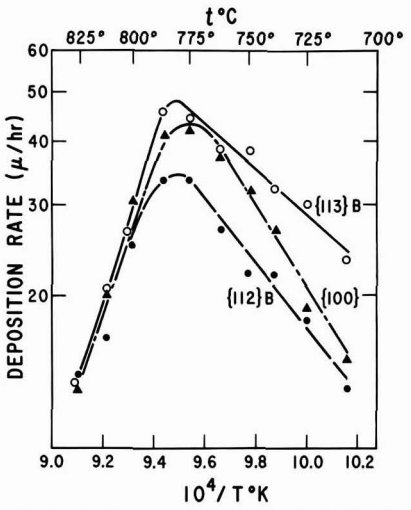

Fig. 4. Effect of substrate temperature on the {113}B, {112}B, and {100} deposition rates.

In the low temperature region before the maximum, the GaAs deposition rate shows a strong orientation dependence. The extent of this effect may be judged from the deposition rates at 750°C as shown in Fig. 5. However, beyond the maxima in the temperature curves, the orientation effects diminish and the curves for all orientations tend to converge. At temperatures below 700°C poor crystal perfection was obvious. However, the higher index orientations had much better surface appearances at these low temperatures. In general, over the entire temperature range from 700° up to 800°C the brightest, most defect-free surfaces were obtained on the {113}A substrates.

The steps involved in nonequilibrium vapor growth processes are generally divided into diffusion and surface reaction steps. Diffusion steps include diffusion of the reactants through the gas up to the substrate surface and diffusion of the products away from the surface. The surface reaction steps consist of adsorption, surface reactions, and desorption. All steps occur in series and if any step is significantly slower than the other steps, it will define the over-all deposition rate. Thus, depending on which is the slow step, deposition processes are often said to be diffusion controlled or surface reaction (kinetically) controlled. In addition to these two divisions, one should also consider a process where the rate is not limited by either a diffusion step or a surface reaction step, but which goes to equilibrium. In this case, the extent of deposition is limited by input rates of the reactants.

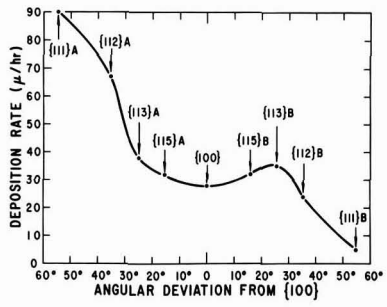

Fig. 5. Effect of substrate orientation on the GaAs deposition rate at 750°C.

Diffusion controlled processes are generally encountered where flow conditions are unfavorable or where adsorption-desorption processes and surface reactions are rapid. Such processes ideally exhibit rates relatively insensitive to temperature and thus have low activation energies. In addition, the reaction rates for diffusion-controlled mechanisms are independent of the substrate orientation (5). Kinetically controlled processes have relatively high activation energies. Since the slow steps either involve the substrate surface or take place on it, the over-all rates for kinetically controlled processes should vary with the crystallographic orientation of the surface. Unfortunately, deposition processes are sometimes so complicated that it is difficult to describe a given process in terms of a single rate limiting step.

The wide differences in deposition rates for various orientations indicate that the rates measured in low temperature regions before the maxima in the curves shown in Fig. 2-4 may represent kinetically controlled processes. This conclusion is further supported by the relatively high activation energies deduced from the slopes of the curves in the low temperature regions. These activation energies range from 15-40 kcal/mole which is in the range expected for surface limited kinetics.

Certainly the system is far from equilibrium in the low temperature region. Computer calculations were carried out to determine the extent of deposition as a function of temperature assuming an equilibrium system. The calculations were based on the actual input rates used in the experiments and the following species were considered: GaCl(g), $GaCl_3$(g), H_2(g), As_4(g), As_2(g), HCl(g), Cl_2(g), and GaAs(s). The thermodynamic values were taken from Day's compilation (6). The results are shown in Fig. 6. Over the entire temperature range the equilibrium extent of deposition decreases with increasing temperature. Experimentally, such a rate-temperature dependence is observed only at higher temperatures (Fig. 2-4).

In order to distinguish further diffusion and surface limited kinetics, a series of experiments was carried out to determine the influence of flow rate on the deposition rate. These experiments were carried out at 750°C, *i.e.*, well within the region where the deposition rate increases with increasing substrate temperature. The total flow rate was increased from 210 up to 840 ml/min while the partial pressures of all reactant species were held constant. Since the reaction tube was unchanged, the linear gas stream velocities and the reactant input rates were varied in this experiment. If the deposition rates were limited by a diffusion process, the rates should increase as the gas stream velocity is increased due to a reduction in the thickness of the diffusion boundary. The results are shown

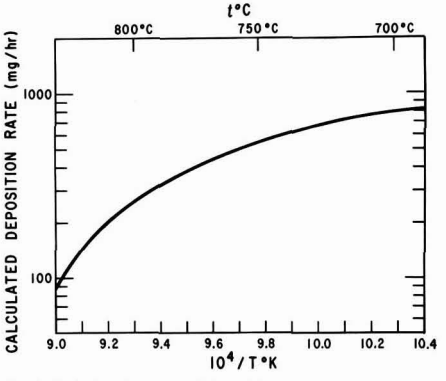

Fig. 6. Calculated extent of deposition as a function of temperature assuming equilibrium.

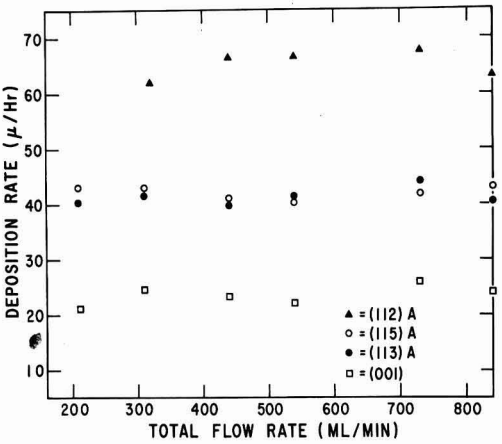

Fig. 7. Effect of total flow rate on the GaAs deposition rates at 750°C.

in Fig. 7. As is evident, the deposition rate is practically independent of the total flow rate. This is also indicative of a kinetically controlled process. This experiment was repeated for the B type orientations with similar results.

Flow rate independence is a necessary but insufficient condition for elimination of diffusion controlled processes since it could be due to peculiar flow conditions such as poor mixing at high flows (7). However, all available evidence is consistent with the concept of a kinetically controlled deposition process in the region where the deposition rate increases with increasing substrate temperature. This evidence may be summarized as (*i*) a strong dependence of the deposition rate on the substrate orientation, (*ii*) rapidly increasing deposition rate with increasing substrate temperature, and (*iii*) insensitivity of the deposition rate to the total gas flow rate.

The rate behavior in high temperature region beyond the maximum may indicate a close approach to equilibrium. Within experimental error the high temperature regions of the curves approximate the shape of the equilibrium curve (Fig. 6) in this region. However, the decreasing rate at high temperatures could also be due to an activated etching process whose rate increases with increasing temperature and becomes the dominant process at temperatures above 800°C. The fact that the {111}B rate was found to be low and relatively constant over the entire temperature range remains unexplained. One possibility is that an impurity is selectively adsorbed at the critical growth sites on the {111}B surface. Perhaps the answer may be found by a study of the effects of gas composition on epitaxial growth. This study is now in progress.

The variation of the deposition rates as a function of the substrate orientation is interesting. The high {111}A deposition rates attest to the ease of arsenic addition to the growing surface. For an ideal {111}A surface, an incoming arsenic makes fewer surface bonds than with any other orientation. However, this same {111}A surface has the greatest deposition rate for the reactant gas composition used in this study. The decrease in polarity effects is also obvious in this series as the surface deviates by greater amounts from a {111} toward the nearest {100}. Thus the differences between the A and B surfaces at 750°C were {111} = 85 μ/hr, {112} = 43 μ/hr, and {113} = 3 μ/hr. This trend confirms the earlier results which indicated no significant polarity effects for the {115} orientation. The increase in deposition rate in the vicinity of the {113}B orientation on the curve shown in Fig. 5 offers support for Sangster's theoretical predictions (3). Thus {113} is a favorable orientation for crystal growth since it tends to combine the good nucleation characteristics of a {100} with the favorable surface packing and stoichiometry of the {111}. Further clarification of the effects of orientation and surface polarity must await completion of the study concerning the effects of vapor composition on the deposition rate.

Acknowledgments

The author wishes to thank Mr. N. Tetlow for supplying the chemical equilibrium computer program used to construct Fig. 6. In addition, the assistance of Mr. D. G. Vieaux with the experimental work is acknowledged. Appreciation is extended to Drs. L. G. Bailey, R. C. Bracken, and G. O. Krause for their helpful suggestions and discussions.

Manuscript received Oct. 9, 1967; revised manuscript received *ca.* Nov. 20, 1967. This paper was presented in part at the Dallas Meeting, May 7-12, 1967, as Electronics Division Recent News Abstract 30.

Any discussion of this paper will appear in a Discussion Section to be published in the December 1968 JOURNAL.

REFERENCES

1. Kh. A. Magomedov and N. N. Sheftal, *Kristallografiya*, **9**, 902 (1964); [*Soviet Physics-Crystallography*, **9**, 756 (1965)].
2. R. A. Taylor, *This Journal*, **114**, 410 (1967).
3. R. C. Sangster in "Compound Semiconductors," pp. 241-253, R. K. Willardson and. H. L. Gorring, Editors, Reinhold Publishing Corp., New York (1962).
4. A. Reisman and R. Rohr, *This Journal*, **111**, 1425 (1964).
5. E. G. Bylander, *ibid.*, **109**, 1171 (1962).
6. G. F. Day, "Heterojunction Device Concepts," prepared for Air Force Avionics Laboratory, Contract AF 33(615)-1988, Varian Associates, September 1966.
7. D. E. Rosner and H. D. Allendorf, *This Journal*, **114**, 305 (1967).

Correction

In the paper by D. M. Brown, P. V. Gray, F. K. Heumann, H. R. Philipp, and E. A. Taft "Properties of $Si_xO_yN_z$ Films on Si," which was published in the March 1968 JOURNAL, pages 311-317, the head for Table I should read:

Table I. Physical properties of pyrolytic films

Effects of Phosphorus Diffusions in Epitaxial Silicon Layers

E. D. Wolley,*[1], R. Stickler, and T. L. Chu*[2]

Westinghouse Research Laboratories, Pittsburgh, Pennsylvania

ABSTRACT

The diffusion of phosphorus into epitaxial silicon has been investigated by evaluating the electrical and structural characteristics of the epitaxial diffused guard-ring junctions. The effects of stacking faults in epitaxial silicon on the junction characteristics were found to depend on the surface condition of the epitaxial layer before diffusion. Localized breakdown, as evidenced by light emission, was observed at the stacking fault grooves only when the epitaxial layer was etched before diffusion. Stacking faults were also found to be transformed into other defects after diffusion; chemical etching of the epitaxial layer also had a great influence on this transformation. Dislocations were observed in the phosphorus-diffused regions. The dislocations occur in hexagonal networks parallel to the diffusion front and come to the surface at the intersection of the junction and the surface in planar devices. Guarded junctions formed by these phosphorus diffusions exhibit localized breakdown with microplasma phenomena. The dislocation density was determined and correlated reasonably well with Prussin's model.

The diffusion technique is used in the further processing of epitaxial silicon for the fabrication of many devices. The diffusion of dopants into silicon crystals to yield high surface concentrations is known to generate dislocations in the crystal (1-8), and a model relating the distribution of dislocations to the diffusion profile has been proposed by Prussin (1). Since other structural defects, such as stacking faults, are frequently present in epitaxial silicon, these defects may undergo transformation during the diffusion process and affect the device performance. In this work, the effects of the diffusion of phosphorus into epitaxial silicon have been studied by evaluating the electrical and structural characteristics of epitaxial diffused planar junctions. The experimental approaches and results are discussed below.

Experimental

A guard-ring test junction shown in Fig. 1 was used for the study of the effects of phosphorus diffusion into epitaxial silicon. This junction design was first used by Goetzberger *et al.* (9) to evaluate resistivity variations in silicon crystals by observing light patterns associated with the reverse breakdown of fabricated devices. In the guarded junction device the outer or guard junction is diffused more deeply than the main central junction and thus has a higher breakdown voltage. The breakdown voltage of the central junction is not limited by surface breakdown or the cylindrical edge (10-13) of a planar junction. Because of the guard junction, the shallow junction would break down uniformly except for imperfections or localized resistivity variations. For visual observation it is necessary to have the shallow junction near enough to the surface (less than 1 μm) so that the light generated in the junction is not totally absorbed in the silicon.

Six groups of epitaxial silicon wafers were prepared for the fabrication of planar epitaxial diffused devices by depositing 15 μm of 0.1 ohm-cm p-type epitaxial layers on p-type substrates, as shown in Table I. Dislocation and stacking fault densities were determined by microscopic counts from one Sirtl etched wafer from each epitaxial group. Groups 1, 3, and 5 specimens were prepared under carefully controlled conditions, and the epitaxial layers were essentially free from stacking faults and had a dislocation density similar to that of the substrate. (Groups 1 and 3, however, were deposited on float-zone substrates and had relatively high dislocation densities.) In the other groups, the mechanical damage generated during the lapping of substrates was intentionally not completely removed, and the epitaxial layers had high concentrations of stacking faults, 3-6 $\times$ 10^4 cm^{-2}, and also high dislocation densities. The epitaxial material was diffused without any etching of the silicon, except for Groups 5 and 6 wafers which were etched, prior to diffusion, with the Sirtl etch (14). The Sirtl etch reveals dislocations and stacking faults in epitaxial silicon in the form of pits and grooves, respectively.

The epitaxial wafers were oxidized for 2 hr in wet argon at 1200°C. The oxide thickness was 12,000Å. A window with an I.D. of 50 μm and an O.D. of 640 μm was opened for the guard-ring diffusion, as shown in Fig. 1. A phosphorus predeposition was done for 30 min at 1000°C in an open-tube system using P_2O_5 as a source and nitrogen as a carrier gas. The P_2O_5 was removed by boiling in H_2O, leaving the original oxide. A redistribution diffusion of 4 hr at 1200°C was done with the first hour in a wet ambient. This gave guard junctions of 12-13 μm depth.

A window for the main junction was etched with a diameter of 410 μm centered over the guard-ring. A two-step phosphorus diffusion was carried out with the predeposition at 900°C for 30 min and the redistribution in a wet ambient for 20 min at 1000°C. The depth of the main junctions diffused in this way was less than 1 μm. A window for contact to the guarded structure, 130 μm I.D. and 380 μm O.D., was etched, and an aluminum layer was vapor deposited. Aluminum was removed from all areas except in the window and then alloyed at 605°C.

For most examinations a pressure contact was made to the devices with a fine tip probe. Reverse voltage was applied to the junction and the breakdown light observed through a light microscope. In order to obtain smaller working distances and to allow observations at greater magnification, some devices were mounted

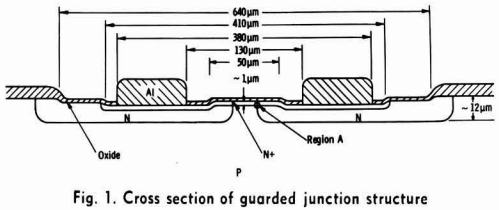

Fig. 1. Cross section of guarded junction structure

* Electrochemical Society Active Member.

[1] Present address: Semiconductor Division, Westinghouse Electric Corporation, Youngwood, Pennsylvania 15697.

[2] Present address: Electronic Sciences Center, Southern Methodist University, Dallas, Texas 75222.

Table I. Epitaxial layers for guarded junction devices

Group	Surface type and resistivity	Substrate treatment	Resistivity of epitaxial layer, ohm-cm	Defects in epitaxial layer
1	Float zone	Chemical polish		1.6×10^4 disloc./cm^2
	200 ohm-cm, p	to remove 50 μm	0.1	1 stacking fault/cm^2
2	Float zone	Chemical polish		1.6×10^4 disloc./cm^2
	200 ohm-cm, p	to remove only 10 μm	0.1	3.6×10^4 stacking faults/cm^2
3	Float zone	Chemical polish		1.6×10^5 disloc./cm^2
	25 ohm-cm, p	to remove 50 μm	0.1	4 stacking faults/cm^2
4	Float zone	Chemical polish		2.2×10^5 disloc./cm^2
	25 ohm-cm, p	to remove only 10 μm	0.1	5.8×10^4 stacking faults/cm^2
5	Czochralski	Chemical polish		160 disloc./cm^2
	1 ohm-cm, p	to remove 50 μm	0.1	3 stacking faults/cm^2
6	Czochralski	Chemical polish		6×10^5 disloc./cm^2
	1 ohm-cm, p	to remove only 10 μm	0.1	6×10^4 stacking faults/cm^2

on TO-18 headers with gold leads bonded to the aluminum alloyed ring contact.

Replica and thinning techniques of sample preparation for the examination of stacking faults and dislocations by the transmission electron microscope (TEM) method have been described elsewhere (15, 16). Transmission electron micrographs will be referred to as TEM. Specimens for light microscope observation were prepared by dissolving the oxide in HF and etching very lightly (5-10 sec) in Sirtl etch (14). Light micrographs will be designated as LM.

Results

Generation of light in reverse breakdown.—In nearly all of the phosphorus-diffused guarded junctions under reverse breakdown, microplasmas (9, 17) were observed at the periphery of the junction, *i.e.*, the intersection of the shallow n^+ diffusion and the guard junction. This region corresponds to the region labeled A in Fig. 1, and as seen from the figure, occurs inside the step in the surface caused by the oxidation during the redistribution diffusion of the guard junction. These microplasmas can be seen in Fig. 2. In some phosphorus-diffused junctions, the concentration of microplasmas at the periphery was more prevalent than in others. Most junctions had at least a few microplasmas in this region. In other devices of Group 1 through 3, microplasmas appeared randomly distributed as shown in Fig. 2(b). The wafers of Groups 1 through 3 all showed microplasmas distributed either randomly or at the periphery as shown in Fig. 2. No pattern characteristic of stacking faults was observed on Group 2 wafers. Again, note that the extent of the breakdown region in Fig. 3(c) is smaller than the step in the silicon surface visible in Fig. 3(a).

Groups 5 and 6 were etched prior to diffusion of the guarded junctions with the Sirtl etch in order to reveal the stacking faults and dislocations. The light emission from the junctions of Group 6 which contained a large number of stacking faults are shown in Fig. 3. Note that the light appears to come from the bottom of the etch groove of the stacking fault and the bottom of the dislocation etch pits. Thus light comes from only part of the stacking fault on the left center and none from the one on the right center. As the reverse voltage was increased, light first appeared in one of the dislocation pits (at B in Fig. 3(b)). Figure 3(c) shows that as the voltage was further increased, light appeared in the other dis-

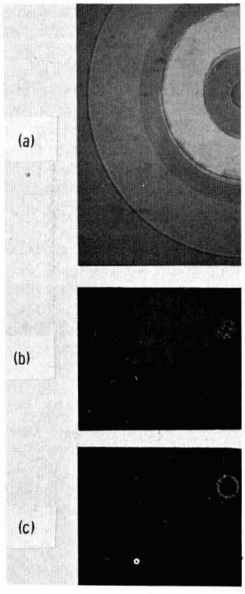

Fig. 2. Microplasma from epitaxial, phosphorus-diffused guarded junctions, epitaxial layer not etched before diffusion: (a, top) guarded N^+P junction with aluminum contact, (b, center) randomly distributed microplasma from a Group 2 wafer, and (c, bottom) microplasma concentrated at the periphery of a junction (region A in Fig. 1) on a Group 1 wafer.

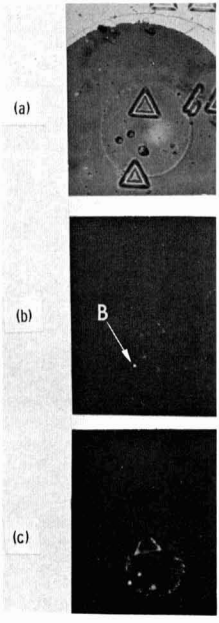

Fig. 3. Microplasmas from epitaxial, phosphorus-diffused, guarded junctions, epitaxial layer etched before diffusion, a Group 6 wafer: (a, top) etch figures by using bright field illumination with no applied bias, (b, center) light generated in one dislocation pit just above the breakdown voltage and (c, bottom) light generated in dislocation pits, stacking fault grooves, and the device periphery at voltages considerably above the breakdown.

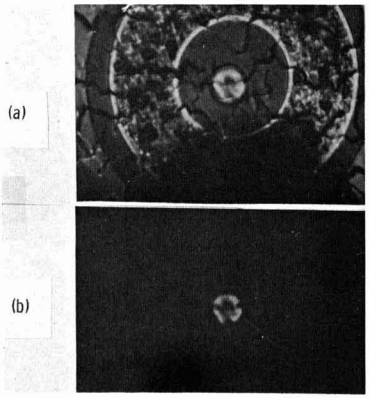

Fig. 4. Light emission from a device on a Group 4 wafer: (a, top) breakdown generated light with bright field illumination, and (b, bottom) breakdown generated light only. No patterns characteristic of stacking faults were observed.

location pits and the stacking fault groove and finally the microplasma at the periphery appeared.

Figure 3 shows that the light associated with the stacking fault appears to be continuous lines not made up of individual points and is more intense at the apices of the fault. Observations as a function of applied reverse voltage showed that the light appeared at the apices before it appeared in the grooves.

Group 4 wafers which also had a large number of stacking faults and dislocations, but were not etched prior to diffusion, did not show any of the well-defined triangular patterns observed in the Group 6 wafers, but yielded diffusion patterns of light modified by the rough surface structure evident in Fig. 4. The lack of well-defined triangular patterns is also evident in Fig. 2 which shows a device from a Group 2 wafer. Group 2 wafers were not etched prior to diffusion.

Dislocation generation in the diffusion process.—Figure 5 shows an alignment cross after diffusion treatment, oxide mask removal in HF, and a short Sirtl etch. Many small pits can be observed in the cross areas as well as in a region approximately 20 μm outside the cross area. In Fig. 6 a network of fine lines can be seen running from the cross area into the surrounding regions protected during diffusion by the oxide mask. These lines always end at a small pit. The cross section and the phosphorus concentration profile in the double-diffused region is also given schematically in Fig. 6. Region A indicates the undiffused area, region B the area under the oxide mask of the first diffusion treatment which was phosphorus-diffused by the lateral double-diffused area underneath the second oxide mask, and region E the double-diffused area. The surface steps resulted from the oxidation treatment to form the various oxide masks.

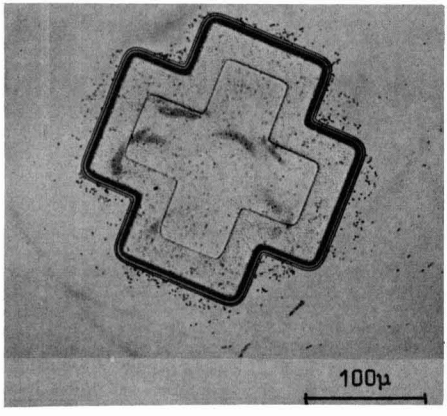

Fig. 5. Alignment cross on a Group 3 wafer after the oxide removal and a 1 min Sirtl etch. Note that the etch figures are concentrated only in and near the phosphorus-diffused areas.

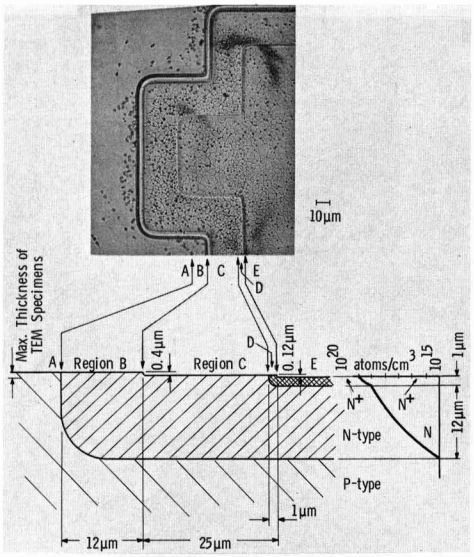

Fig. 6. Schematic cross-section through phosphorus-diffused epitaxial layer shown in Fig. 5. Schematic phosphorus concentration profile is on the right.

After light microscope examination, similar areas on the same wafer were thinned from the substrate side for TEM examination. The maximum thickness of a TEM specimen is indicated in Fig. 6, from which the layers examined by TEM can be deduced. Figure 7 is a TEM from an area close to the outer edge of the alignment cross. Dislocation lines and networks are revealed in the region B, see Fig. 7(a). In the single-diffused region C, see Fig. 7(b), several dislocation networks of varying mesh size appear to be arranged on top of each other, Fig. 7(b). In the TEM of Fig. 7(c), the regions C, D, and E are visible. Clearly, a decrease in the network mesh size in region D can be seen, while remnants of coarse and fine networks are present in the double-diffused region E. The smaller mesh size in region D can be explained by a phosphorus concentration gradient parallel to the layer surface due to lateral diffusion underneath the oxide mask.

Modification of stacking faults.—The appearance of a test diode area in the epitaxial layers containing high numbers of stacking faults (Group 4 wafers) after oxide removal and a short Sirtl etch is shown in Fig. 8. Stacking fault triangles can be seen in the undiffused regions. However, in the diffused regions the stacking fault triangles are completely absent. Only a few traces of stacking fault lines in the single-diffused region can be seen, while in the double-diffused regions numerous faint lines oriented along <211> directions ending in small etch pits can be seen. The star-like configuration of the lines seen in Fig. 8 are almost exactly the same size as the stacking fault triangles. This suggests a correlation of the stars to the former sites of the stacking fault tetrahedrons. The faint lines may represent the remaining crystallographic defects after a rearrangement in the fault area during the diffusion treatment.

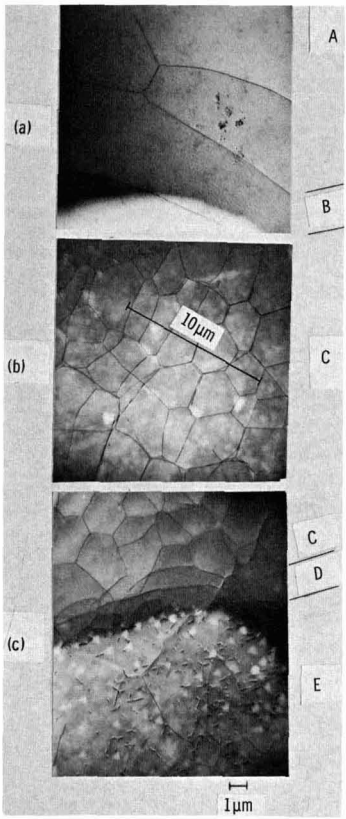

Fig. 7. TEM of various regions shown in Fig. 5 and 6. The letter designations at the right identify the regions labeled in Fig. 6: (a, top) low dislocation density region A, (b, center) note the superposition of networks of different mesh sizes, (c bottom) note the smaller mesh density in region D.

Further evidence of the modification of stacking faults after diffusion is shown in Fig. 9. A phosphorus-diffused epitaxial layer that had been etched prior to diffusion to reveal the stacking fault defects was etched a second time after the diffusion. The initially sharply grooved etch lines became flat-bottomed. In addition, many faint lines were revealed, oriented along <211> directions and ending in small pits.

Figure 10(a) is a TEM typical of stacking faults in epitaxial wafers which were not phosphorus-diffused. Figure 10(b) is a TEM of the remnant of a stacking fault in a phosphorus-diffused wafer of Group 4. The banded contrast of Fig. 10(a) and the absence of it in Fig. 10(b) is typical of all the observations. Note that in Fig. 10(b) one of the dislocations of the network generated by phosphorus diffusion is parallel to the stacking fault remnant indicating the possibility of some sort of interaction of the fault and dislocation. A TEM of the bottom of a stacking fault groove of a phosphorus-diffused region of a Group 6 wafer is shown in Fig. 11. The dislocations tend to lie in <211> directions which is the same as shown in the LM of Fig. 9.

Discussion

In the groups of wafers which were not Sirtl etched before diffusion, microplasmas were observed predominately near the periphery of the guarded diode (at A in Fig. 1). A plausible explanation for these microplasmas is that they occur at dislocations generated during the phosphorus-diffusion of the guard

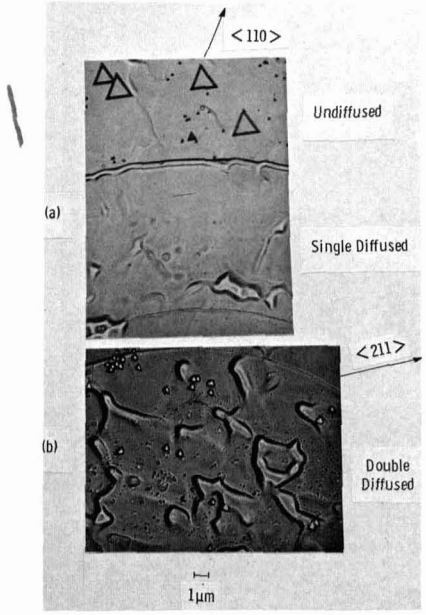

Fig. 8. LM showing the etch figures of a Group 4 wafer Sirtl etched after the phosphorus diffusion. The stacking fault grooves in the undiffused region and the remnant of a stacking fault (single straight line) in the single-diffused area (region C in Fig. 6) are shown in (a, top); (b, bottom) shows details of a double-diffused area, note fault lines ending in small etch pits often pointing in three <211> directions.

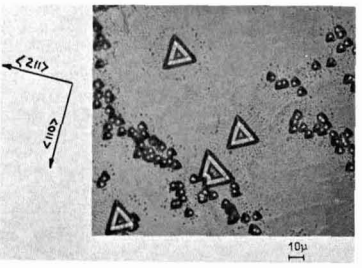

Fig. 9. Etch figures in a phosphorus-diffused epitaxial layer, Sirtl etched prior to diffusion. Note the flat-bottomed triangle etch grooves and faint lines in <211> directions ending in small etch pits.

junction. The generation of these dislocations could result from the phosphorus diffusion itself, as discussed later in this section, and/or from strain resulting from the difference of coefficient of expansion of Si and SiO_2 (18). Region A of Fig. 1 corresponds to the boundary between the regions A and B of Fig. 6 where the dislocations are inclined to the surface because the phosphorus gradient of the guard junction diffusion is perpendicular to the surface. Thus these dislocations would intersect the shallow junction and possibly serve as sites for localized breakdown.

Regarding the light associated with the stacking faults and dislocation etch pits of wafers etched before diffusion, one explanation is that breakdown occurs because of the curvature of the junction (10-13) resulting from the surface contouring. Evidence of the effect of etching on surface topography can be seen in Fig. 12. The groove profile was deduced from the contrast effects produced by shadow casting the Si surface with Pd (at an angle of 45°) prior to the

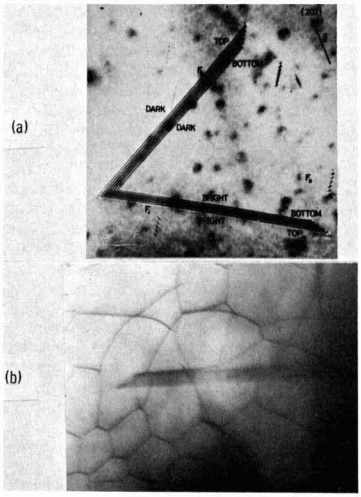

Fig. 10. (a, top) TEM of stacking faults showing banded contrast typical of undiffused material, (b, bottom) TEM of a remnant of a stacking fault in phosphorus-diffused area of a Group 6 wafer (same as diffraction condition).

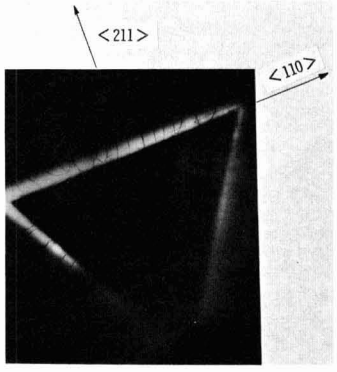

Fig. 11. TEM of the bottom of an etch groove of a Group 6 wafer. Note that dislocations tend to be in <211> directions. Only the bottom of the groove can be seen because other areas are too thick for electron transmission.

carbon deposition for a replica. This contrast was interpreted as shown in Fig. 13(a) which allowed a determination of the depth of the etch groove. As can be seen from the schematic in Fig. 13(b), the outer slope of the etch groove deviates only slightly from the (111) stacking fault plane, while the inner, heavily faceted slope seems not to correspond to any low-index crystal plane. Sharp lines at the bottom of the grooves are clearly visible, revealing the V-shaped form of the groove.

Since the main junction of the guarded junction is 1 μm or less deep, it can be seen from Fig. 13(b) that the junction will have a small radius of curvature at the bottom of the groove and will consequently have a lower breakdown voltage. It is also apparent from Fig. 12(a) that the curvature of the diffused junction at the intersection of the grooves will be greater than along the grooves themselves. Thus the light from reverse breakdown would appear first and be more intense at these points as was observed in Fig. 3. Queisser and Goetzberger (19) observed light only from the apices of stacking faults. Since in their samples they did not observe light from all apices they conjectured that the breakdown might be due to

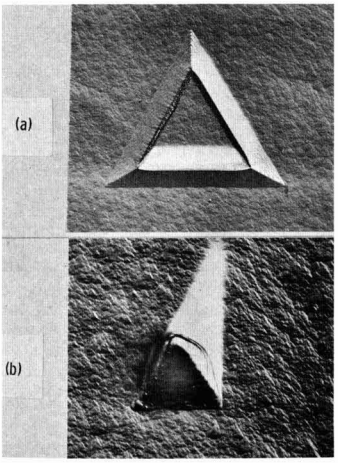

Fig. 12. Electron micrograph of a direct carbon replica of a Group 6 wafer showing (a, top) a stacking fault etch groove, and (b, bottom) a dislocation etch pit.

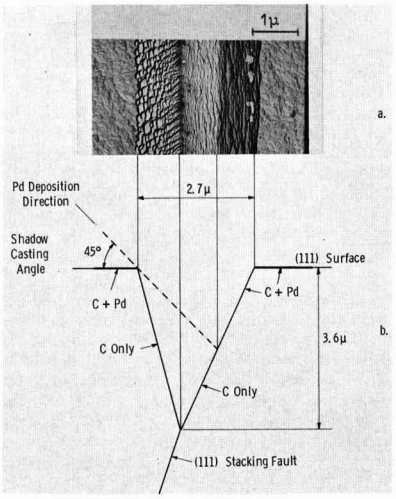

Fig. 13. Profile of a stacking fault etch groove resulting from the Sirtl etch of an epitaxial silicon layer. (a, top) Electron micrograph of direct carbon replica of etch groove along stacking fault, (b, bottom) schematic cross-section of epitaxial layer showing contrast features in etch groove due to shadow casting.

precipitates such as heavy metals or SiO_2 at the stair-rod dislocation bundles that exist there. Since the stacking faults were visible in the micrographs of their diodes, the wafers were undoubtedly subject to some etching during the processing and thus breakdown at the apices might occur for the same reasons (*i.e.*, curvature of the junctions) postulated above. On the other hand, in our junctions dislocations were present in the grooves as well as at the apices, and thus precipitation at the dislocations or the dislocations themselves might also be responsible for the preferential breakdown.

The uniformity of the light from the grooves favors the curved junction hypothesis. Further support for this hypothesis comes from the fact that no light emission corresponding to stacking faults was evident in those wafers which were etched prior to diffusion. However, this argument may be partially negated by the difference in the configuration of dislocations gen-

erated in the two types of wafers during the diffusion process (compare Fig. 10 and 11).

We also feel that the curved junction hypothesis is the explanation for the intense light observed at the dislocation pits such as seen in Fig. 3. The curvature of the junction at the bottom of such a pit should be large as is apparent from the replica of a dislocation pit shown in Fig. 12(b).

We do not intend to argue that breakdown cannot occur at dislocations. In fact, it appears likely that the breakdown at the edge of the guarded junctions occurs as a direct or indirect result of the dislocations generated ahead of the phosphorus-diffusion front during the diffusion of the deeper guard junction or at the edge of the oxide window (18). The fact that dislocations occur beyond the extent of the phosphorus diffusion under the oxide can be determined from Fig. 6. In Fig. 3(c) it will be noted that the microplasma which might be associated with these dislocations is less intense and occurs at a higher reverse voltage than the light associated with the dislocation etch pits in the central part of the junction.

The total number of dislocations generated by the two-step phosphorus diffusion shown in Fig. 7 agrees quite well with the model proposed by Prussin (1). Prussin derives a formula for the total number of dislocations N per unit length in a diffused layer which is given by

$$N = \beta/\alpha\,[C_s - C(b)] \qquad [1]$$

where β is the linear lattice contraction coefficient, α is the component in z direction (any arbitrary direction in the plane of the diffusion), C is the surface concentration of the solute, and $C(b)$ is the concentration at the point b, which is a point in the direction of the diffusion at which the strain from the point to the surface is relieved by the generation of dislocations. If as in a TEM examination of a relatively deeply diffused layer we look at a region of thickness t which is less than b, then [1] becomes

$$N = \beta/\alpha\,[C_s - C(t)] \qquad [2]$$

The thickness of the specimen examined by TEM lies between 0.5 and 1.0μ. We assume that the maximum value of t in [1] which would influence the generation of dislocations in this layer would be about 1.5μ. The diffusion profile calculated from the sheet resistivity junction depth and background resistivity using Irving's (20) curves and assuming a Gaussian distribution is

$$C = 2 \times 10^{20} \exp\left[\frac{-x^2}{13.8}\,\mu^2\right]$$

from which $C_s - C(1.5\mu) = 3 \times 10^{19}$. The linear contraction is given by

$$\beta = \left[1 - \frac{r_{sol}}{r_{Si}}\right] N^{-1} \qquad [3]$$

where r_{sol} is the radius of the solute, r_{Si} is the radius of the silicon, and N is the atom concentration of silicon (5×10^{22} atom/cm^3). Lawrence (7) calculates β using a volumetric contraction or $\beta = [1 - (r_{sol}/r_{Si})^3]\,N^{-1}$ which appears inconsistent with the model of Prussin. Using Queisser's (2) proposed value of 1.07Å for the radius of the ionized phosphorus donor and 1.17Å for the radius of silicon and [3], β equals 1.7×10^{-24} cm^3/atom.

Joshi and Wilhelm (5) determined that the dislocations forming regular hexagonal arrays in phosphorus-diffused wafers were almost pure edge type. If we assume the dislocations in Fig. 7 are almost pure edge type and measure the number of dislocations per centimeter (N) in a plane perpendicular to the dislocations, then α is equal to the magnitude of the Burgers vector, or approximately 4×10^{-8} cm.

Substituting the above values of α, β, and $C_s - C(1.5\mu)$ into [2] gives $N \sim 1 \times 10^3$ dislocations/cm. In Fig. 7(b) there are 7 lines crossing the line perpendicular to the dislocations which is 10μ in length yielding a value of 7×10^3 dislocations/cm for N. The agreement between the measured and calculated values of N is relatively good considering the approximations involved. Joshi and Wilhelm (5) also found reasonably good correlation between the density of dislocations near the surface and that calculated from Prussin's model.

The fact that there is some sort of transformation of stacking faults in epitaxial layers, both as-grown and Sirtl-etched before diffusion, is evident from the LM and TEM results. The fact that etch grooves were not developed by the Sirtl etch in the as-grown wafers and became flat-bottomed in the previously Sirtl-etched wafers indicates a change in the lattice energy associated with the stacking faults. Further evidence of some rearrangement of the lattice structure is evident from the change in contrast patterns of the stacking fault after phosphorus diffusion as shown in Fig. 10. Further evidence of a relationship between stacking faults and dislocations are the star-like patterns observed in Fig. 8 and the lines perpendicular to the fault sides in Fig. 9.

It has been shown that this transformation takes place only in the phosphorus-diffused regions. Thus it is probable that the transformation is a result of interaction of the stacking faults with the dislocations generated by the phosphorus diffusion. There is some evidence for such a hypothesis in that a dislocation line is parallel to the stacking fault remnant in Fig. 10(b).

We propose the interaction of dislocations and stacking faults and dislocations generated by the phosphorus diffusion as a possibility for the transformation and not as a model. The exact mechanism of the transformation cannot be deduced from this work.

Summary and Conclusions

1. Microplasmas were observed most frequently near the periphery of the phosphorus-diffused guarded junctions. These microplasmas may have resulted from dislocations generated by the phosphorus diffusion of the guard junction intersecting the shallow-diffused junction.

2. No light from preferential breakdown characteristic of the pattern of stacking faults was observed in wafers which were not etched prior to diffusion. Figure 2(b) is typical of devices on such unetched wafers and shows no triangular patterns.

3. In wafers Sirtl-etched before diffusion, light was observed at the bottom of stacking fault grooves and dislocation etch pits. The preferential breakdown was attributed to the curvature of the shallow junction resulting from the junction following the surface contour.

4. The density of dislocations generated as a result of the mismatch of the atomic radii of phosphorus and silicon and the gradient present from the diffusion process was determined and compared with the model of Prussin. Experimental and calculated values compared favorably.

5. A change in the nature of stacking faults resulting from phosphorus diffusion was observed. From etching results it was concluded that the lattice energy as associated with the fault was decreased or redistributed.

Acknowledgments

The authors wish to thank H. F. John for suggesting and encouraging this work. We also acknowledge the assistance of S. Hillbeck in the diode fabrication and analysis, and of W. Hughes in the preparation of TEM and LM specimens. Figure 10(a) was provided by Dr. G. R. Booker, University of Oxford. This work was supported in part by NASA, George C. Marshall Space Flight Center, under Contract NAS8-11432.

Manuscript received Aug. 11, 1967; revised manuscript received Oct. 26, 1967. This paper was pre-

sented at the Buffalo Meeting, Oct. 10-14, 1965, as an Electronics Division Recent News Paper.

Any discussion of this paper will appear in a Discussion Section to be published in the December 1968 JOURNAL.

REFERENCES

1. S. Prussin, *J. Appl. Phys.*, **32**, 1876 (1961).
2. H. J. Queisser, *ibid.*, **32**, 1776 (1961).
3. G. H. Schwuttke and H. J. Queisser, *ibid.*, **33**, 1540 (1962).
4. J. Washburn, G. Thomas, and H. J. Queisser, *ibid.*, **35**, 1909 (1964).
5. M. L. Joshi and F. Wilhelm, *This Journal*, **112**, 185 (1965).
6. W. Czaja, *J. Appl. Phys.*, **37**, 3441 (1966).
7. J. E. Lawrence, *This Journal*, **113**, 819 (1966).
8. E. Levine, J. Washburn, and G. Thomas, *J. Appl. Phys.*, **38**, 81 (1967); **38**, 87 (1967).
9. A. Goetzberger, B. McDonald, R. Haitz, and R. M. Scarlett, *ibid.*, **34**, 1591 (1963).
10. Von K. H. Zschauer, *Z. Naturforsch.*, **19A**, 653 (1964).
11. S. R. Hofstein and G. Warfield, *IEEE Trans. on Electron Devices*, **ED-12**, 66 (1965).
12. G. Gibbons and J. Kocsis, *ibid.*, 193 (1965).
13. S. M. Sze and G. Gibbons, *Solid State Electronics*, **9**, 831 (1966).
14. E. Sirtl and A. Adler, *Z. Metallkunde*, **52**, 529 (1961).
15. G. R. Booker and R. Stickler, *Brit. J. Appl. Phys.*, **13**, 446 (1962).
16. R. Stickler, *J. Sci. Instruments*, **41**, 523 (1964).
17. J. M. Fairfield and G. H. Schwuttke, *J. Appl. Phys.*, **37**, 1536 (1966).
18. R. J. Jaccodine and W. A. Schlegel, *ibid.*, **37**, 2429 (1966).
19. H. J. Queisser and A. Goetzberger, *Phil. Mag.*, **8**, 1063 (1963).
20. J. C. Irving, *Bell System Tech. J.*, **41**, 387 (1962).

Strain Effects Around Planar Diffused Structures

J. M. Fairfield* and G. H. Schwuttke

Components Division, International Business Machines Corporation, East Fishkill Laboratories, Hopewell Junction, New York

ABSTRACT

Dislocations have been found to extend for considerable distances outside of planar diffused structures in silicon and to affect the electrical properties of the diffused junctions. The mechanism of dislocation propagation outside of phosphorus-diffused structures has been studied by x-ray diffraction microscopy and other techniques. It is shown that these dislocations are propagated through an anomalously large compressive stress that results from large strains in some high-concentration phosphorus-diffused structures. These strains cannot be attributed to the residual effects of substitutional phosphorus atomic mismatch with the silicon lattice. The anomalous stress and dislocations usually appear after an oxidizing diffusion or drive-in cycle at temperatures less than 1150°C. Also, the dislocations are much less likely to occur in (100) or (110) oriented surfaces as opposed to (111) surfaces.

In the semiconductor industry, impurity diffusion is a very common fabrication process for transistors and diodes. Typical diffusions result in localized lattice strain, which often is relieved through the formation of dislocations and other lattice disorder. Principally, the strain is believed to result from the mismatch between the ionic radius of an impurity atom that is occupying a substitutional site and the covalent radius of the silicon (1, 2). The dislocations usually appear as dislocation networks confined within the diffused structure and often are accompanied by precipitation effects, which may also relieve the crystallographic strain. This type of crystal disorder has been widely studied, particularly for phosphorus and boron as the diffusants, by employing a variety of techniques (3-11). In addition, other investigators have reported that dislocations may propagate outside the diffused areas: both below the diffusion front and, for planar structures, laterally under the oxide diffusion mask (12-16). This latter phenomenon is important in semiconductor device fabrication since these dislocations would extend through the electrical junctions of the devices and have potential deleterious effects on the electrical characteristics of the devices.

There has been some confusion about these "outside" dislocations (*i.e.*, outside the diffusion structure) with respect to (*i*) their nature, (*ii*) the mechanism by which they form and propagate, and (*iii*) the conditions under which they occur. However, recently these questions have been at least partially clarified and resolved. In an earlier report (16) we presented evidence that the dislocations outside the diffused structure are distinct from and often in addition to the diffusion-induced dislocation networks within the structure and that they nucleate at the boundaries of the planar structures and propagate outward. Also, Schwuttke and Wilhelm (17) have recently confirmed by electron microscopy that the dislocations of the networks within the diffused area bend up to the surface at the planar boundaries and do not extend significantly into the undiffused regions.

The outward propagation of the outside dislocations is by means of macroscopic stress transmitted from the diffused structure. Lawrence (18) has suggested that this stress results from relatively small residual strains not fully relieved by crystal disorder within the diffused area. He further states that, in otherwise unstrained material, the residual strain necessary to nucleate outside dislocations is only realized when the total concentration of diffusant is greater than about 5×10^{16} cm^{-2} for both boron and phosphorus. However, Duffy *et al.* (19) have observed these outside dislocations for total concentrations less than 3×10^{16} cm^{-2} of phosphorus. Furthermore, recent measurements of lattice contraction by Cohen (20) tend to indicate that the maximum stress in diffused areas, similar to those investigated by both Lawrence and Duffy, is in itself not excessively greater than the yield stress of silicon at elevated temperatures, which is about 2×10^9 dynes/cm^2, as estimated from an extrapolation

Key words: semiconductor, silicon, diffusion, dislocations, stress, strain.

* Electrochemical Society Active Member.

of data of Pearson *et al.* (21) or from the investigations of Patel and Chaudhuri (22).

It would seem improbable that smaller residual strains would generate sufficient stress to nucleate and propagate dislocations to significant distances outside the diffused areas. Joshi *et al.* (23) have reported residual strains in phosphorus-diffused areas of $\sim 4 \times 10^{-4}$ which would result in stresses that are marginally sufficient for dislocation formation; however, these authors have apparently used total concentrations well above 5×10^{16} cm^{-2}. Thus, the conditions and the mechanism by which the dislocations form outside the diffused structure are still unclear, and further study is required.

These outside dislocations, around the periphery of diffused emitters (emitter edge dislocations) have been directly correlated with a reduction in transistor grain (β or h_{fe}) (19, 24). In addition, since they extend through the base of a transistor, they may encourage emitter-to-collector shorts, i.e., pipes, through a possible localized dislocation-enhanced diffusion mechanism (25). Also, they may influence the characteristics of the collector junction. Indeed, Loro (26) has reported a collector junction degradation that can be attributed to dislocations extending through the collector junction caused by the emitter diffusion. Finally, for the case of modern integrated circuitry, this type of dislocation may extend from one device or isolation diffusion into another and create potential coupling problems. Therefore, we have further investigated these outside dislocations, principally for boron and phosphorus as diffusants, with emphasis on understanding both the mechanism and the control of their formation. We have studied the nucleation and propagation of these dislocations and their relationship to diffusion conditions, crystal disorder inside the diffused structure, and the macroscopic strains as independently determined. This report describes our investigation.

Experimental Procedure

Silicon slices were cut from dislocation-free Czochralski or Lopex single crystals, lapped, and chemically polished to remove surface damage and strain. Wafer orientations were mainly (111), but (110) and (100) orientations were used in a few specific experiments; thicknesses were between 0.5 and 1.0 mm.

Both blanket diffusions over entire wafers and planar diffusions using standard oxide masking techniques were performed; masking oxides were grown in steam at 1000°C. Most diffusions were accomplished by a two-step process consisting of a deposition and a drive-in cycle similar to that reported previously (19, 27). The deposition cycle was 970°C for phosphorus and 1100°C for boron; impurity sources were phosphorus oxychloride, phosphorus pentoxide, or diborane; and the ambient was nitrogen with a small amount (~1%) of oxygen. The drive-in cycle was usually 970°C for 1¼ hr in an oxidizing ambient; however, some experiments were conducted using temperatures of up to 1200°C with decreasing times. Also, inert ambients were used for a few special experiments. Finally, some diffusions were made using the evacuated capsule technique (28) with a powdered silicon alloy as the source and, generally, with similar times and temperatures as above, though a few such diffusions were made for very long times.

Junction depths were measured by beveling and copper staining, and sheet resistances were measured by a four-point probe. In all cases, the surface concentrations were at, or very near, saturation. An example of a phosphorus profile is shown in Fig. 1. The total concentrations were determined by activation analysis [see ref (19)]; and the electrically active concentrations were determined by incremental sheet resistance measurements (29) and an extrapolation of Irwin's curve to these high concentrations. The electrically active curve is an approximation, since the accuracy of this extrapolation is uncertain; however, it would be safe to say that a significant amount of phosphorus is not electrically active and thus exists in a state other than substitutional, in agreement with pre-

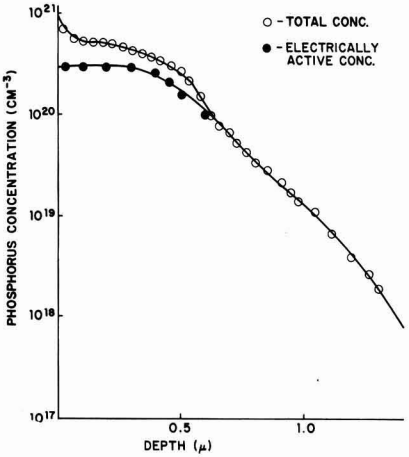

Fig. 1. Diffused phosphorus concentration profiles after a drive-in cycle of 1¼ hr at 970°C in an oxidizing ambient. Total concentrations were determined by activation analysis, and electrically active concentrations were determined by incremental sheet resistance measurements.

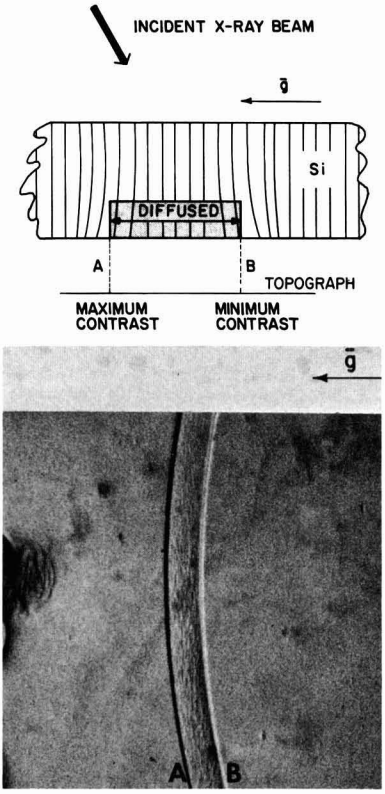

Fig. 2. Transmission diffraction contrast around planar diffused structures: a (top), schematic diagram of diffused structure exerting a compressive strain on surrounding crystal; b (bottom), x-ray topograph of similar structure.

vious investigations (29, 30). It is not possible to discuss strain contribution of a single representative atom because the state of a significant portion of them is unknown.

The crystallographic damage in and around the diffused areas was investigated by x-ray transmission diffraction microscopy, using scanning oscillator technique (SOT) (9) to record topographs of entire wafers, and by transmission electron microscopy (4, 8). SOT topographs were used extensively to study dislocation and precipitation structure in a manner described previously (9, 31) and to analyze strain effects as described in the next paragraph. Electron microscopy was used to examine the crystal structure of the surface layers of some representative samples. Specimens for electron microscopy were chemically thinned from the reverse side to about 2000Å.

Strain effects were determined by the sign of anomalous x-ray diffraction contrast around the boundary discontinuity of planar structures and by the degree of bowing induced in a wafer by a blanket-diffused layer on one side. For the first technique, Howard and Schwuttke (32, 33) have shown that the apparent sign of anomalous transmitted x-ray diffraction contrast (*i.e.*, either dark or light contrast for an anomalously strong or weak diffracted x-ray beam) can be used to determine the direction of lattice plane curvature, which is due to strains. Hence, the nature of anomalous x-ray contrast on SOT topographs can be used to determine the sense of lattice strain. An example is illustrated in Fig. 2a and b in which a diffused structure exerts a compressive strain on the surrounding lattice, bending the lattice planes in the indicated direction. Following Howard and Schwuttke, the diffracted contrast will be high when the diffraction vector $\bar{g}$ (or a significant component of $\bar{g}$) has the same direction as the radius of curvature of the strained lattice planes, as at point "A," and will result in a black line on the topograph, Fig. 2b. When the direction of $\bar{g}$ is opposite to the radius of lattice plane curvature, as at point "B," the contrast is low and results in a white line. Therefore, the white-black contrast across the diffused boundaries in the direction of $\bar{g}$ (Fig. 2b) is indicative of compressive strain around the diffused structure. Similarly a black-white contrast, in the same direction, indicates tensile strain. For the present study, this technique was used to determine the sense of the strain only although, in principle, it could be used for quantitative strain measurements as well.

In addition, the magnitude of the stress in a diffused layer was studied by measuring the degree to which a blanket-diffused layer macroscopically strains a wafer. The bowing of a wafer owing to a very thin diffused layer was determined by measuring wafer curvature before and after the layer was removed, employing a light section microscope and a technique developed by Glang *et al.* (34). The data were interpreted by regarding this diffused layer as a thin film of some other material deposited on the silicon wafer as the substrate and using elastic plate theory to analyze the stress-strain relationships of this system in a manner first used by Stoney (35) for thin deposited metal films, and subsequently improved and used by others for a variety of materials (36). Accordingly, the deflection δ of a circular wafer under strain from a thin film is given by

$$\delta = 3\left(\frac{1-\nu}{E}\right)\frac{t_f}{t_s^2}\rho^2\sigma_f \qquad [1]$$

where E and ν are Young's modulus and Poisson's ratio of silicon; t_f and t_s are the thicknesses of the film and substrate; ρ is the distance from the center; and σ_f is the stress in the film. Assuming $t_f << t_s$ and following Stoney's analysis, one can relate the maximum stress in the wafer to the film stress by

$$\sigma_s(\max) = -4\,\sigma_f\left(\frac{t_f}{t_s}\right) \qquad [2]$$

Equations [1] and [2] can be used to relate deflection to stress in the diffused layer and the wafer. For our application, very thin layers (0.1-0.3μ) were removed by anodic sectioning in order to determine the distribution of stress in the diffused layer. The effective ratio t_f/t_s was less than 10^{-3}; and the substrate can be considered as unchanged by the removal of the thin layers. Deflection measurements were taken every 25 mils along a $<\bar{1}10>$ and a $<11\bar{2}>$ diameter of (111) wafers to about 50 mils from an edge. The experimental uncertainty of each deflection measurement is $\pm 0.5\mu$ (34); and the final uncertainties can be judged accordingly.

Results

Generally, phosphorus diffusions, in which maximum or near maximum surface concentrations and oxidizing ambients were used, resulted in dislocations outside the planar diffused structure (*i.e.*, outside dislocations) even when the total electrically active phosphorus concentration was 2 x 10^{16} cm^{-2} or a little lower. Their formation was not significantly affected by the presence or absence of the original mask during drive-in. These dislocations have been described in ref. (16); and a detailed analysis of their physical structure will be published elsewhere. They are illustrated by the contrast pattern in Fig. 3a around the boundaries of the planar structures, which are the triangles and the circular area, and also by the relatively straight lines in the electron micrographs, Fig. 3b and c. The abnormal contrast within the planar areas in Fig. 3a and the network pattern at the extreme right of Fig. 3c are due to the normal, interior diffusion-induced dislocations. The occurrence of the outside dislocations can be directly related to the conditions of the process steps, as will be described in more detail later in this section.

The dislocations themselves appear as dislocation loops in the primary slip planes {111}. They extend laterally out into the undiffused regions for distances of ~300μ and perpendicularly down into the silicon for distances up to 20μ from the surface as shown in Fig. 4, in which the indicated amounts have been removed by controlling etching. (Note that the diffusion-induced dislocations within the diffused regions are confined to within 0.5μ of the surface or about 1/3 of the junction depth, in agreement with other investigators.) Therefore, the outside dislocations would extend well through the active regions of a transistor with this type of phosphorus diffusion as the emitter, and they should logically cause potential problems for transistor electrical properties through either a degradation of gain through carrier recombination in the base, poor collector junction quality, or pipes owing to an enhanced diffusion in the dislocation areas. The mode of dislocation propagation was primarily through slip in the plane of diffusion. It is interesting to note that the presence of metallic impurities tended to restrict the outward propagation of the dislocations. Figure 5 shows a topograph and an electron micrograph of outside dislocation loops where an excessive amount of gold was present. The loops appear to be pinned at specific points, presumably by small metallic precipitates that are smaller than the resolution of this micrograph, *i.e.*, <50Å. A similar phenomenon has been reported by Batavin (37), who found evidence that SiO_2 particles inhibited the propagation of dislocations outside of boron diffused areas.

Empirically, the presence of the outside dislocations was accompanied by an anomalous macroscopic strain effect associated with the planar diffused structure: in Fig. 3a, the white-black strain pattern across the windows in the direction of $\bar{g}$ is indicative of a com-

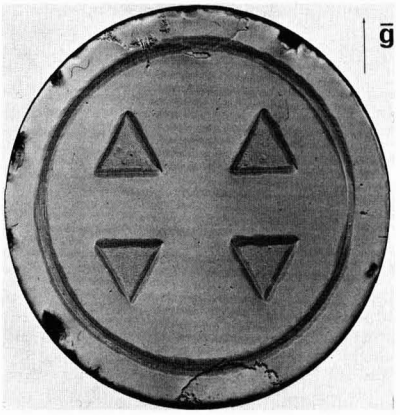

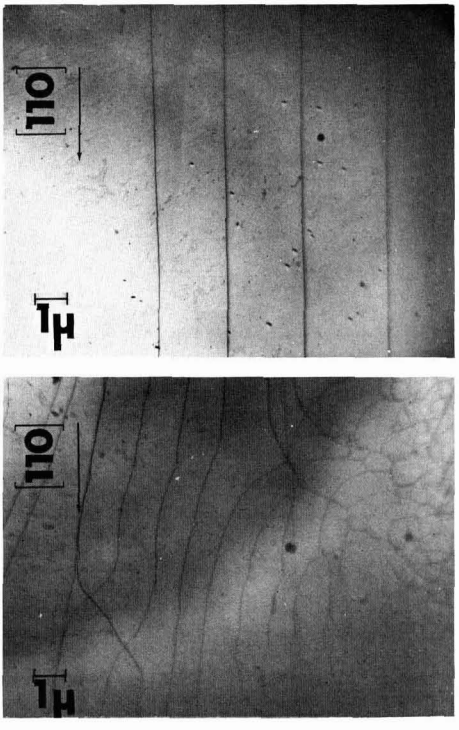

Fig. 3. High-concentration phosphorus structures; impurity profile and diffusion procedure are similar to that of the example in Fig. 1; triangle side = 0.5 cm: a (top), SOT x-ray topograph (220) reflection; b (center), electron micrograph of undiffused area about 60μ from diffusion boundary; c (bottom), electron micrograph of a small section at the planar boundary.

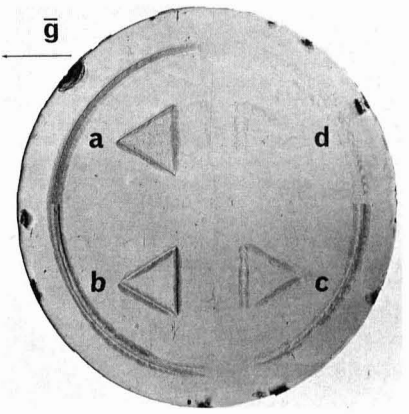

Fig. 4. SOT x-ray topograph of diffused structures similar to Fig. 3 with the following thicknesses of surface removed: a, nothing removed; b, 0.5μ; c, 10.0μ; d, 19.0μ.

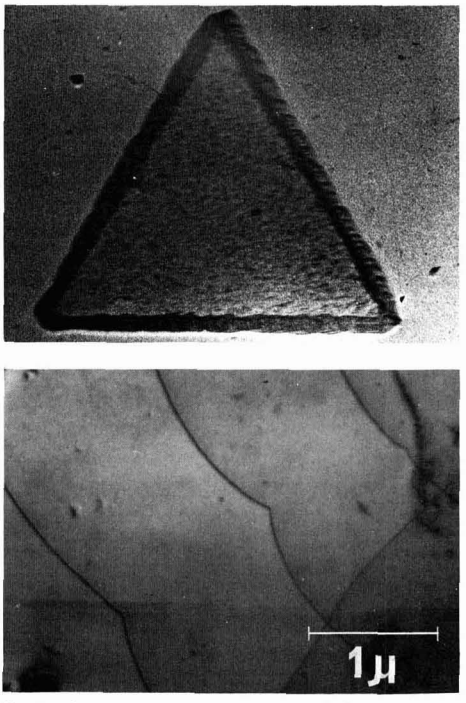

Fig. 5. Phosphorus diffused structures with large amounts of gold added: a (top), x-ray topograph; b (bottom), electron micrograph outside of diffused area.

pressive strain surrounding the diffused structure. However, as seen in Fig. 4, areas a and b, the stress switches to tensile when 0.5μ is removed from the surface. The compressive nature is unexpected since a substitutional phosphorus atom in the silicon lattice has a smaller ionic radius than the silicon covalent radius and should stretch the neighboring covalent bonds, resulting in a tensile strain effect around the periphery.

The actual compressive effect can be seen more clearly in Fig. 6b, which is the topograph of a two-cycle planar diffusion with only a very small amount of oxygen in the ambient of the drive-in cycle (970°C). Here is a case of stress that is anomalous in sense but not of sufficient degree to cause outside dislocations. Figure 6a is an x-ray topograph of the same structure with the oxide diffusion mask still on the wafer surface, indicating that the oxide mask opposes and, in this case, reverses the resultant strain. This is logical since the strain in a thermally grown oxide mask is compressive (38) and would tend to bend the lattice planes toward the center of a window (opposite to the case illustrated in Fig. 6b). In practice, when the anomalous strain, *i.e.*, compressive, approaches a value sufficient to cause outside dislocations, it dominates over the influence from the mask.

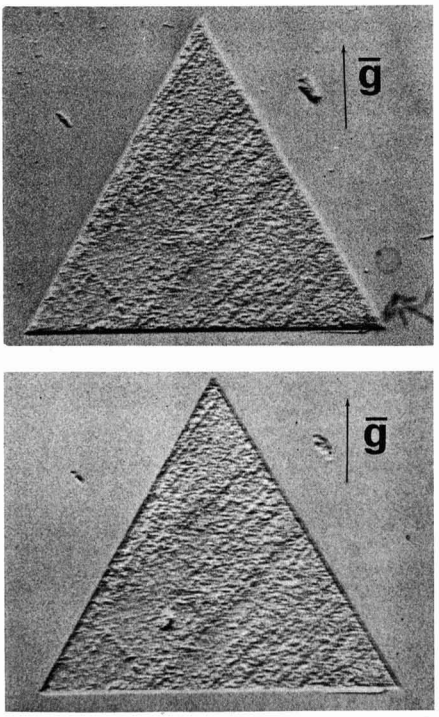

Fig. 6. SOT x-ray topograph of high-concentration phosphorus-diffused structures illustrating anomalous strain effects: a (top), oxide mask on wafer; b (bottom), oxide mask removed.

However, the formation of dislocations reduces its magnitude and may return the strain to a case dominated by the oxide mask; thus, the apparent strain, or stress, may switch sign according to the formation of dislocations or the removal of the mask, giving the effect of "stress jumping" (33).

Conversely, dislocations around boron diffused structures appear only for deep diffusions performed at the higher temperatures (1200°C) from maximum surface concentrations regardless of the diffusion technique used. Figure 7a is the SOT topograph of a section of planar boron diffused wafer whose profile is shown in Fig. 7b. The degree of dislocation around the outside is variable. Lesser junction depths, *e.g.*, $< 8\mu$ for a similar profile, yield much fewer or no dislocations. The dislocations extend for about the same distances as phosphorus but appear in a variety of forms.

Irrespective of dislocation formation, the strain around boron diffused structures was always tensile, as would be expected, since boron also has a small ionic radius relative to silicon. These dislocations around boron diffused structures were not studied as extensively, but they appear to be caused by tensile stress which may well result from residual strain effects of the substitutional boron atoms when total concentrations greater than 10^{17} cm^{-2} are involved.

Finally, the specific relationship of the phosphorus process steps to the anomalous strain will be described in the final paragraphs of this section. First in (111) oriented wafers, after an open-tube deposition cycle only, the macroscopic strain is anomalous in sign, *i.e.*, compressive, but not of sufficient magnitude to cause dislocations, a case similar to that shown in Fig. 6. After an oxidizing drive-in at lower temperatures, at about 1000°C, both dislocation and anomalous strain effects almost always appeared. The degree of stress in these phosphorus diffused layers was determined by measurements of bowing of blanket-diffused wafers,

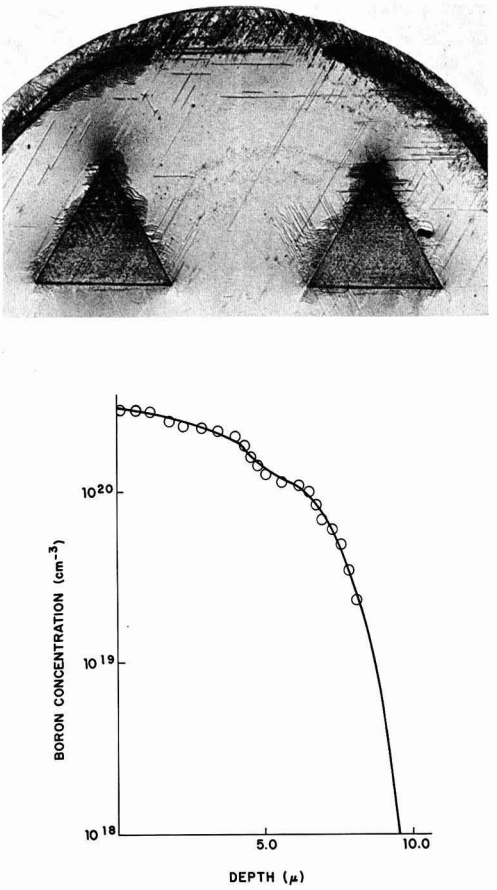

Fig. 7. a (top), SOT x-ray topograph of high concentration, deep boron diffused planar structure; b (bottom), electrically active impurity profile, total concentration is $\sim$ 1.3 x 10^{17} cm^{-2}.

whose diffusion utilized this two-cycle process with an oxidizing drive-in at 970°C. The stress was compressive, bowing the wafer down away from the diffused side, in agreement with that indicated by the sign of the x-ray contrast, and the values ranged from 3-8 x 10^9 dynes/cm^2. This high stress was confined to within about 0.5μ of the surface, confirming the apparent stress switching in Fig. 4 by the removal of 0.5μ of surface. Figure 8a shows the actual deflection of one wafer; each deflection value represents the average of two values taken at opposite points, *i.e.*, $+\rho$ and $-\rho$, in the manner of Glang *et al.* (34). Also shown are "deflection" values taken on an undiffused wafer to illustrate qualitatively the sensitivity for this application. The crystallographic direction, along which the deflection was measured, had no measurable influence. Figure 8b shows stress values on a few wafers as a function of distance from the surface. There is considerable scatter, sometimes even on the same wafer, but the values are generally equal to or greater than 3 x 10^9 dynes/cm^2, above the yield stress of silicon. By way of comparison, stress values in boron diffused layers were around 1.5 x 10^9 dynes/cm^2 and were tensile, as expected.

If inhomogeneous precipitation occurred within the phosphorus planar structure, the anomalous strain was less, and the peripheral dislocation loops were much less likely to occur. In particular, if many points of large precipitates appeared within the diffusion, shown

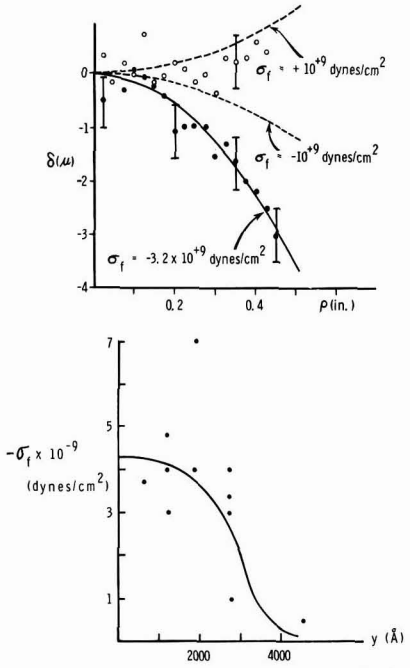

Fig. 8. Data from wafer bowing experiments: a (top), closed circles are deflection values of blanket phosphorus diffused wafer and open circles are similar measurements of an undiffused wafer; b (bottom), stress values as a function of depth in phosphorus diffused wafers.

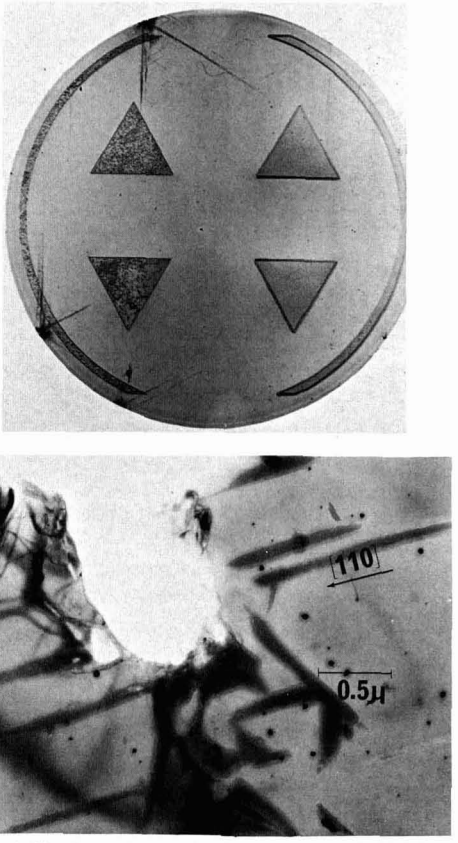

Fig. 9. Phosphorus planar diffused structures, two of which have large precipitates: a (top), x-ray topograph; b (bottom), electron micrograph of a section of one large precipitate, precipitate is indicated by white area since it dissolved during thinning operation.

in Fig. 9 by the points of abnormally high contrast in two of the planar triangles, the peripheral dislocations did not occur; and the macroscopic stress was tensile, in contrast to the normal case without large precipitates. These precipitates normally did not occur if the diffusion system was clean and reasonably careful procedures were employed. They appeared to be nucleated at or near the surface through contaminants or cool areas on the wafer during the deposition cycle. Sheet resistance and junction depth measurements showed that the electrically active phosphorus concentration was not significantly affected by the formation of the large precipitates. Figure 9b is a transmission electron micrograph of a section of one such large precipitate, which is amorphous in structure except for a small portion just outside the main precipitate which appears as platelets oriented parallel to {111} planes. Conversely, electron micrographs of interior areas of the more common planar structures, those that caused compressive strain and outside dislocations, revealed very few visible precipitates of any size. Since all of these high-concentration diffusions contain significant amounts of phosphorus in excess of that which is electrically active, as indicated by Fig. 1 and by the investigations of others (29, 30), excess phosphorus in the more common diffused structures must exist either interstitially as single atoms or in small clusters (<20Å).

In addition, certain modifications in the diffusion procedure could reduce or eliminate the peripheral outside dislocations. These conditions are, in themselves, significant; they are specified here and discussed in the next section. First, the dislocations usually did not occur on wafers oriented in the (100) or (110) plane though the strain was still compressive. Second, if the drive-in cycle utilized a nonoxidizing ambient, strain decreased significantly, sometimes switching to tensile; and the outside dislocations again did not form. Total concentrations were comparable to the case of an oxidizing ambient illustrated in Fig. 1 or for the wafer in Fig. 3. Third, if the drive-in cycle was done at higher temperatures (1150°-1200°C), regardless of the ambient the dislocations did not form; and the stress was tensile ($<10^9$ dynes/cm^2) even for concentrations greater than 5×10^{16} cm^{-2}. Finally the evacuated sealed capsule diffusion process did not produce the outside dislocation loops, except in a few cases where excessively long diffusion times were employed, which yielded junction depths of greater than 10μ. The strain around all these structures was tensile, similar to the case of boron. However, if a wafer was phosphorus diffused by a capsule technique with high surface concentration and subsequently oxidized at 1000°C, the outside dislocations appeared; and the strain switched to compressive. This did not happen for boron capsule diffused wafers.

Discussion

First, in order to relate the macroscopic stress measured experimentally in blanket-diffused layers to the stress in undiffused material around planar structures, the stress-strain conditions of the problem, which are illustrated in Fig. 10a, must be considered in some detail. In this way, the stress available for dislocation formation can be estimated and compared with the results.

The surface loading at the sides required to confine the planar structure is represented by F' in Fig. 10b, and a reactive force F is exerted on the undiffused material, also at the planar boundaries. The shearing

interaction in the x-z plane is of lesser degree owing to both the lower value of shearing modulus in silicon and the reduction of coherency across the x-z plane through the formation of the interior diffusion induced dislocation networks. Thus, the forces at the side boundaries of the planar structure are related to the stress in the film by

$$F' = -F \approx -\int_o^a \sigma_f \, dy \qquad [3]$$

where F is in units of force per unit length and a is the effective depth of anomalous stress. In order to find the stresses at a given distance r from the diffusion boundary, certain limitations of the dimensions can be made in order to simplify the problem. The dimensions of interest are greater than the electrical junction depth and roughly limited by the maximum dislocation propagation. Therefore, the problem can be restricted by

$$\begin{aligned} y_{(\max)} &\approx 20\mu << t \\ x_{(\max)} = z_{(\max)} &\approx 200\mu << D \\ x_{(\min)} = y_{(\min)} = z_{(\min)} &> 2a \end{aligned} \qquad [4]$$

where D represents the wafer diameter ($\sim$2 cm) and t represents the wafer thickness (>0.5 mm). Based on these limitations, we can regard the substrate as a semi-infinite body. Now the two-dimensional problem is treated by considering a thin (with respect to l) slab at $z = 0$ and analyzing the stress distribution around the origin, see Fig. 10b. It would be reasonable from inequalities [4] that the shear force can be considered as concentrated at the surface, *i.e.*, $a \to 0$. With this assumption, the problem is similar to that first solved by Flamant (39), following whom the stress distributions are

$$\begin{aligned} \sigma_x &= -\frac{2F}{\pi} \frac{x^3}{\left((x^2+y^2)\right)^2} \\ \sigma_y &= -\frac{2F}{\pi} \frac{xy^2}{\left((x^2+y^2)\right)^2} \\ \tau_{xy} &= -\frac{2F}{\pi} \frac{x^2 y}{\left((x^2+y^2)\right)^2} \end{aligned} \qquad [5a]$$

and the maximum shear stress would be given by

$$\tau_{(\max)} = \frac{-F}{\pi} \frac{x}{(x^2+y^2)} \qquad [5b]$$

The applicability of assuming that the force is concentrated at the surface can best be shown by actually considering a distributed stress. This is shown in the Appendix (see Eq. [6]), and it is seen that Eq. [5] can be used to estimate the stresses in the undiffused areas of the silicon when only one edge of the planar structure is near the point of interest, a case that includes the greater portion of the problem. The effects of surface loading at other boundaries can be calculated by superposition of two-dimensional-type solutions. For example, the effect of the planar boundary at the opposite side, $x = -w$, is not significant until r becomes comparable to w. For $r > w$, the stresses fall off more rapidly with distance; and, for $r >> w$, the stresses fall off as x^{-2} instead of x^{-1} as would be dictated by Eq. [5]. The effects of surface loading at perpendicular surfaces, $z = \pm(\frac{1}{2})l$, are of similar magnitude.

If the reasonable assumption is made that the stresses in the planar structures are similar in magnitude to the stresses in the blanket diffused layers, it is seen that stresses can be above the yield stress of silicon in the neighborhood of the planar boundary and can remain greater than the flow stress (22) for considerable distances into the undiffused areas. It is important to note that precise quantitative comparison is inappropriate in this application, since these dislocations propagated at elevated temperatures and the stress measurements were made at room temperature. However, it is logical that these anomalous compressive stresses directly cause the deeply penetrating dislocations at the edges of the appropriate phosphorus diffused planar structures. The stresses decrease as the inverse of the distance in the direction of applied force

$$\sigma_x \sim \tau_{(\max)} \sim x^{-1} \qquad (x > y = \text{const.})$$

and as the inverse of the distance squared perpendicular to the applied force

$$\sigma_y \sim \tau_{(\max)} \sim y^{-2} \qquad (y > x = \text{const.} \neq 0)$$

The distribution of dislocations qualitatively conforms with these relations; dislocations extend considerable distances in both directions but considerably further parallel to the surface, *i.e.*, in the direction of applied force. For smaller diffused structures, the stresses and dislocation distribution fall off more rapidly, as has been confirmed experimentally; but the dislocations still extend well through the base of a transistor with the resulting deleterious effects. The fact that dislocation formation is most favored for (111) oriented wafers as opposed to (100) and (110) is most likely because, for the case of (111) wafers, the applied force is in the plane of the primary slip system.

It is apparent from this investigation that the high stress, which causes dislocations outside of relatively shallow phosphorus emitter type diffusions, cannot result from residual strains from substitutional atomic phosphorus atoms but must result through some other mechanism that is dependent upon procedure. This conclusion might appear to be contradictory to Lawrence's investigation (18); however, it is not: Lawrence studied high temperature (1200°C) diffusions exclusively and, thus, did not consider the dislocations

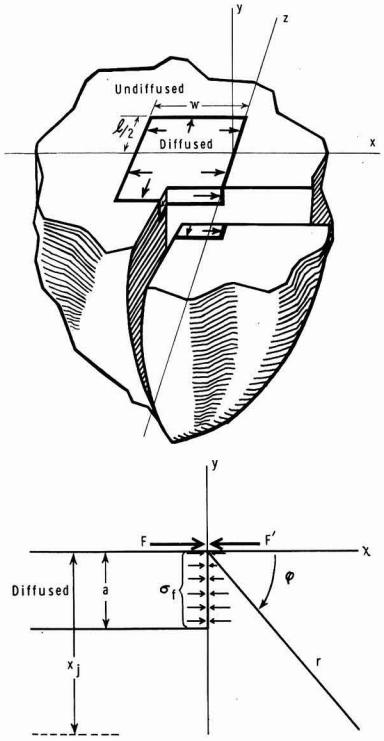

Fig. 10. a (top), Schematic diagram of stress effects from a planar structure; b (bottom), cross section at $z = 0$.

that are of primary interest in this investigation. It is possible that dislocations outside of deep boron structures are related to residual mismatch strains of substitutional atoms. The measured stress values in boron diffused silicon ($\sim 1.5 \times 10^9$ dynes/cm^2) would indicate that sufficient stress might be available.

At this time, the source of the anomalous compressive strain is uncertain; however, it might be speculated that it is related to the phosphorus atoms in excess of the substitutional (see Fig. 1) as is suggested by the requirements of maximum concentrations and an oxidizing ambient. The oxidation of the phosphorus diffused surfaces would even result in a supersaturation of excess phosphorus since the advancing oxide front rejects phosphorus (40). Assuming that the excess phosphorus in this supersaturated state exists interstitially or as very small (<20Å) interstitial type clusters, it could dilate the lattice and cause compressive strain around the planar structures. If larger areas of incoherent precipitation exist, these could act as sinks for the excess phosphorus that would otherwise dilate the lattice structure to induce compressive strain and, therefore, result in the expected lower tensile strains and no outside dislocations.

Summary

An anomalous, compressive macroscopic strain appeared around high concentration (though relatively shallow) phosphorus emitter-type diffused structures when an oxidizing diffusion or drive-in cycle was employed at temperatures less than 1150°C. This compressive stress cannot be due to residual strains from substitutional phosphorus atoms. It was often found to be of sufficient magnitude to cause dislocation nucleation and propagation for significant distances into the undiffused silicon; such dislocations commonly occurred in (111) oriented silicon wafers but were much less likely to occur in (100) and (110). The probability of dislocation formation outside of the diffused areas is significantly reduced if the diffusion or drive-in cycles are performed in an inert ambient or at higher temperatures, *i.e.*, in the neighborhood of 1200°C.

Acknowledgment

The authors wish to thank Karl Brack for providing the electron micrographs used in this study and C. Hoogendoorn for the x-ray topography. Part of this work was sponsored under Government Contract AF19(628)-5059.

Manuscript received Aug. 3, 1967; revised manuscript received Oct. 30, 1967.

Any discussion of this paper will appear in a Discussion Section to be published in the December 1968 JOURNAL.

APPENDIX

We now establish the applicability of regarding the force as concentrated at the surface, and, thereby, the stress distributions [5]. If the magnitude of the stress is assumed constant down to a where it abruptly drops to zero, a is still considered small compared to r; and the origin is adjusted slightly to

$$(0, -a/2, 0)$$

Then, Flamant's solution becomes

$$\sigma_x = \frac{-2\sigma_f}{\pi} \int_{-a/2}^{+a/2} \frac{x^3}{[x^2 + (y - \xi)^2]^2} d\xi \qquad [6]$$

with similar expressions for σ_y and τ_{xy}.

It is readily seen that Eq. [6] goes quickly to Eq. [5] as a is allowed to go to zero. For the application of this investigation, the force can be regarded as concentrated at the surface.

We also wish to point out that, with respect to the three-dimensional problem, a more rigorous approach would involve considering a distribution of concentrated point forces acting at the surface of the semi-infinite substrate and using the principle of superposition, see Timoshenko and Goodier (41). Such solutions are not difficult; but they are long, appear burdensome, and tend to distract from the physical significance of the problem. The requirements of this investigation do not require this degree of rigor.

REFERENCES

1. H. J. Queisser, *J. Appl. Phys.*, **32**, 1776 (1961).
2. S. Prussin, *ibid.*, **32**, 1876 (1961).
3. G. H. Schwuttke and H. J. Queisser, *ibid.*, **33**, 1540 (1962).
4. J. Washburn, G. Thomas, and H. J. Queisser, *ibid.*, **35**, 1906 (1964).
5. P. F. Schmidt and R. Stickler, *This Journal*, **111**, 1188 (1964).
6. W. Czaja and G. H. Wheatly, *J. Appl. Phys.*, **35**, 2782 (1964).
7. R. J. Jaccodine, *Appl. Phys. Letters*, **4**, 114 (1964).
8. M. L. Joshi and F. Wilhelm, *This Journal*, **112**, 185 (1965).
9. G. H. Schwuttke, *J. Appl. Phys.*, **36**, 2712 (1965).
10. H. Rupprecht and G. H. Schwuttke, *ibid.*, **37**, 2862 (1966).
11. E. Levine, J. Washburn, and G. Thomas, *ibid.*, **38**, 81 and 87 (1967).
12. J. M. Sukhodreva, *Soviet Phys.-Solid State*, **6**, 311 (1964).
13. Y. Sato and H. Arata, *J. Appl. Phys. (Japan)*, **3**, 511 (1964).
14. M. Ino, T. Kawamura, and M. Yasufuku, *ibid.*, **3**, 492 (1964).
15. I. A. Blech, E. S. Meieran, and H. Sello, *Appl. Phys. Letters*, **7**, 176 (1965).
16. G. H. Schwuttke and J. M. Fairfield, *J. Appl. Phys.* **37**, 4394 (1966).
17. G. H. Schwuttke and F. Wilhelm, *Bull. Am. Phys. Soc.*, **12**, 120 (1967).
18. J. E. Lawrence, *This Journal*, **113**, 819 (1966).
19. M. C. Duffy, F. Barson, J. M. Fairfield, and G. H. Schwuttke, *This Journal*, **115**, 84 (1968).
20. B. C. Cohen, *Solid-State Electron.*, **10**, 33 (1967).
21. G. L. Pearson, W. T. Read, and W. L. Feldmann, *Acta Met.*, **5**, 181 (1957).
22. J. R. Patel and A. R. Chaudhuri, *J. Appl. Phys.*, **34**, 2788 (1963).
23. M. L. Joshi, C. H. Ma, and J. Makris, *ibid.*, **38**, 715 (1967).
24. J. M. Fairfield, G. H. Schwuttke, M. C. Duffy, and F. Barson, Recent News paper presented at the Philadelphia Meeting of the Society, Oct. 9-14, 1966 as RN Abstract 25.
25. F. Barson, Private communication.
26. A. Loro, *Solid-State Electron.*, **9**, 904 (1966).
27. M. C. Duffy, D. W. Foy, and W. J. Armstrong, *Electrochem. Technol.*, **5**, 29 (1967).
28. W. J. Armstrong and M. C. Duffy, *ibid.*, **4**, 475 (1966).
29. E. Tannenbaum, *Solid-State Electron.*, **2**, 123 (1961).
30. R. A. McDonald, G. G. Ehlenberger, and T. R. Huffman, *ibid.*, **9**, 807 (1966).
31. G. H. Schwuttke, AFCRL-64-542 (1964).
32. J. K. Howard and G. H. Schwuttke, "Advances in X-ray Analysis," 11, G. R. Mallet and J. B. Newkirk, Editors, Plenum Press, New York (1967); Also 1966 Pittsburgh Diffraction Conference, Pittsburgh, November 1966.
33. G. H. Schwuttke and J. K. Howard, *J. Appl. Phys.*, **39**, March 1968.
34. R. Glang, R. A. Holmwood, and R. L. Rosenfeld, *Rev. Sci., Instr.*, **36**, 7 (1965).
35. G. G. Stoney, *Proc. Roy. Soc.*, **A82**, 172 (1909).
36. A. A. Brenner and F. Senderoff, *J. Research Natl. Bur. Standards*, **42**, 105 (1949).
37. V. V. Batavin, *Soviet-Physics Solid State*, **8**, 2478 (1967).
38. R. J. Jaccodine and W. A. Schlegel, *J. Appl. Phys.*, **37**, 2429 (1966).
39. M. J. Flamant, *Compt. Rend.*, **114**, 1465 (1892); see also M. J. Boussinesq, *ibid.*, **114**, 1510 (1892).
40. M. M. Atalla and E. Tannenbaum, *Bell System Tech. J.*, **39**, 933 (1960).
41. Timoshenko and Goodier, "Theory of Elasticity," McGraw Hill Publishing Co., New York (1951).

Preparation and Properties of Thin Film Boron Nitride

Myron J. Rand* and James F. Roberts

Bell Telephone Laboratories, Inc., Allentown, Pennsylvania

ABSTRACT

Clear, vitreous films of boron nitride up to 6000Å thick have been deposited on a variety of substrates at 600°-1000°C by a reaction between diborane and ammonia in hydrogen or inert carrier gas. Deposition rate may be readily adjusted to 50-1000 Å/min. Most samples were made at either 600° or 800°, with some attendant variation in film properties. The 600° material contains some residual B-H bonding. The film is essentially amorphous to electron diffraction. The refractive index is 1.7-1.8, the 1 MHz dielectric constant ~ 3½, the dielectric strength ~5×10^6 v/cm, and the 25°C resistivity $\geq 10^{14}$ ohm-cm. The band gap is 3.8 ev and the phonon temperature in the neighborhood of 2000°K. For semiconductor junction protection boron nitride has no advantage over silicon nitride. 600° deposition directly on Si has produced surface charges as low as 4×10^{11}/cm², but there are room-temperature drifts, and high-field conduction also. BN deposited at 800° on Si is electrically similar to silicon nitride. Etching of BN film also presents the same problems as does silicon nitride. BN is not as good a barrier against sodium ion permeation. Attack by atmospheric moisture over a long period has varied from insignificant to extensive conversion to orthoboric acid.

BN film on Si dopes the substrate with boron at temperatures above 900°C in inert ambient. Uniform junction depths are produced. D-C conductivity in 500-4000Å films has been studied from room temperature to 270°C. With fields $\geq 10^6$ v/cm BN film shows stable, nonohmic conductivity which is independent of polarity. The 25°C d-c conduction is describable over at least seven decades of current by $J \propto E^n$, n = 13-15, where J = current density, E = field strength. The 600°-deposited BN is the more conductive and can carry 0.1 amp/cm² indefinitely. Log J *vs.* $E^{1/2}$ at 25° is linear, and the slope of the curve is in good agreement with the theoretical value for a Frenkel-Poole conduction mechanism. Possible use of BN as a thin film varistor is discussed.

The preparation and properties of pyrolytic boron nitride have been reviewed in ref. (1). BN, ordinarily regarded as an insulator, may also be considered a wide band-gap III-V semiconductor, and it displays multiband electro-, photo-, and cathode-ray luminescence (2). The crystal structure is very similar to that of graphite. Data on the pure compound are thus of intrinsic interest for potential electronics uses, but much of the literature on conventional commercial BN is valid only for the particular sample studied because of the oxide impurity and the strong anisotropy resulting from hot-pressing.

There is very little formally published work on thin film boron nitride. Films less than 1μ thick have been prepared by Haberecht *et al.* (3) and characterized as capacitor dielectrics. The method used was a low-pressure, static pyrolysis of B-trichloroborazine vapor on a substrate heated to 700°-1400°C. The films were microcrystalline, with a minimal degree of short-range order (so-called "turbostratic") to x-rays. They probably contained residual chlorine. Crystalline films have also been made at Raytheon Company (4) from $BCl_3 + NH_3$ at 1100°-1300°C.

We report here the first results of a study of thin film boron nitride made by vapor deposition from a reaction between diborane and ammonia. This system was chosen because high-purity reactants are available, and because the product should not be contaminated by anything except, possibly, residual bonded hydrogen. Also, a favorable free energy change offers the hope that the reaction will be complete at relatively low temperatures. The over-all reaction is

$$B_2H_6 + 2NH_3 \rightarrow 2BN + 6H_2$$

$$\Delta F^\circ \ (900^\circ K) = -165 \text{ kcal/mole}$$

$$(1100^\circ K) = -177 \text{ kcal/mole}$$

The reaction occurs in separable steps (5). At room temperature there is immediate formation of a stable white solid borohydride, the diammoniate of diborane

$$B_2H_6 + 2NH_3 \rightarrow (NH_3)_2BH_2^+ \ BH_4^-$$

which at $\geq$ 200° rearranges to the ring compound $B_3N_3H_6$ (borazine), and some polymeric material $(BNH_2)_n$. Stronger heating drives off the hydrogen progressively, forming polymeric $(BNH)_n$ and finally BN.

The results reported here summarize some eighty runs in a single-slice deposition apparatus. The many variables of operation have not been investigated exhaustively, but it is evident that a smooth, transparent, and adherent thin film is obtained reliably over a considerable range of conditions. The potential applications for which the material has been examined include semiconductor surface protection and sodium diffusion barrier, boron diffusion source, and thin film dielectric or varistor. Most films were 1000-6000Å thick.

Deposition of Thin Film BN

Apparatus.—Figure 1 is a simplified schematic diagram of the apparatus. The substrate rests on a molybdenum pedestal which is inductively heated at 3 Mc. The reaction vessel is fused silica; all tubing is stainless steel. An important feature is the mixing of the reactants only after they enter the reactor and the heating of the reactor wall to at least 200°C. This prevents the deposition of the solid borohydride compound and is essential in obtaining a vitreous film. The substrate is heated after establishing the ammonia flow, with the diborane introduced last and turned off first. Without adequate ammonia a smooth film of amorphous boron is deposited. A green color in the burnoff flame is a sensitive indicator of the presence of gaseous boron compounds.

Deposition conditions.—The reaction was carried out at 600° to 1080°C, with most of the work at 600°

Key words: Boron nitride, thin films, vapor deposition, conduction, varistors.

* Electrochemical Society Active Member.

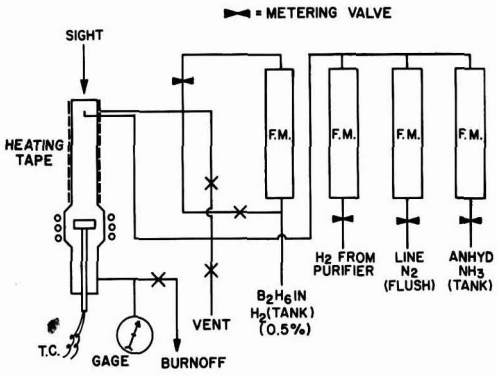

Fig. 1. Schematic diagram of deposition equipment

and 800°. The substrate was usually silicon, but Ta, Mo, Ge, and fused silica were also coated. Film thicknesses were monitored continuously during growth: at 600° simply by color, and at ≧ 800° by measuring emitted light intensity fluctuations at 6000Å caused by interference in the growing film (6). Hydrogen ambient was used most commonly and is preferred at present on the basis of film properties, but the reaction was also successful in nitrogen or helium. For these latter the tank diborane diluent was nitrogen, so that the only hydrogen present was the reaction by-product. Other conditions of operation are given in Table I.

Rates.—Observed deposition rates are not true kinetic rates since they vary with transport rate of reactants. Furthermore, there is considerable evidence that there is a reaction at the heated tube wall. Deposition rate is sensitive to the proximity of the wall: in a straight-walled tube the rate is 2-4 times faster than in the slightly bulged tube (see Fig. 1). BN films are more nonuniform than SiO_2 or silicon nitride films made in the same equipment at the same temperature. Furthermore, a freshly cleaned reaction tube depresses the deposition rate. All these observations suggest a reactant, probably borazine, being supplied by a local wall reaction.

The 800° deposition rate is only about 1.5 times faster than the 600° rate, and the 1000° rate is slower than the 800° (probably because of premature reaction at some distance from the substrate). The rate is proportional to the diborane concentration, but the influence of ammonia is anomalous. The ammonia concentration used was at least ten times that of B_2H_6, yet in the NH_3/B_2H_6 = 10-20 range the rate was sensitive to NH_3 concentration. Furthermore, the proportionality is inverse (more NH_3 decreased the rate, and to a power greater than one). Probably ammonia, or one of its pyrolysis products, acts as a chain terminator for some free-radical mechanism. At any rate, it is evident that the reaction sequence is complicated and that the conditions used are unsuitable for a study of kinetics.

Boron nitride deposition, like silicon nitride deposition from SiH_4 and NH_3, is much slower in the presence of traces of water vapor. One tank of so-called anhydrous ammonia gave persistent low deposition rates; when it was transferred to another apparatus used for Si_3N_4 deposition, rates were one-third normal, and tests indicated that the film was actually mostly SiO_2. This result is typical of the presence of moisture, of the order of 200 ppm.

Table I. Operating conditions

	Range	Most common
Total flow rate, l/min	0.5-4.5	3.0
Linear velocity, cm/sec	1-10	6.8
% B_2H_6	0.01-0.2	0.04
% NH_3	0.4-5	0.7
NH_3/B_2H_6	10-80	17
Deposition rate, A/min	50-700 (in H_2 or He)	125-600
	200-1900 (in N_2)	~1000

Physical Properties of the Film

Spectra.—The identification of the deposited film as boron nitride rests primarily on examination by infrared spectra and electron diffraction. Spectra of commercial boron nitrides may be found in ref. (7-9). Our thin-film spectra are shown in Fig. 2. The chief features are a strong asymmetric band near 1380 cm^{-1}, undoubtedly the B-N stretch, and a weaker, sharper band near 790 cm^{-1}. Both are considerably broader in the film deposited at 600° and shifted to slightly lower frequencies, indicating a more disordered structure on the atomic level. The weak absorption at 3430 cm^{-1} is most probably hydroxyl impurity, strongly H-bonded, for example adsorbed molecular water. In addition, the 600° film shows a band at 2500 cm^{-1}, the B-H stretching region, and thus contains some residual hydrogen-containing polymeric material.

Crystallinity.—Grazing-angle electron diffraction shows broad, diffuse rings whose positions are in agreement with the established pattern for hexagonal boron nitride. From line widths the crystallite sizes (near the surface) are estimated as follows:

Deposition temp, °C	600	800	900	950
Size, Å (±15%)	10	20	30	65

The 600° BN film thus has about as much crystalline order as steam-grown silica. The figures above are for hydrogen ambient; films made in nitrogen have a larger crystallite size, but no value more than 80Å has been found for any deposition conditions.

Band gap.—No published measurement of the band gap of hexagonal boron nitride could be found. A BN film 0.6μ thick was deposited at 800° on fused silica to study transmission in the 185-750 mμ range. There are no bands in the visible. Absorption commences at about 340 mμ, but the absorption edge is not as sharply defined as for crystalline materials. Figure 3 is a plot of the square root of the absorption coefficient *vs.* the photon energy. There is a discontinuity in slope similar to those shown by Si and Ge (10). From the two intercepts on the zero absorption axis (11) an energy gap of 3.8 ev is calculated. The phonon temperature is about 2000°K, but the absorption data are not of the precision required for good accuracy in this figure.

Refractive index.—Film refractive index, as determined by ellipsometer, varies considerably. Hexagonal BN, with its graphite-like structure, is highly anisotropic; furthermore, the degree of crystallinity varies with deposition temperature. Results below are

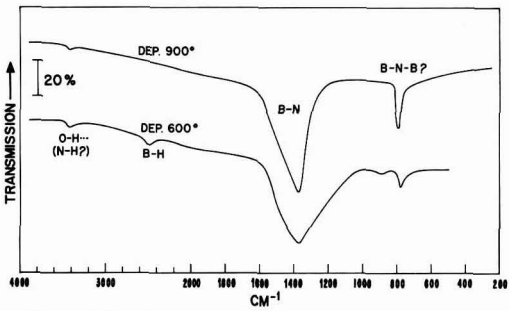

Fig. 2. Infrared spectra of boron nitride films deposited at 900°C (upper curve) and 600°C. The curves have been displaced for clarity.

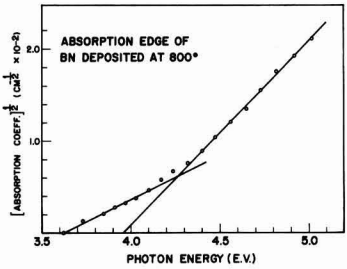

Fig. 3. Macfarlane-Roberts plot of absorption edge of BN deposited at 800°C.

reliable to ±0.03:

Deposition temp. °C	950	900	800	600
Refractive index, 541 mμ	1.70	1.73	1.75	1.80

These values are for films deposited in hydrogen. Films made in nitrogen at 800° have crystallite sizes like those made in hydrogen at 950°, and correspondingly show $n \sim 1.70$.

Adherence.—Generally, BN film adherence to the substrate has been entirely satisfactory. An occasional occurrence of peeling during etching indicates that it is not so adherent as deposited silica or silicon nitride. Adherence to Ge substrates, however, was unsatisfactory, possibly because of nitriding. Although film appearance was normal immediately after deposition, if the film was disturbed, *e.g.*, by tweezers, local puckering and reticulation appeared instantly. In the course of a few days this effect spread entirely across the Ge slice.

Surface properties.—BN films are quite hydrophobic. Water contact angles from 42° to as high as 80° have been measured, even after many days' exposure to atmospheric moisture.

Film surfaces are quite smooth. Relatively few surface features were visible to 8000X electron microscopy, and even these few were low hillocks rather than fissures or other kinds of film discontinuities.

Sodium drift and diffusion experiments.—Tests of the film as a diffusion barrier were carried out with ^{22}NaCl. Unlike silica films, however, diffusion of sodium in a voltage field and straight thermal diffusion gave very different pictures of the permeability. At 400°C, with the surface bias plate at +4 to +10v (field about 10^5 v/cm) for 1 hr, no sodium ion drift was detected in any boron nitride film. No charge storage was detected.

Thermal diffusion profiles are shown in Fig. 4. The data show considerable scatter, but it is immediately evident that deposition temperature influences the result. In the film deposited at 850° the steep drop in Na ion concentration with depth is like that shown by an oxygen-free pyrolytic silicon nitride. Note, however, the single datum point, at 2100Å, which is a decade higher than the previous one and which seems to indicate a pileup of sodium at some sort of barrier, since beyond this point none could be detected. The film structure was examined by step-etching and electron diffraction, and it was found that the crystallite size was ~ 30Å at the original surface but decreased with depth; at 2100Å and beyond the film was essentially amorphous, *i.e.*, size < 10Å. This correlation between crystallinity and permeability has also been reported recently for silicon nitride films. (12)

Boron nitride deposited at 600° is not a barrier to sodium ion diffusion. All the profiles are relatively flat, even the one for diffusion conditions of 1 hr at 400° instead of 22 hr at 600°.

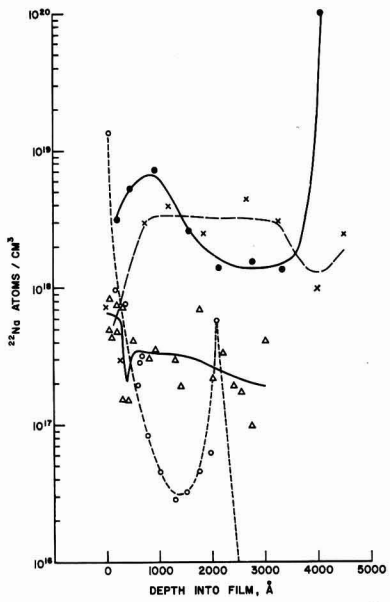

Fig. 4. Sodium diffusion profiles in boron nitride films: ---○--- 5000Å film deposited at 850°, diffused 22 hr at 600°C in forming gas; ——●—— 4100Å film deposited at 600°, diffused as before; —+—△—— two samples of a 3100Å film deposited at 600°, diffused as before; —-X-—4500Å film deposited at 600°, diffused 1 hr at 400°C in room air.

Chemical Properties

Etching.—Bulk boron nitride is considered highly resistant to all aqueous acids and bases and is slowly attacked by high concentrations of water vapor. Thin film BN behaves similarly. Buffered HF etches at < 10 Å/min. Some samples could be etched at ~ 35 Å/min by 3% hydrogen peroxide at 80°C, but this solution is destructive to conventional etch-resist films. A deposited silica film might be used for masking, but if this method is chosen, one might as well etch with hot phosphoric acid, as is done with silicon nitride (13). Boiling H_3PO_4 at 180° etches boron nitride at about 150 Å/min.

A BN film on silicon was exposed to boiling methanol vapor for 1½ hr with no change in appearance, thickness, or film weight (±1% sensitivity). This treatment would have dissolved any boric oxide. With a 2-hr exposure to 100° steam or boiling water there was little thickness change, but the film became hazy. Microscopic examination revealed numerous shallow blisters or craters, with film fragments curled back at the edges, as if lateral attack (or separation of laminae) were the chief effect.

Anodization.—Since BN film is difficult to etch, several attempts to convert it to the oxide by anodization (14) were made. All failed because the film peeled from the substrate. This is further evidence that boron nitride adherence is not so tight as that of silicon nitride.

Silicon doping.—From free energy data one would predict that silicon may reduce boron nitride to boron and form Si_3N_4. In other words, if BN is deposited on Si at temperatures at which diffusion rates of boron in Si are significant, the substrate may be doped. This does indeed occur: with deposition at 900° and above, the rather flat capacitance-voltage traces invariably obtained in MIS measurements indicated plainly that the substrate surface was low-resistivity p-type.

Figure 5 shows results of two experiments on deliberate doping of 4 ohm-cm n-type silicon from a BN

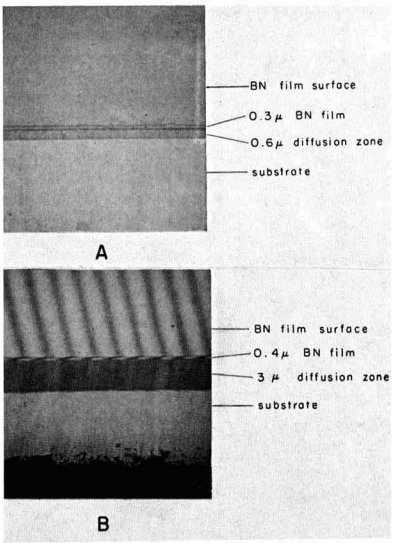

Fig. 5. Angle-lapped and stained sections showing use of boron nitride film as a diffusion source. (A) 1½ hr in nitrogen, 1100°, (B) 2 hr, 1150° helium.

film source. The upper picture is the angle-lapped and stained interface after 1½ hr in nitrogen at 1100°C; for the lower, 2 hr at 1150° in helium. Junction depths are quite uniform. There was little change in the appearance of the deposited film.

Boron nitride film should thus be useful as a restricted area boron diffusion source. The diffusion should be carried out in inert ambient; any water or oxygen present would convert the nitride to the oxide, and the high vapor pressure of the oxide would result in some doping outside the desired area. As a solid diffusion source BN has the advantages of thermal stability, constant composition, and simplicity of deposition compared to B_2O_3-SiO_2 codeposits.

Weathering phenomena.—It has already been mentioned that boron nitride, in both massive and thin film form, is slowly attacked by water vapor. Thus there are grounds for concern about BN film stability with prolonged exposure to the atmosphere. Indeed, changes with time are observed; these appear to depend on the conditions of deposition, and probably on other factors as well. They range from the trivial to the catastrophic.

A freshly deposited BN film is not as hard as SiO_2 or Si_3N_4, but it is not readily scratched by stainless steel tweezer tips. It will remain this way indefinitely if stored in a desiccator. If stored in room ambient, it will become soft enough to scratch in a few weeks. A broad, shallow absorption band develops near 3300 cm^{-1} in the spectrum; this is hydrogen-bonded hydroxyl, and indicates adsorption or absorption of molecular water. There are no other significant spectrum changes.

Some specimens have shown a much more serious form of attack, whose manifestation is the appearance of single-crystal boric acid (identified by electron diffraction) growing out of the film surface. A particularly severe example is shown in Fig. 6. B_2O_3 and HBO_2 are probably intermediates, judging by the behavior during heating and cooling cycles. Such extensive hydrolytic attack is seldom seen in films deposited in hydrogen at 600°. Perhaps one in four of the 800° films eventually showed a few crystals. But almost all the films made in inert ambient, nitrogen or helium, developed serious cases of the boric acid pox, some in only one or two weeks. For this reason the deposition

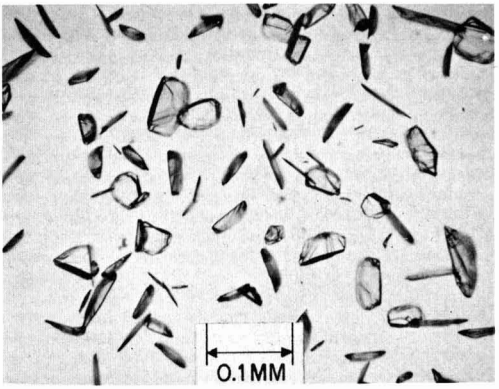

Fig. 6. Boric acid crystals growing from a boron nitride film made in nitrogen at 670°, after 5 months exposure to room atmosphere. Magnification *ca.* 150X.

of films in inert ambient was not pursued, even though it should produce a purer product. The presence of residual bonded hydrogen seems to be associated with BN film resistance to water attack.

Electrical Properties

Surface charge.—Most of the BN films were deposited on silicon, and a number of samples of MIS capacitor structures were made by evaporating 10 mil diameter Al field plates onto the film. Adherence of the Al was normal. In some cases the substrate was oxidized in steam at 1000° to provide a 1000Å SiO_2 layer under the nitride deposited afterwards. A summary of the MIS results appears in Table II.

Films deposited on bare Si in hydrogen at or above 800°C behave electrically like those of silica or silicon nitride in showing the so-called anomalous shift as the bias range is increased in the negative direction, and also in showing hysteresis loops as the scan is retraced. The interfacial surface charge was high, in the 2-5x10^{12} range.

BN deposited over SiO_2 gave C-V traces which shifted with time as though some sort of slow polarization or structural alteration were occurring at room temperature. A similar effect has been observed with thick phosphorus-glass layers on SiO_2 (15), and also on lead glass (16), but only at elevated temperatures. On one sample measurements of the flat-band voltage shift as a function of field-plate voltage and time were made. The extent of shift was the same when the sample was held at +25 or −25v, although of course the directions were opposite. At a given voltage the shift was linear with log time, at least up to 2 hr.

Table II. Summary of MIS measurements (measuring frequency = 1 MHz)

Dep'n temp, °C	Ambient	Substrate	Capacitors	Surface charge density (× 10^{-11} cm^{-2})	Comments
900	H_2	SiO_2/Si	3	5.3-6.9	Shifts with time
850	H_2	Si	4	23-25	Normal curve
800	H_2	Si	20	32-52	Normal curve
800	H_2	SiO_2/Si	12	28-34	Shifts with time
800	N_2	Si	5	7.5-8	Anomalous behavior, see text
800	He	Si	3	4	
600	H_2	Si	16	4-8	Conduction; capacity drift
600	H_2	SiO_2/Si	6	6.4-6.9	Shifts with time
	H_2	fast states*	2	1.0-1.1	At 100 KHz

* By the technique of ref. (25).

The sample deposited on bare Si in nitrogen exhibited a different sort of anomaly. Scans from 0 to −15v looked normal, but at higher negative voltages the insulator capacitance decreased. After stress at 30v or more a pronounced knee appeared in the step of the C-V trace, and the capacitance had decreased by 20%. These effects may be due to film conductivity. The same sample measured two months later, after boric acid crystals had appeared, was highly conducting at 1v. The inert-ambient deposits did have low surface charges, as Table II indicates, but because of susceptibility to hydrolysis they were not further investigated.

BN deposited in hydrogen on bare Si at 600° was also in the 4-8x10^{11} surface charge range, but here the evidence of high conductivity was pronounced; the samples could not be measured on a capacitance bridge, and required a capacitance meter such as the Boonton Model 71A. A typical C-V curve for these samples is shown in Fig. 7. The usual limiting insulator capacitance does not seem to be reached. (The curves finally do level off at about −40v, however.) Some upward drift of capacitance is seen at constant large negative bias.

Dielectric constant.—On conducting samples like those just described no accurate dielectric constant can be determined. For 800-1800Å BN deposited at 800°C on Si some twenty measurements on three different samples at 1 MHz gave $K = 3.7 \pm 0.3$ (range).

Dielectric strength.—The "room temperature" breakdown strength of BN deposited at 800° is 6x10^6 v/cm, and of the film deposited at 600°, 4x10^6 v/cm. These values are probably low because of resistive heating of the film by high-field conduction. This property, which is shown to a surprising degree for a material ordinarily considered an insulator, is perhaps the most interesting feature of these films, and is discussed in detail in the next section.

Nonohmic Conductivity

Recently there have been reports of high-field nonohmic d-c conductivity in thin films of silicon nitride made by the SiH_4-NH_3 process (17), the $SiCl_4$-NH_3 process (18, 19), and by reactive sputtering (20, 21). Evaporated SiO_x insulating films also show the phenomenon (22). Conductivity depends strongly on conditions of film deposition, and there are conflicting results on whether it is polarity-dependent. Various conduction mechanisms have been proposed, particularly the Frenkel-Poole and Schottky types. Obviously, present knowledge is fragmentary, but at any rate it seems to be widely known that silicon nitride films can pass considerable current (by semiconductor standards) without destruction, and thus have a built-in protection against occasional overload.

Thin film boron nitride, as described here, also shows stable, strongly nonohmic high-field conductivity, to such an extent that films of 1000Å or thinner may be useful in integrated circuits as thin film varistors or voltage-limiters. As with the other films, the conductivity depends on deposition conditions, particularly the deposition temperature, and thus must be governed largely by the structure of the film. The effects of thickness, electrode material and area, polarity, and temperature were also examined and are summarized below.

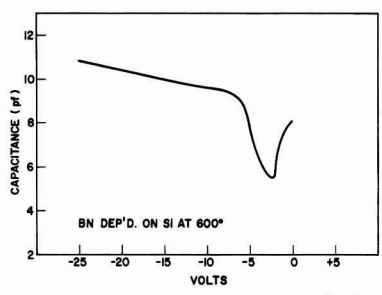

Fig. 7. Typical MIS curve for BN deposited at 600°C on Si

Method of measurement.—The voltage source was a bank of dry cells discharging through a 20K potentiometer which allowed selection of any appropriate applied potential over the range 0-500v. This potential was read on a Keithley 610B electrometer. The current in the sample circuit was read on a Keithley 414 micromicroammeter. A 1-megohm resistor in the measuring circuit protected the instruments against surges caused by sample breakdown. For conductivity work the film samples were deposited on 0.001 ohm-cm n-type silicon and an array of 10 and 20-mil aluminum or gold electrodes applied by evaporation through a mask. The back of the Si slice was coated with evaporated gold. The sample was mounted in a micrometer-drive positioner and the electrode dots contacted with a 7-mil brass probe.

For measurements at elevated temperatures the Si slice was scribed and broken into chips containing two dots each. After a brief ultrasonic cleaning to remove scribing debris the chips were mounted on TO-18 headers and gold wire bonded to the electrode. Conventional mounting and bonding techniques and temperatures had no adverse effect on the BN films. The assembly was mounted in a small copper oven and measurements taken at various temperatures between 75° and 270°C.

Measurements were always made by scanning the current-voltage curve several times with both increasing and decreasing voltages, and frequently points were taken out of sequence. The first application of high field caused a permanent decrease in resistance; thereafter the samples were quite stable. For this reason each sample was aged ("formed," in the language of some authors) at 10^{-1} −10^{-2} amp/cm^2 for a few minutes before the measurements were begun.

At no time was any emission of light observed.

Effect of certain parameters.— Film deposition temperature has a strong effect on conductivity. Most of the samples measured had been prepared at either 800° or 600°; the latter has about 10^4 times greater high-field conductivity at a given field strength. However, the ohmic component, *i.e.*, the conductivity at $\leq 10^5$ v/cm, is about the same. Conductivity increases with temperature, with an activation energy of 1.0-1.1 ev in the ohmic region. In the nonohmic regions this quantity decreases with increasing field strength.

Changing from Al to Au electrodes had no effect on the conductivity. Increasing the area fourfold also had no effect on the current density *vs.* field strength curves. Reversing polarity had little or no effect: with some samples a few per cent difference was observed, but the curves were of the same form. Varying film thicknesses from 500 to 4000Å was also without effect, as long as field strength was considered.

Results and discussion.—Figures 8 and 9 summarize the results of many measurements on films deposited at 800° and 600°C, respectively. It is evident that up to ~ 10^5 v/cm BN film shows only minute and ohmic electronic conductivity. Resistivities are $\geq 10^{14}$ ohm-cm at room temperature and ~10^{12} ohm-cm at 200°C. At higher fields this behavior is gradually overwhelmed by a conductivity describable by $J \propto E^n$, where n = 13-15. The transition is more gradual for the film deposited at 600°, and occurs at lower fields. The negative resistance in the breakdown region is not stable.

For a varistor the 600° film would be preferred, since it is both more conductive and more stable. A 1000Å-thick film should be capable of dissipating up to ~ 15 w/cm^2 continuously. As an aid in visualizing the possible use of the BN film, Fig. 10 presents its charac-

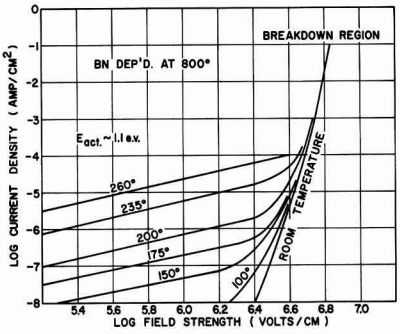

Fig. 8. D-C conductivity of 500-4000Å BN films deposited at 800°C on 0.001 ohm-cm n-Si.

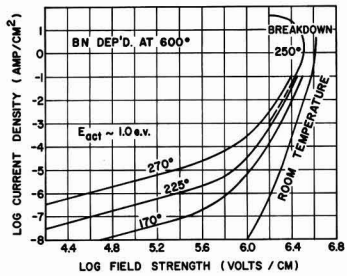

Fig. 9. D-C conductivity of 2000Å BN film deposited at 600°C on 0.001 ohm-cm n-Si.

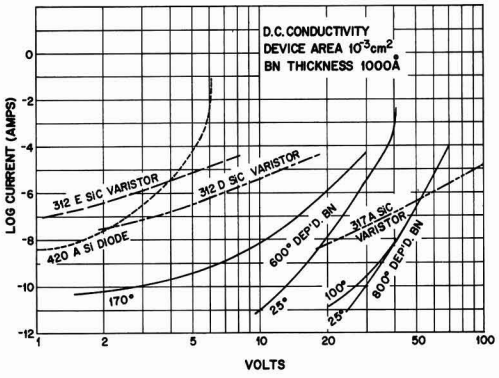

Fig. 10. Characteristics of 1000Å BN film as a varistor. Silicon carbide and regulator diode devices, reduced to the same area, are included for comparison. (Identifications are Western Electric Co. codes.)

teristics on the same scale with those of commercially available silicon carbide varistors and a regulator diode reverse characteristic. For comparability all of the devices have been reduced to the same active-element area, 10^{-3} cm^2. It is evident that the BN film, particularly the 600° film, occupies a potentially useful intermediate position between the others; furthermore, the SiC varistor and the Zener diode are not currently manufactured in thin film form. Note that for the SiC device the current varies as about the fourth power of the voltage; for 600° BN the exponent at room temperature is about 13; and for the diode it varies from near unity to 50 or more.

Many of the experimental observations given above have implications for the mechanism of conduction. For example, the fact that the current does not decrease with time, coupled with its nonohmic behavior, rules out any large contribution from ionic conduction. Models of space-charge limited flow (23) predict current density dependence varying between V^2/l^3 and V^3/l^5, depending on region and on whether a single or double-injection model is assumed (l is the thickness). This seems rather far removed from the $J \propto (V/l)^{13}$ dependence observed. An impurity-band conduction mechanism would have a low activation energy and would give an ohmic characteristic.

In Fig. 11 the room temperature conductivity data are replotted as log current density *vs.* the square root of field strength. Very good straight lines are obtained over seven decades of current for both the 600° and 800°-deposited films. Two possible mechanisms have this characteristic: conductivity limited by electron emission into the insulator from the electrode (Schottky emission), or by the field-assisted thermal excitation of electrons from traps into the conduction band of the insulator (Frenkel-Poole effect).

The Schottky emission equation may be written

$$J = AT^2 \exp\left\{-\frac{e}{kT}\left[\phi - \left(\frac{eE}{4\pi\epsilon_i}\right)^{1/2}\right]\right\}$$

where J = current density, A = the Richardson-Dushman constant, theoretically 120 amp cm^{-2} deg^{-2} for emission into a vacuum, T = absolute temperature, e = electronic charge, k = Boltzmann constant, ϕ = barrier height, E = field strength, ϵ_i = permittivity of the insulator = $K\epsilon_0$, K = dielectric constant of the insulator, ϵ_0 = permittivity of free space = $8.85\text{x}10^{-12}$ farad/meter. At a given temperature the Schottky equation yields

$$\ln J = \text{constant} + \frac{e^{3/2}}{2kT(\pi\epsilon_i)^{1/2}} \cdot E^{1/2} \qquad [1]$$

For the Frenkel-Poole effect the barrier lowering in the presence of a field (24) is $2(e^3E/4\pi\epsilon_i)^{1/2}$, that is, twice that for Schottky emission. The difference is a consequence of considering the positively charged trap fixed in position as the electron is removed from it, instead of considering the electron moving away from an image charge in the conductor. As a result, the Frenkel-Poole equation corresponding to Eq. [1] lacks the 2 in the denominator. Thus in principle the two kinds of conduction could be distinguished by the value of the slope of the ln J *vs.* (field strength)$^{1/2}$ plot. Some authors argue that there are so many assumptions involved both in equations and the method of measurement that a mere factor of 2 does not offer safe grounds for decision.

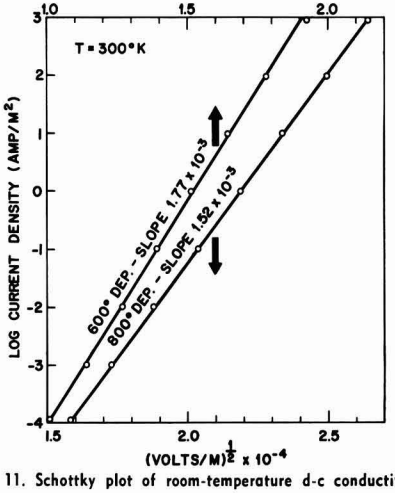

Fig. 11. Schottky plot of room-temperature d-c conductivity of BN film.

When the high-frequency (optical) dielectric constants of the BN film are used, the theoretical slope of Eq. [1] is calculated to be 0.82×10^{-3} (v/meter)$^{-1/2}$ for the 600° BN and 0.84×10^{-3} for the 800° BN. These values would of course be $1.6_6 \times 10^{-3}$ if the factor of 2 is removed. The experimental slopes (Fig. 11) are 1.77×10^{-3} for 600° BN and 1.52×10^{-3} for 800° BN. The results are thus in better agreement with a Frenkel-Poole than with a Schottky-type conduction mechanism.

Acknowledgments

The authors are indebted to H. E. Nigh for MIS measurements, to J. Drobek for electron microscopy and electron diffraction, to J. V. Dalton for radiosodium drift and diffusion work, and to P. F. Schmidt for film anodization experiments. In addition, much helpful discussion and advice were provided by L. P. Adda, M. C. Waltz, and P. F. Schmidt. Dr. R. Haberecht of Texas Instruments kindly supplied copies of the talks cited in ref. (3).

Manuscript received Aug. 18, 1967; revised manuscript received Nov. 9, 1967. This paper was presented at the Dallas Meeting, May 8-12, 1967, as Abstract 87.

Any discussion of this paper will appear in a Discussion Section to be published in the December 1968 JOURNAL.

REFERENCES

1. For a summary of the preparation and properties of pyrolytic BN, see "Vapor Deposition," C. F. Powell, J. H. Oxley, and J. M. Blocher, Jr., Editors, pp. 663-7, John Wiley & Sons, Inc., New York (1966).
2. S. Larach and R. E. Shrader, *Phys. Rev.*, **104**, 68 (1956).
3. R. J. Patterson, R. D. Humphries, and R. R. Haberecht, Papers presented at the Pittsburgh Meeting of the Society, April 15-18, 1963, Abstract 103, and the New York Meeting, Sept. 29-Oct. 3, 1963 as Abstract 197; R. R. Haberecht, R. J. Patterson, and R. D. Humphries, Paper presented at the Annual Meeting of the Conference on Electrical Insulation, National Research Council, Washington, D. C., 1964. Abstracts of these papers were published by The Electrochemical Society and in National Academy of Sciences—National Research Council Pub. No. 1238 (1965).
4. "Research on Thin Film Tunnel Cathodes, Recombination Cathodes, and Similar Cold Cathodes," Report No. 10, Contract No. DA28-043-AMC-00035(E), March-June, 1965, *et seq.*; Raytheon Co. See also the reports under Contract No. DA28-043-AMC-01343(E).
5. "Boron, Metallo-boron Compounds, and Boranes," R. M. Adams, Editor, p. 590, Interscience, New York (1964).
6. J. F. Roberts, To be published.
7. E. G. Brame, Jr., J. L. Margrave, and V. W. Meloche, *J. Inorg. Nucl. Chem.*, **5**, 48 (1957).
8. P.-C. Li and M. P. Lepie, *J. Amer. Ceram. Soc.*, **48**, 277 (1965).
9. R. Geick, C. H. Perry, and G. Rupprecht, *Phys. Rev.*, **146**, 543 (1966).
10. G. C. Macfarlane and V. Roberts, *ibid.*, **97**, 1714 (1955); **98**, 1865 (1955).
11. T. S. Moss, "Optical Properties of Semiconductors," p. 37, Academic Press, Inc., New York (1959).
12. J. Drobek and J. V. Dalton, Recent News paper presented at the Philadelphia Meeting of the Society, Oct. 9-14, 1966.
13. W. van Gelder and V. E. Hauser, *This Journal*, **114**, 869 (1967).
14. P. F. Schmidt and D. R. Wonsidler, *ibid.*, **114**, 603 (1967).
15. E. H. Snow and B. E. Deal, *ibid.*, **113**, 263 (1966).
16. E. H. Snow and M. E. Dumesnil, *J. Appl. Phys.*, **37**, 2123 (1966).
17. V. Y. Doo and D. R. Nichols, Paper presented at Philadelphia Meeting of the Society, Oct. 9-14, 1966 as Abstract 146; H. Lawrence and C. Simpson, *ibid.*, as Abstract 159.
18. S. M. Sze, *J. Appl. Phys.*, **38**, 2951 (1967).
19. M. J. Grieco, F. L. Worthing, and B. Schwartz, *This Journal*, in press.
20. S. M. Hu and L. V. Gregor, *ibid.*, **114**, 826 (1967).
21. S. M. Hu, Paper presented at the Philadelphia Meeting of the Society, Oct. 9-14, 1966, as Abstract 150.
22. L. E. Terry, U. S. Atomic Energy Commission SC-TM 315-63 (14).
23. M. A. Lampert, *RCA Rev.*, **20**, 682 (1959); M. A. Lampert and A. Rose, *Phys. Rev.*, **121**, 26 (1961); M. A. Lampert, *Phys. Rev.*, **125**, 1 (1962), *inter alios*.
24. J. Frenkel, *Phys. Rev.*, **54**, 647 (1938).
25. E. H. Nicollian and A. Goetzberger, *Appl. Phys. Letters*, **7**, 216 (1965).

Intense Interjunction Strain in Phosphorus-Diffused Silicon

E. D. Jungbluth* and H. C. Chiao*

The Bayside Laboratory, Research Center of General Telephone and Electronics Laboratories Incorporated, Bayside, New York

ABSTRACT

Extensive strain effects are revealed by x-ray topography in the areas between shallow junctions formed by selective-area phosphorus diffusion in silicon. Diffusion-induced strains extend at least 500μ laterally into the nondiffused portion of the substrate and penetrate to ¼ of the junction depth. Unusual x-ray contrast effects are observed in that both extinction contrast and Borrmann effects simultaneously operate to reveal strain gradients when the lattice adjusts to compensate for stresses introduced by impurity diffusion. These residual unrelieved stresses can be minimized by stress-relief mechanisms involving the generation of dislocations.

Previous investigators have demonstrated that planar impurity diffusion techniques can introduce imperfections into semiconductor substrates (1-3). Dislocation arrays and precipitates can result from the diffusion of impurity atoms of boron and phosphorus into silicon. These defects are generally attributed to stresses arising from solute concentration gradients and total impurity content. Similar effects may also occur when zinc is diffused into GaAs (4). Diffusions are normally accomplished by selectively diffusing through windows opened up in oxide masks by photolithographic techniques. Strain effects at the boundaries of Si-SiO_2 interfaces have been analyzed

* Electrochemical Society Active Member.

by x-ray topography (5). One would normally expect that subsequent diffusions through the oxide windows would result in lattice defects which would be confined to the diffused area. Recently, Lawrence has shown that impurity diffusions cause dislocation formation not only within the diffused region but also outside or in the nondiffused portion of the matrix (6). He observed that impurity-induced lattice strain contributes to dislocation formation in nondiffused zones wherein the dislocations appear as parallel or intersecting lines. Joshi *et al.* (7) have measured residual strain levels in phosphorus diffused silicon by means of x-ray line-broadening. The observed broadening results from residual strains only and is attributed to insufficient penetration of the diffusion-induced dislocations from inside the diffused layers.

In this paper, direct evidence of the effects of residual strain in phosphorus diffused silicon is presented by means of x-ray transmission topography (8). The residual strain is distributed into the nondiffused zones but is not as well defined as the deformed regions reported by Lawrence (6). Indeed, deformations large enough to create dislocations do not occur in the present case. Residual strains, hereafter referred to as interjunction strains, are shown to arise as a consequence of the diffusion process and are intimately related to the creation of diffusion-induced dislocations.

Experimental

The silicon wafers used in this study were Czochralski grown and solution doped with boron to an average concentration ranging from 10^{19} to 2 x 10^{15} atoms/cm^3. The wafers were oriented for the (111) plane and polished either electrochemically or mechanically. The results reported are independent of surface preparation and substrate doping concentration. The diffusion masks were formed by thermal oxidation at 1100°C in a wet oxygen ambient. The resulting oxide thickness was 5000Å.

The diffusion windows were opened in the oxide by KTFR photoresist and etching techniques. The photomask pattern consisted of large square or triangular windows 0.200 in. on a side or circles of 0.200 in. diameter. The diagonal corners of the square windows are oriented approximately in the $[\bar{1}10]$ and $[11\bar{2}]$ directions.

Standard diffusion techniques using a P_2O_5 vapor source and N_2 carrier gas were employed. Temperature and time of diffusions were 1100°C and 1 hr, respectively, resulting in measured junction depths in the order of 2μ. The electrically measured surface concentrations were about 5 x 10^{20} atoms/cm^3, although the actual impurity content is probably higher (9).

Crystal defects were analyzed using an x-ray transmission topographical method similar to the Lang method (10). Molybdenum $K_{\alpha 1}$ radiation was employed under the condition that $\mu t \simeq 1$ (μ is the linear absorption coefficient and t the thickness of the wafer) so that the normal expected mode of diffraction would be by extinction contrast. In practice, this means that structurally imperfect regions should diffract x-rays more intensely than perfect regions. Frequently a reversal of x-ray contrast or a reduction of x-ray intensity accompanying strained regions is simultaneously observed with intensity enhancement. This reduction of x-ray intensity is known as the Borrmann effect. Similar simultaneous displays have been observed to sharply delineate window patterns cut into SiO_2 masks on silicon substrates (5).

Results

Several investigators have demonstrated that silicon exists in a state of compression due to a mismatch in thermal expansion coefficients when SiO_2 is thermally grown on Si substrates. Blech and Meieran (11) critically analyzed x-ray topographical displays of strains at oxide steps on Si, and x-ray contrast effects at edges of thin films grown or deposited on single crystal substrates have been attributed by Haruta (12) to strain gradients. Substrates which are in a uniform state of compression due to thin films covering the entire substrate appear in x-ray topographs similar to topographs recorded prior to thin film deposition. Strain gradients, at oxide edges for instance, give rise to x-ray intensities which sharply define the window patterns cut into the oxide. This is clearly demonstrated in Fig. 1 where the contrast is relatively uniform between windows formed in an SiO_2 diffusion mask on silicon. The diffraction vectors are indicated in each figure. Frequently, even after a high concentration emitter type diffusion, the observed contrast appears similar to Fig. 1 except within the diffused areas where diffusion-induced dislocations are observed. That is, the contrast between diffused junctions remains unchanged which implies an unaltered substrate perfection.

In the course of this study, a characteristic type of interjunction strain associated with the diffusion process was observed. The remaining portions of this paper characterize the strain gradient responsible for the observed contrast effects and describes the conditions necessary to control the occurrence of these effects. Finally, a mechanism is suggested to explain these interjunction strain effects.

The x-ray topograph of Fig. 2 was recorded after diffusion. There are obviously two distinct differences in the defect display when compared to Fig. 1: (*i*) diffusion-induced dislocation arrays are confined to each diode area, and (*ii*) pronounced dark regions, at each corner of the diffusion mask, extend into the nondiffused portion of the matrix. These dark regions or strain lobes are the so-called interjunction strains. The visibility of such effects in x-ray topographs is a consequence of the strain gradients which result from the lattice adjustment to stresses introduced by the impurity diffusant.

The visibility of strain gradients is also strongly dependent on the reflection chosen. In Fig. 3 the characteristic pattern is completely dissimilar in both its geometrical shape and recorded contrast. Between the four corners of four different junctions the contrast not only reverses (*i.e.*, Borrmann effect is operative) but also the strain gradient appears as a four cornered re-entrant curve which extends over 2500μ to the adjacent junction areas. However, between parallel sides of adjacent junctions the x-ray contrast is dark, indicating diffraction by extinction contrast.

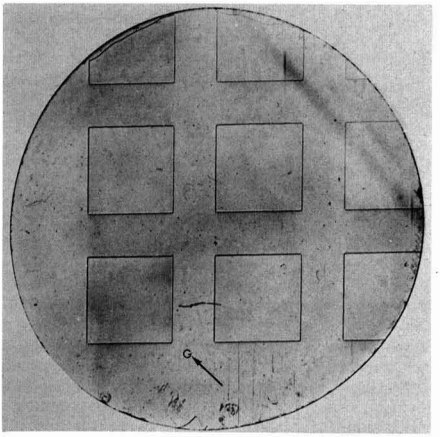

Fig. 1. X-ray topographical displays of strain gradients at oxide edges cut into an SiO_2 diffusion mask on Si; $\bar{g} = [\bar{1}10]$.

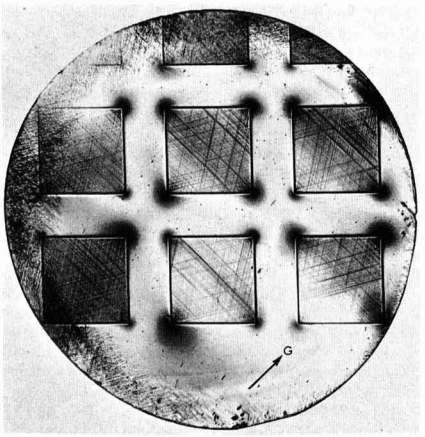

Fig. 2. Pronounced interjunction strain gradients (strain lobes) which extend laterally 500μ into the nondiffused matrix at the four corners of the diffusion mask; $\bar{g} = [11\bar{2}]$.

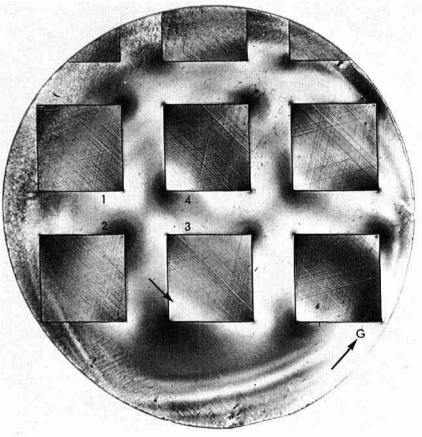

Fig. 4. Interjunction strain lobes visible by extinction contrast in a direction paralleling $\bar{g}$ and by Borrmann effects in a direction perpendicular to $\bar{g}$; arrow indicates reverse contrast within the diffused area; $\bar{g} = [1\bar{1}\bar{1}]$.

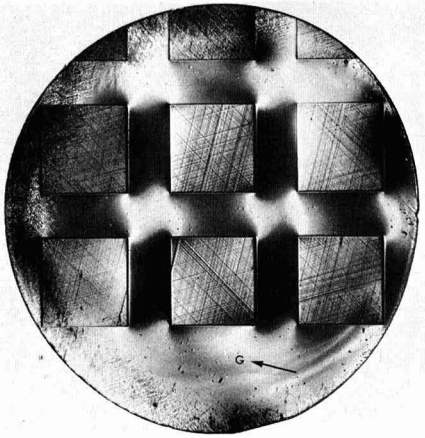

Fig. 3. Contrast variation of interjunction strain gradients for $\bar{g} = [\bar{2}11]$; visibility by extinction contrast between parallel sides of adjacent junctions and by Borrmann effects between four corners of four adjacent junctions.

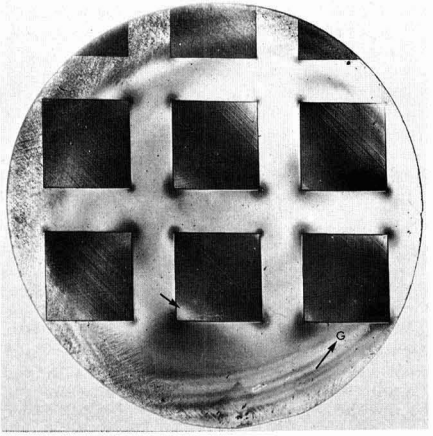

Fig. 5. Corresponds to Fig. 4 except that the oxide has been chemically removed; all four interjunction strain lobes are visible by extinction contrast only; $\bar{g} = [1\bar{1}\bar{1}]$.

The four strain lobes again appear in Fig. 4 when the operating diffraction vector $\bar{g}$ is $[1\bar{1}\bar{1}]$. Now however, the two lobes parallel to $\bar{g}$ (at areas 2 and 4) are visible by extinction contrast (dark regions) while the two lobes perpendicular to $\bar{g}$ (at areas 1 and 3) are visible over large areas by Borrmann effects (white regions) and by extinction contrast at the tips of the sharp corners. An indication of inelasticity is observed in Fig. 5 where all four strain lobes are visible after chemically removing the oxide. Apparently a portion of the strain is built into the oxide as indicated by the visibility of all four strain lobes by extinction contrast ($g = [11\bar{1}]$) in contradistinction to the observation made in Fig. 4. Note also that the strain gradient defining the SiO_2 window pattern is still visible even though the SiO_2 has been removed. The intense interjunction strain concentration lies on {111} planes and arises as a consequence of the diffusion cycle. The strain is inelastic inasmuch as it is equally well observed after removing the oxide mask, although the character of the strain pattern does depend on whether the diffusion mask is intact or removed from the substrate (compare Fig. 4 and 5).

Generally, each highly faulted diffused area contributes to an enhanced x-ray intensity (Fig. 5) which may not be directly related to the diffusion-induced line defects. However, the intensity within the junction areas at the sharp corners appears to reverse contrast or appear white (see arrow in Fig. 4 and 5) while outside the junction the strain contrast is dark. Apparently the fault vector corresponding to the strain lobes is directional. That is, the fault vector is tilting the lattice planes in different directions at the corner boundary separating the diffused/nondiffused matrix.

So far, three distinct strain effects, other than dislocation formation, have been observed: (*i*) strain gradients which sharply delineate oxide boundaries (Fig. 1); (*ii*) extensive residual strain effects at oxide boundaries which extend outside and into the diffused areas (Fig. 4 and 5), and (*iii*) an additional strain built into the oxide due to the diffusion cycle (Fig. 4 and 5).

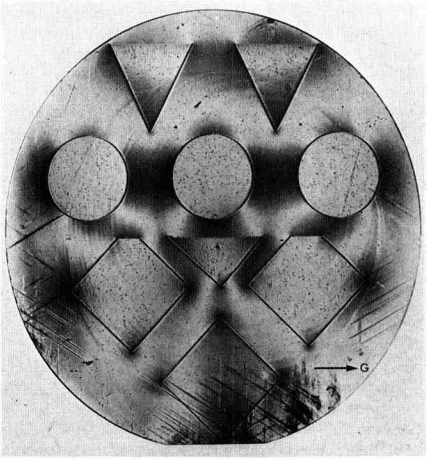

Fig. 6. Low vapor pressure phosphorus diffusion revealing pronounced interjunction strain gradients and no diffusion-induced dislocations; $\bar{g} = [11\bar{1}]$.

Using similar diffusion conditions, the occurrence of interjunction strains was found to be independent of the cooling rate. Also under simulated diffusion conditions (without the vapor source), these strain effects were not observed. However, by changing only the vapor pressure of the source it was possible not only to control the occurrence of interjunction strains but it was also possible to control the generation of diffusion-induced dislocations (13). Under low vapor pressure (Fig. 6) no diffusion-induced dislocation arrays are detected by x-ray topography. However the interjunction strain effects are quite pronounced and their occurrence is independent of the particular shape of the window openings. Only the character of the strain pattern is altered by window geometry. The dark spots throughout the wafer are defect markings introduced during the surface polishing. Under high vapor pressure (Fig. 7) each diode is highly dislocated or faulted as evidenced by the excessive intensity within each junction area. However no interjunction strain is evident. Juleff and LaPierre (14) have observed the extension of strain, originating at locally diffused regions in the Si substrate, into epitaxial Si layers grown over the diffused Si substrate. Even in this case the observed strain effects clearly define the diffused junction geometry, although in some cases diffusion-induced dislocations do propagate laterally from the junction into the non-diffused areas of Si.

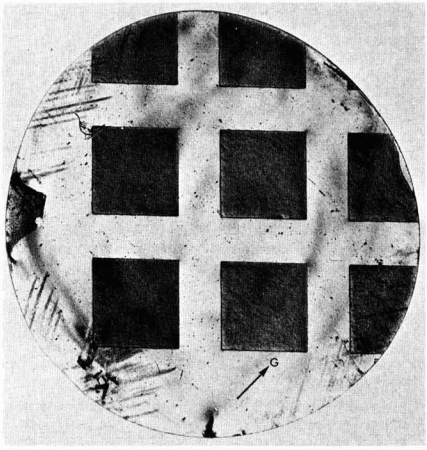

Fig. 7. High vapor pressure phosphorus diffusion revealing no interjunction strain gradients and highly faulted junction areas; $\bar{g} = [11\bar{1}]$.

Discussion

The deformed regions between diffused junction areas are clearly related to the generation of dislocations within the junction area. These dislocations are caused by the contraction of the silicon lattice due to the diffusion of smaller phosphorus atoms. The difference in the tetrahedral covalent radii between Si and P is 0.07Å. Joshi *et al.* (7) have reported that the lattice parameter of Si decreases with increased amounts of phosphorus when solution doping techniques are employed in growing Si crystals. Furthermore, the lattice parameter, a_o, in phosphorus diffused Si (very high concentrations) more nearly corresponds to the value of a_o in lightly solution doped Si, probably as a consequence of strain relief and lattice relaxation when diffusion-induced dislocations are

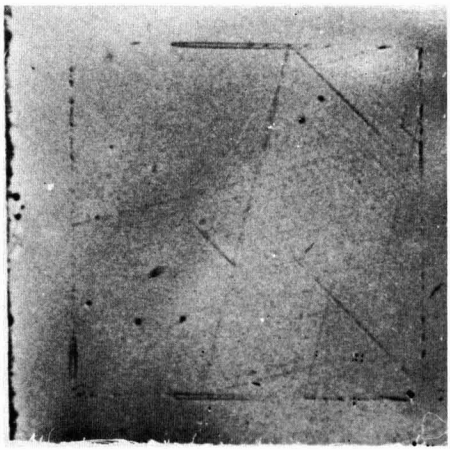

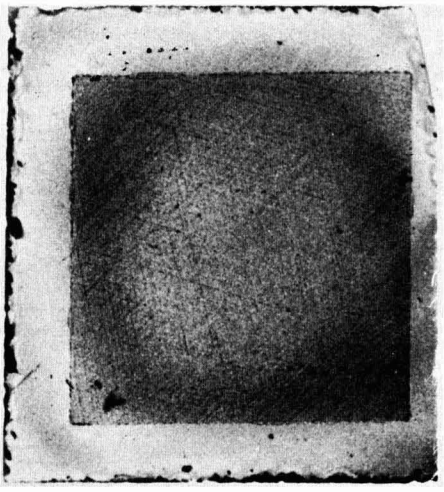

Fig. 8. X-ray topographs recorded after removal of 1.3μ of Si; (a) junction area sectioned from sample shown in Fig. 2; (b) junction area sectioned from sample shown.

formed. Joshi *et al.* (7) have measured by x-ray line broadening techniques the average strain levels associated with diffusion-induced dislocations and an additional residual strain in diffused silicon layers. The interjunction strain effects observed in our x-ray topographs confirm the existence of these residual strains. Such residual strains are distributed laterally into the nondiffused matrix. The dependence of these strains on the absence of misfit-type dislocations agrees with their observations of lattice parameter variations *vs.* dopant level. Joshi interprets the presence of residual strains in thin surface layers as being due to an insufficient penetration of the diffusion-induced dislocations (7). The distribution of dislocations in samples which showed interjunction strain (*i.e.*, Fig. 2) and samples without interjunction strain (*i.e.*, Fig. 7) was measured by x-ray topography after shallow Si layers were removed by anodic oxidation techniques. A series of topographs were recorded after each incremental removal of 1000Å of Si. In Fig. 8, 1.3μ of Si have been removed from the diffused side (junction depth $x_j = 2\mu$) of each specimen shown in Fig. 2 and 7. Most of the dislocations have been removed in Fig. 8a while a high density still remains in Fig. 8b indicating a movement of dislocations deeper into the substrate toward the junction. The interjunction strains seen in Fig. 2 are no longer visible after 0.5μ of Si has been removed.

A final observation should be made. The interjunction strains observed in this report do not appear similar to the deformations, observed by Lawrence (6), which result in dislocations formed within highly restricted zones of the nondiffused matrix. He has observed that total impurity stress relief is affected by the type of dislocation formed. Our observations imply that total stress relief, resulting in minimum impurity-induced strain in the nondiffused lattice, occurs when the junction is heavily faulted. This seems to be a consequence of the total number of dislocations formed and their movement into the substrate. Relaxation of solute lattice contraction stresses is affected by the generation of dislocations which, under the conditions stated, balance the impurity-induced strain due to solute indiffusion.

Summary

Extensive interjunction strain gradients are manifestly observed by x-ray topography. The visibility of such strains is dependent on both the strain gradients due to high concentration impurity diffusions and on the operating reflection employed. Their occurrence is dependent on the magnitude of the unrelieved residual stress which can be compensated by stress-relief generation of dislocations. The depth of penetration of such strains is about ¼ of the junction depth and extends at least 500μ laterally from the junction-area boundary.

Acknowledgments

The authors gratefully acknowledge the assistance of R. J. Modena and Virgil Ragusin in some of the experimental work.

Manuscript received May 2, 1967; revised manuscript received *ca.* Oct. 30, 1967.

Any discussion of this paper will appear in a Discussion Section to be published in the December 1968 JOURNAL.

REFERENCES

1. H. J. Queisser, *J. Appl. Phys.*, **32,** 1176 (1961).
2. G. H. Schwuttke and H. J. Queisser, *ibid.*, **33,** 1540 (1962).
3. M. L. Joshi and F. Wilhelm, *This Journal,* **112,** 185 (1965).
4. J. F. Black and E. D. Jungbluth, *ibid.*, **114,** 188 (1967).
5. E. S. Meieran and I. A. Blech, *J. Appl. Phys.*, **36,** 3162 (1965).
6. J. E. Lawrence, *This Journal,* **113,** 819 (1966).
7. M. L. Joshi, C. H. Ma, and J. Makris, *J. Appl. Phys.*, **38,** 725 (1967).
8. E. D. Jungbluth and H. Chiao, *Bull. Am. Phys. Soc.*, **12,** 672 (1967).
9. E. Kooi, *This Journal,* **111,** 1383 (1964).
10. A. R. Lang, *J. Appl. Phys.*, **30,** 1748 (1959).
11. I. A. Blech and E. S. Meieran, *ibid.*, **38,** 2913 (1967).
12. K. Haruta and W. J. Spencer, *ibid.*, **37,** 2232 (1966).
13. R. A. McDonald, G. G. Ehlenberger, and T. R. Huffman, *Solid St. Electron.*, **9,** 807 (1966).
14. E. M. Juleff and A. G. LaPierre, *Int. J. Electronics,* **20,** 273 (1966).

Technical Notes

Phase Transformations in the System Cu_2S-Ag_2S

R. B. Graf

United Aircraft Corporation, Research Laboratories, East Hartford, Connecticut

Both end members of the system Cu_2S-Ag_2S have been of interest for many years as naturally occurring minerals as well as for their electrical properties. Cu_2S has been of importance as a rectifier material and Ag_2S is a semiconductor that has a polymorphic transformation at 177°C. This phase transformation is accompanied by an abrupt electrical resistivity change of about 3 orders of magnitude and has been mentioned as being suitable for a-c switching applications (1). In addition to this phase transformation, it was considered that the equilibrium diagram (2) (Fig. 1) might contain other invariant points which would exhibit interesting electrical properties. The points selected for this investigation were: the eutectoid reaction between acanthite (Ag_2S) and jalpaite ($Cu_{0.45}Ag_{1.55}S$) to form argentite at 106°; the phase transformation in jalpaite to form argentite at 117°; and the eutectoid reaction between orthorhombic chalcocite (Cu_2S) and stromeyerite (CuAgS) (not shown in Fig. 1) at 67°. The transformation of acanthite (Ag_2S) to argentite was investigated using thin films as well as bulk pieces to determine if the large change in resistivity could be obtained easily in thin film samples.

The compounds were formed by reacting the elements (99.999% purity) in evacuated and sealed glass tubes. The reactants were sintered at 400°C until none of the free elements remained visible, and the formation of the compounds was verified by powder x-ray diffraction. The samples for resistivity measurements were fabricated by compressing powders which had been filed from the sintered ingots. The powder compacts, which were 0.250 in. in diameter and 0.125 in. long, were pressed in a split die so constructed as to make it possible to press a chromel-alumel thermocouple into the center of the pellet. At this same time

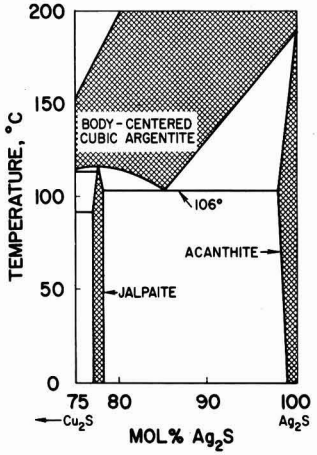

Fig. 1. The system $Cu_{0.45}Ag_{1.55}S$-Ag_2S

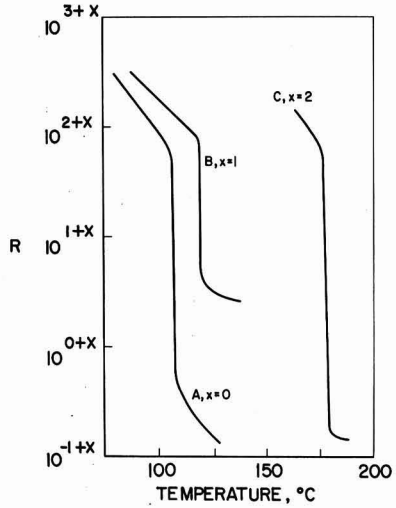

Fig. 2. Resistance *vs.* temperature for: A, acanthite-jalpaite eutectoid reaction; B, transformation of jalpaite to argentite; C, transformation of acanthite to argentite in thin film form.

gold powder was pressed onto either side of the pellet to form electrodes. The thin films of Ag_2S were formed by evaporating silver onto glass substrates which were then heated with sulfur at 200°C in sealed glass tubes. Electrodes of silver paste were spaced on the film so as to make the sample resistance about 10,000 ohms at approximately 170°. Because of the known ionic conductivity in Ag_2S, the electrical resistivity measurements were made by passing a constant, 60 cycle current of 100 ma through the samples and measuring the voltage change as a function of temperature. The voltage was measured with a Moseley log converter and the output of the log converter was plotted against the output of the thermocouple on a Moseley x-y plotter. Such an arrangement makes it possible to obtain the transformation time for a sample of a given size. A heating rate of 5°C/min was used for all samples.

The resistance changes on heating the samples *vs.* temperature are shown in Fig. 2. The eutectoid reaction between acanthite and jalpaite (curve A) begins at 106° and is essentially over at 110°. On cooling the sample, the reverse reaction exhibits about 12° hysteresis, measured at the mid-point of the highest slope. Heating and cooling the sample through 12 cycles does not change the characteristics of the plot; the heating curve is almost exactly reproduced and the cooling curve is reproduced to within ±1.5°. Jalpaite, which also transforms to argentite on heating, has a resistance change as shown by curve B. The transformation begins at 117° and is over at 120°. There is about 7° hysteresis on cooling. Curve C in Fig. 2 depicts the resistance change in a thin film of Ag_2S on a ¼ in. square glass substrate as it was heated through the transition temperature of 177°. This reaction occurs over a temperature span of 3° and the reverse reaction had about 6° hysteresis. The transformation in a sample of Ag_2S 0.125 in. thick and 0.250 in. in diameter occurred over a temperature span of 2° or 3°C. The eutectoid reaction between orthorhombic chalcocite (Cu_2S) and stromeyerite (CuAgS) at 67° to form hexagonal high-chalcocite (not shown in Fig. 2) is accompanied by an increase in resistance of less than one order of magnitude and does not occur as quickly as the others, being spread over a temperature range of 20°.

These results indicate that by using invariant points on a phase diagram, it may be possible to obtain solid-solid reactions which would be suitable for a-c switching in those cases where switching time is not so important. The transformation times may be varied by using thin films of the materials on the proper substrates.

Acknowledgment

The author would like to acknowledge the valuable assistance of Jane Pinto in various phases of the experimental work.

Manuscript received Oct. 26, 1967.

Any discussion of this paper will appear in a Discussion Section to be published in the December 1968 JOURNAL.

REFERENCES

1. R. G. Cope and H. J. Goldsmid, *Brit. J. Appl. Phys.*, **16**, 1501 (1965).
2. B. J. Skinner, *Econ. Geol.*, **61**, 1-26 (1966).

Gas Phase Etching of Sapphire

II. Fluorinated Hydrocarbons

H. M. Manasevit

Autonetics, A Division of North American Rockwell Corporation, Anaheim, California

Of various processes and techniques that have been used to etch and/or polish inorganic oxide systems, the least used but probably the most desirable approach is a gas phase process. Until quite recently, no gas phase etchant was reported in the literature that would etch-polish sapphire at what might be considered a reasonable rate (about 1 μm/min). However, studies in our laboratories have indicated that a host of different gas-phase etchants will etch-polish sapphire. The successful etch-polishing of sapphire with sulfur tetrafluoride (SF_4) and sulfur hexafluoride (SF_6) has already been reported (1). Only two ori-

entations were studied, $(11\bar{2}3)$ and $(1\bar{1}02)$ of sapphire, with the former showing preferential polish while the latter etched under comparable conditions.

Since the probable aluminum product of etching with the sulfur fluorides is AlF_3 (indications of AlF_3 epitaxy on Al_2O_3 were obtained at temperatures of 1150°C) (1), it was anticipated that other fluorine containing compounds were possible sapphire etchants. From a fundamental point of view, knowledge of the etching capability of hydrogen fluoride and fluorine would be interesting, but their reactivity with Pyrex and quartz deterred study with these materials in our epitaxial system. Therefore, we chose to consider the etching potential afforded by a most readily available group of fluorine containing compounds, the fluorinated hydrocarbons. These compounds are relatively inexpensive, have low toxicity levels, are easily handled, seem to be stable at room temperature, and are commercially available in a reasonably good purity.

To date, seventeen fluorocarbon gases have been examined as possible etch-polish agents for sapphire. As will be shown, some of these have a potential as dislocation etchants for different sapphire orientations.

Experimental

Studies were performed in a vertical reactor system similar to that previously described (2). It includes a tank of inert carrier gas, such as helium, upstream from a tank of the "etchant" to be studied. These are connected via Matheson No. 607 and No. 600 flowmeters, respectively, to a stainless steel manifold joined to the quartz reactor by a Teflon connector. For liquid fluorinated hydrocarbons, a portion of the carrier gas is bubbled through the liquid stored in a stainless steel container, passed into the flowing ambient kept at approximately one atmosphere total pressure, and directed into the reactor. Carrier gas flow rates were arbitrarily set at 2.5 liters/min. The gases are passed over a substrate resting on an Al_2O_3 spacer covering a carbon pedestal inductively heated to the etching temperature. The spacer seems to help provide a more even heat distribution and to reduce reaction between the etching gases and the carbon pedestal. Pedestal temperatures were measured with an optical pyrometer, and uncorrected values are reported. The actual substrate temperature is estimated to be 50°-100° lower than the observed 1450°C etching temperature used to compare the etch-polishing ability of the fluorinated hydrocarbons.

To facilitate the experiments, the studies included mostly those fluorinated hydrocarbons that have relatively low boiling points. The effect of etching-gas concentrations up to about 1 m/o (mole per cent) was investigated and compared with all of the fluorinated hydrocarbons noted in Table I.

Results and Discussion

Carbon tetrafluoride (CF_4) was the only fluorinated hydrocarbon in Table I that did not attack sapphire at 1450°C during a 30-min period at 0.5 m/o concentration with either He or H_2 as the carrier gas. The other compounds were found to etch and/or polish sapphire to different degrees in helium. Some of the etchants revealed major defects in the sapphire, others left carbonaceous residues, and some revealed dislocation arrays.

Table I. Fluorinated hydrocarbons studied as etchants for sapphire at 1450°C

Chemical formula	Common name
CHF_3	Fluoroform
$CHClF_2$	Chlorodifluoromethane
$CHCl_2F$	Dichlorofluoromethane
CH_2F_2	Methylene fluoride
$CClF_3$	Chlorotrifluoromethane
CCl_2F_2	Dichlorodifluoromethane
$CBrF_3$	Bromotrifluoromethane
CF_4	Carbon tetrafluoride
C_2F_6	Hexafluoroethane
C_2ClF_3	Chlorotrifluoroethylene
C_2ClF_5	Monochloropentafluoroethane
$C_2Cl_3F_3$	1, 1, 2-Trichlorotrifluoroethane
$C_2Cl_2F_4$	1, 2-Dichlorotetrafluoroethane
C_3F_8	Perfluoropropane
C_3F_6O	Hexafluoroacetone
C_4F_8	Octafluorocyclobutane
C_4F_8	Perfluorobutene-2

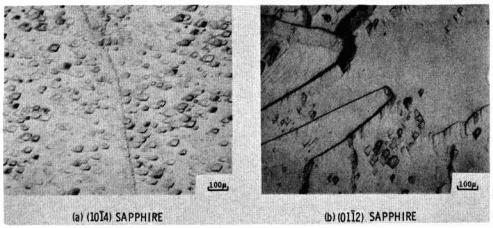

Fig. 1. Dislocation structure revealed by etching with hexafluoroacetone (C_3F_6O) for (a) $(10\bar{1}4)$ sapphire; (b) $(01\bar{1}2)$ sapphire.

As with the sulfur fluorides, selectivity for sapphire orientation was also demonstrated by the fluorocarbon etchants. For example, hexafluoroacetone polished $(11\bar{2}3)$ sapphire but roughened both $(10\bar{1}4)$ and $(01\bar{1}2)$ Verneuil sapphire at the same gas concentration. The effect of this etching is indicated in Fig. 1, both a and b.

By bubbling He through the liquid fluorocarbon 1, 1, 2-trichlorotrifluoroethane ($C_2Cl_3F_3$) equilibrated at 0°C and passing the gases over the heated substrate, considerable etching was found for the $(10\bar{1}4)$ and $(11\bar{2}0)$ sapphire (Fig. 2). $C_2Cl_2F_4$, 1, 2-dichlorotetrafluoroethane, revealed structure in basal plane (0°) sapphire (Fig. 3a) and an unusual oval-type defect structure in $(01\bar{1}2)$ sapphire (Fig. 3b).

Except for Fig. 3b, the figures referred to heretofore have been found to be typical surface etch characteristics for the different sapphire orientations noted and, in general, are produced by almost all of the fluorocarbon etchants, especially when concentrations exceeding 1 m/o are used. Reasonable polishing of most orientations studied, however, has been achieved with many of the fluorocarbons when etchant concentrations are kept below about 0.5 m/o. As might be expected, less etch-pitting and surface character were

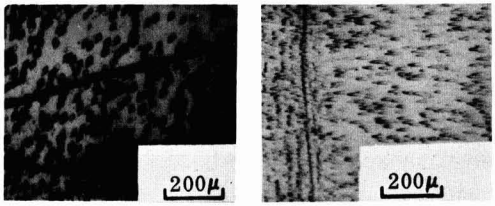

Fig. 2. Dislocation structure revealed by etching with trichlorofluoroethane ($C_2Cl_3F_3$) for (a) $(10\bar{1}4)$ sapphire; (b) $(11\bar{2}0)$ sapphire.

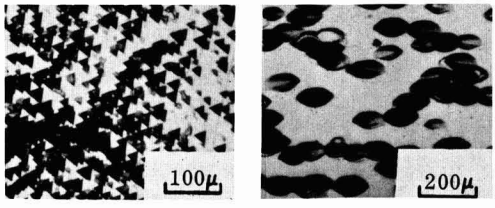

Fig. 3. Dislocation structure as revealed by etching with 1, 2 dichlorotetrafluoroethane ($C_2Cl_2F_4$) for (a) (0001) sapphire; (b) $(01\bar{1}2)$ sapphire.

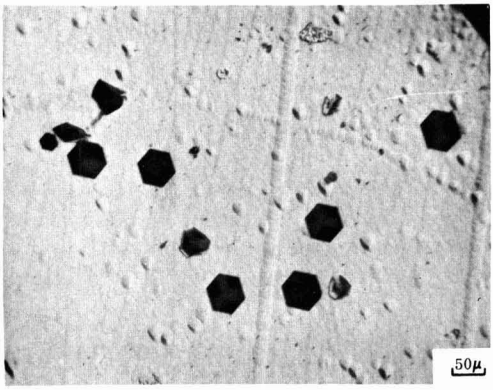

Fig. 4. Defect structure revealed in basal plane Czochralski ruby by etching with chlorotrifluoromethane ($CClF_3$).

obtained when good quality Czochralski sapphire was exposed to the etchants. This is demonstrated in Fig. 4 for basal plane Czochralski ruby etched by monochlorotrifluoromethane ($CClF_3$). The origin of the defect that caused the large hexagonal pits, which are prominent in a field of comparatively few pyramidal etch pits, is not known. Figure 5 was produced by etching $(01\bar{1}2)$ sapphire with octafluorocyclobutane (C_4F_8). The tombstone-like etch pits were usually found to be characteristic of this orientation. The oval pits produced in $(01\bar{1}2)$ sapphire by 1, 2-dichlorotetrafluoroethane ($C_2Cl_2F_4$) (Fig. 3b) may have been caused by a different type of etching species and reaction.

The reactivity of chlorotrifluoromethane ($CClF_3$) as compared to CF_4 is undoubtedly due to the weakening of the C-F bond by the presence of the less electronegative Cl ion in the molecule. Although hexafluoroethane (C_2F_6) is completely saturated like CF_4, the C-C bond is susceptible to rupture, thereby providing the reactive species.

It was observed that when linear C-C double bonds or C-H bonds are present in the structure of the fluorinated hydrocarbon, etching also produced sooty surfaces, especially at the higher gas concentrations. Some of the minor carbon contamination may be attributed to impurities in the gas, but major carbon deposits are more likely due to the cleavage of these bonds in the bulk material. Therefore, complete saturation of the C atoms by halogens, at least one of which is fluorine, seems to be required in choosing a fluorocarbon etchant: for example, hexafluoroethane (C_2F_6), perfluoropropane (C_3F_8), dichlorodifluoromethane (CCl_2F_2), and/or monochloropentafluoroethane (C_2ClF_5). Octafluorocyclobutane (C_4F_8), a fluorocarbon with a ring structure, produced some dark product at 1450°C but etched sapphire at a rather rapid rate at relatively low concentrations compared to the linear chained materials studied. This suggests a weaker C-C bond in the ring structure, with bond breakage making more fluoride per molecule per unit time available for etching. It was also observed that 1, 2-dichlorotetrafluoroethane ($C_2Cl_2F_4$) possessed the capability of etching sapphire at about 0.1 μm/min at temperatures as low as 950°C (observed uncorrected optical pyrometer reading). (Other highly fluorinated hydrocarbons in the group have not been evaluated at this relatively low temperature.) It is not known if a change in the etching mechanism occurred at 950°C, producing aluminum products other than AlF_3. This might be the case if different carbon-fluorine radicals are produced, *e.g.*, $:CF_2$ (difluorocarbene) or $\cdot CF_3$ (trifluoromethyl radical), at different temperatures.

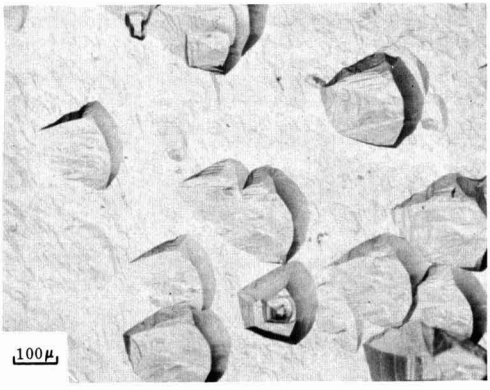

Fig. 5. Effect of etching $(01\bar{1}2)$ sapphire with octafluorocyclobutane (C_4F_8).

It is indeed difficult to write reasonable equations to explain the etching of sapphire without knowing the products of the reaction with the fluorinated hydrocarbons. Some of the products that collected on the cool reactor wall could be vacuum distilled at room temperature; some seemed water soluble; others had to be scraped off the walls or undercut with $HF\text{-}HNO_3$ solutions for removal. It is probable that many of the reactions involve, as previously suggested, the formation of free radicals containing at least one carbon-fluorine bond that might react with Al_2O_3 to produce AlF_3 (volatile at 1450°C) and other products. For dichlorodifluoromethane, a plausible reaction scheme is proposed by the following equations

$$(a)\ CCl_2F_2 \xrightarrow[\Delta]{} Cl_2\uparrow + \underset{1450°C}{:CF_2},\ \text{via pyrolysis}$$

$$(b)\ Al_2O_3 + 3{:}CF_2 = 2AlF_3\uparrow + 3CO\uparrow$$

If more complex fluorinating agents are used as etchants, a study of the reaction products could disclose new materials, perhaps polymers containing aluminum-carbon bonds as well as other fluorinated carbon by-products.

Addendum

Under the etching conditions previously described, a number of inorganic fluorides other than SF_4 and SF_6 were also found to etch sapphire. These include the chlorine fluorides (ClF_3 and ClF_5), nitrogen trifluoride (NF_3), and phosphorus pentafluoride (PF_5). These, of course, produce no organic by-products but introduce in some cases a problem in handling because of their room temperature chemical reactivity with glass flowmeters and other materials.

Conclusions

The etching capabilities of a number of fluorinated hydrocarbons have been demonstrated. These materials show promise of being new reagents for evaluating the quality and improving the surfaces of sapphire prior to its use as a substrate for epitaxy.

Acknowledgment

The author wishes to express his thanks to W. I. Simpson, J. E. Coker, and F. Erdmann for their assistance in the etching studies, to T. J. LaChapelle for suggesting the study, and to James Beeman and the Linde Company for supplying the Czochralski wafers.

This study was supported in part by the Naval Electronics Systems Command under Contract NObsr 93145.

Manuscript received Nov. 16, 1967; revised manuscript received *ca.* Jan. 10, 1968. This paper was

presented at the Chicago Meeting, Oct. 15-19, 1967, as Abstract 183.

Any discussion of this paper will appear in a Discussion Section to be published in the December 1968 JOURNAL.

REFERENCES

1. H. M. Manasevit and F. L. Morritz, *This Journal*, **114**, 204 (1967).
2. H. M. Manasevit, D. H. Forbes, and I. B. Cadoff, *Trans. AIME*, **236**, 275 (1966).

Thermally Activated Diffusion of Electronic Carriers in Iron Phosphate Glasses

Gary S. Snow*[1]

Department of Ceramic Engineering and Materials Research Laboratory, University of Illinois, Urbana, Illinois

Hansen (1) recently measured conductivity and Seebeck coefficient on phosphate glasses containing 45 m/o (mole per cent) P_2O_5. The remaining 55 m/o consisted of FeO and MgO in various proportions. In the 45% P_2O_5-55% FeO composition the ratio of $[Fe^{3+}]$ to $[Fe^{2+}]$ was varied over a wide range. This data offers an excellent opportunity to check the agreement between the experimentally observed dependence of resistivity on valence state distribution and that predicted by the hopping model. Hansen discussed his data qualitatively in terms of the hopping mechanism; however, there are inconsistencies in his discussion which should be clarified.

If the electronic carriers move by a thermally activated diffusion process, the conductivity can be written

$$\sigma = \frac{nq^2d^2zP\nu e^{-\Delta E/kT}}{6kT} \qquad [1]$$

where n is the carrier concentration, q is the charge on the carrier, d is the jump distance, z is the number of nearest neighbor sites, P is the probability that a particular nearest neighbor site will be available to receive a carrier, k is Boltzmann's constant, T is the absolute temperature, ν is a frequency factor characteristic of the lattice vibrations, and ΔE is the energy necessary to remove the lattice distortion around the trapped carrier. In this equation Hansen omitted the factor P which is extremely dependent on the valence state distribution. Evaluation of this factor allows one to obtain a quantitative fit between Eq. [1] and Hansen's experimental data.

In the iron phosphate glasses studied by Hansen let x be the fraction of the iron ions which are in the Fe^{3+} state, let y be the fraction of the cations which are iron, and let c_0 be the total concentration of cations. Then if one assumes that conduction occurs by hopping of electrons from Fe^{2+} sites to Fe^{3+} sites, the carrier concentration will be equal to the concentration of Fe^{2+} ions; thus $n = (1-x)yc_0$. Assuming that phosphorous ions and iron ions of either valence have equal probability of being on any given cation site, the probability that a particular nearest neighbor site will be available to receive a carrier is just equal to the fraction of the cation sites which are occupied by Fe^{3+} ions; thus $P = xy$. Using these relations, Eq. [1] then becomes

$$\sigma = Ke^{-\Delta E/kT}y^2(1-x)x \qquad [2]$$

where

$$K = \frac{c_0q^2d^2z\nu}{6kT} \qquad [3]$$

It should be noted that the same equation results if the carriers are assumed to be holes moving from Fe^{3+} sites to Fe^{2+} sites, in which case $n = xyc_0$ and $P = (1-x)y$.

In Fig. 1 and 2 the data of Hansen is compared with this theory. In plotting Eq. [2], ΔE was obtained as a function of x and y from Hansen's data, and K was chosen as 563 $(\text{ohm-cm})^{-1}$. There is excellent agreement between the experimental data and the calculated points. From Fig. 1 it is apparent that another transport mechanism becomes dominant below $y = 0.05$.

Taking $K = 563$ $(\text{ohm-cm})^{-1}$ an order-of-magnitude value for ν can easily be calculated from Eq. [3]. Assuming a simple cubic distribution of cation sites and taking c_0 as approximately 10^{22} cm^{-3}, then $z = 6$ and $d = 4.7 \times 10^{-8}$ cm. The other parameters are known constants. The resulting value for ν is 6.5×10^{12} sec^{-1} which is in good agreement with the expected value of the vibrational frequency of the lattice.

Since d can be treated as independent of x and y, it appears likely that electronic transfer always occurs between nearest neighbor iron sites, at least for $y > 0.05$ (10 m/o FeO).

Allersma and Mackenzie (2) have shown that the Seebeck coefficient data which Hansen obtained for iron phosphate glasses qualitatively fits the following equation developed by Heikes (3) for the hopping

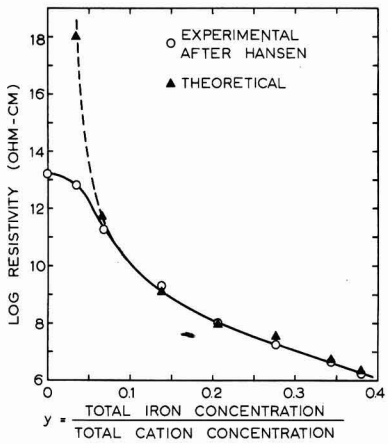

Fig. 1. Logarithm of resistivity at 200°C as a function of the fraction of the total cations which are iron. Experimental data was taken from Fig. 1 of ref. (1). Theoretical points were calculated from Eq. [2] using the ΔE values from Fig. 1 of ref. (1) and taking $K = 563$ $(\text{ohm-cm})^{-1}$.

* Electrochemical Society Active Member.

[1] Present address: Inorganic Materials Science Division, 1123, Sandia Corporation, Albuquerque, New Mexico.

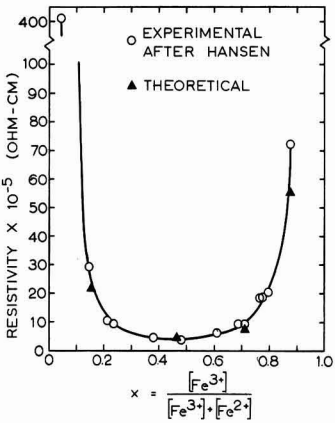

Fig. 2. Variation of resistivity with $x = [Fe^{3+}]/[Fe_{total}]$ at 200°C for glasses containing 55% FeO-45% P_2O_5. Experimental data was taken from Fig. 4 of ref. (1). Theoretical points were calculated from Eq. [2] using ΔE values from Fig. 3 of ref. (1) and taking $K = 563$ (ohm-cm)$^{-1}$.

mechanism

$$\alpha = \frac{k}{q} \ln \frac{n_o - n}{n} \qquad [4]$$

In Eq. [4] α is the Seebeck coefficient, n is the concentration of carriers (equal to $[1-x]yc_o$ if the carriers are electrons and equal to xyc_o if they are holes), n_o is the concentration of accessable sites (equal to yc_o in either case), and q has the sign of the charge carrier. It is worth noting that Eq. [4] becomes

$$\alpha = \frac{-k}{|q|} \ln \frac{x}{1-x} \qquad [5]$$

and fits the data over the entire range of x whether the carriers are holes or electrons; thus, it is not necessary that the sign of the carriers change when the Seebeck coefficient goes from positive to negative as was concluded by previous investigators (1, 2). From the currently available data no conclusions can be drawn concerning the sign of the charge carrier.

In order to calculate the carrier mobility, Hansen obtained the carrier concentration from the equation $n = n_o \exp(-q\alpha/k)$. He took n_o as the absolute difference between the ferric and ferrous concentrations. This assumption contradicts the data since it would result in an infinite resistivity at $x = 0.5$ rather than a minimum as shown in Fig. 2. Hansen obtained values for the frequency factor ν which were extremely dependent on ΔE and on his choice of valence state distribution. In the present analysis ν is independent of these parameters as one would expect.

This treatment yields a carrier mobility which (at 200°C in the 55% FeO glass) varies from 1.3×10^{-8} cm^2/v-sec to zero as the concentration of carriers goes from zero to yc_o.

The correlation between Hansen's data and Eq. [2] and [5] strongly supports the treatment of electronic conduction in the iron phosphate glasses as a thermally activated diffusion process. It appears doubtful that conduction in a partially filled 3d band would have this dependence on valence state distribution.

Acknowledgment

This work was supported in part by the U.S. Atomic Energy Commission, Contract No. AT(11-1)-1198.

Manuscript received July 24, 1967; revised manuscript received Dec. 18, 1967.

Any discussion of this paper will appear in a Discussion Section to be published in the December 1968 JOURNAL.

REFERENCES

1. K. W. Hansen, *This Journal*, **112**, 994 (1965).
2. T. Allersma and J. D. Mackenzie, Technical Report No. 4, Contract No. Nonr-591(21), December 1966.
3. R. R. Heikes, A. A. Maradudin, and R. C. Miller, *Ann. Phys.*, **8**, 733 (1963).

Brief Communications

Impurity Heterogeneities and Multiple-Beam Interferometry

D. C. Johnston, A. F. Witt,* and H. C. Gatos*

Department of Metallurgy and Center for Materials Science and Engineering, Massachusetts Institute of Technology, Cambridge, Massachusetts

Multiple-beam interferometry (1) combined with high resolution etching techniques has been successfully employed for revealing relative microscopic concentration changes of impurities in InSb. In view of the fact that "rate striations" intentionally introduced into single crystals allow the precise determination of microscopic rates of crystal growth (2), it was possible to demonstrate further in the present study that multiple-beam interferometry can directly reveal relationships between microscopic rates of growth and impurity concentration. The impurity present in the crystals was tellurium (about 10^{17}/cm^3).

* Electrochemical Society Active Member.

Figure 1 depicts the "off-core" region of a single crystal of InSb pulled in the <111> direction with seed rotation and subjected to controlled vibrations (frequency 12 per sec). The interference fringes were aligned in a vertical direction (1). In this way a uniform impurity distribution or complete absence of impurities would be reflected by the appearance of straight and parallel interference fringes aligned from top to bottom (a perfectly flat semiconductor surface after etching). Under the present experimental conditions a relative decrease or increase in impurity concentration (depressions or elevations on the etched semiconductor surface, respectively) will appear as

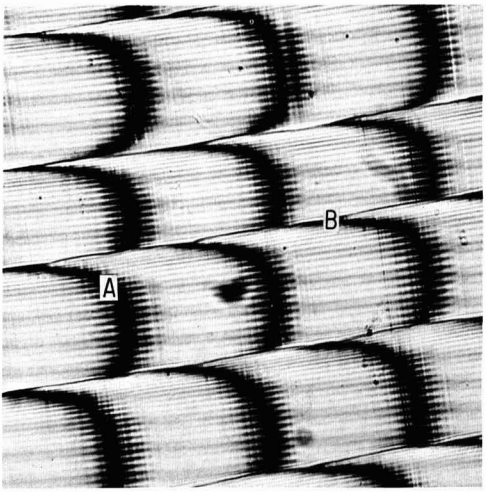

Fig. 1. Interferogram of an "off-core" region of InSb grown in the <111> direction (top to bottom) exhibiting pronounced "remelt" rotational striations, B. The abrupt interference fringe deflections to the left, A, associated with the rotational striations reflect a sharp decrease in impurity concentration. The "rate striations" are also clearly seen (see text). Magnification 700X.

deflections of the fringes to the left and right, respectively. Tellurium impurities decrease the etching rate of InSb under the present experimental conditions. Figure 1 shows abrupt fringe deflections to the left, A, which are associated with slightly curved rotational striations, B, traversing from left to right. The rate striations are readily visible as small spikes emanating from the fringes. Thus the fringe pattern permits the simultaneous determination of microscopic growth rates and the associated impurity concentration changes.

The information contained in the interferogram of Fig. 1 can best be extracted by analyzing the pattern of the individual fringes running from top to bottom (along the growth axis). The separation of the rate striations reflects the growth rate changes associated with rotational striations as discussed in detail elsewhere (2). It can readily be seen that immediately below each remelt striation the growth rate assumes very small values which gradually increase (increasing spacing of subsequent spikes proceeding from top to bottom) before they become very small again at the next striation. The abrupt fringe deflections to the left associated with rotational striations indicate a sharp drop in impurity concentration in the area of decreased growth rate. With increasing growth rate (below the remelt striations) the fringes move to the right indicating a relative increase in impurity concentration. The observed concentration changes on either side of each striation is consistent with the corresponding growth rate changes discussed in detail elsewhere (2).

Figure 2 depicts the "off-core" to "on-core" transition region in a single crystal (InSb) pulled in the <111> direction with seed rotation (no rate striations were introduced). On the left-hand side, A, (off-core region) the impurity concentration decrease associated with the rotational striation is clearly visible. The on-core regions, B, (increasing in area from left to right) are characterized by the strong fringe deflections to the right which correspond to a marked increase in impurity concentration. This region which grows under a relatively constant vertical microscopic growth rate (2) exhibits impurity concentration fluctuations which clearly are not related to vertical growth rate changes and thus indicate the operation of a growth mechanism different from that in the off-core region. Unexplained is also the small impurity concentration decrease in the off-core, C, region just preceding the transition to the "core" region.

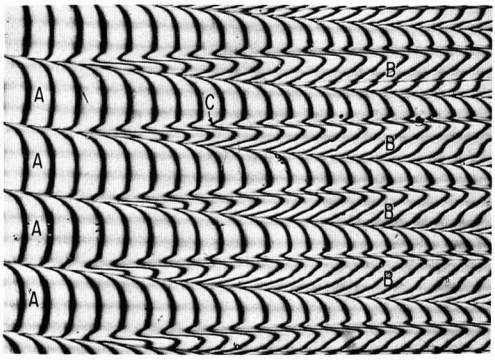

Fig. 2. Interferogram of an etched "off-core" to "on-core" transition region of InSb grown in the <111> direction (top to bottom). Note impurity concentration changes in the off-core region (on the left side, A) associated with rotational striations (same as in Fig. 1). The on-core regions, B, exhibit strong fringe deflections to the right corresponding to increased impurity concentration. Within the core regions very pronounced impurity concentration variations are visible (changes in slopes of the deflected interference fringes). A small but readily visible impurity concentration decrease is present in the off-core region adjacent to the "core" region, C. See text. Magnification *ca.* 470X.

The ultimate value of the present-type interferogram depends on the availability of quantitative relationships between etching rates and impurity concentration for varying etching times. Actually in our experiments it was found that the ratio of the interference fringe deflections remained constant for a given impurity concentration change over a wide range of etching times (30 sec to 3 min) and etchant compositions. Consequently it appears that the relative dependence of the etching rate on impurity concentration is invariant. Thus it is expected that etching rate calibrations with known impurity concentrations will permit the determination of absolute impurity concentrations and concentration changes on a microscale.

Acknowledgment

This work was supported by the National Science Foundation under contract GK-1653.

Manuscript received Jan. 4, 1968.

Any discussion of this paper will appear in a Discussion Section to be published in the December 1968 JOURNAL.

REFERENCES

1. S. Tolansky, "An Introduction to Interferometry," John Wiley & Sons, Inc., New York (1962).
2. A. F. Witt and H. C. Gatos, *This Journal*, **115**, 90 (1968).

On the Trapping Level Disposition in Cadmium Sulfide

Paul A. Faeth[1]

Lewis Research Center, National Aeronautics and Space Administration, Cleveland, Ohio

The tendency has been to consider trapping states in CdS as being in different classes depending on their position within the energy gap (1) and the particular phenomena being observed. It appears, however, that there is a regularity in their values and that these states might be considered as part of a single energy scheme. Such an idea has been proposed by Klasens (2) among others for luminescent and trapping centers in ZnS.

The electron trapping level disposition within the band gap of CdS has been found to include the values of 0.05, 0.14, 0.25, 0.41, 0.63, and 0.83 ev (3). These values are the averages obtained using various experimental techniques and several methods of calculation, and are given as energy displacements, E_t, from the conduction band. Deeper states have been established which are thought to act as hole traps (1). Studies involving the deeper states indicate these levels occur at $E_t = 1.2$ ev (1, 4) and 1.56 ev (1,5). A self-activated luminescent level at 1.98 ev has been reported by Lehmann (6). Usually all levels do not appear simultaneously in one crystal although that could happen. When levels do appear, however, they occur very near the values mentioned above and are listed in Table I.

A study of trapping states in cadmium sulfide (7) revealed that the experimentally determined trap energies can be related to one another and to the band gap energy E_g of 2.4 ev. The disposition of energy levels can be represented by the equation

$$E_i = a - (bi - ci^2) \qquad [1]$$

where a, b, and c are constants and i is a whole number which numbers successive energy levels E_i. A similar formulation is used for preliminary evaluations of molecular spectra (8). The constants of Eq. [1] can be determined from the values of E_t in Table I. The choice of a starting point for the energy level progression is arbitrary. As an example, a case for $i = 0$ is given at line 11 in Table I for which situation $a = 2.406$, $b = 0.475$, and $c = 0.0238$ ev. A level at 0.031 ev (1) is generated which might be related to the exciton level observed by Reynolds *et al.* (9) at about 0.028 ev or the optical absorption reported at $\sim 40\mu$ by Manabe *et al.* (10). The wavelengths in microns corresponding to E_i and $E_g - E_i$ are listed in Table I and represent regions where photoactivity is observed in CdS.

The energy scheme suggested above may represent part of a band system, in a spectroscopic sense, extending across the energy gap of CdS. A plot of Eq. [1] is parabolic and is suggestive of similar parabolas observed for molecular species such as CN and CuH, for example (8). As the conduction band is approached from the valence band, a "band head" appears to be formed by the trap levels near the conduction band. The system could be tied to the conduction band or the valence band or both. The system limit at the valence band is not as well defined. Fine structure associated with these levels seems likely in view of the recent work of Bryant and Cox (11) involving luminescent emission from CdS. Such structure associated with all levels might give the appearance of a continuous trapping spectrum. Assignments due to specific transitions, however, are not available at this time.

[1] Present address: ITT Industrial Laboratories, Fort Wayne, Indiana.

Table I. Experimental and calculated values of the trapping spectrum of CdS

	E_t	i	E_i	λ_i	$E_g - E_i$	$\lambda_{g,i}$
1	—	10	0.031	40.0	2.378	0.521
2	0.05	9	0.055	22.5	2.351	0.527
3	0.14	8	0.130	9.531	2.276	0.543
4	0.25	7	0.245	5.057	2.161	0.573
5	0.41	6	0.411	3.015	1.995	0.621
6	0.63	5	0.625	1.982	1.781	0.696
7	0.83*	4	0.886	1.398	1.520	0.816
8	1.2	3	1.195	1.037	1.211	1.024
9	1.56	2	1.551	0.799	0.855	1.451
10	1.98	1	1.955	0.634	0.451	2.747
11	2.4	0	2.406	0.515	0.0	—

* More recent studies concerning this level indicate this value may be larger; 0.86 ev (14).

The exact identity of the species involving the energy scheme suggested above is unknown. The levels have been postulated as states of complex impurity-vacancy systems in the bulk. The addition of impurities to crystals stimulates the development of these levels. They seem to occur even in the absence of deliberate doping. The incorporation of impurities might cause slight shifting (Franck-Condon) of potential minima associated with the trapping centers, thus causing some transitions to be unlikely while others are more likely to occur. Previous studies of electrical properties of CdS as affected by sorbed gases have indicated a possible correlation between the amounts of sorbed gases and the appearance of trapped electron populations (7, 12, 13). Such studies suggest the traps may be related to surface states.

Manuscript received Dec. 16, 1967; revised manuscript received Jan. 17, 1968.

Any discussion of this paper will appear in a Discussion Section to be published in the December 1968 JOURNAL.

REFERENCES

1. R. H. Bube, "Photoconductivity of Solids," John Wiley & Sons, Inc., New York (1960).
2. H. A. Klasens, *This Journal* **100**, 72 (1953).
3. K. H. Nicholas and J. Woods, *Brit. J. Appl. Phys.*, **15**, 783 (1964).
4. E. Grillot, *J. Phys. Radium*, **17**, 624 (1956).
5. E. A. Taft and M. H. Hebb, *J. Opt. Soc. Am.*, **42**, 249 (1952).
6. W. Lehmann, *This Journal*, **113**, 788 (1966); *ibid.*, **113**, 449 (1966).
7. P. A. Faeth, *ibid.*, **114**, 511 (1967).
8. G. Herzberg, "Molecular Spectra and Molecular Structure I. Spectra of Diatomic Molecules," D. Van Nostrand and Co., New York (1957).
9. D. C. Reynolds and R. G. Wheeler, Extract des Comptes rendus du 7e Congres International; Physique des Semiconductors, Paris (1964).
10. A. Manabe, A. Mitsuishi, and H. Yoshinaga, *Japan. J. Appl. Phys.*, **6**, 593 (1967).
11. F. J. Bryant, and A. F. Cox, *J. Phys. Stat. Sol*, **14**, 427 (1966).
12. C. E. Reed and C. G. Scott, *Brit. J. Appl. Phys.*, **15**, 1045 (1964); **16**, 471 (1965).
13. P. Mark, *J. Phys. Chem. Solids*, **26**, 959 (1965).
14. F. J. Bryant and A. F. L. Cox, *Brit. J. Appl. Phys.*, **16**, 1065 (1965).

Eagle-Picher guarantees dependable supply—ultra-high purity

You're *sure* with Eagle-Picher, unsurpassed source of all these products in ultra-high purity compound and metal form. Over 30 years ago, Eagle-Picher made Gallium metal recovery practical while separating Germanium from Zinc concentrates. And as a result of constant purification and upgrading since that time, Eagle-Picher today, for example, supplies Germanium and Gallium Oxides with *minimum* spectrographic purities of 99.9999% and Germanium and Gallium metals with spectrographic purities over 99.99999%! So Eagle-Picher compounds and metals continue to lead in quality and dependability for the rigid, precise demands of the semiconductor industry.

EAGLE-PICHER COMPOUNDS AND METALS

BORON: Ultra-high purity elemental Boron; Tribromide; Oxide. **CADMIUM:** Ultra-high purity Cadmium Metal; Sulfide, powder, crystal chips, melt and vapor phase crystals; Cadmium Selenide and Cadmium Telluride powder. **GALLIUM:** Metal; Sesquioxide, Trichloride. **GERMANIUM:** First Reduction Metal; Intrinsic Metal; Single Crystals; Dioxide; Tetrachloride; Tetrabromide; Tetraiodide; Monoxide; Diiodide; Sodium Metagermanate; Sodium Heptagermanate. **ZINC:** Metal; Sulfide, powder, crystal chips, melt and vapor phase crystals; Zinc Selenide and Zinc Telluride powders.

For complete information . . . clip and mail today!

Eagle-Picher Industries, Inc. • Electronics Division • Dept. JES-468• Miami, Oklahoma 74354

Gentlemen: Yes, I would like to have more information on Eagle-Picher Compounds and Metals.

Name_____ Title_____

Firm_____

Address_____

EAGLE EP PICHER

Since 1843

EAGLE-PICHER INDUSTRIES, INC.

General Office
Cincinnati, Ohio 45202

Now Pellon offers you three polishing systems to serve your <u>total</u> polishing needs

first

PAN disposable polishing discs set the standard for quality in the nation's finest laboratories

then

PAD-K semi-permanent polishing tool surface converts any lapping and grinding machine into a polishing machine capable of producing light band finishes in volume production

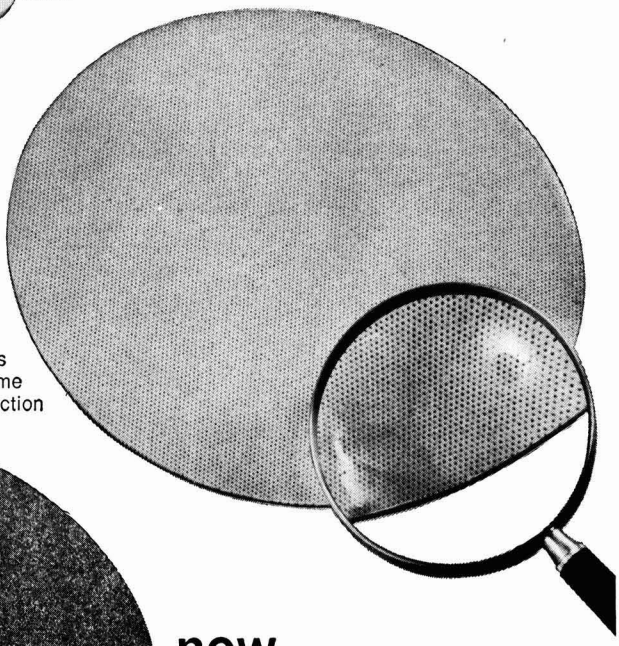

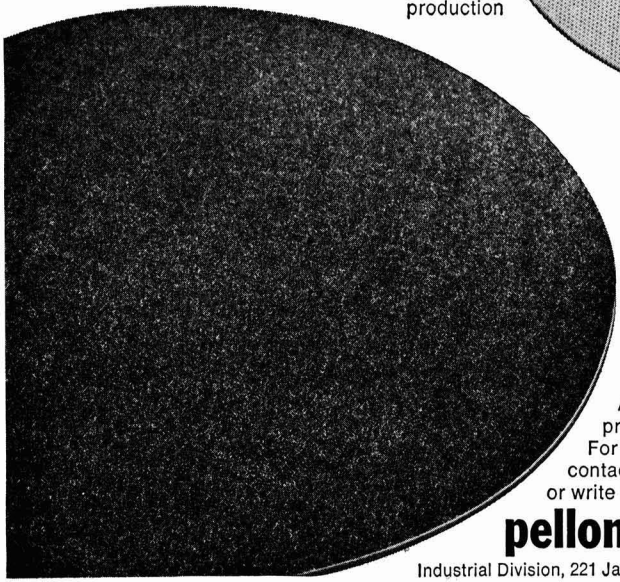

now

PXL micro-porous pileless suede pads for soft structures and final polishing. Corrosion resistant for chemo-mechanical polishing. Available plain and with pressure sensitive adhesive backing. For further information, contact your Pellon distributor or write to:

pellon corporation

Industrial Division, 221 Jackson Street, Lowell, Mass. 01852

ELECTROCHEMICAL SOCIETY

NEWS AND REVIEWS

APRIL
1968

Remarks on the Theory of Electrophoretic Deposition

William F. Pickard

Department of Electrical Engineering, Washington University, Saint Louis, Missouri

ABSTRACT

Following a definition of "electrophoretic," electrophoretic deposition is discussed as a three-step process: (*i*) the charging phase in which the particles to be deposited are given a net electrostatic charge; (*ii*) the transporting phase in which the now charged particles are moved in some specified fashion; and (*iii*) the collecting phase in which the transported particles reach their destinations and are discharged. The characteristics of each of these phases are discussed, and various illustrative examples are given.

The term "electrophoretic" is commonly used to designate those motion phenomena which arise from the direct coulombic action of an electric field on unneutralized charge contained in matter. Thus, either

$$\underset{\text{(particle)}}{\vec{F} = Q\vec{E}} \qquad \underset{\text{(extended region)}}{\text{or } \vec{F} = \int_V \rho\vec{E}dV + \int_S \eta\vec{E}dS} \qquad [1]$$

will provide a fundamental description of the causative process; in this equation, $\vec{F}$ is the force produced by the electric field $\vec{E}$ acting either on the total charge Q of a particle or on the volume (ρ) and surface (η) densities of free charge which characterize an extended region. However, the utilization of electrophoretic force for particle deposition depends not so much on elegant solutions of this equation coupled with the laws of mechanics as it does on careful practical engineering within which the nature of electrophoretic motion is but one of several important factors. For this reason, and also because of the great diversity of possible applications, electrophoretic deposition as a field has resisted formalization. Even so, it is useful to analyze an electrophoretic process by splitting it somewhat arbitrarily into three phases: (*i*) a "charging" phase within which the particles (objects, entities, things, etc.) to be deposited are charged and started on their trajectories; (*ii*) a "transporting" phase within which the particles are moved near to some specified destination (it is within this phase that Eq. [1] finds its chief utility); and (*iii*) a "collecting" phase within which the particle trajectories terminate and the particles are discharged.

These three phases are discussed sequentially in the next three sections of this paper. To make the discussion exhaustive will not, however, be possible since books could be devoted to any one of the phases. Neither will it be possible to erect an elegant mathematical framework within which to cast the discussions since much of the underlying electrochemical theory is but inadequately developed; and, in any event, the associated mathematics is decidedly nonlinear. Rather, the author will attempt to characterize the types of problems encountered and to outline some of the methods of solution developed to date.

Finally, before proceeding to descriptions of the several phases of deposition, it is informative to consider a simple example of an electrophoretic process. In the 1740's G. M. Bose (1) discovered the capillary siphon effect illustrated in Fig. 1. Here the efflux of water from a nozzle fastened to a metal container is much increased by applying a high voltage to the container; in addition, the formerly thin stream breaks up into a cone of spray. (That this phenomenon is electrophoretic can also be inferred from the fact that the region adjacent to the orifice often appears luminous when viewed under low light intensities.) The splitting then can be made as follows: (*a*) the metal container, functioning as an "emitter," injects charge into the liquid which is then coulombically pushed outward away from the nozzle; the container is thus the precursor of the gun used in modern electrocoating; (*b*) the charged liquid droplets then move away toward the basin under the influence of gravity and of the applied electric field. Since particle trajectory, not particle deformation, is important here and since the electric field will be essentially constant over the particle, the particle form of Eq. [1] is the more appropriate; and (*c*) the basin, functioning as a "collector," receives the droplets and bleeds off their charge.

The Charging Phase

A feature common to most electrophoretic systems is a metallic electrode called an emitter which injects free charge into the system. This charge is transferred, either by conduction or by an electrochemical reac-

REVIEW SECTION

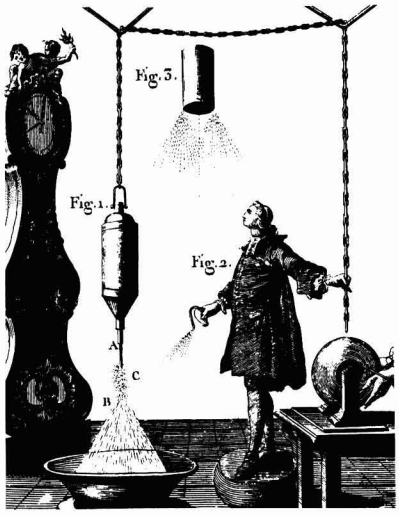

Fig. 1. The capillary siphon as illustrated in an old print (2). *Vide* text.

tion, to matter coming into fairly intimate contact with the emitter. In the former case the electrode design is most often dictated by mechanical considerations, although it is necessary that the surface be kept clean of any nonconducting films which would inhibit charge transfer; in the latter it is commonly controlled by the need for a high surface field and suitably reactive electrode material to enhance the reaction, and for this reason electrodes with small curvature radii are preferred.

If the particles charged at the emitter surface are the ones on which the charge was desired, the charging process can be termed "direct"; otherwise it can be termed "indirect" since one or more charge transfers will be needed to effect the desired charging. As stated above, the three criteria for designing a direct charging process are (*i*) that there be no insulating barrier at the emitter surface, (*ii*) that the surface field be high enough to effect the transfer, and (*iii*) that, in the case of an electrochemical reaction, the emitter surface be compatible with the particles to be charged. In the case of an indirect process the charge is acquired by capturing directly charged particles dielectrophoretically. Thus, a directly charged particle, moving into the neighborhood of a particle to be indirectly charged, induces a dipolar charge distribution on it and in consequence is attracted; if the trajectories of the two particles were appropriate initially, this interaction will lead to trajectory modifications terminating in collision and capture. Obviously, emitter design for an indirect process will emphasize the production of high densities of directly charged particles since this will promote indirect charging.

Two examples will serve to make these considerations more concrete. First, a classic example of a direct charging process is given by the static field, conductance separator (3) used in a variety of mineral purification processes; this is illustrated in Fig. 2. A mixture of conducting (solid dots) and insulating (hollow dots) particles is dumped onto a revolving charged cylinder. The conducting particles are directly charged at once and are drawn off toward the other electrode, falling eventually into hopper C; the insulating particles are weakly held to the revolving electrode by a dielectrophoretic interaction with its modest surface field until they have been rotated far enough for gravity to draw them off into hopper I. Second, the electrostatic precipitation of flue dust (4, 5) provides an excellent example of an indirect

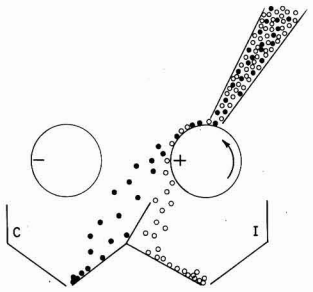

Fig. 2. Schematic illustration of a conductance separator. *Vide* text.

charging process; this is illustrated schematically in Fig. 3. Here a high voltage corona wire is run up the center of a grounded pipe. Gas, flowing axially in the pipe, is ionized by the wire and the resultant ions repelled into the gas stream where, electrodiffusing, they collide with and/or are attracted to particles of dust. The dust particles so charged are then attracted to the pipe where they are collected.

The Transporting Phase

In the transporting phase the trajectories of individual charged particles are considered. Each trajectory is specified by a set of initial conditions and the equation

$$\mu \frac{d^2\vec{r}}{dt^2} = QV\vec{E}_o(\vec{r};t) + \vec{M}(\vec{r};t) - \lambda\left(\frac{d\vec{r}}{dt} - \vec{v}\right) \quad [2]$$

where $\vec{r}$ is a vector describing the particle's position, μ is the particle's mass, V is a scaling factor to describe the magnitude of the electric field, $\vec{E}_o$ is the value of the applied field when $V = 1$, $\vec{M}$ is the mechanical (gravitational, convective, *etc.*) force, and λ is the coefficient of viscous drag and $\vec{v}$ the velocity of the medium surrounding the particle. In addition, of course, it is also necessary to set up and solve equations for $\vec{v}$, $\vec{E}_o$, and $\vec{M}$; these equations are coupled to Eq. [2] since (*i*) $\vec{E}_o$ is influenced by space charge which is in turn influenced by the density of charged particles, and since (*ii*) by Newton's third law the viscous retardation which the particle experiences produces an acceleration of the fluid surrounding it. Obviously Eq. [2] and its subsidiary equations form a system too complicated to admit of a useful closed form solution in any significant number of cases, and one is reduced to analyzing it to extract rules of thumb.

First, although $\vec{M}$ and $\vec{v}$ can be thought of as being in some sense mechanical perturbations on the basic electrophoretic process, they are of considerable significance. $\vec{M}$ includes, for example, the force of gravity, constraints introduced by various surfaces, and buoyancy. Of these, gravity and buoyancy are the more important, mechanical constraints normally being significant only in the charging and collecting phases. As an illustration, gravity is of prime importance in electrostatic ore beneficiation, the separation normally being effected using crossed electrical and gravitational fields. Conversely, gravitation is much less important in the electrodeposition of paint from aqueous media since its effects on the paint particles tend to be annulled by the buoyancy of the water. $\vec{v}$ is often one of the parameters of the system as, for example, in the case of electroprecipitation of flue dust. However, it

may be due largely, or in significant part, to motions set up in the fluid by the electrophoretic process itself, and in this case it could impair process efficiency. It has, for instance, been found (6) that conduction currents as small as 1 pA/cm^2 can produce in insulating liquids motions so large as to render uninterpretable the usual carrier mobility measurements; and there is no reason to suppose that similarly significant effects will not exist at the much higher currents used in electrodeposition.

Second, if one neglects $\vec{M}$ and $\vec{v}$, Eq. [2] becomes

$$\mu \frac{d^2\vec{r}}{dt^2} + \lambda \frac{d\vec{r}}{dt} = Q V \vec{E}_o(r) P(\omega t) \qquad [3]$$

if the physically realistic assumption of periodic E_o is made. The inertia and viscous drag terms on the left of Eq. [3] can sometimes be manipulated by changing the size of the objects transported, but size is often dictated by other factors. The relative importance of these terms depends on the exact application, but, in processes where $\vec{M}$ is neglected, drag normally predominates.

The term on the right of Eq. [3] is the one over which the engineer has greatest control, it being possible (*i*) to manipulate Q and V to some extent, (*ii*) to specify arbitrarily the periodic function $P(\omega t)$, and (*iii*) to vary $\vec{E}_o(\vec{r})$ over a wide range by designing so-called "field electrodes" which may or may not include prominently the emitter and collector. The optimal settings of these quantities vary greatly from application to application. Normally, however, the a-c components of $P(\omega t)$ produces a primarily oscillatory motion of the charged particle, the amplitude of the oscillation decreasing as $1/\omega$; the d-c component produces the desired translation. To increase efficiency, then, $P(\omega t)$ should possess a moderately low ripple factor unless transient peaks are useful in promoting better particle charging as in electroprecipitation. Also, $|\vec{E}_o(\vec{r})|$ is commonly adjusted to be monotonically decreasing along a particle trajectory so that the particle will tend not to acquire a new charge at or near the collector and subsequently move off on a new trajectory.

Finally, if the device has been capably engineered, then the charged particles will arrive in the neighborhood of the collector with some suitable spatial distribution. This may be relatively loosely specified as, for instance, in the case of the separator shown in Fig. 2 where it is necessary merely to get the conducting particles into hopper C. Or it may be relatively stringent as, for instance, in the case of electrically depositing a uniform coating of paint in metal parts moving along an assembly line.

An example of these considerations is provided by the electrostatic precipitator (*cf.* Fig. 3). Here the principal velocity is axial, and mechanical forces are not of primary importance if the gas velocity is sufficiently high and if turbulence is suppressed; in practice these conditions are not always easy to fulfill (5). Inertial effects are normally outweighed by viscous drag, but reentrainment of precipitated particles in the gas stream is a real problem, and hence the collector field should be kept low. On the other hand, it is desirable to have as large a Q as possible, and this is facilitated by emitter fields strong enough to produce ionization. Thus, the coaxial geometry shown produces a most suitable $\vec{E}_o$. $VP(\omega t)$ is commonly adjusted to give a d-c level near sparkover and an a-c level producing, near the emitter, copious ionization at waveform crests and quenching of any sparkover at minima. Finally, the criteria on the distribution of transported particles at the collector are very loose, it being required merely that there be no radical nonuniformities over the collector surface.

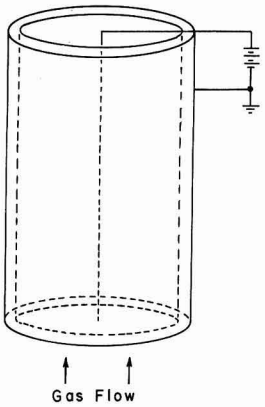

Fig. 3. Schematic illustration of an electrostatic precipitator. *Vide* text.

The Collecting Phase

In the collecting phase the transported particles settle on a surface which normally bleeds off their net charge. Thus, in some limited time after touchdown, the electrical force holding the particle has shifted from electrophoretic toward dielectrophoretic and the particles are held by (*i*) adhesive, (*ii*) dielectrophoretic, and (*iii*) other mechanical forces. Cases in which adhesion predominates represent electrocoating processes, while those in which dielectrophoresis predominates usually represent electroseparation processes. "Other mechanical forces" could include, for example, the vertical component of gravity holding the particle in a surface depression or small surface hairs which tend to trap the particles; an illustration of the latter would be an electrostatically dusted plant leaf [*cf.* 7, 8)]. The problems of collection arising in these several cases are radically different.

In electrocoating applications [*cf.* (9)] there is no question of designing the collector since this has normally been set by the requirements of the product into which it is to be assembled or by other forces beyond the engineer's control: all one can try to do is work with the existing constraints. It is normally required (*i*) that the coating be of some specified thickness, (*ii*) that it be of some specified uniformity, and (*iii*) that the process be as efficient as possible. Thickness is commonly controlled by adjusting the coating time, that is, either the collector or the emitter is moved or the unit is turned off when the coating is thick enough. Uniformity is often provided by the insulating properties of the coating which reduce the surface electric field as the coating thickens thus promoting deposition elsewhere; that is, the asperities on the collector's front surface will be coated first, followed by smooth areas on the front and ultimately by the rear surface and various recesses. In addition, coating uniformity can obviously be aided by rotating the collector or by causing the emitter to revolve around it. In many processes, electrostatic crop dusting, for example, the increase of efficiency compared to the no field case is so great that one is not strongly motivated toward optimization. But, if it is necessary to optimize one should use suitable carriers for the coating material, properly prepare the collector's surface as, for example, by degreasing, and have a good charging phase.

In electroseparation adhesion is not commonly a problem, and the requirements on particle distribution are typically much simpler, being "not too nonuniform" for electroprecipitation and "into the correct

hopper" for ore beneficiation. Moreover, one is able to control to a large extent the collector shape. There are two problems of note. First, lightweight conducting particles tend to acquire the collector's charge and be repelled toward the emitter. And second, the particles collected may be held to the collector's surface by slow charge loss or other electrical processes, and build up a thick and undesirable coating. The designer's job is then to produce a collector which disposes of the particles in an acceptable manner, and, to this end, three expedients have been adopted. First, the collector is so arranged that gravity will tend to pull the particle off in a suitable direction; thus, the precipitator shown in Fig. 3 should be arranged vertically rather than horizontally. Second, the surface electric field of the bare collector is made as small as possible since recharging of the collected particles commonly increases with this quantity; thus, where recharging is a problem, it is designed with large curvature radii. Third, where necessary, the collected particles can be dislodged mechanically and allowed to drop under the influence of gravity; thus, the collectors in flue dust precipitators are commonly subjected to a mechanical rapping.

Conclusion

Rather than boldly assaying the *tour de force* of knotting together this diversity of loose ends, I would like to conclude with a description of yet another class of experiments which will serve to explain why in defining "electrophoretic" at the start of this paper I chose to stipulate that the action of the electric field on the entity transported be "direct" and "Coulombic."

Specifically, many organisms exhibit galvanotactic behavior; that is to say, they tend to move in predictable directions in an applied electric field. This phenomenon has long been known (10), and appears, like the phenomena discussed above, to have commercial application (11). An interesting example of galvanotaxis is provided (12) by the motile colonial alga *Volvox* which, when subjected to an electric field, swim toward and accumulate at the cathode, unless surprisingly, they have been conditioned by several days of suitable light deprivation, in which case they move toward the anode.

From this one might conclude that the galvanotactic response could be described as "behavioral" or "volitional." But, recent researches (13) have indicated that galvanotaxis in ciliates is often the result of a reversal of ciliary beat related to cytoplasmic depolarization. In either case, it would seem that the phenomenon is electrophysiological or electropsychological in nature rather than electrophysical.

And hence the restrictions imposed in defining "electrophoretic" served to rule out those depositional phonemena which, though incontestably electrical in origin, are not readily explained by the direct action of the applied electric field on the net free charge of the transported object.

Manuscript received November 28, 1967. This paper was presented at the Dielectro- and Electrophoretic Deposition Symposium at the Chicago Meeting, October 15-19, 1967, as Abstract 144.

Any discussion of this paper will appear in the Discussion Section to be published in the December 1968 JOURNAL.

References

1. G. M. Bose, *Phil. Trans. Roy. Soc.*, **43**, 419 (1745).
2. J. A. Nollet, "Recherches sur les Causes Particulières des Phénomenès Electriques," Les Frères Guerin, Paris (1749).
3. O. C. Ralston, "Electrostatic Separation of Mixed Granular Solids," Elsevier, Amsterdam (1961).
4. H. E. Rose and A. J. Wood, "An Introduction to Electrostatic Precipitation in Theory and Practice," 2nd Ed., Constable, London (1966).
5. H. J. White, "Industrial Electrostatic Precipitation," Addison-Wesley, Reading (1963).
6. T. J. Lewis, Annual Report Conference on Electrical Insulation and Dielectric Phenomena (1967). To be published.
7. S. E. Law and H. D. Bowen, *Trans Amer. Soc. Agric. Engr.*, **9**, 501 (1966).
8. S. E. Law, "Bibliography of Electrostatic Dusting and Spraying," Department of Biological and Agricultural Engineering, North Carolina State University, Raleigh, North Carolina (1967).
9. R. L. Yeates, "Electropainting," Draper, Teddington (1966).
10. W. Biedermann, "Electrophysiology," Macmillan, London (1896).
11. R. B. Northrup, *IEEE Trans. Biomed. Engr.*, **BME-14**, 191 (1967).
12. O. P. Terry, *American J. Physiol.*, **15**, 235 (1906).
13. S. Dryl and A. Grebecki, *Protoplasma*, **62**, 255 (1966).

Unsolved Problems Concerning Metal Surfaces and Corrosion[1]

Herbert H. Uhlig*

Department of Metallurgy and Materials Science, Massachusetts Institute of Technology, Cambridge, Massachusetts

Almost any worthwhile discipline, whether in the humanities or in the sciences, has its unsolved problems. And it is often true that an inventory of the contributions made by any viable discipline reveals many additional contributions that would be welcome were they available. The study of metal surface properties and of metal reaction rates (corrosion) fits this description. On a practical level, a quick survey shows that research on metal surfaces has already contributed appreciably to the development of catalysts for chemical processing, to the reduction of friction and wear of metals, and to prolonging the life and safety of metal equipment exposed to aggressive environments. On a scientific level, the relation between adsorption on transition metal alloys and unfilled d electron levels has contributed better insight into both the mechanism of catalysis (1) and the nature of passive films (2-4) accounting for the excellent corrosion resistance of chromium, titanium,

[1] Presented at Dedication of Graduate Center for Materials Research, University of Missouri, Rolla, Mo., October 31, 1967.

* Electrochemical Society Active Member.

stainless steels, Monels, and related metals.[2] Furthermore, current knowledge of heterogeneous reaction rates has been appreciably advanced by the well-established electrochemical theory of corrosion and by the Wagner theory of metal oxidation at elevated temperatures. Increased meaning has been given to potential and polarization measurements beyond anything available during the early development of classical electrochemistry. As a result, it is now possible to calculate instantaneous reaction rates from rapid polarization data, a technique that proves especially valuable in assessing metals for use in the human body. Advances in electrode kinetics have contributed a clearer insight into factors which add efficiency to corrosion inhibitors. On the other hand, they also identify with devices such as the fuel cell which has captured public attention because of its high theoretical efficiency and its possible alleviation of air pollution. But the advances which are necessary to move the fuel cell out of the laboratory into large-scale commercial use, still remain undiscovered among the properties of metal surfaces.

Advances in Corrosion Science and Engineering

To list all of the many technological advances that have benefitted from corrosion research is not my present purpose. In a brief outline such as this, one should however at least mention the advent of the rust-resistant stainless steels which first appeared on the scene about 50 years ago as a result of empirical probing. They made an initial major impact on the synthetic nitric acid industry, on design of cutlery and hospital equipment, and on architectural and automotive trim. Similarly the technique of cathodic protection, a long-established development resulting from basic studies of electrochemistry by Sir Humphrey Davy, has made it feasible to transport gas and oil, as is now done, over thousands of miles through buried steel piping securely guaranteed against corrosion. Any unpredictable deterioration of such piping is not tolerable because of catastrophic consequences, particularly with internal gas pressures reaching 1000 psi. Furthermore the classical galvanized corrosion-resistant coatings on steel, first patented in France as early as 1836, still find increasing use today for marine and atmospheric exposures. Some recent applications extend the life and safety of steel automobile frames and accessory equipment exposed to corrosive salt applied to snow-laden streets of northern climates. Mention can also be made of corrosion control methods applied to steam boilers such as deaeration of feed water and the addition of various chemical inhibitors in order to increase the efficiency and safety of boiler operation and at the same time to materially reduce the cost of generated power. It is not always realized that use of commercial corrosion inhibitors in a variety of industries, including the utilities, plays an important part in supporting our industrial economy.

[2] For illustration, the good catalytic properties of Pd for the ortho-para hydrogen conversion are retained, more or less, by Pd-Au alloys so long as the d band of electronic energy levels in Pd remain unfilled. At 60 A/o (atom per cent) Au, the d band becomes filled by donor electrons of alloyed Au, resulting in poorer catalytic properties for alloys of this or higher Au compositions, paralleling the properties of pure Au (1).

Similarly, in the Cu-Ni alloy system, the alloys are passive so long as the d band of energy levels remain unfilled (2, 3). Passivity in this case is measured by an observed passive current density lower in value than a critical current density needed to achieve passivity in polarization curves for the alloys in 1*N* H_2SO_4 (Fig. 1). As Cu is added to Ni, the single 4s electron of the Cu atom fills the 1.6 vacancies per surface atom of Ni, increasing the critical current density and also the passive current density (Fig. 2). At the composition at which the d band is 100% filled, or any composition above this value, the passive current densities disappear (or critical and passive current densities intersect) and the alloys up to and including pure Cu are therefore not passive. Other elements alloyed with Cu-Ni alloys may also be a source of donor electrons. In single-phase solid solution alloys, it is observed that alloyed Zn contributes 2 electrons per atom (4), (and hence one Zn is equivalent to two Cu atoms in the Ni alloy), Al contributes 3 electrons (5), Ga contributes 3 electrons, and Ge contributes 4 electrons (6) per atom as is expected from the number of electrons in the outermost orbits of these elements. In each case, the alloy loses its passive characteristics very near to the composition corresponding to 100% filled d band. These results support the view that the passive film on such alloys has an adsorbed structure rather than a structure consisting of a single or mixed stoichiometric metal oxide.

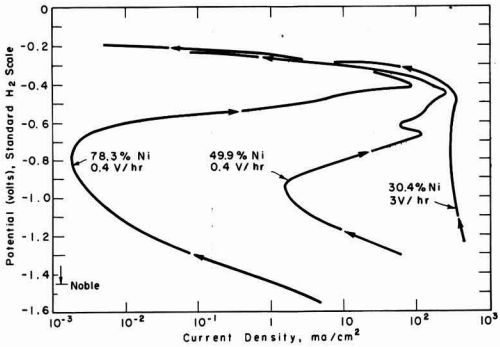

Fig. 1. Potentiostatic anodic polarization curves for 78.3% Ni-Cu, 49.9% Ni-Cu (unfilled d bands) and 30.4% Ni-Cu (filled d band) in 1*N* H_2SO_4, 25°C. Rates of potential change as shown.

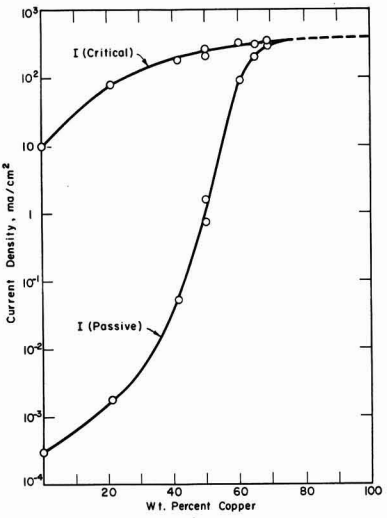

Fig. 2. Critical current densities and passive current densities for Cu-Ni alloys in 1*N* H_2SO_4, 25°C. The d band of electronic energy levels is filled by electrons from Cu at about 60% Cu.

They are employed, for example, to increase the life of automotive engines (as added to lubricating oils), heat exchangers, storage tanks, distribution piping, air conditioning equipment, pickling tanks, and steam lines.

Recent corrosion research has produced titanium alloys containing a few tenths per cent palladium with greatly improved resistance to aggressive acids. Alloyed steels are available, much less expensive than stainless steels, which do not need painting or other types of maintenance. They make use of an adherent natural rust film which essentially protects the underlying metal from further attack. Their promise derives from the present high labor costs of painting which, over the life of a steel structure, may exceed the original cost of construction. Mention might also be made of anodic protection, a new technique for corrosion control in the chemical industry which resulted from fundamental studies of passivity. Using a moderate electric current at controlled potential, it is possible to employ ordinary steels in contact with hot corrosive acids avoiding the extremely high reaction rates which otherwise occur. Cathodic protection in similar applications require uneconomically high current densities attended by undesirable gas evolution.

Unsolved Problems

The number of unsolved problems relating to metal surfaces is limited only by human imagination. Potentially important advances could obviously be made through improved catalysts, better lubricants, and more efficient corrosion inhibitors, to name but a few. And it should also be recognized perhaps that any scientific breakthrough on knowledge of surfaces has an immediate impact on several fields rather than on one field alone. Hence fundamental research in corrosion, about which the writer is most familiar, is in position to benefit present knowledge of catalysis (*e.g.*, effect of d electron vacancies, mentioned earlier, or the structure and composition of initially formed films on metals) or of our present understanding of lubrication and wear (through studies of mechanically activated chemical reactions such as occur in fretting corrosion or in cavitation-erosion) or of devices which depend on electron emission (through studies of surface films).

The unsolved problems of today which exert pressure for some satisfactory practical solution are usually approached either empirically or more effectively through some depth of scientific understanding. Basically, the most important unsolved problem of metal surfaces is the achievement of an adequate scientific understanding. Is the passive film on stainless steels a metal oxide or is it instead an adsorbed complex of oxygen and water? It makes a great difference if one plans to expend development funds for improving protective surface films by the particular approaches of anodizing or of low-temperature oxidation. Or what is the optimum chemical structure of a nontoxic corrosion inhibitor suited to avoid rusty water in steel distribution mains? Polyphosphates, the action of which is little understood, are used by many communities, but how should one best go about finding a better inhibitor? Or to cite a more spectacular example, by what basic mechanism do high-strength metals fail unexpectedly by cracking when exposed to natural environments? Does an electrochemical mechanism apply, or does a brittle surface film continuously rupture, or does the surface instead undergo reduction in energy (hence favoring the crack process) because of environmental adsorption? All three mechanisms have been suggested. The practical problem presents a serious bottleneck to engineering designs making use of high-strength materials whether for the aircraft, hydrospace or aerospace programs. If one includes threatened stress corrosion cracking of high-nickel alloys used for atomic energy installations, it is obvious that this unsolved surface problem alone affects progress in practically every important outpost of modern technology. Again, the best approach to overcoming environmental cracking depends very much on which mechanism is finally shown to apply. Otherwise, the approach remains a shotgun effort with scattered results.

At least three scientific areas must be expanded if a more satisfactory background on surface problems is to become available. These are: (*a*) studies of electrode kinetics, (*b*) studies on the nature of initially formed surface films on metals, (*c*) studies of how metals subject to a tensile stress interact with their environments.

Under the subject of electrode kinetics, more general quantitative information is needed, including that related to adsorption and desorption of ions and of organic complexes on metals as a function of applied potential. Additional information is required, for example, on factors both within the metal and within the environment which influence the Tafel constants expressing anodic dissolution rates of metals.

Regarding surface films, more information is needed on the composition and structure of passive films common to the stainless steels, and which are also germane to the phenomenally passive metals like tantalum and hafnium. For thicker oxide films which form at elevated temperatures, the question arises as to the role of space charges, reaching a distance of 10,000Å into the oxide, on both surface properties and on the oxidation mechanism. How do small additions of rare earth metals improve the spalling characteristics of oxide films, thereby improving high temperature oxidation resistance? What is the nature of the chemical reaction between metals and their environment during fretting corrosion (caused by sliding surfaces)? It is known that in air at room temperature, iron frets to form particles of metallic iron and of α Fe_2O_3, but in H_2S it is FeS that forms and in CO_2 the reaction product is $FeCO_3$.

In problems of environmental cracking, called stress corrosion cracking, what is the role of complex ions and what part does the corrosion potential play in determining initiation or rate of cracking? What are detailed factors in the metal which determine whether dislocations emerge and which determine their half life at a metal surface during which adsorption presumably occurs? What are the effects of impurities, lattice structure and alloying components on densities of emergent dislocations? What are the chemical properties of surface dislocations which account for NO_3^- adsorbing, or otherwise interacting with iron, causing subsequent cracking, and which also account for the ineffectiveness of Cl^- to cause the same damage? Or in austenitic stainless steels, which are essentially iron-base alloys, what are the properties of surface imperfections which make Cl^- damaging and NO_3^- nondamaging?

Conclusions

Fundamental knowledge necessary to solve various surface problems of the kind described have traditionally been supported on a hit-or-miss basis fluctuating with the number of military or industrial crises at any given moment. The modest accumulated science of metal surfaces presently at hand has been helpful, but unfortunately not adequate to contribute what is needed for continuing technological progress. The establishment of materials science centers, of which the present center at the University of Missouri is a welcome example, promises to supply more of the science which is now missing. Contributions of such research centers to surface properties, and to corrosion problems in particular, are patiently awaited by many of those who hope to use materials to optimum advantage when exposed, as they most always are, to some environment which affects their ultimate properties and useful life. In the long run, increased attention to chemical and surface properties of materials, on par with mechanical or physical properties, will lead to a better evaluation of the environmental effects which are becoming increasingly important to modern engineering design. This kind of information must be available, of course, for both metallic and nonmetallic materials, because all materials are subject to some degree of environmental damage, the extent of which sensitively bears on their satisfactory incorporation into some machine or structure.

At one time I recommended (7) that corrosion research would greatly benefit through the continuous support provided by a National Institute of Corrosion Control established on a smaller scale but similar to our well-known National Institutes of Health. Perhaps the need for such an Institute is made less urgent by the several materials science centers which have since been established. Yet the variety of problems which are inherent to advanced materials and which fully occupy present research facilities all over the nation, suggest that a special coordinated research effort at such a national center with specific emphasis on chemical and surface properties deserves further consideration. The added functions which such an Institute could provide, for example, are (*A*) detailed expect attention to corrosion engineering problems of broad public concern affecting the many small businesses and communities unlikely to undertake a broad range research program on their own initiative. (*B*) The effective dissemination of general corrosion control know-how to all those able to make use of it. (*C*) The

support and prosecution of fundamental research on properties of surfaces supplying new knowledge not only on metal reaction rates but also on other properties of value to related scientific disciplines similarly concerned with surface behavior.

In whatever way it is finally accomplished, we stand as a nation to benefit from research programs, considered in depth, which bring the many disciplines of the physical sciences to bear on solutions of surface problems. Only a relatively short time ago these problems, including corrosion phenomena, were considered, like the weather, to be unpredictable and hardly amenable to scientific insight. The dedication of this Graduate Center of Materials Research at Rolla symbolizes our entry into a more enlightened era of materials research.

Manuscript received December 17, 1967.

References

1. A. Couper and D. Eley, *Discussions Faraday Soc.*, **8**, 172 (1950).
2. H. Uhlig, *Z. Elektrochem.*, **62**, 700 (1958).
3. J. Osterwald and H. Uhlig, *This Journal*, **108**, 515 (1961).
4. D. Stolica and H. Uhlig, *ibid.*, **110**, 1215 (1963).
5. F. Mansfeld and H. Uhlig, Paper Presented at the Chicago Meeting of the Society, Oct. 15-19, 1967, as Abstract 54.
6. F. Mansfeld and H. Uhlig, Unpublished observations.
7. H. Uhlig, *Corrosion*, **18**, 311t (1962).

DIVISION NEWS

Dielectrics and Insulation Division

The Annual Luncheon and Business Meeting of the Dielectrics and Insulation Division will be held during the Spring Meeting of the Society in Boston, Mass., May 5-9, 1968. As a continuation of the policy of offering an outstanding speaker for the occasion, Jerome B. Wiesner, Provost of the Massachusetts Institute of Technology and former Scientific Advisor to Presidents Kennedy and Johnson, will speak on a topic of current interest. Dr. Wiesner is internationally known for his interest in the relationships between scientific and governmental affairs.

During the Business Meeting the presentation of the first T. D. Callinan Award will be made. Details on the award are given below.

The Luncheon and Business Meeting will be held in the Bay State Room of the Statler Hilton Hotel from 12:15 to 2:00 P.M. on Monday, May 6. Tickets may be purchased in the Registration area at the Statler Hilton.

Donald M. Smyth,
Secretary

T. D. Callinan Award Of the Dielectrics and Insulation Division

In recognition of their contributions to the study of anodic oxide growth mechanisms, J. A. Davies and J. P. S. Pringle, Atomic Energy of Canada, Ltd., Chalk River Nuclear Laboratory, Chalk River, Ont., Canada, have been selected as joint recipients of the T. D. Callinan Award. Their work, which was reported in a group of separate and joint publications, extended over the period 1962 through 1967. Within this period Dr. Davies and Dr. Pringle developed and used Beta-ray spectroscopy and radiotracer techniques as an experimental tool for the study of anodic oxide growth mechanisms. The reliability of the results obtained with this technique is perhaps its most outstanding feature and has substantially contributed to an understanding of the mechanism involved.

Dr. Pringle's recent participation at the 1967 Dallas Meeting was based on a continuation and extension of these techniques and dealt with the concentration profiles of atomic species within anodic oxide tantalum film. His presentation was well received and represented one of the outstanding contributions at the Divisional level.

With the presentation of this award, the Dielectrics and Insulation Division inaugurates a new program which originated during Dr. B. Eichbaum's Chairmanship. The Division through this award seeks recognition of recent meaningful contributions. Consistent with these objectives the award bears the name Thomas D. Callinan who during his life generously contributed both his time and energy to the growth and development of the Division in addition to being its Divisional Editor on the JOURNAL and member of the Board of Directors of the Society.

Presentation of the T. D. Callinan Award will take place at the Division Luncheon and Business Meeting being held in the Spring of 1968.

Edward M. DeSilva,
Vice-Chairman

Industrial Electrolytic Division

The Nominating Committee of the Industrial Electrolytic Division, comprised of E. F. Kiefer, V. J. Cable and R. M. Hunter, Chairman, presents the following slate of nominees for the two-year terms for each of the offices listed:

Chairman—T. R. Beck, Boeing Scientific Research Laboratories, Seattle, Wash.

Vice-Chairman—J. H. Nichols, Monsanto Co., St. Louis, Mo.

Secretary-Treasurer—R. N. Hyer, Vulcan Materials, Co., P. O. Box 545, Wichita, Ka., J. H. Sullivan, Dow Chemical Co., Midland, Mich., and L. E. Vaaler, Union Carbide Corp., P.O. Box 6116, Cleveland, Ohio.

The election of officers will be held at the Division's annual luncheon and business meeting May 8, 1968 during the Boston Meeting of the Society.

Clifford A. Hampel,
Chairman

SECTION NEWS

Chicago Section

On January 11, 1968 the Chicago Section met at the Chicago Engineers Club to hear Z. Andrew Foroulis, Esso Research and Engineering Co., Florham Park, N. J., present a paper "On the Kinetics of Iron Dissolution in Acid Chloride Solutions."

The following is a summary:

The mechanism of the corrosion of iron in acid chloride solutions is examined in detail. Galvanostatic transients are used to investigate dissolution kinetics. Influences of potential, pH and ferrous iron concentration on steady-state dissolution and deposition reactions are illustrated. Dependency of the hydrogen evolution reaction on pH and potential are also considered for this system.

On February 15, 1968 the Chicago Section met at the Chicago Engineers Club, to hear Dr. James H. Greenwald, St. Catherine Hospital, Heart

Campbell, King, and Turner Take Office in Boston

Ivor E. Campbell

Cecil V. King

Dennis R. Turner

As a result of the recent annual election in which the voting was by mail ballot, Ivor E. Campbell has been elected the new President (1968-1969) of The Electrochemical Society, Cecil V. King has been elected Vice-President (1968-1971), and Dennis R. Turner has been elected Secretary (1968-1971). They will take office on May 9, 1968.

Dr. Campbell, Engineering Manager, Semiconductor Division, Westinghouse Electric Corp., Youngwood, Pa., replaces Harry C. Gatos, who will continue as a Past-President on the Board of Directors.

Dr. King, American Gas & Chemicals, Inc., New York, N. Y., begins his first year of his three year term as Vice-President.

Dr. Turner, Supervisor of Basic Electrochemical Development at Bell Telephone Laboratories, Inc., Murray Hill, N. J., begins his first year of his three year term as Secretary.

Dr. Turner's three-year term of office starts with the completion of the Boston Meeting. However, with the resignation of Dr. Richard F. Bechtold as Secretary, the Board of Directors at their meeting on January 5, 1968 appointed Dr. Turner to fill Dr. Bechtold's unexpired term.

Other offices not affected by this election are those of the two Vice-Presidents and Treasurer, N. Corey Cahoon, Charles W. Tobias, and R. Homer Cherry, respectively.

Station, East Chicago, Ind., speak on "Artificial Renal Dialysis."

The following is a summary:

Artificial renal dialysis is only now becoming widely established as a practical technique. Individuals whose kidneys, for one reason or another, have ceased to function at a level adequate to maintain life, can now be helped with long term dialysis at home or in community dialysis units. Modern techniques provide for calculable maintenance of physiological balance, functionally equivalent to the clearance of the natural kidney, where separation of crystaloids and colloids in solution is accomplished by the difference in their passage through a semipermeable membrane. Crystalloids diffuse through the membrane readily while colloids pass very slowly or not at all. Special considerations must be given to maintaining electrolyte and pH stability during treatments.

I. H. Pronger,
Secretary

Midland Section

On January 30, 1968 the Midland Section of the Society held a meeting in the Research Auditorium of The Dow Chemical Co. in Midland. Prior to the meeting a dinner in honor of the speaker, Dr. F. Hubbard Horn, was held at the Hickory House.

Dr. Horn, Manager of a Semiconductor Group at General Electric Research and Development Center, presented a brief illustrated summary of the rapid developments in silicon devices, beginning with the simplest junction rectifier through the very complex integrated circuit devices in present and anticipated usage. The principal theme was concerned with a plea for better, more workable parameters for initial selection of silicon which would allow better control and more predictable results during the complex processing steps leading up to final integrated circuits. Considerable enthusiastic audience discussion followed the presentation.

John A. Van Westenburg,
Secretary-Treasurer

National Capital Area Section

The National Capital Area Section held its first meeting of 1968 on February 1st at the American University, Beeghly Chemistry Building. Ernst M. Cohn, National Aeronautics and Space Administration, was guest speaker and spoke on "Fuel Cell Forecasts and Practical Problems," in which he described various types of fuel cells, the problems encountered and their possible uses. For practical application, he believes that a major breakthrough is required. Present fuel cells have relatively short lives, about three months, require too much space and are too heavy per Kw.

San Francisco Section

The January 17, 1968 meeting of the San Francisco Section was held at the Holiday Inn, South San Francisco.

Chairman Cox announced the appointment of a nominating committee composed of M. E. Sibert, Chairman, Scott Lynn and Walt Benzing. The report of this committee will be made at the March or April meeting and ballots will be mailed prior to the May meeting to all members.

The meeting was then turned over to Ted Katan who introduced the speaker of the evening, H. Gerischer, who has been visiting the University of California at Berkeley. Dr. Gerischer is Professor of Physical Chemistry and Director of the Institute of Physical Chemistry and Electrochemistry at the Technical University of Munich. He described in his talk the reactions that occur at a semiconductor electrode in an attacking environment, and described the injection and extraction of holes and electrons that occur in addition to the anodic and cathodic processes that occur at metal electrodes. The experimental studies of the corrosion of germanium and gallium arsenide were discussed and evidence for the role of chemical attack was presented.

The First Regional Technical Conference was held at the Hilton Inn in San Francisco on March 7. Ed Duffek was Chairman of the Conference which comprised the following guest speakers and subjects:

"Mechanisms of Electrolytic Decomposition of Semiconductors," H. Gerischer, Director, Institute of Physical Chemistry, Techn. Hochnschule, Munich, Germany.

"Heterogeneous Nucleation in Vapor Deposition and Thin Epitaxial Monocrystals," G. M. Pound, Professor, Materials Science Department, Stanford University, Stanford, California.

"Electrodeposited Magnetic Films," I. W. Wolf, Manager, Materials and Devices Section, Ampex Corp., Redwood City, Calif.

"Epitaxial Growth of GaAs, InAs, and Their Alloys," M. E. Jones, Director, Materials Science Research Laboratory, Texas Instruments, Inc., Dallas, Texas.

"Evolution of Performance Versus Cost in Semiconductor Technology," C. S. Roberts, Consultant, Materials and Processes.

A. E. Hultquist,
Secretary

PEOPLE

A. H. Andersen, after 30 years of service, has retired from his position as assistant vice-president, Research and Development of Shawinigan Chemicals Ltd., Montreal, Canada.

Robert Bakish has been promoted to vice-president, Research and Development of Republic Foil Inc., Danbury, Conn.

Karl V. Kordesch, Union Carbide Corp., Parma, Ohio, in recognition of his work in fuel cell research, was decorated with the Wilhelm Exner Medal by Austrian Chancellor Dr. Josef Klaus at ceremonies held last December 15 in Vienna. The medal was bestowed on behalf of the Austrian Society for Industry and Commerce, the oldest organization in Austria concerned with advances in industry and commerce.

Dr. Kordesch, a native of Vienna, received his Ph.D. degree from the University of Vienna in 1948. His thesis was on the separation of amino acids. In addition to his interests in organic chemistry, air electrodes for galvanic cells—and later fuel cells—became his main field of investigation.

In 1955 Dr. Kordesch joined the National Carbon Division of Union Carbide in Cleveland as a member of the battery research group. The alkaline "Energizer" battery was one of his main areas of study and basic patents on this system are in his name. Within a few years fuel cell research was intensified and in 1958 he became head of the fuel cell research group at the National Carbon Research Laboratories. He is at present serving in the same capacity for the Electronics Division of Union Carbide at Parma.

Henry B. Linford, professor of Chemical Engineering, Columbia University, New York, N. Y., has been awarded the "Great Teacher Award" for 1968, sponsored by the Society of Older Graduates of Columbia University. The award was presented at the society's annual dinner held at the Columbia University Club on January 10.

Professor Linford, who has been a member of the Columbia faculty for 27 years, was cited, in part, as "a dedicated teacher of undergraduates valuing always the close contact with students which has inspired them to emulate your example."

He joined the Columbia faculty in 1941 as an instructor in chemical engineering. He was an assistant professor from 1946 to 1949, when he became associate professor of chemical engineering. He has been a full professor since 1952.

Hans R. Neumark has retired after 30 years of service from his position as corporate director of Government Liaison with Allied Chemical Corp., and now serves as an independent consultant to the aerospace and chemical industry in the field of chemical propellants and related matters such as handling and safety procedures.

Soeren S. Nielsen has recently been appointed to the Technical Committee on Underwater Propulsion of the American Institute of Aeronautics and Astronautics.

Mr. Nielsen is manager-new products development, Gould-National Batteries, Inc., St. Paul, Minn. As a member of the committee he will be involved with special projects, annual meetings, and monitoring the publica-

Boston Meeting Committee

W. William Harvey

Emerson H. Newton

Martin Weinstein

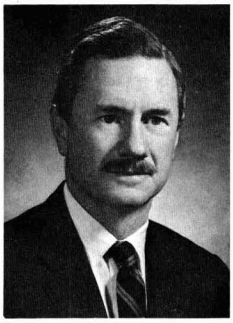

Mario D. Banus

Ralph B. Soper

Martin S. Frant

Members of the Boston Meeting Committee under General Chairman W. William Harvey (Kennecott Copper Corp.) are: Emerson H. Newton (Arthur D. Little, Inc.) Vice-Chairman; Martin Weinstein (Tyco Laboratories, Inc.) Secretary; Mario D. Banus (MIT Lincoln Laboratory) Arrangements; Ralph B. Soper (Semiconductor Processing Co. Inc.) Registration; Martin S. Frant (Orion Research, Inc.) Entertainment. Photographs not available on: Charles Levy (Swift Laboratories, Inc.) Finance; and Mrs. Charles Levy, Ladies' Program.

133rd National Meeting

Boston Pops

A number of tables at the famed Boston Pops Concert will be available for members and guests attending the National Meeting on Wednesday, May 8th. The Pops Concerts, under the direction of Arthur Fiedler, have been a Boston tradition for many years. The usually staid and respectable Symphony Hall resounds to the members of the Boston Symphony playing light classical music and to the sounds of champagne bottles popping. Instead of the usual stiff-backed seats, the floor of Symphony Hall contains tables and chairs; wine, champagne, soft drinks, and light refreshments are served during the concert.

The program begins at 8:30 P.M.

The concerts are extremely popular and the local committee has only been able to get a limited number of seats. These will be sold at $5.00 each at the registration desk.

Private means of transportation will have to be arranged.

Martin S. Frant
Entertainment Committee

People continued

tions of the institute in the areas of underwater propulsion.

Peter N. Rigopulos, general manager, Diaflo Products Division, Amicon Corp., Lexington, Mass., has been elected vice-president of that company.

Mr. Rigopulos directed Amicon's ultrafiltration membrane development toward practical application as well as world-wide use and has headed the Diaflo Products Division since its inception.

Before joining Amicon, he shared management responsibilities at General Electric Co. for the development of fuel cells that provided power for the Gemini spacecraft. He authored numerous patents and applications and is coinventor of key elements in the Gemini fuel cell system.

Lockhart B. (Buck) Rogers, head of Purdue University's productive, six man analytical chemistry division, has been named recipient of the Fisher Award in Analytical Chemistry presented by the American Chemical Society.

Dr. Rogers received an M.A. degree in 1939 and a Ph.D. degree in 1942 from Purdue University under the direction of Earle R. Caley (now at Ohio State University). After completing graduate work, he taught at Stanford University for four years and then joined Oak Ridge National Laboratory, where he served as a group leader in analytical research until 1948. He then taught at MIT for 3 years and in 1961 he joined the Purdue faculty.

At Purdue, and MIT where he formerly taught, Dr. Rogers has been a key figure in strengthening the analytical chemistry programs. With 1963 Fisher Awardee Dr. David N. Hume he injected more organic quantitative analysis in MIT's undergraduate

courses and promoted the use of unknowns that were "live problems." At Purdue, he helps juniors in quantitative analysis tackle problems such as the quantitative determination of amino acids by solution chromatography and spectrophotometry and the determination of the amount of material in a gas chromatographic peak.

His publications, numbering more than a hundred, span areas including organic analytical reagents, electrochemical methods, spectrophotometry, thermal methods, radioactive methods, fluorescence, nuclear magnetic resonance, and gas chromatography.

OBITUARY

Stanislaus Skowronski

We regret to record the death of Stanislaus Skowronski on January 13, 1968. Mr. Skowronski, one of our oldest members, joined the Society in 1907 and was made an honorary member in 1961. He was born in Bex, Switzerland on July 8, 1881, came to this country as a young man, and graduated as a chemical engineer from Massachusetts Institute of Technology in 1904. He was naturalized and married in 1910.

After two years with the Republic Rubber Co. he joined the American Smelting and Refining Co. in New Jersey and later became research engineer with the Raritan Copper Works, and finally with the International Smelting and Refining Co. which was acquired in 1914 by the Anaconda Co. He retired in 1956. Until retirement he was for several years an adjunct professor at the Polytechnic Institute of Brooklyn.

Mr. Skowronski published more than twenty-five papers devoted largely to copper refining on which he became an authority. He presented a paper before the Society in 1927 on "Twenty-Five Years of Progress in the Electrolytic Refining of Copper."

Mr. Skowronski was active in the affairs of The Electrochemical Society and was a member of the Board of Managers from 1935 to 1938.

BOOK REVIEWS

"High-Temperature Materials and Technology," Edited by I. E. Campbell and E. M. Sherwood. Published by John Wiley & Sons, Inc., New York, 1967. 1022 pages; $27.50.

This volume is part of The Electrochemical Society Series and is a revision of the earlier "High-Temperature Technology" (Wiley 1956). In most cases it is completely rewritten by established authorities in a particular aspect of the topic. It is divided into

sections dealing with the chemistry of high-temperature reactions and species, materials (metals, oxides, cermets, sulfides, etc.) for high temperature, methods of attaining high temperature and measurements of temperature and materials properties at high temperatures.

All in all, this cohesive collection serves multifunctions: to cover the field, to instruct the initiate and to serve as a data and reference source for the experienced. In addition to the research scientist, it is also to be highly recommended to the materials engineer and could be easily used as an auxiliary text or source book for the person engaged in or pursuing a degree in Materials Science.

It is to be recommended highly for those who are engaged both in research and applications in this area of endeavor, for it covers adequately the theoretical and practical aspects of the materials used for high-temperature and the techniques for observing and measuring phenomena at these temperatures.

"The Chemistry of Molten Salts," by Harry Bloom. Published by W. A. Benjamin, Inc., New York, 1967. 184 pages; $10.00.

The vogue today is topics courses in the various fields of science. To serve this type of course, generally advanced, in which a number of specific topics are covered, text books are appearing. This book introduces the student to the field of molten salt chemistry, covers most of the pertinent physical and chemical aspects of the topic and covers the structure, thermodynamics, solutions, optical and transparent properties, and specific metal molten salt solutions and applications. There is a small number of problems for the student.

This book will be useful to students and technicians.

NEW BOOKS

"The Palladium Hydrogen System," by F. A. Lewis. Published by Academic Press, New York, 1967. 178 pages; $9.00.

An up-to-date coverage of the theoretical considerations governing the behavior of hydrogen in palladium and its effect on the structural and other properties of palladium. Thermodynamic factors and diffusion parameters are discussed fully.

"Low Noise Electronics," by W. P. Jolly. Published by American Elsevier Publishing Co., Inc., New York, 1967. 149 pages; $5.00.

The subtitle, "An Introduction to Quantum and Electron Beam Electronics," is well served by the author's coverage of noise phenomena in masers, lasers, electron beam tubes, parametric amplifiers, etc. It is a simple and understandable introduction to this topic.

"Trace Characterization-Chemical and Physical," Edited by W. W. Meinke and B. F. Scribner. Published by National Bureau of Standards, Wash-

ECS Membership Statistics

The following three tables give a breakdown of membership as of January 1, 1968. In Table I it should be noted that the totals appearing in the right-hand column are not the sum of the figures in that line since members belong to more than one Division. The totals listed are the total membership in each section.

Table I. *ECS Membership by Sections and Divisions*

Section	Division: Battery	Corrosion	Dielectrics & Insulation	Electrodeposition	Electronics	Electro-Organic	Electrothermics & Metallurgy	Industrial Electrolytic	Theoretical Electrochemistry	No Division	Total as of 1/1/67	Total as of 1/1/68
Chicago	40	30	8	33	45	12	14	13	27	6	162	161
Cleveland	56	26	2	36	44	11	23	25	49	7	192	186
Detroit	33	35	3	54	23	13	13	10	45	4	120	130
Midland	4	6		2	9	3	9	16	8		47	45
Metropolitan-New York	155	99	34	141	230	41	94	75	140	24	690	690
Niagara Falls	8	11	3	14	28	3	27	38	11	5	107	104
Pacific N. W.	13	11	5	16	7	2	5	14	20		52	52
Philadelphia	48	31	13	45	77	15	23	25	52	10	214	220
Pittsburgh	10	42	8	27	56	6	34	29	38	1	164	163
San Francisco	22	14	6	23	88	7	17	15	28	1	162	164
National Capital Area	48	34	8	36	45	6	11	4	49	3	168	173
Ontario-Quebec	8	19	4	20	20	1	32	30	30		114	110
Boston	46	34	11	38	118	12	30	8	58	6	256	267
S. Calif.-Nevada	46	35	9	55	125	13	23	17	66	4	254	257
Mohawk-Hudson	18	22	8	12	24	3	10	2	18	3	80	75
Columbus	8	17	3	16	22	2	21	9	15	1	70	75
Indianapolis	10	7	8	12	29	5	7	2	17	1	70	62
North Texas	7	12	3	8	84	4	8	3	15	3	117	123
South Texas	1	4	1	1	4	1	1	4	2	1	20	20
Non-Section	158	155	42	153	162	60	104	121	202	79	731	735
TOTAL as of Jan. 1, 1967	715	659	163	760	1231	208	515	468	859	158	3790	
TOTAL as of Jan. 1, 1968	739	644	179	742	1240	220	506	460	890	169		3812

Table II. *ECS Membership by Grade*

	Total as of 1/1/67	Total as of 1/1/68
Active	3452	3463
Faraday (active)	24	25
Deutsche Bunsen Gesellschaft (active)	19	19
Life	19	20
Emeritus	97	98
Honorary	9	8
Associate	70	54
Student	98	125
Representatives of Patron and Sustaining Members	127	122
	3915	3934
Delinquent	168	141
Total	4083	4075

Table III. *ECS Patron and Sustaining Membership*

	Total as of 1/1/67	Total as of 1/1/68
Patron Member Companies	14	14
Sustaining Member Companies	128	126

ington, D. C. Monograph 100 (1967), 580 pages; $4.50.

The effect of trace constituents upon the properties of materials and their qualitative and quantitative detection are well covered. This should be, at the above price, a welcome addition to the chemist's book shelf.

"Protective Coatings for Metals," 3rd Ed. by R. M. Burns and W. W. Bradley. ACS Monograph 163 Published by Reinhold Publishing Corp., New York, 1967. 735 pages; $25.00.

This monograph covers protective anticorrosion coatings, both inorganic and organic, on corrodible metals. Composition, application structure and techniques of evaluation of these coatings are covered.

"High-Temperature High-Resolution Metallography," Edited by H. I. Arronson and G. S. Ansell. Published by Gordon & Breach Science Publishers, New York, 1967. 382 pages; $25.00.

This volume contains the proceedings of a symposium held in Chicago, Ill., February 15, 1965 by the Metallurgical Society covering such topics as field-ion, field emission, thermoionic emission, and transmission electron microscopy, both from theoretical and applications points of view.

"Ferroelectricity," Edited by E. F. Weller. Published by American Elsevier Publishing Co., Inc., New York, 1967. 318 pages; $29.00.

Current progress and new approaches to the field of ferroelectronics are represented in this series of papers originating at the 1966 symposium on Ferroelectricity held at the General Motors Research Laboratories, Warren, Mich.

"Molten Salts Handbook," Edited by G. J. Janz. Published by Academic Press, Inc., New York, 1967. 588 pages; $25.00.

This fairly comprehensive data source covers the physical, thermodynamic, and electrochemical properties of molten salts. In addition it reports on spectral and structural data and on the experimental techniques and preparation of fused salts. It serves a much needed function of gathering the data on a multitude of systems.

"Fundamentals of Gas-Surface Interactions," Edited by H. Saltsburg, J. N. Smith, Jr., and M. Rogers. Published by Academic Press, Inc., New York, 1967. 557 pages; $14.50.

A review of gas-surface phenomena and presentation of recent research and ideas in this field are represented in this collection of papers from a symposium held in San Diego, Calif. in December 1966 under the auspices of the General Dynamics Corp. and the Air Force Office of Scientific Research. Three major areas are covered: The Surface and Its Characteristics; Adsorption and Reaction of Gases on or with Surfaces; and Scattering Processes, including Energy and Momentum Transfer.

"Protection Against Corrosion by Metal Finishing," Edited by N. Ibl, K. M. Oesterle, and A. L. Saboz. Published by Forster-Verlag AG, Zurich, Switzerland, 1967. 347 pages;

The proceedings of the International Conference held in Basel, Switzerland on November 22-25, 1966 include electroplating processes from a fundamental and applied viewpoint as well as covering other techniques such as vapor-plating, evaporation, passivation, etc.; applications of organic coatings and their properties are also discussed.

"The Principles of Current Methods for the Study of Electrochemical Reactions," by Boris B. Damaskin. Translated from the Russian by Gleb Mamantov. Published by McGraw-Hill Publishing Co., New York, 1967. 110 pages; $4.95.

Covers potentiostatic, galvanostatic, and AC methods for study of reactions. The double layer contributions to the theory of the above methods are not taken into account but are discussed in a separate concluding reaction. Thus, the mathematics are simplified. Circuit diagrams and applications are included.

"Infrared Spectroscopy in Surface Chemistry," by Michael L. Hair. Published by Marcel Dekker, Inc., New York, 1967. 315 pages; $15.75.

Starting with the simple presentation of the theories of surface chemistry and infrared spectroscopy, the book proceeds to treat in detail—adsorbent and adsorbate interactions on known systems such as silica surfaces, metals and metal oxide surfaces. It appears to be an excellent review and starting point for those interested in solid-gas phase interactions.

"Organic Polymers," by Turner Alfrey and Edward F. Gurnee. Published by Prentice-Hall, Inc., Englewood, N. J., 1967. 131 pages; $3.25 (paperbound) $6.00 (cloth bound).

This second volume in the Prentice-Hall series in Materials Science presents an introduction to the use and properties of organic polymers from fundamental considerations. It is in keeping with a trend in the study of materials science of presenting a number of inexpensive monographs that can be tied together to form a study course of many dimensions for both student and active research workers. This particular series seems to be starting off well.

NEWS ITEMS

New Sustaining Member

Syncro Corporation, Oxford, Mich., the parent organization of Syncrotech, Incorporated, Edgerton, Ohio, has recently joined the distinguished list of Sustaining Members of The Electrochemical Society.

Syncro Corporation and its subsidiaries serve industry through the production of various electromagnetic and electrostatic devices. The organization employs roughly 500 employees in facilities located in Michigan and Ohio, producing such items as hand tools, alternator and ignition systems, brake controls, aluminum electrolytic capacitors, doped metal oxide capacitors, delay line components, and thick film circuit components.

1968 Gordon Research Conferences

The Gordon Research Conferences will be held in New Hampshire from June 10 to August 30 at Colby Junior College, New London; New Hampton School, New Hampton; Kimball Union Academy, Meriden; Tilton School, Tilton; Proctor Academy, Andover; and from June 24 to August 23 at the Crystal Inn, Crystal Mountain, Wash.

Meetings are held in the morning and in the evening, Monday through Friday, with the exception of Friday evening.

Requests for attendance at the Conferences, or for additional information,

Continued on page 120C

Out-of-Print Volumes Now Available

The Society has found, regrettably, that its members and subscribers have had difficulty procuring out-of-print volumes of Extended Abstracts of past National Meetings, as well as special volumes of proceedings from these meetings. This fault has now been remedied.

You can now purchase, at reasonable cost, all those volumes, formerly out of print by ordering directly from Johnson Reprint Co., 111 Fifth Ave., New York, N. Y. 10001. An invoice covering each purchase will be included in the shipping package.

Table I lists, by Division, meeting, and volume number, those publications that are now available. Contents of these volumes may be determined by reference to the pertinent meeting program. Spring National Meeting programs are to be found in the March issues and Fall National Meeting programs in the August issues of the JOURNAL. Table II (p. 119C) lists an Index to Society Meeting Symposia 1963—1968.

Corrosion Division does not offer individual Extended Abstract volumes.

Volumes prior to 1963, issued by individual Divisions of the Society, are available from University Microfilms, 300 N. Zeeb Rd., Ann Arbor, Mich. 48106.

Table I.

Meeting Chronology		122	123	124	125	126	127	128	129	130	131	132
Date		Fall 1962	Spr. 1963	Fall 1963	Spr. 1964	Fall 1964	Spr. 1965	Fall 1965	Spr. 1966	Fall 1966	Spr. 1967	Fall 1967
Battery Division	Order No.			B-1		D-1		F-1		H-1		J-1
	Vol. No.	none		8		9		10		11		12
	Pages	128		152		136		113		174		148
Dielectrics & Insulation Division	Order No.		A-2		C-1		E-1		G-1	H-2	I-2	J-2
	Vol. No.		none		1		2		3-1	3-2	4-1	4-2
	Pages		153		52		88		44	77	120	128
Electro-Deposition Division	Order No.			B-2		D-2		F-2		H-3		J-3
	Vol. No.			1		2		3		4		5
	Pages			82		82		66		60		40
Electronics Division*	Order No.		A-1	B-3	C-2	D-3	E-2	E-3	G-2	H-4	I-3	J-4
	Vol. No.		12-1	12-2	13-1	13-2	14-1	14-2	15-1	15-2	16-1	16-2
	Pages		168	144	246	129	339	90	122	90	104	80
Electro-Organic Division	Order No.			B-4			E-3				I-4	
	Vol. No.			1			2				3	
	Pages			40			76				96	
Electrothermics & Metallurgy Division	Order No.		A-3	B-5	C-3	D-4	E-4	F-4	G-3	H-5		J-5
	Vol. No.		1-1	1-2	2-1	2-2	3-1	3-2	4-1	4-2		5
	Pages		82	114	120	182	192	142	62	82		68
Industrial Electrolytic Division	Order No.						E-5		G-4		I-5	
	Vol. No.						1		2		3	
	Pages						48		170		62	
Theoretical Electrochemistry Division	Order No.		A-4		C-4		E-6		G-5		I-6	
	Vol. No.	none	1		2		3		4		5	
	Pages	128	122		208		72		114		128	

*Including Semiconductors and Luminescence

Special Symposium Volumes

Joint Symposium—Electric Insulation, Electronics, and Electrothermics & Metallurgy Divisions	Order No.	A-2
	Vol. No.	none
	Pages	153
Joint Symposium—Dielectrics & Insulation, Electronics, and Electrothermics & Metallurgy Divisions	Order No.	I-1
	Vol. No.	none
	Pages	45

Index to Society Meeting Symposia 1963-1968

BATTERY DIVISION

Symposium	Order No.	Vol. No.	Date
Battery Testing	B-1	8	124 F63
Characteristics of Electrodes	F-1	10	128 F65
Charging Characteristics of Batteries	F-1	10	128 F65
Electrolytic Diaphragms & Battery Separators	E-5	1	127 S65
Fuel Cells	B-1	8	124 F63
Fuel Cells	D-1	9	126 F64
Fuel Cells	H-1	11	130 F66
Fuel Cells	—	—	134 F68
General Sessions	B-1	8	124 F63
General Sessions	D-1	9	126 F64
General Sessions	F-1	10	128 F65
General Sessions	H-1	11	130 F66
General Sessions	J-1	12	132 F67
General Sessions	—	—	134 F68
Leclanche Cells	H 1	11	130 F66
Nature of Silver Oxide	F-1	10	128 F65
Nonaqueous Electrolyte Batteries	J-1	12	132 F67
Sealed Cells & Mechanisms of Operation	B-1	9	126 F64
Sealed Secondary Cells	B-1	8	124 F63
Silver-Zinc Batteries	—	—	134 F68
Zinc Electrode Cells	J-1	12	132 F67

CORROSION DIVISION

Symposium	Order No.	Vol. No.	Date
Corrosion of Architectural Materials	—	—	134 F68
Corrosion in Desalination	—	—	134 F68
Corrosion Inhibition by Organic Compounds	—	—	128 F65
Corrosion Kinetics and Mechanism	—	—	130 F66
Corrosion of Multilayer Deposits	—	—	134 F68
Corrosion by Nonaqueous Media	—	—	128 F65
Electron and Optical Microscopic Studies of Corrosion Processes	—	—	124 F63
General Sessions	—	—	126 F64
General Sessions	—	—	128 F65
General Sessions	—	—	132 F67
General Session	—	—	134 F68
High Temperature Corrosion in Aqueous and Other Media	—	—	124 F63
Liquid Metal Corrosion and Phenomena	D-4	2-2	126 F64
Mechanical Properties of Oxide Corrosion Products	—	—	132 F67
Metallurgical Factors Affecting the Corrosion Processes	—	—	126 F64
Microbiological Corrosion	—	—	128 F65
Properties of Oxide Corrosion Products	—	—	126 F64

DIELECTRICS AND INSULATION DIVISION

Symposium	Order No.	Vol. No.	Date
Anodic Oxides	C-1	1	125 S64
Anodic Oxides	I-2	4-1	131 S67
Anodic Oxide in Films	G-1	3-1	129 S66
Conduction Mechanisms in Dielectric Films	I-2	4-1	131 S67
Conduction Mechanisms in Thin Films	C-1	1	125 S64
Conduction Phenomena in Dielectric Films	G-1	3-1	129 S66
Contact Failure Arising from the Formation of Insulating Film	J-2	4-2	132 F67
Deposited Thin Film Dielectric Materials	—	—	134 F68
Dielectric Oxides	E-1	2	127 S65
Electrets and Related Electrostatic Charge Storage Phenomena	J-2	4-2	132 F67
Electrolytic Capacitor Technology	J-2	4-2	132 F67
Failure Mechanisms in Thin Films	I-2	4-1	131 S67
Ferroelectrics Materials	—	—	134 F68
General Session	A-2	—	124 S63
General Session	C-1	1	125 S64
General Session	E-1	2	127 S65
General Session	K	5-1	133 S68
Growth Mechanisms in Thin Films	I-1	—	131 S67
High Dielectric Ceramics and Crystals	E-1	2	127 S65
Measurement of Thin Film Properties	H-2	3-2	130 F66
Optical Properties of Dielectric Films	K	5-1	133 S68
Photoresist Technology and Applications	K	5-1	133 S68
Polarization in Dielectric Films	G-1	3-1	129 S66
Silicon Nitride	H-2	3-2	130 F66
Theory of Dielectric Behavior	K	5-1	133 S68
Thin Films for Electronic Applications	A-2	—	123 S63

ELECTRODEPOSITION DIVISION

Symposium	Order No.	Vol. No.	Date
Corrosion of Multilayer Deposits	—	—	134 F68
Dielectrophoretic and Electrophoretic Deposition	J-3	5	132 F67
Electrodeposition from Nonaqueous Media	B-2	1	124 F63
Electroforming and Electromachining	H-3	4	130 F66
General Sessions	B-2	1	124 F63
General Sessions	D-2	2	126 F64
General Sessions	F-2	3	128 F65
General Sessions	H-3	4	130 F66
General Sessions	J-3	5	132 F67
Mechanisms of Electrodeposition	D-2	2	126 F64
Physical Properties and Structures of Electrodeposits	B-2	1	124 F63
Precious Metal Plating	D-2	2	126 F64
Thin Film Technology	F-2	3	128 F65

ELECTRONICS DIVISION

Symposium	Order No.	Vol. No.	Date
Color Television Phosphor Screen Applications	E-2	14-1	127 S65
Compound Semiconductors	D-3	13-2	126 F64
Device Technology	G-2	15-1	129 S66
Diffusion	E-2	14-1	127 S65
Diffusion and Oxidation	J-4	16-2	132 F67
Doped Films	J-4	16-2	132 F67
Electrical Contacts to Semiconductors	—	—	134 F68
Epitaxial Growth	J-4	16-2	132 F67
Epitaxy	I-3	16-1	131 S67
Epitaxy	E-2	14-1	127 S65
Epitaxy	D-3	13-2	126 F64
Epitaxy and Compounds	G-2	15-1	129 S66
General Sessions	J-4	16-2	132 F67
General Sessions	K	17-1	133 S68
Growth Mechanisms in Thin Films	I-1	—	131 S67
High Dielectric Ceramics & Crystals	E-1	2	127 S65
Ion Implantation	J-4	16-2	132 F67
Lasers and Related Materials	E-2	14-1	127 S65
Luminescence	A-1	12-1	123 S63
Luminescence	C-2	13-1	125 S64
Luminescence	E-2	14-1	127 S65
Luminescence	G-2	15-1	129 S66
Luminescent and Laser Materials	K	17-1	133 S68
Materials and Processes	D-3	13-2	126 F64
Materials for Thermoelectric, Semiconductor and Optical Applications	A-1	12-1	123 S63
Measurement of Thin Film Properties	H-2	3-2	130 F66
Measurement of Thin Films	F-3	14-2	128 F65
Miscellaneous Semiconductors	H-4	15-2	130 F66
Optical Masers	A-1	12-1	123 S63
Optical Masers	C-2	13-1	125 S64
Passivation	D-3	13-2	126 F64
Passivation	I-3	16-1	131 S67
Photosensitive Materials for Electronic Applications	—	—	134 F68
P-N Junctions	I-3	16-1	131 S67
Preparation and Properties of Single Crystals for Acoustical, Optical and Microwave Applications	K	17-1	133 S68
Processing	E-2	14-1	127 S65
Processing Semiconductors	F-3	14-2	128 F65
Refractory Materials for Electron Devices	B-5	1-2	124 F63
Semiconductors	A-1	12-1	123 S63
Semiconductors	B-3	12-2	124 F63
Semiconductors	C-2	13-1	125 S64
Semiconductors	D-3	13-2	126 F64
Semiconductors	E-2	14-1	127 S65
Semiconductors	F-3	14-2	128 F65
Semiconductors	G-2	15-1	129 S66
Semiconductors	I-3	16-1	131 S67
Semiconductors	J-4	16-2	132 F67
Semiconductor Compounds	F-3	14-2	128 F65
Silicon Growth and Diffusion	H-4	15-2	130 F66
Silicon Oxide and Silicon Technology	H-4	15-2	130 F66
Silicon Oxide and Surfaces	H-4	15-2	130 F66
Structural Features	E-2	14-1	127 S65
Surface Oxides	G-2	15-1	129 S66
Surfaces	E-2	14-1	127 S65
Surfaces of Semiconductors	F-3	14-2	128 F65
Techniques for Devices	A-1	12-1	123 S63
Thin Films	E-2	14-1	127 S65
Thin Films for Electronic Applications	A-2	—	123 S63

ELECTROTHERMICS AND METALLURGY DIVISION

Symposium	Order No.	Vol. No.	Date
Applied Thermodynamics in High Temperature Systems	—	—	127 S65
Carbide Composites	—	—	131 S67
Electrochemical Effects on the Mechanical Properties of Metals	A-3	1-1	123 S63
Electron and Ion Beam Science and Technology	C-3	2-1	125 S64
Electron and Ion Beam Science and Technology	K	6-1	133 S68
Electron Microprobe	D-4	2-2	126 F64
General Sessions	E-4	3-1	127 S65
General Sessions	F-4	3-2	128 F65
General Sessions	G-3	4-1	129 S66
General Sessions	J-5	5	132 F67
General Session	K	6-1	133 S68
General Session	H-5	4-2	130 F66
Graphite	G-3	4-1	129 S66
Growth Mechanisms in Thin Films	I-1	—	131 S67
High Temperature Technology	A-3	1-1	123 S63
Liquid Metal Corrosion and Phenomena	D-4	2-2	126 F64
Materials in Space (Educational Lecture)	—	—	131 S67
Molten Salts	E-4	3-1	127 S65
Oxidation in the Reentry Environment	H-5	4-2	130 F66
Plasmas and High Temperature Materials	H-5	4-2	130 F66

Preparation and Purification of Ultra-Pure Materials	—	—	134 F68
Protective Coatings	J-5	5	132 F67
Refractory Materials for Electron Devices	B-5	1-2	124 F63
Solid-Vapor Reactions	A-3	1-1	123 S63
Strengthening Mechanisms in Nonmetallics	E-4	3-1	127 S65
Thin Films for Electronic Applications	A-2	—	123 S63
Ultrapure Materials	B-5	1-2	124 F63
Zirconium and Its Alloys	F-4	3-2	128 F65

ELECTRO-ORGANIC DIVISION

Symposium	Order No.	Vol. No.	Date
Biochemical Energy Conversion Processes	B-4	1	124 F63
Electrochemical Oxidation of Organic Compounds	I-4	3	131 S67
Electrochemical Reactions of Organic Molecules in Nonaqueous Solutions	K	3	133 S68
Electrochemistry in Nonaqueous Media	I-4	3	131 S67
Elucidation of Organic Electrodes Processes	E-3	2	127 S65
General Session	B-4	1	124 F63
General Session	E-6	3	127 S65
General Session	E-3	2	127 S65
Industrial Electro-Organic Chemistry	E-3	2	127 S65
Industrial Electro-Organic Processes	I-4	3	131 S67
Radical Formation in Electro-Organic Reactions	B-4	1	124 F63

INDUSTRIAL ELECTROLYTIC DIVISION

Symposium	Order No.	Vol. No.	Date
Advances in the Chlor-Alkali Industry	G-4	2	129 S66
Chlorates and Perchlorates	K	4	133 S68
Current Distribution and Electrode Design	I-5	3	131 S67
Electrodialysis	K	4	133 S68
Electrolytic Diaphragms & Battery Separators	E-5	1	127 S65
Gas Electrodes	G-4	2	129 S66
General Sessions	—	—	123 S63
General Sessions	C-4	2	125 S64
General Sessions	K	4	133 S68
Graphite	G-3	4-1	129 S66
Industrial Electro-Organic Chemistry	E-3	2	127 S65
Mass Transport in Electrochemical Processes	C-4	2	125 S64
Production of Chlorine without Caustic	E-5	1	127 S65
Production and Uses of Mercury Cell Sodium Amalgam	I-5	3	131 S67

THEORETICAL ELECTROCHEMISTRY DIVISION

Symposium	Order No.	Vol. No.	Date
Adsorption in Electrode Processes	K	6	133 S68
Anodic Oxide Films	A-4	1	123 S63
Electrochemical Reactions of Organic Molecules in Nonaqueous Solutions	K	6	133 S68
Electrode Processes	G-6	—	129 S66
Electrolytic Solutions	C-4	2	125 S64
Elucidation of Organic Electrodes	E-3	2	127 S65
Fuel Cells	D-1	9	126 F64
General Sessions	A-4	1	123 S63
General Sessions	G-5	4	129 S66
General Sessions	I-6	5	131 S67
General Session	K	6	133 S68
Mechanisms of Electrodeposition	D-2	2	126 F64
Molten Salts	E-4	3-1	127 S65
Solid Electrolytes	A-4	1	123 S63
Structure and Characteristics of Surface Reaction Products	I-6	5	131 S67

News Items continued

should be addressed to W. George Parks, Director, Gordon Research Conferences, University of Rhode Island, Kingston, R. I. 02881. Mail for the office of the Director from June 10 to August 30, 1968 should be addressed to W. George Parks, Director, Gordon Research Conferences, Colby Junior College, New London, N. H. 03257.

Dates and topics of interest to ECS members are as follows:

Colby Junior College
New London, N. H.

June 24-28 Catalysis
July 1-5 Polymers
July 15-19 Scientific Information Problems in Research
July 22-26 Corrosion
July 29-Aug. 2 Elastomers
Aug. 19-23 Separation and Purification

New Hampton School
New Hampton, N. H.

June 10-14 Environmental Sciences: Water
July 8-12 Statistics in Chemistry and Chemical Engineering
July 15-19 Radiation Chemistry
July 22-26 Organic Reactions and Processes
Aug. 12-16 Analytical Chemistry

Kimball Union Academy
Meriden, N. H.

June 17-21 Research at High Pressure
July 15-19 Particle-Solid Interactions
July 22-26 Chemistry at Interfaces
July 29-Aug. 2 Solid State Studies in Ceramics
Aug. 12-16 Chemistry and Physics of Solids
Aug. 19-23 Infrared Spectroscopy
Aug. 26-30 Non-linear Optic Effects

Tilton School
Tilton, N. H.

June 17-21 Interaction and Transport
July 8-12 Chemistry and Physics of Space
Aug. 12-16 Dissolution and Crystallization of Calcium Phosphates
Aug. 19-23 Thin Films
Aug. 26-30 Physics and Physical Chemistry of Biopolymers

Proctor Academy
Andover, N. H.

June 10-14 Dielectric Phenomena
June 17-21 Dynamics of Molecular Collisions
July 8-12 Radical Ions
July 29-Aug. 2 Energy Coupling Mechanisms

Crystal Inn
Crystal Mountain, Wash.

July 1-5 Chemistry and Physics of Coatings and Films
July 8-12 Physical Metallurgy
July 22-26 Quantum Solids and Fluids
July 29-Aug. 2 High Temperature Chemistry
Aug. 12-16 Chemistry and Physics of Paper

ADVERTISER'S INDEX

POSITIONS AVAILABLE

Please address replies to the box number shown c/o The Electrochemical Society, Inc., 30 East 42 St., New York, N. Y. 10017.

Manager, Applied Physics—excellent, established company seeks top-level scientist to head corporate applied research department, in areas of solid-state semiconductors, thin films, thick films, integrated and hybrid circuitry. Manager Electrochemistry—with extensive applied research experience in power sources such as batteries or fuel cells to develop new product lines. Reply Box B-33.

Research Chemists—major research and development projects in electrochemistry with major emphasis on electroplating. Reply Box B-34.

Materials and Processes Development—to develop workable solid-state memory and logic monolithic chip materials and processes for masking, photoresist, etching, oxidizing, diffusing, evaporating, and sputtering technologies. Reply Box B-35.

ATTENTION, MEMBERS AND SUBSCRIBERS

Whenever you write to The Electrochemical Society about your membership or subscription, please include your Magazine address label to ensure prompt service.

ATTACH LABEL HERE

Change of Address

To change your address, please give us five weeks' advance notice. Place magazine address label here. Print your NEW address below. If you have any question about your subscription or membership, place your magazine label here and clip this form to your letter.

Mail to the Circulation Department, The Electrochemical Society, Inc., 30 East 42 St., New York, N. Y., 10017.

name

address

city state zip code

Call for Papers
134th National Meeting
Montreal, October 6-11, 1968

Divisions which have scheduled sessions are listed overleaf, along with symposium topics.

1. Symposium Papers.

Authors desiring to contribute papers to a symposium listed overleaf should check first with the symposium chairman to ascertain appropriateness of the topic.

2. General Session Papers.

Each of the several Society Divisions which meets in Montreal can plan a general session. If your paper does not fit readily into a planned symposium, you should specify "General Session."

3. To Submit a Meeting Paper.

Each author who submits a paper for presentation at a Society National Meeting should do three things:

A—Determine whether the meeting paper is to be submitted to a Society journal for publication. If so, see below for details.

B—No later than May 15, 1968, submit three copies, on the form printed overleaf, of a 75-word abstract of the paper to be delivered. You may use a facsimile of the form if necessary. These abstracts are required for publication in the printed program of the meeting.

C—No later than July 1, 1968, submit three copies of an extended abstract of your paper. See below for details. No deadline extension is possible.

Send all material to The Electrochemical Society, Inc., 30 East 42 St., New York, N. Y. 10017.

4. Meeting Paper Acceptance.

Notification of acceptance for meeting presentation, along with scheduled time, will be mailed to authors with general instructions no earlier than two months before the meeting. Those authors who require more prompt notification are requested to submit with their abstracts a self-addressed postal card with full author-title listing on the reverse.

5. Extended Abstract Book Publication.

Division programs will be the subject of an extended abstract volume in a manner prescribed by the Society Board of Directors. The volume is published by photo offset directly from typewritten copy submitted by the author. Therefore, special care should be given to the following typing instructions to insure legibility.

A—Abstracts are to be from 500-1000 words in length (two pages single-spaced) and are to contain to whatever extent practical all significant experimental data to be presented during oral delivery.

B—Please send original and two copies of the abstract typed single-spaced. Use white bond paper, size 8½ x 11 inches, with 1¼ margins on all sides. Typing guide forms are available from Symposium Session Chairman and from National Headquarters.

C—Title of paper should be in capital letters. Author(s) name and affiliation should be typed immediately below. It is not necessary in the heading or body to designate paper as "Extended Abstract" or to quote the divisional symposium involved.

D—Submit all copy, including figures, symbols and corrections, in black ink. No handwritten corrections, please. Submit graphs on onion skin without grids, or on graph paper specifically designed for offset reproduction; strip-on tape is acceptable.

E—Paste figures within typing dimensions indicated, with lettering no smaller than ⅛ inch. Submit only the important illustrations. Avoid use of half-tones except where absolutely necessary. Type captions no wider than figure dimensions and paste in proper place in the abstract. Place figure caption at bottom of figure. Place table title at top of table.

F—Mail to The Electrochemical Society. Inc., unfolded.

G—Please note that the extraordinarily low price of the extended abstract volume is made possible only through your strict adherence to these instructions. Any deviation threatens this low cost.

6. Manuscript Publication in a Society Journal.

Presentation of a paper at a Society National Meeting incurs no obligation to publish. However, all meeting papers upon presentation become the property of The Electrochemical Society, Inc., and should be submitted as promptly as possible in full manuscript form in order to be considered for publication in a Society publication. The Society "Instructions to Authors," are available from National Headquarters, set forth manuscript style and format.

Montreal Meeting Symposia Plans—Fall 1968

No later than May 15, 1968, submit three copies, on the form overleaf, of a 75-word abstract of the paper to be delivered. No later than July 1, 1968, submit three copies of an extended abstract, 500-1000 words. Send all material to The Electrochemical Society, Inc., 30 E. 42 St., New York, N. Y. 10017

Battery Division Symposia Plans

The program for the Fall Meeting in Montreal, October 6-11, 1968 in addition to a general session will include the regular biennial symposium on Fuel Cells and a special symposium on Silver-Zinc Batteries.

Fuel Cells

Papers are solicited from those active in research and development on fuel cells of all types. Contributions ranging from fundamental aspects of electrode behavior and electrocatalytic phenomena to performance of fuel cells and fuel cell batteries in relation to design are desired. Questions and suggestions concerning the program should be addressed to the Program Chairman, R. R. Witherspoon, General Motors Research Laboratories, Warren, Mich. 48090.

Silver-Zinc Batteries

A symposium consisting completely of invited papers and reviews thereof will be held as a separate session lasting approximately four and one-half days. The symposium, cosponsored by the Air Force Aero Propulsion Laboratory, will feature papers on the history, electrode chemistry and electrochemistry, thermodynamics, mass transport, materials and manufacturing techniques, separators, and specifications, applications and performance of silver-zinc batteries. After editing, the contents of the symposium will be published as a hard-bound book which will bring together for the first time under one cover the science and technology of this high-energy electrochemical battery. This is not a closed meeting; attendance by all will be welcome.

Chairman for this symposium is J. J. Lander, Delco-Remy, Division of General Motors, Anderson, Ind. 46011.

Corrosion Division Symposia Plans

Three symposia in addition to general sessions are planned for the Fall 1968 Meeting of the Corrosion Division in Montreal.

Corrosion of Multilayer Deposits

Corrosion of Multilayer Deposits will be held jointly with the Electrodeposition Division. Chairmen for this symposium are: Karl Willson, Harshaw Chemical Co., 1945 E. 97 St., Cleveland, Ohio 44106 and E. J. Seyb, Jr., M&T Chemicals Inc., 1700 East Nine Mile Rd., Detroit, Mich. 48220.

See listing under **Corrosion and Electrodeposition Symposium Plans.**

Corrosion in Desalination

Corrosion in Desalination will be chaired by M. J. Pryor, Olin Matheson Chemical Corp., Metals Research Division, 275 Winchester Ave., New Haven, Conn. 06511.

Corrosion of Architectural Materials

Corrosion of Architectural Materials will be chaired by Henry Leidheiser, Jr., Center for Surface and Coatings Research, Lehigh University, Bethlehem, Pa. 18015.

Those desiring to present papers at these symposia are requested to communicate directly with the symposium chairman. Several sessions of general papers will also be included.

The Corrosion Division will also institute on a trial basis a short session devoted to research results of newsworthy interest. Presentation time will be limited to 5 minutes and an abstract must be available at the meeting for posting. Permission to appear on the program must be obtained from the Chairman of the Division at the meeting. No advance permission is required.

Corrosion and Electrodeposition Divisions Symposium Plans

Corrosion of Multilayer Deposits

The Corrosion and Electrodeposition Divisions have scheduled a joint symposium on Corrosion of Multilayer Deposits for the Fall 1968 Meeting in Montreal.

This symposium will include reports on systems including at least one applied metallic deposit (vapor, electroless or electrolytic). Subsequent or concurrent layers may be metallic or nonmetallic. Papers are particularly solicited on chromium-chromium oxide on steel, conversion and organic coatings over metal layers as well as multilayer metal coatings over metallic or plastic substrates.

Inquiries and suggestions should be addressed to either of the Symposium Chairmen: E. J. Seyb, M&T Chemicals Inc., 1700 East Nine Mile Rd., Detroit, Mich. 48220 or K. S. Willson, Harshaw Chemical Co., 1945 East 97 St., Cleveland, Ohio 44106.

Dielectrics and Insulation Divisions of Symposium Plans

Deposited Thin Film Dielectric Materials

A symposium on Deposited Thin Film Dielectric Materials is scheduled for the Fall 1968 Meeting in Montreal.

There will be a number of invited papers; contributed papers are also being solicited.

Categories of subject matter being actively considered for the symposium include: (a) studies on the electrical and mechanical properties of deposited thin film dielectrics; (b) new techniques for the deposition of thin film dielectrics; (c) properties and applications of thin film dielectrics.

This symposium is particularly directed to the new sputtering technology, new means of evaporative deposition, and recent advances in vapor deposition techniques for preparation of dielectric thin films.

Suggestions and questions are welcome, and should be directed to the Chairman of the Symposium. F. Vratny, Bell Telephone Laboratories, Inc., Murray Hill, N. J., is Chairman.

Ferroelectrics

A symposium on Ferroelectric Materials is scheduled. The following topic areas are being actively considered for the sessions: (a) growth and characterization of ferroelectric crystals, (b) phenomenological and theoretical treatments of ferroelectricity, (c) dielectric properties of single crystals, polycrystal and composite materials, (d) domain structure and polarization reversal, (e) optical and electro-optic properties, and (f) device applications of ferroelectric materials.

There will be a number of invited speakers; contributed papers are also being solicited. Suggestions and questions concerning this symposium are welcome, and should be directed to the Chairman, Leslie E. Cross, Materials Research Laboratory, The Pennsylvania State University, University Park, Pa. 16802.

Electronics Division Symposia Plans

Electrical Contacts to Semiconductors

The Electronics Division is sponsoring a special symposium on Electrical Contacts to Semiconductors to be held at the Fall 1968 Meeting in Montreal. The fundamentals of the physics, chemistry, and metallurgy of ohmic contacts will be explored, and advances of technological importance will be discussed. The program is to include both con-

tributed papers and invited speakers. Papers are being solicited on such topics as: theory of ohmic contacts, techniques of ohmic contact fabrication, evaluation of contact properties, modes of contact failure, composite contacts, special property contacts (e.g. optical transparency, thermal conductivity).

Any questions or suggestions should be addressed to the Symposium Chairman, Bertram Schwartz, Bell Telephone Laboratories, Inc., Murray Hill, N. J. 07974.

Photosensitive Materials for Electronic Applications

This symposium will cover the properties and uses of photosensitive materials in the electronics industry. Topics which will be considered for the program include xerography, photochromism, novel photographic techniques, photochemistry (e.g. photoresists), vidicons, storage phosphors etc. Papers on the above or closely related topics are solicited.

Questions concerning this symposium should be addressed to the Symposium Chairman, Erik M. Pell, Manager, Physics Research Laboratory, Xerox Corp., 800 Phillips Rd. Webster, N. Y. 14580.

Electrothermics and Metallurgy Division Symposium Plans

Preparation and Purification of Ultra-Pure Metals

A symposium on Preparation and Purification of Ultra-Pure Metals in addition to general sessions will be held at the Fall 1968 Meeting in Montreal. This symposium forms the first of a series planned by the Division to deal with materials of particular interest to Society members.

Papers are solicited from those active in research and development of these metals. Invited key-note speakers will survey theory and methods for preparation, purification, and determination of residual elements in ultra-pure metals.

Sessions will encompass contributions on preparation by electrochemical deposition, electron beam melting and volatilization; purification by zone refining, electrochemical and vaporization methods, determination of residual elements by micro-chemical techniques, and influence of residual elements on chemical and physical properties.

Inquiries and suggestions should be directed to either of the cochairmen: W. C. Cooper, Noranda Research Centre, 240 Hymus Blvd., Pointe Claire, Quebec, Canada or W. W. Smeltzer, Department of Metallurgy and Materials Science, McMaster University, Hamilton, Ont., Canada.

75-Word Abstract Form—Montreal Meeting October 6-11, 1968

Mail no later than May 15, 1968 to The Electrochemical Society, Inc., 30 East 42 St., New York, N. Y. 10017

Abstract No......
(do not write in this space)

.....
(Title of paper)

.....

.....
(Author) (Underline name of author presenting paper)

.....
(Business Affiliation)

.....
(Address)

(Type your abstract in this space—double space with two carbon copies on plain white paper.)

Division and Symposium .....

Do you require any audiovisual equipment? ☐ **35 mm (2x2 in.) slide projector;** ☐ **3¼ x 4 in. slide projector;** ☐ **other (specify)** _____.

Is a full length paper on this work to be submitted for Society publication? ☐ **Yes** ☐ **No**

Papers presented before a national technical meeting become the property of the Society and may not be published elsewhere without written permission of the Society.

For Office Use

Extended Abstract rec'd: ..... **requested:** .....

Sent to: .....

75-word Abstract sent to: ..... **date:** .....

SUSTAINING MEMBERS (CONTINUED)

Fairchild Semiconductor Corp.,
Palo Alto, Calif.

FMC Corp.,
Inorganic Chemicals Div.,
Buffalo, N. Y.
Inorganic Chemicals Div.,
South Charleston, W. Va.

Foote Mineral Co.,
Exton, Pa.

Ford Motor Co.,
Dearborn, Mich.

General Motors Corp.,
Allison Div., Indianapolis, Ind.
Delco-Remy Div., Anderson, Ind.
Research Laboratories Div., Warren, Mich.

General Telephone & Electronics Laboratories, Inc., Bayside, N. Y.

Globe-Union, Inc.,
Milwaukee, Wis.

B. F. Goodrich Chemical Co.,
Cleveland, Ohio

Gould-National Batteries, Inc.,
Minneapolis, Minn.

Great Lakes Carbon Corp.,
New York, N. Y.

Harshaw Chemical Co.,
Cleveland, Ohio (2 memberships)

Hercules Inc.,
Hercules Research Center,
Technical Information Div.,
Wilmington, Del.

Hill Cross Co., Inc.,
West New York, N. J.

Honam Electric Industrial Co.,
Kwangju City, Korea

Honeywell, Inc.,
Minneapolis, Minn.

Hooker Chemical Corp.,
Niagara Falls, N. Y. (2 memberships)

HP Associates,
Palo Alto, Calif.

Hughes Research Laboratories, Div. of Hughes Aircraft Co., Malibu, Calif.

International Business Machines Corp.,
New York, N. Y.

International Minerals & Chemical Corp.,
Skokie, Ill.

International Resistance Co.,
Philadelphia, Pa.

ITT Federal Laboratories, Div. of International Telephone & Telegraph Corp.,
Nutley, N. J.

Jones & Laughlin Steel Corp.,
Pittsburgh, Pa.

K. W. Battery Co.,
Skokie, Ill.

Kaiser Aluminum & Chemical Corp.,
Metals Div. Research,
Permanente, Calif.
Div. of Metallurgical Research,
Spokane, Wash.

Kawecki Chemical Co.,
Boyertown, Pa.

Kennecott Copper Corp.,
New York, N. Y.

Leesona Moos Laboratories, Div. of Leesona Corp., Great Neck, N. Y.

Arthur D. Little, Inc.,
Cambridge, Mass.

Lockheed Aircraft Corp.,
Missiles & Space Div.,
Sunnyvale, Calif.

Mallinckrodt Chemical Works,
St. Louis, Mo.

P. R. Mallory & Co.,
Indianapolis, Ind.

Melpar, Inc.,
Falls Church, Va.

Mobil Oil Corp.,
Dallas, Texas

Monsanto Chemical Co.,
St. Louis, Mo.

M&T Chemicals Inc.,
Detroit, Mich.

Nalco Chemical Co.,
Chicago, Ill.

National Cash Register Co.,
Dayton, Ohio

National Lead Co.,
New York, N. Y.

National Steel Corp.,
Weirton, W. Va.

North American Aviation, Inc.,
El Segundo, Calif.

Northern Electric Co.,
Montreal, Que., Canada

Norton Research Corp.,
Cambridge, Mass.

Owens-Illinois Glass Co.,
Toledo, Ohio

Pennsalt Chemicals Corp.,
Philadelphia, Pa.

Phelps Dodge Refining Corp.,
Maspeth, N. Y.

Philips Laboratories, Inc.,
Briarcliff Manor, N. Y.

Pittsburgh Plate Glass Co.,
Chemical Div.,
Pittsburgh, Pa.

Potash Co. of America,
Carlsbad, N. Mex.

Radio Corp. of America
Electronic Components and Devices,
Lancaster, Pa.
RCA Victor Record Div.
Indianapolis, Ind.

Republic Foil Inc.,
Danbury, Conn.

Reynolds Metals Co.,
Richmond, Va.

Shawinigan Chemicals Ltd.,
Montreal, Que., Canada

Sonotone Corp.,
Elmsford, N. Y.

Sprague Electric Co.,
North Adams, Mass.

Stackpole Carbon Co.,
St. Marys, Pa.

The Standard Oil Company of Ohio,
Cleveland, Ohio

Stauffer Chemical Co.,
Dobbs Ferry, N. Y.

Syncro Corp.,
Oxford, Mich.

Texas Instruments, Inc.,
Dallas, Texas
Metals and Controls Corp.,
Attleboro, Mass.

3M Company,
St. Paul, Minn.

Titanium Metals Corp. of America,
Henderson, Nev.

Tyco Laboratories, Inc.,
Waltham, Mass.

Udylite Corp.,
Detroit, Mich. (4 memberships)

United States Steel Corp.,
Pittsburgh, Pa.

Upjohn Co.,
Kalamazoo, Mich.

Varian Associates,
Palo Alto, Calif.

Western Electric Co., Inc.,
Chicago, Ill.

Wyandotte Chemicals Corp.,
Wyandotte, Mich.

Yardney Electric Corp.,
New York, N. Y.

THE ELECTROCHEMICAL SOCIETY PATRON MEMBERS

Aluminum Co. of Canada, Ltd., Montreal, Que., Canada

Dow Chemical Co.
Chemicals Dept., Midland, Mich.
Metals Dept., Midland, Mich.

General Electric Co.
Capacitor Dept., Hudson Falls, N. Y.
Chemical Laboratory, Knolls Atomic Power Laboratory, Schenectady, N. Y.
Chemical Systems and Processes Laboratory, Research and Development Center, Schenectady, N. Y. (3 memberships)
Direct Energy Conversion Operation, West Lynn, Mass.
Lamp Div., Cleveland, Ohio
Materials & Processes Laboratory, Large Steam Turbine-Generator Dept., Schenectady, N. Y.

The International Nickel Co., Inc., New York, N. Y.

Olin Mathieson Chemical Corp.
Chemicals Div., Research Dept., New Haven, Conn.

Union Carbide Corp.
Divisions:
Carbon Products Div., New York, N. Y.
Consumer Products Div., New York, N. Y.

Westinghouse Electric Corp.
Electronic Tube Div., Elmira, N. Y.
Lamp Div., Bloomfield, N. J.
Molecular Electronics Div., Elkridge, Md.
Semiconductor Div., Youngwood, Pa.
Research Laboratories, Pittsburgh, Pa.

THE ELECTROCHEMICAL SOCIETY SUSTAINING MEMBERS

Airco Speer Electrodes and Anodes, St. Marys, Pa.

Allen-Bradley Co., Milwaukee, Wis.

Allied Chemical Corp., General Chemical Div., Morristown, N. J.

Aluminum Co. of America, New Kensington, Pa.

American Metal Climax, Inc., New York, N. Y.

American Potash & Chemical Corp., Los Angeles, Calif.

American Smelting and Refining Co., South Plainfield, N. J.

American Zinc Co., St. Louis, Mo.

American Zinc Co. of Illinois, East St. Louis, Ill.

The M. Ames Chemical Works, Inc., Glens Falls, N. Y.

Ampex Corp., Redwood City, Calif.

Armco Steel Corp., Middletown, Ohio

Bell Telephone Laboratories, Inc., New York, N. Y. (2 memberships)

Bethlehem Steel Corp., Bethlehem, Pa. (2 memberships)

Boeing Co., Seattle, Wash.

Burndy Corp., Norwalk, Conn.

Canadian Industries Ltd., Montreal, Que., Canada

Carborundum Co., Niagara Falls, N. Y.

Chrysler Corp., Detroit, Mich.

Clevite Corp.
Burgess Battery Div., Freeport, Ill. (2 memberships)

Cominco Ltd., Trail, B. C., Canada (2 memberships)

Corning Glass Works, Corning, N. Y.

Cyclops Corp., Universal-Cyclops Specialty Steel Div., Bridgeville, Pa.

Diamond Alkali Co., Painesville, Ohio

Wilbur B. Driver Co., Newark, N. J.

E. I. du Pont de Nemours & Co., Inc., Wilmington, Del.

Eagle-Picher Industries, Inc., Electronics Div., Joplin, Mo.

Eastman Kodak Co., Rochester, N. Y.

Eltra Corp.
Prestolite Div., Toledo, Ohio
C&D Batteries, Conshohocken, Pa.

Engelhard Industries, Inc., Newark, N. J.

The Eppley Laboratory, Inc., Newport, R. I.

ESB Inc., Philadelphia, Pa. (2 memberships)

Esso Research and Engineering Co., Engineering Technology Div., Florham Park, N. J.

Exmet Corp., Bridgeport, Conn.